MODELLING AND APPLICATION OF ADVANCED THERMAL STORAGE MATERIALS

A Thesis Presented

by

Anthony Joseph Rawson

BEng (Mechanical) (Honours 1) BSci (Physics) (Distinction) (*Newcastle)*

to

The Graduate Office of the University of Newcastle

In Partial Fulfilment of the Requirements

for the Degree of Doctor of Philosophy

Specialising in Mechanical Engineering

Submitted January, 2016

Supervisors – Prof. Erich Kisi and Dr Heber Sugo

This thesis contains no material which has been accepted for the award of any other degree or diploma in any university or other tertiary institution and, to the best of my knowledge and belief, contains no material previously published or written by another person, except where due reference has been made in the text. I give consent to the final version of my thesis being made available worldwide when deposited in the University's Digital Repository, subject to provisions of the Copyright Act 1968.

Anthony J. Rawson,

ABSTRACT

Instantaneous availability of power is taken for granted in much of the developed world. Provided a fuel source is unlimited and readily available, the expectation of instant power is readily fulfilled with available technology. However, it is now accepted that human kind's most utilised fuels (coal, oil and natural gas) are in fact diminishing and their availability cannot be guaranteed as demand outstrips supply. Not only supply limitations exist, the burning of these fuels contributes heavily to dangerous climate change. Thus technology needs to be developed to efficiently utilise fuels intermittently or take advantage of other energy sources which may also be intermittent.

Thermal energy storage devices store heat energy through sensible heating, a phase change or a combination of the two. A device can be coupled to a power cycle to provide thermal inertia to the system. Power cycles that generate electricity from an intermittent heat source are an obvious application. Applications also exist in industrial processes requiring continuous heat for drying or a chemical reaction and control of air temperature in sensitive environments.

Many thermal energy storage devices exist, tailored to particular temperature ranges and storage capacities. This thesis introduces the Miscibility Gap Alloy as a potential thermal storage technology. Miscibility Gap Alloys overcome a number of the shortcomings of molten salt, paraffin and sensible storage media but their properties are not yet well communicated.

Material properties, lifetime estimates, economic characteristics and implementations of Miscibility Gap Alloys are discussed in this dissertation. Through

analysis of these aspects a number of novel methodologies, theories and devices were developed.

The Lattice Monte Carlo method was successfully employed to model effective conductivity of binary composites. The results of these analyses and existing homogenisation models were generalised for volume fraction and constituent conductivity ratio through a novel concept titled ‘microstructural efficiency’. This work enabled the effective thermal conductivity (and indeed any 2^{nd} rank tensor property obeying Fick’s Law) to be estimated with great accuracy for a number of idealised and common morphologies with generality in volume fraction and conductivity ratio of constituents.

Best practice manufacturing methods for different Miscibility Gap Alloys were identified through experiment and presented. This led to knowledge of the morphology of the materials (including potential porosity). From this, good estimates were made of all material properties relevant to the alloys use as thermal storage. The hypothesised material property advantages of Miscibility Gap Alloys are thus confirmed and compared with the existing state of the art.

A discussion of the long term behaviour of Miscibility Gap Alloys follows. Consideration is given to diffusion as well as mechanical and chemical dominated aging mechanisms. It was found that diffusion dominated aging is most likely for systems with non-negligible solubility of the components and where discrete large powders undergo large temperature changes through cycling. Mechanical effects should not contribute beyond the first few cycles as the matrix deforms to accommodate any mismatch in thermal expansion. Chemical aging is likely for systems exposed to air or water but may be mitigated through isolation of the material.

Establishment of material and long term properties of the alloys enables a discussion of the comparative economics of using Miscibility Gap Alloys as thermal storage. The alloys are shown to be extremely competitive compared to existing thermal energy storage solutions. They have a higher capital cost generally, due to the high cost of metals. However, the infrastructure and maintenance costs required are a fraction of that for most other thermal storage media.

Finally a number of potential implementations are introduced ranging from thermal inertia for power production to heating for the drying of foods. Detailed calculations and engineering drawings are provided for an air heater device intended for room heating. Specific methods of storage for concentrated solar thermal plants are described before more exotic implementations are presented.

The thesis concludes with a summary of work and a critical evaluation of the potential of Miscibility Gap Alloys as thermal storage media. Potential work for future research is provided with guidance as to how it might be initiated.

CITATIONS

Material from this thesis has been published in the following form:

A.J. Rawson, H. Sugo, E. Kisi, T. Fiedler, Effective Conductivity of Cu-Fe and Sn-Al Miscibility Gap Alloys, International Journal of Heat and Mass Transfer, 77 (2014) 395-405.

A.J. Rawson, H. Sugo, E. Kisi, Characterising Thermal Properties of Miscibility Gap Alloys for Thermal Storage Applications, in: Solar2014: The 52nd Annual Conference of the Australian Solar Council, Melbourne, Australia, 2014.

A.J. Rawson, E. Kisi, C. Wensrich, Microstructural Efficiency: Structured Morphologies, International Journal of Heat and Mass Transfer, 81 (2014) 820-828.

H. Sugo, D. Cuskelly, A. Rawson, E. Kisi, High Conductivity Phase Change Materials for Thermal Energy Storage - Miscibility Gap Alloys, in: Solar2014: The 52nd Annual Conference of the Australian Solar Council, Melbourne, Australia, 2014

T. Fiedler, I. Belova, A. Rawson, G. Murch, Optimized Lattice Monte Carlo for Thermal Analysis of Composites, Computational Materials Science, 95 (2014) 207-212.

ACKNOWLEDGEMENTS

The author of this dissertation would like to acknowledge the following professional organisations:

The University of Newcastle, for supervision use of facilities and general support through the duration of the candidates PhD.

The Australian Renewable Energy Agency (ARENA), formerly the Australian Solar Institute (ASI), for a motivating scholarship.

The author would like to specially acknowledge the hard work and direction provided from his supervisors:

Professor Erich Kisi

Dr. Heber Sugo

The author of this dissertation would like to acknowledge the following friends, colleagues and family:

Dr. Thomas Feidler

Dr. Chris Wensrich

Professor Graeme Murch

Professor Irina Belova

Professor Chris Howard

Professor Michael Carpenter

Jemima Emily Jackson

Lynette and Alan Rawson

Shaun Joseph Carter

The Condors:

~~David~~ Bradney

Mohammed ‘Moei’ Hasan

Samuel ‘Swann’ Evans

Syed Imran ‘Dhost’ Shafiq

Dylan ‘Dyran’ Cuskelly

Joss ‘Special K’ Kesby

Alex ‘Postie’ Post

Hoda

TABLE OF CONTENTS

LIST OF TABLES

LIST OF FIGURES

NOMENCLATURE

Latin alphabet

Symbol		As a super/subscript
A	Area	
C	Heat Capacity, Stiffness	
D	Diffusivity	
E	Young's Modulus	
F	Helmholtz Free Energy	
G	Gibb's Free Energy	
H	Enthalpy	
L	Length	Liquid
N	Number, Number of atoms	
Q	Heat Transfer	
R	Universal Gas Constant	
S	Entropy, Compliance	
T	Temperature	
U	Internal Energy	
V	Volume	
c	Mass Specific Heat Capacity, Cost, Concentration	
d	Dimensionality	
e	Thermal Effusivity	Per Unit Energy
h	Mass Specific Enthalpy	
i		Index

Symbol		As a super/subscript
k	Thermal Conductivity	
m	Mass	
n	Number of moles	Index
p	Pressure	Constant Pressure (Isobaric)
q	Heat Flux	
r	Radius, Rate	
t	Time	Total
u	Mass Specific Internal Energy, Load factor	
v	Mass Specific Volume, Velocity	
Constant Volume (Isochoric)		
x	Cartesian coordinate, Molar Composition	

Greek Alphabet

Symbol		As a super/subscript
Δ	Increment of …	
∇	Grad of …	
α	Thermal Diffusivity	A-rich alpha phase (matrix)
β		B-rich beta phase (distributed)
γ	Surface Energy	
ε	Strain, Linear Thermal Expansion Coefficient	
η	Efficiency, Equilibrium Approach	
κ	Phase Gradient Energy	
λ	Latent Heat of Transition	
μ	Chemical Potential, Dynamic Viscosity	Microstructural
ν	Poisson's Ratio	
ρ	Density	
φ	Volume Fraction	
ϕ		Phase
ψ	Mass Fraction	

Abbreviations

Symbol		As a super/subscript
Nu	Nusselt Number	
Pr	Prandtl Number	
Re	Reynolds Number	
atm		Atmospheric
bcc	Body Centred Cubic Crystal Structure	
bct	Body Centred Tetragonal Crystal Structure	
fcc	Face Centred Cubic Crystal Structure	

Other Notations Let a be arbitrary

$\vec{a}$	Vector
$\underline{a}$	Tensor
$\dot{a}$	Temporal Rate of Change

CHAPTER 1: INTRODUCTION AND SYNOPSIS

The first brief chapter of this thesis provides a motivational background to the reader who may then appreciate the context and detail of the Author's inquiry into Miscibility Gap Alloys as a thermal storage solution.

A nine year-old report written at the bequest of NATO stated in its preface that 'The world must prepare for a future without fossil fuels' [1]. For humans to enjoy this prospective 'utopia' technology must advance to accommodate our current and future lifestyles. This current dissertation is one of many that will contribute to independence from finite energy resources and perhaps even the schisms that result from competition over such assets.

All renewable resources (perhaps with the exception of hydro and geothermal resources) are intermittent. A power cycle operating directly from them cannot generate continuous electrical power. If a portion of the renewable energy source could be stored during the periods it was exploitable, constant supply could be attained. Energy storage methods are as diverse as energy sources and vary in operation, expense and durability

This thesis is concerned mainly with solar radiation as an energy source. The Suns electromagnetic energy is converted to heat when absorbed by a material. The material will experience an increase in internal energy, physically manifesting as an increase in temperature or causing a phase transformation to occur. Conversion of this internal energy to a convenient form for human consumption requires a power cycle. Contemporary humanity prefers energy in electrical form and thus a variety of power cycles exist that convert heat to electricity.

The daily electrical power demand of a typical human enterprise is not constant. Generally the peak load of a city will occur after the sun sets (Figure 1) when consumers are using power for lighting, cooking and heating [2]. The primary challenge for most thermal storage solutions is to extend the electrical supply period beyond the daylight hours to include this peak load. If the thermal storage capacity of the solar thermal power plant is great enough to outlast the night, the plant could run continuously. Thermal storage has the potential to make solar thermal a base-load power option.

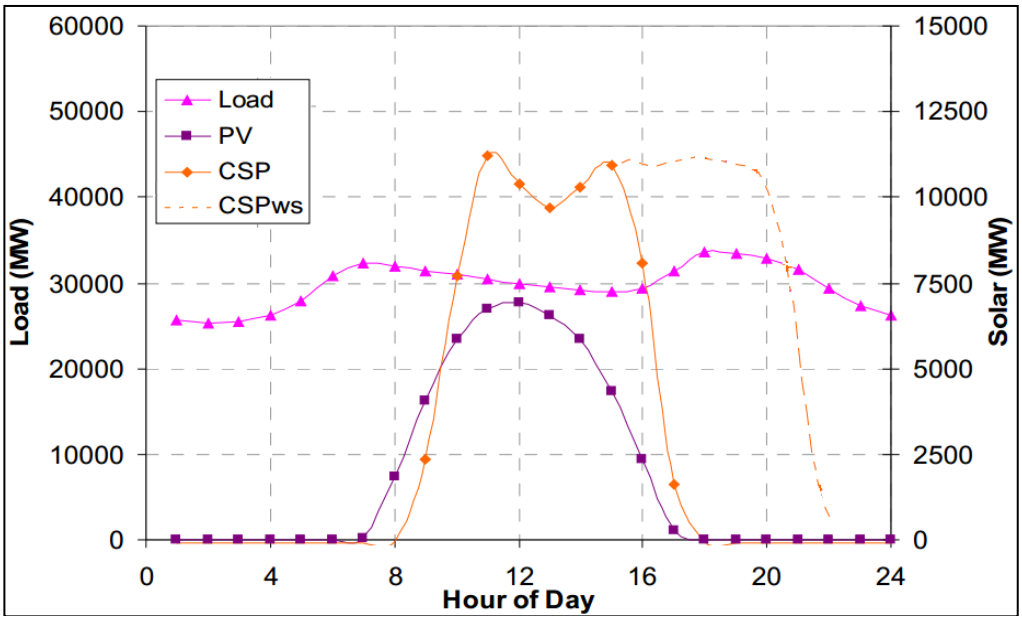

Figure 1. The typical load and supply for a winter's day in South West USA. Photo Voltaic (PV), Concentrated Solar Power (CSP) and Concentrated Solar Power with additional thermal storage (CSPws) are shown superimposed over the load. Edited, original [2].

Conventional power cycles that generate electricity may be improved through thermal storage. A typical Rankine, Brayton or more exotic 'turbomachinery' based power cycle benefits from stability in thermodynamic parameters at the turbine inlet. Thermal inertia at this point smooths and ideally maintains a constant temperature within the fluid.

Thus a turbine stage can be designed to achieve higher efficiency for a narrower band of fluid thermodynamic conditions.

Thermal storage is also of use for stabilising temperatures in applications apart from power generation. Spaces inhabited by humanity, our companions, technology and food are often required to be maintained at a liveable temperature. A thermal storage device can be utilised to maintain a comfortable environment for humans, plants and animals. Machinery and electronic devices that generate heat or are sensitive to temperature changes benefit from the stabilising effect of thermal inertia. Many industrial processes require elevated temperatures for chemical reaction or drying. These industries may find efficiency gains and cost savings in utilising thermal inertia. This research has investigated a new class of thermal storage material, Miscibility Gap Alloys, designed for a wide variety of applications.

The goal of this thesis was to provide all elements necessary to confidently commercialise Miscibility Gap Alloys as a thermal storage material. Material properties, lifetime estimates, economics and a description of applications are required to implement this novel material. These elements are introduced in a logical order through the thesis.

Chapter 2, immediately following, provides a review of literature related to both thermal storage materials and the physics required to understand their performance. Through this review the context of Miscibility Gap Alloy thermal storage is highlighted. The necessary theoretical and computational methods are introduced in chapter 3. Once the scientific and engineering background has been rigorously analysis and results can be discussed. Chapter 4 describes the results of Microstructural Efficiency analyses. Chapter 5 then discusses the manufacturing methods for the alloys and their likely morphologies.

Provided both the morphology and the means of homogenising material properties on morphology the material properties can be accurately estimated. Chapter 6 describes the lifetime of the alloys through the results of computational modelling and discussion of mechanical and chemical phenomena. Provided lifetime estimates and accurate material properties the economic case for Miscibility Gap Alloys is made in chapter 7. Chapter 8 may then provide detailed practical implementations of Miscibility Gap Alloy thermal storage as the material properties, lifetime estimates and economics have been established. The thesis then concludes and recommendations are made on which the candidates research may be furthered.

Appendices follow the thesis proper. Appendix A provides a listing of nominal thermal properties for state of the art thermal storage materials. Appendix B is a derivation of laws of mixtures for equilibrium thermal properties. Appendix C is a table of a number of identified Miscibility Gap Alloys from the patent literature [3]. A derivation of the growth-decay equations used in diffusional aging modelling is provided in Appendix D. Tabular data for the thermal properties of the six Miscibility Gap Alloys investigated in detail through chapters five, six and seven are provided in Appendix E. Appendix F shows estimates for constituent material prices. Appendices G and H explain in detail the economic analysis presented in chapter seven. Appendices I and J provide engineering drawings and analysis for the air heater device introduced in §8.1. An additional special appendix is provided in the form of a compact disc with demonstrations of the utilised algorithms (written as MATLAB® scripts).

CHAPTER 2: LITERATURE OVERVIEW

This chapter provides the reader with an historic and scientific context for research and application discussed in later chapters. This chapter also serves to demonstrate the innovation of the Author's contribution to the field. Minimal technical theory is developed in this chapter instead being introduced in detail in those following.

2.1. Global Energy Resources

Energy resources exist in a variety of forms and are distributed heterogeneously around the globe. Discovery and exploitation of energy resources has led to amazing changes to regions otherwise left undeveloped or pristine. Take the Gulf States of the Middle East, upon discovery and exploitation of oil reserves in the early 1900s, huge world cities grew from humble fishing villages (Figure 2). However, exploitation of energy reserves does not always lead to social development and often damages the natural environment irreparably (Figure 3 shows extensive deforestation in the Amazon rainforest).

Energy resources may be defined as renewable or non-renewable. Renewable energy resources are those that are replenished over a time scale comparable to that at which the resource is consumed. Solar, wind, geothermal and tidal resources are clearly renewable whilst biomass resources are arguably renewable. Non-renewable resources are those that either require geological timescales to be replenished or may not be replenished. These include hydrocarbon based resources (coal, oil natural gas) and nuclear fuels (^{235}Uranium and ^{239}Plutonium)

Figure 2 Doha's modern history involves rapid development over the last 30 years following significant development and continued exploitation of oil and gas reserves [4].

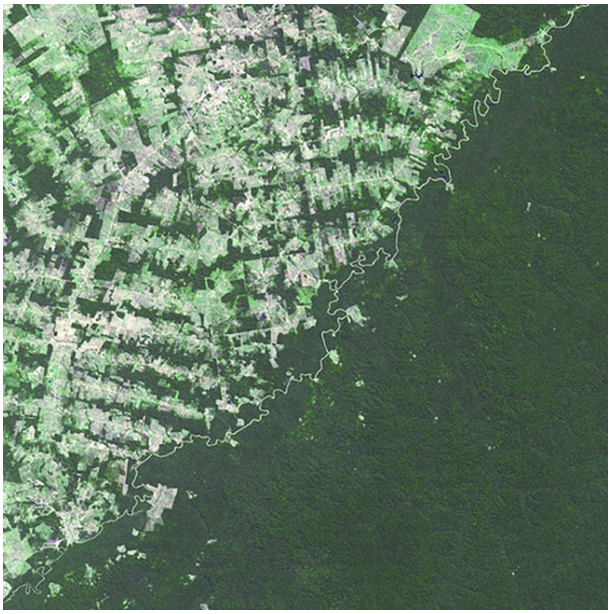

Figure 3 Satellite image of the border of Bolivia (Left) and Brazil (Right). Bolivia's forests have suffered significant deforestation for use as both a commodity and fuel [5].

The International Energy Agency annually releases a document titled 'Key World Energy Statistics'. This document summarises the current production and consumption of different energy resources around the globe. Figure 4 indicates the dominance of non-renewable energy resources in global energy supply over the last 40 years. As of 2013 the proportion of global energy supply from all renewables was on the order of 1.2%.

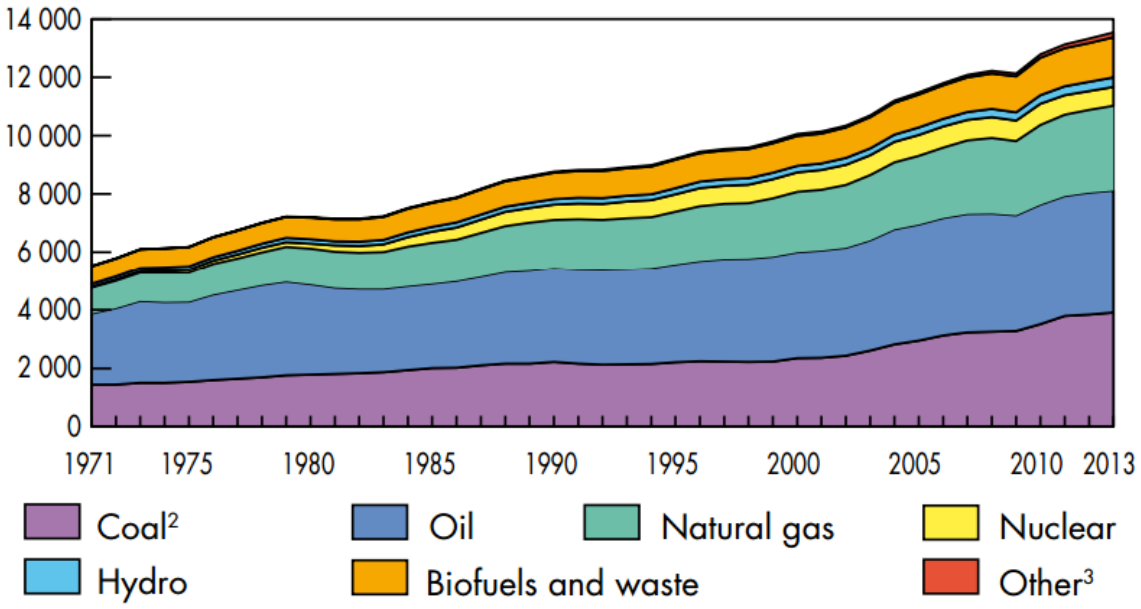

Figure 4 Historical World (including international aviation and international marine bunkers) total primary energy supply in Million Tonnes of Oil Equivalent (11.63×10^9 kWh). [2]Peat and Oil Shale are aggregated with Coal. [3]Includes geothermal, solar and wind [6].

The current dominance of energy supply by non-renewable fuels is due primarily to their historic importance and established infrastructure. Energy resources at the scale humanity uses now were not conceived of prior to the industrial revolution (arguably beginning in England in the 18th century [7]) involving the uptake of the coal fired steam engine. Machinery based industry boomed throughout England and spread around the globe off the back of coal. The discoveries of Faraday and Maxwell [8] in the mid-19th Century led to a practical understanding of electromagnetism and eventually led to electric power

generation[1] for domestic consumption. The established technology for converting coal through combustion to mechanical energy could now be furthered to produce electrical energy. The invention and improvement of automated transport increased the demand for other fossil fuels (oil products and natural gas) that could be better transported. The early to mid-20th Century saw a much greater understanding of radiation and its sources. This led to exploitation of radioactive resources (like Uranium) as nuclear energy sources.

Renewable energies were restricted to mostly hydro power and small scale applications of wind energy through this period. It was not until the widespread realisation of the limited availability of non-renewable resources and the acknowledgement of the negative environmental impacts of burning hydrocarbon fuels that renewable energies became salient.

At this time the development of renewable energy technology is 200 to 300 years behind that of existing non-renewable infrastructure. Although a great deal of technology is transferable, considerable effort is required in developing renewable energy infrastructure to the technological level that non-renewable resources currently enjoy. It is little wonder that renewable energies do not yet contribute comparatively to global energy supply and that they appear relatively expensive.

The negative environmental impact of utilising hydrocarbon and nuclear fuel as energy sources has been the main driver behind the adoption of renewable energy sources. Combusting hydrocarbon fuels results in the emission of CO_2, CO, SO_2, Nitrous Oxides and particulate matter. These products contribute directly to global warming, acid rain or

[1] Hereafter referred to as power generation.

respiratory disease in humans and animals. The available supply of non-renewable energy resources is limited and concerns about demand outstripping supply have driven investment in renewables as an alternative. Investment in renewable energy can reduce dependence on polluting forms of energy production, decrease dependence on imports and even lead to export of energy and energy intensive products.

Modern governments and their progressive citizens do recognise the boon that renewable energy resources are to a Country. However, distributing renewable energy is considerably more involved than hydrocarbon or nuclear fuels. This is clear when comparing the energy density of these fuels to typical energy storage media (comically in Figure 5 and seriously in Figure 6). Though batteries and thermal storage materials are relatively low in energy density they are reusable whilst fuels are not. For example thermal storage of 0.5 kWh/L might appear miniscule but if the storage is utilised daily for 20 years that is equivalent to 1.46 GWh/L over the lifetime.

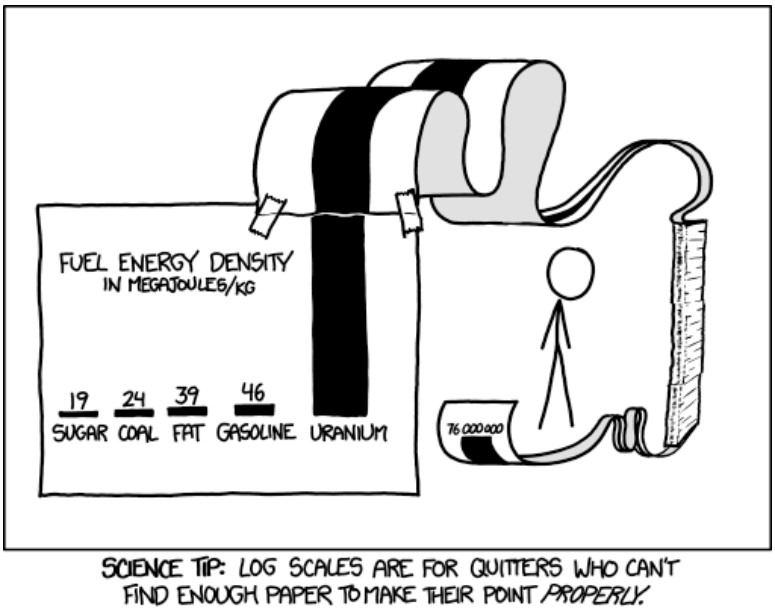

Figure 5 Comical comparison of mass specific energy densities of common fuels [9].

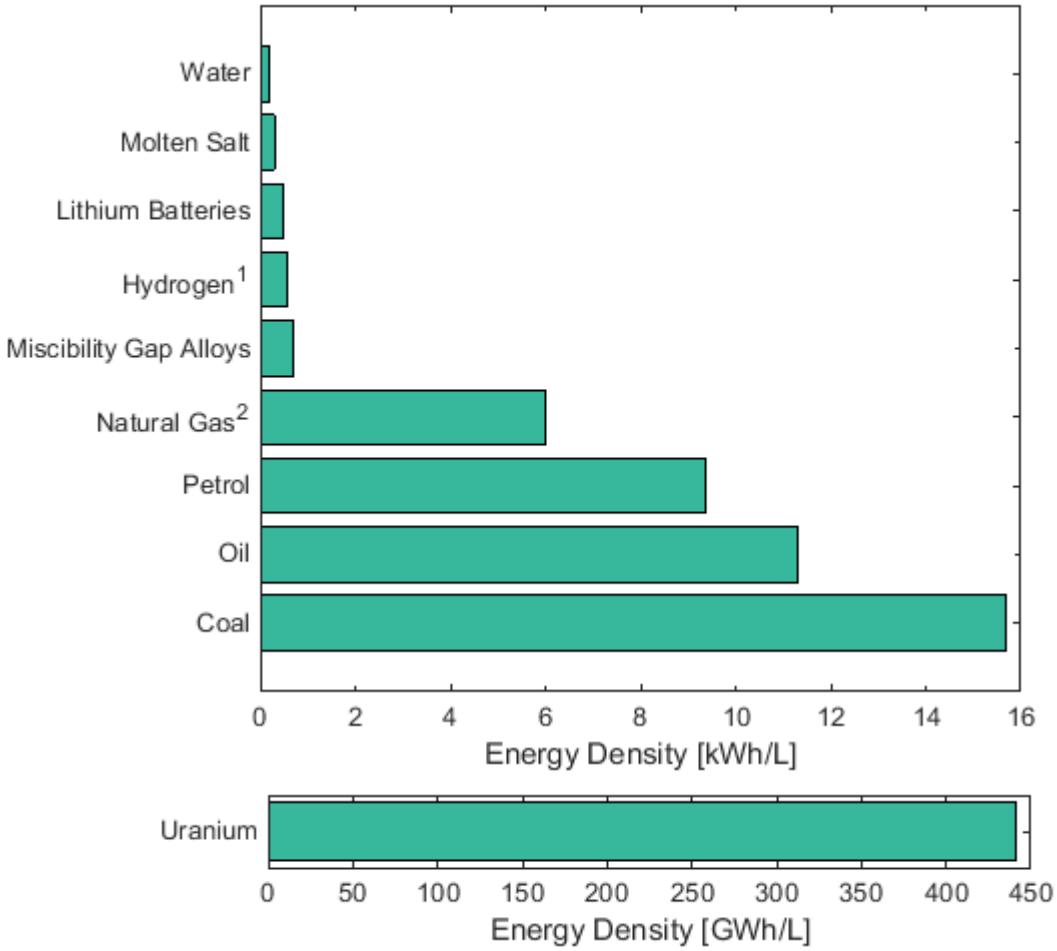

Figure 6 Comparison of volumetric energy densities of common fuels and energy storage media. [1]Hydrogen compressed to 20 MPa at room temperature. [2] Natural gas at a density of 456 kg/m^3. Uranium is more conveniently plotted on its own (or on a log scale). Energy storage in Molten Salt and Miscibility Gap Alloys is over ΔT = 100 °C.

If a nation could overcome the challenges of renewable energy resource use and distribution, it could experience significant, sustainable wealth. Energy resources might be converted to fuels that are more energy dense for export (e.g. electrolysis of water to produce hydrogen) or used to create products with high embodied energy (like aluminium metal or fertilisers) to trade. Distribution of electrical energy from nations with large renewable energy resources to those without can be achieved through construction of high capacity power transmission lines [10]. Renewable resources converted to electrical energy

may also be used domestically to improve the quality of life and health of citizens with a range of positive outcomes. Through developing emerging technology a nation may convert renewable energy into continuous wealth.

2.2. Renewable Energy Resources

Solar, hydro, wind, tidal, geothermal and biomass energy resources exist with varying availability around the globe. Solar resources are significant in Australia, parts of North America, South America and Africa but are very limited in most of Asia and Europe. Hydropower requires a source of water at elevation and thus is impractical in flat dry countries. Wind resources are abundant in regions with appropriate climatic conditions. Tidal power takes advantage of large differences in sea level and must be placed in coastal areas. Geothermal resources either require a region with considerable tectonic activity or concentrations of subterranean radioactive material. Biomass resources require human intervention and fertile land to be considered renewable. Each renewable energy resource has advantages and disadvantages.

Solar resources suffer from both intermittent and cyclic supply variation. Solar radiation has short term intermittency due to cloud cover whilst longer term seasonal variations occur for resources away from the Earth's equator. Solar resources are also obviously not available at night. Intermittency and cyclic supply variation in solar resources may be overcome by converting the electromagnetic energy of incident radiation to heat.

To accommodate an intermittent thermal resource a number of storage techniques have been developed. Thermal energy may be converted to many different forms of energy through many different processes; however losses are incurred in each conversion step.

Thermal energy may be converted to electrical energy through thermodynamic engines (e.g. steam engines) coupled to generators which may be subsequently stored in a chemical reaction (a battery) or in an electric field (a capacitor). Instead the mechanical energy of the engine might be used to drive a fluid against the force of gravity to a tank at a higher altitude. It is also possible to store the thermal energy as 'thermal energy'! Thermal storage most generally refers to the storage of heat in a material from which it may be extracted at a later time.

2.3. Thermal Storage in the Literature

The capacity to store useful heat energy has been a technological challenge throughout human history. Transport of energy in combustible materials has been apparent since humans first utilised fire for cooking and warmth 1.5 million years ago [11]. Evidence also exists whereby certain rocks were heated under flame to store heat either for cooking [12] or to maintain a comfortable temperature in bedding. Early 'refrigeration; was achieved through energy storage in the melting of ice [13].

Through the industrial revolution, the age of steam engines, pressurised steam vessels stored heat and mechanical energy with the capacity to recharge the system [14]. Once technology to safely store large volumes of hydrocarbon fuel and achieve a sustainable supply was found, the need for such thermal storage was lessened. Towards the end of the 20^{th} century heavy reliance on non-renewable fuels was clearly negatively affecting the human environment leading to a greater focus on more sustainable use of finite resources and renewable energies including intermittent heat resources like solar

radiation. This led to renewed interest in energy storage that could be integrated into existing methods of energy generation and consumption.

Thermal storage materials are preferably energy dense; such that little material is required, conductive; such that charging and discharging is fast, durable; so that they may be used many times and cheap; so that they are affordable. A large number of materials have been suggested in literature as potential thermal storage media. Multiple highly cited review papers exist in a range of journals listing and categorising thermal storage materials on type, temperature range though rarely on durability or cost [15-22]. A review of existing and suggested materials is given below in an effort to place the Miscibility Gap Alloys within the broad field of research.

The state of the art in thermal storage materials may be broadly categorised as sensible or phase change systems. Figure 7 describes how sensible and latent heating occur for a pure material undergoing melting. Sensible Heat Thermal Energy Storage systems do not utilise a phase change and thus rely completely on the heat capacity and temperature range of the storage system. Generally research in this field involves finding economic and simple solutions rather than emphasising exceptional material properties. Very high heat capacity (> 1000 J/kgK) materials that are stable over large temperature ranges are required for sensible heat storage.

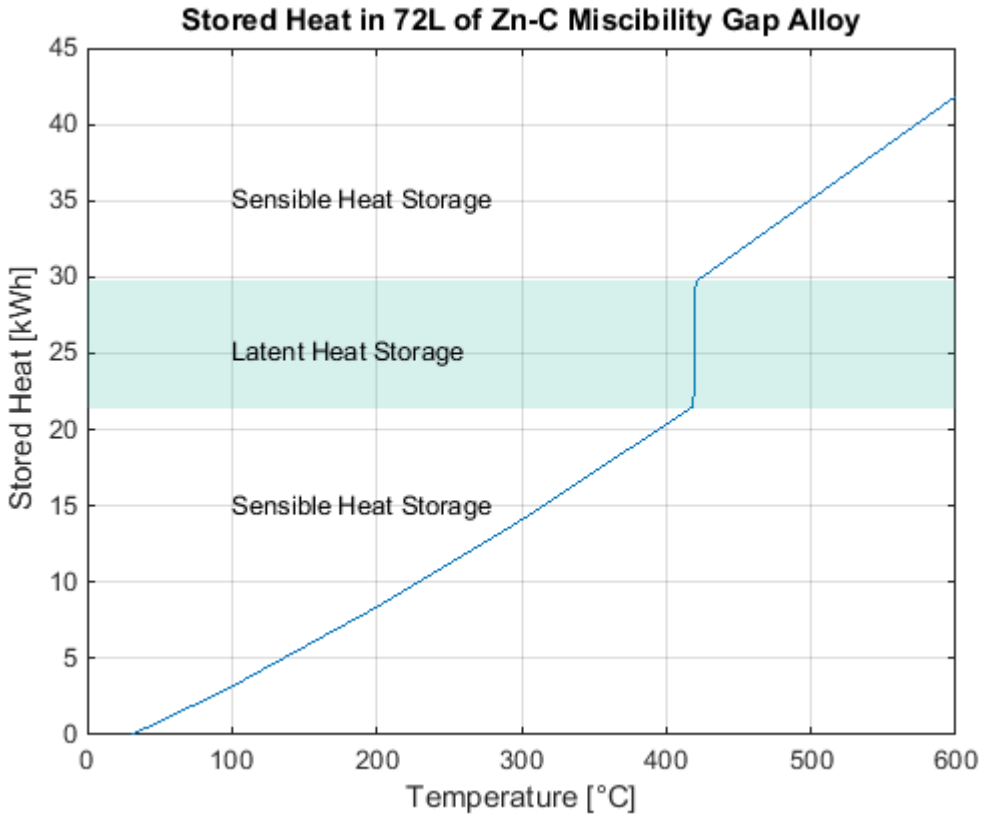

Figure 7 Schematic describing energy storage as sensible heat and in a phase change in a Miscibility Gap Alloy. If melting is occurring a great deal of energy may be stored with little increase in temperature.

Solid sensible heat storage media like cast iron, concrete, graphite, rocks, and sand are commonly encountered in literature [4, 9-11]. These materials are generally cheap with poor energy density (<0.1 kWh/L) and low thermal conductivity (<5 W/mK). Cast iron was identified as having a considerable energy density by Hasnain, though the much higher cost was also mentioned [10]. Laing investigated N4 concrete as a potential solution [4]. Concrete based storage was found to suffer from low thermal conductivity (<1.5 W/mK) [12] and had some issues with elimination of water. Graphite shows some potential due to its high thermal conductivity (up to 200 W/mK) and moderate heat capacity (~700 J/kgK)

[11]. Beds of rocks and sand were also reviewed by Hasnain with favourable results for moderate temperatures [10].

Liquid sensible storage media are almost invariably molten salts. A number of molten salts have been identified as potential storage materials with exceptional heat capacities (>1000 J/kgK) [13]. The most prevalent and investigated molten salts are Potassium and Sodium Nitrates. Unfortunately all molten salts discussed in the literature suffer from extremely low thermal conductivity (<1 W/mK) and most are very reactive with steel pressure tubing [10]. Most salts are also likely to decompose to potentially hazardous chemicals at moderate temperatures [10]. Thermal oils have also been used as liquid sensible storage materials. These oils are restricted in upper operating temperature (<300 °C) due to chemical decomposition and also suffer from very low thermal conductivity (< 1 W/mK) [8][22]. The need to pump these molten storage materials adds a parasitic energy loss to the entire plant (~5%) reducing overall efficiency.

Phase change thermal energy systems have higher energy density and may operate over smaller temperature ranges than sensible heat systems. Researchers have identified many salts and salt eutectics, paraffin waxes and other materials that undergo phase changes at useful temperatures. These materials generally have low conductivity (<1 W/mK), and a wide variety of costs however they achieve higher energy density than most sensible storage materials. Limited work has involved the use of metals as phase change materials.

Salts and eutectics of salts used as phase change materials are very widely documented in the literature with a large number of different materials and combinations [15, 19, 22, 23]. Temperatures range from 10 °C up to near 1700 °C [23] though some

rather exotic salts are required for very high temperatures. The most investigated salts for phase change storage are fluorides and chlorides based on cost and heat of fusion [20, 23], hydroxides, nitrates and carbonates are widely investigated. Both Kenisarin and Zalba give extensive lists of salts and eutectics and their thermal properties [15, 23]. The toxicity of decomposition products of salts has been highlighted [23]. The severe limitation of low salt thermal conductivity has been discussed and augmentation methods suggested [22]. Heat exchanger design is a critical research area in implementing salt based PCM systems.

Metals have received some attention in the literature though the realities of encapsulation and operation have not been thoroughly explored. An extensive list of possible eutectics involving aluminium, copper, lead, magnesium, silicon and zinc were given by Liu in 2012 [22]. Another list of suggested alloys is available in Kenisarin's extensive review [23]. Al-Mg-Zn alloy was proposed as a latent heat storage material by J. Q. Sun et. al. in 2007 though the miscibility of the alloy with its encapsulating material was not identified [24]. In 2012 Khare et. al. investigated a range of metals simply using a commercial materials selection program [17]. The authors concluded that eutectics of Al, Mg, Si and Zn were useful for high temperature storage. Limited analysis was given on the charge/discharge characteristics of the metals. An alloy of Al and Si was discussed in 2013 as a potential candidate and its performance with a heat transfer fluid of NaK[2] was analysed

[2] Mixtures of sodium and potassium are liquid over large composition and temperatures ranges. The liquid has a relatively high heat capacity and very good thermal conductivity characteristics. It finds use as a heat transfer fluid in nuclear and some solar thermal power generation applications. Unfortunately the fluid is extremely reactive when exposed to air or water [25] J.P. Kotzè, T.W.v. Backström, High Temperature Thermal Energy Storage Utilising Metallic Phase Change Materials and Metallic Heat Transfer Fluids, Journal of Solar Energy Engineering, 135 (2013) 1-6..

[25]. In space heating some low melting temperature metals were suggested by P. Tatsidjodoung et al. though their cost was given as a critical detriment [26].

2.4. Miscibility Gap Alloys

Miscibility Gap Alloys are the focus of this thesis and are believed to be an excellent alternative to the materials previously discussed in some cases. A Miscibility Gap Alloy as defined in the patent literature [3] is a composite of two or more constituents that show very little miscibility. The lower melting temperature constituent (constituents) is (are) completely encapsulated by the higher temperature constituent which provides a rigid matrix to support the melting constituent (constituents). This ‘inverted’ microstructure is not obtained through typical casting manufacturing methods, as this would distribute the higher melting temperature constituent. Powder metallurgy has been utilised to obtain the necessary morphologies though other manufacturing methods have been envisioned [3]. Figure 8 shows the typical morphology of an alloy of this type. Miscibility gap alloys have thermal conductivities in the range of 30 to 300 W/mK and energy densities from 0.1 to 1.2 kWh/L [27, 28]. Miscibility Gap Alloys described in this work are limited to less than 50% volume fraction of the distributed phase. As the materials are a recent invention they have not been implemented commercially at the time of writing.

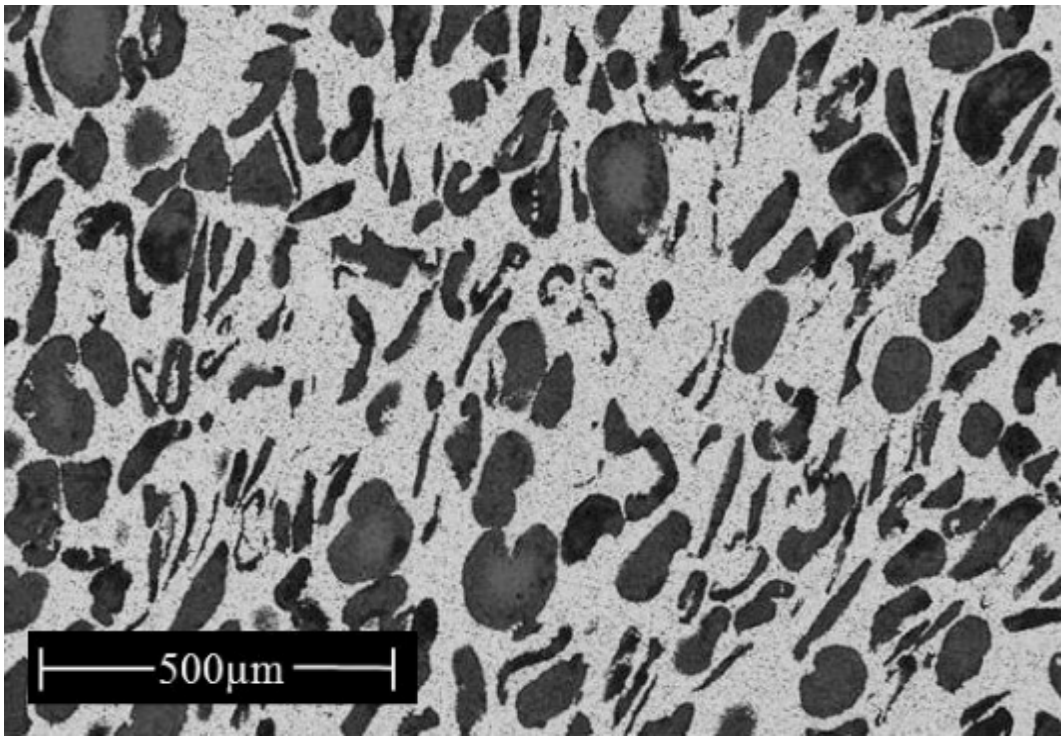

Figure 8 Mg-Fe Miscibility Gap Alloy morphology demonstrated through a Back Scattered Electron Microscope image [29] The darker phase is Magnesium, the lighter is Iron.

2.4.1. Definition

A Miscibility Gap Alloy is a mixture of two or more (usually metallic) constituents that exhibit strongly immiscible behaviour whereby the highest melting temperature constituent physically encapsulates the others (Figure 9). Upon injection of heat to the system, the lower melting temperature constituents melt, absorbing energy equal to the latent heat of fusion without flowing from their original position. This storage is in addition to the sensible heat gained through temperature change.

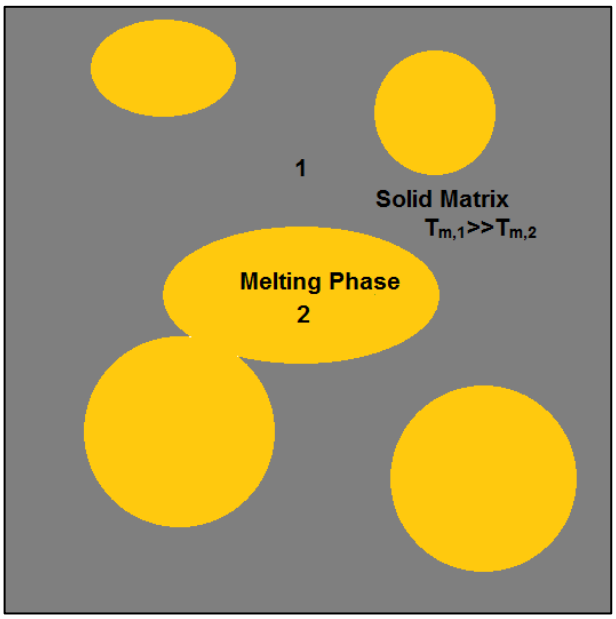

Figure 9 A simple schematic of a binary miscibility gap alloy where 1 is the matrix phase and 2 is the lower melting temperature (distributed phase) phase.

An example of a Miscibility Gap Alloy is the Tin-Aluminium system (a phase diagram is shown in Figure 10. Below the eutectic temperature of 228 °C an extremely aluminium rich fcc phase coexists with a tin rich body centred tetragonal bct phase. The solid solution phases have so little solubility of the other constituent they are practically pure aluminium and tin phases. The bct phase melts at ~228 °C. Solubility increases with temperature for the liquid phase but not considerably over the intended operation range (± 50°C from melting). Upon cooling the liquid will reject a small amount of aluminium either to the matrix or in nucleation of new fcc crystals before the bct phase crystallises.

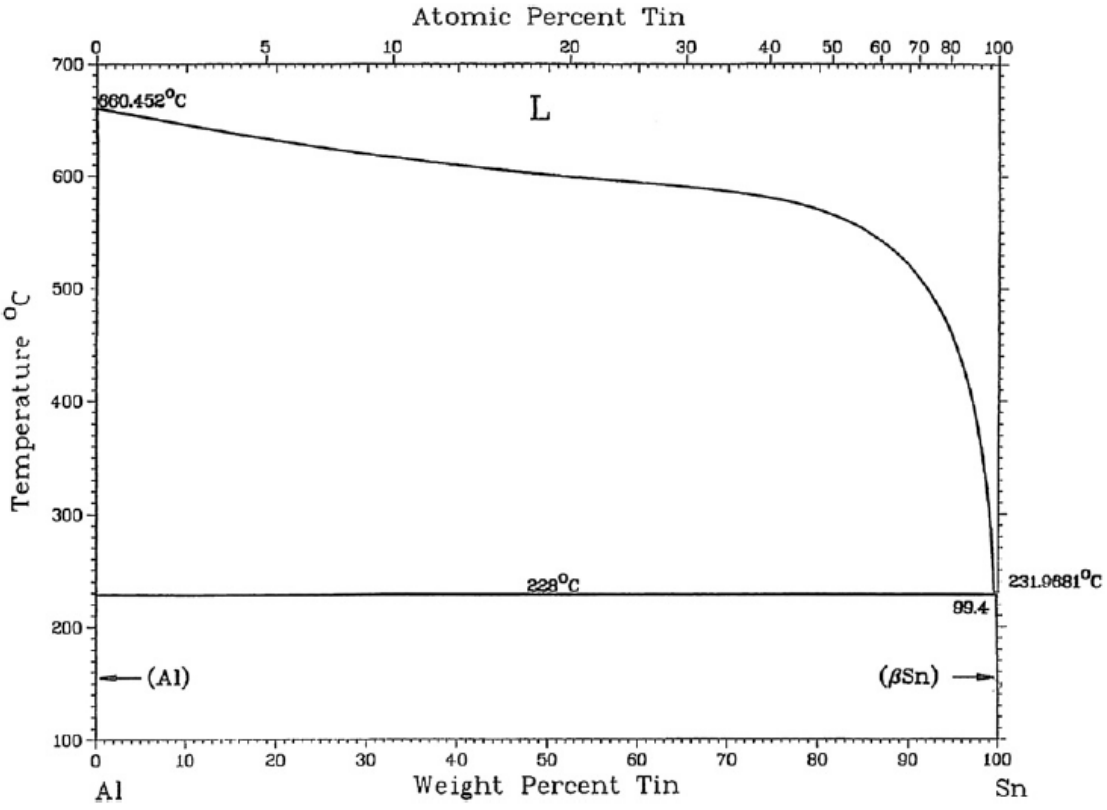

Figure 10 Phase diagram of tin and aluminium [93]

Miscibility Gap Alloys as thermal storage devices benefit from very high energy density and extremely high thermal conductivity relative to other common storage materials. Table 1 summarises the key benefits of these thermal storage materials.

Table 1 Properties and related benefits of Miscibility Gap Alloys as a thermal storage medium

Property	Benefit
Two orders of magnitude improvement in thermal conductivity over conventional systems	Very fast charge and discharge rates and reduced heat exchange area (fewer pipes).
Heat is delivered and retrieved by conduction alone through the material bulk.	Removes the need for pumping infrastructure and expensive finned heat exchangers
High volumetric energy density	System takes up less space, smaller footprint
Range of materials for different storage temperatures	Specific MGA selected for a particular application
Narrow temperature range on delivery	Optimised thermal cycle for a small range of working fluid conditions
Thermally and chemically stable	Simple encapsulation (some matrices require an airtight encapsulation), latent and encapsulating phases are inert and extremely long life time
Common and safe materials	Low material cost per kWh, very low running costs, community acceptance, recyclable

Over 90 Miscibility Gap Alloys have been identified and more are being investigated at the time of writing this thesis. These different alloys are listed in Appendix C.

2.4.2. Development

The development history of Miscibility Gap Alloys is obviously brief at the publishing of this thesis. The work of this thesis is to provide the physical, manufacturing and economic characteristic of the materials. As such, the bulk of this initial development work does not yet exist.

Miscibility Gap Alloys were discovered by Heber Sugo, Erich Kisi and Dylan Cuskelly in 2012 [28]. The group was previously heavily involved in the synthesis and analysis of various ceramics using powder metallurgical methods. The concept of encapsulating a low melting temperature constituent within a high melting temperature

matrix was not novel, however the identification of immiscibility as a necessary step and the use of metallic systems was not apparent in literature at the time of development. The researchers created two different systems, Sn-Al and Cu-Fe, using typical powder metallurgy techniques to produce specimens that behaved as expected. The candidate was brought into the group the following year to develop the concept further.

2.5. Comparison of Thermal Storage Properties

The following chart (Figure 11) provides a comparison of common thermal storage materials in terms of their thermal conductivity and energy density. Metals (including semiconductors) are seen to have the highest thermal conductivity and energy density of the categories analysed here. Miscibility Gap Alloys have similar properties to metals as they are generally composites of metallic constituents. Sensible heat storage has low energy density but a great range in thermal conductivity. Phase change salts have high energy density but suffer from low conductivity. Molten salts have moderate energy densities but low thermal conductivities. Waxes and Oils have very low conductivity and poor energy density.

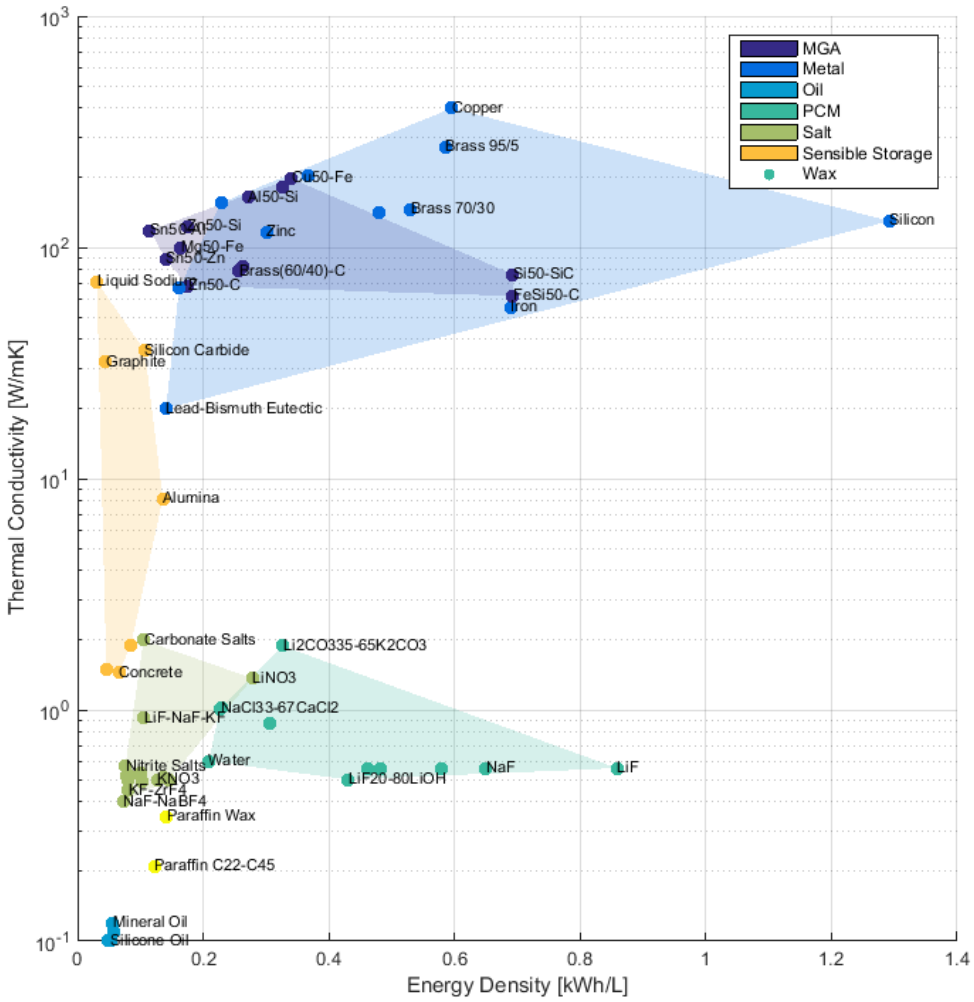

Figure 11 Graphical representation of energy density and thermal conductivity for a number of thermal storage materials. Energy density includes 100°C of sensible heating. Thermal conductivity for MGA composites is evaluated using the Maxwell-Eucken homogenisation method (§3.1.5). Note that the thermal conductivity axis is logarithmic.

A summary of the thermal properties of a number of thermal storage materials is provided in Appendix A, ordered on type and energy density. The materials are categorised according to whether they are Molten Salts, Phase Change Materials, Sensible Heat Media, Metals or Miscibility Gap Alloys.

2.6. Cost of Thermal Storage Systems

Material properties are not the only consideration necessary when selecting an appropriate thermal storage material. The cost of implementing a thermal storage system is of course pertinent. The costs might be broadly separated into material and infrastructure costs. The cost of material per kWh of stored energy may be determined with knowledge of the energy density, matter density and material cost on a mass basis. The raw material may also require further manufacturing to be suitable as a thermal storage material, introducing an additional manufacturing cost. The infrastructure necessary for a thermal storage system is highly dependent on the material properties of the storage medium, particularly the thermal conductivity. If the thermal conductivity is particularly low, a large heat exchange surface is required or heat might be better transferred through convection to a molten flowing storage medium.

An obvious goal for thermal storage system design is to maximise energy storage whilst minimising cost. Unfortunately, these two objectives often conflict. State of the art thermal storage systems frequently utilise molten salts, waxes or oils with very low thermal conductivities. To transfer adequate heat to the storage material the fluid must be pumped rapidly through heat exchangers to convect heat to and/or from another fluid. Latent heat systems store large amounts of thermal energy as a reversible material phase change, often an order of magnitude more than that of sensible heat systems [21]. If either phase has low thermal conductivity, significant capital must be invested in enhancing heat transfer from the stationary freezing or melting mass [30].

Numerous authors have published insightful papers regarding the current cost of implementing thermal storage systems and forecasting where the price might head in the

future. Price and Kearney described in 1999 the current cost of implementing a molten salt thermal storage system appropriate for a solar trough power cycle to be 15 USD/kWh and that the cost should move to 10 USD/kWh by 2015 [31]. In 2001 Pacheco et.al. described a molten salt thermocline with a quartz filler showing that a 20 USD/kWh storage cost was possible [32]. In 2010 Turchi et. al. performed cost modelling for overall electricity cost in central receiver and solar trough style power cycles [33]. The authors utilised a cost of 30 USD/kWh dropping to 20 USD/kWh for a central receiver whilst in solar trough arrangements 80 USD/kWh dropping to 25 USD/kWh for over a period of 10 years. Both arrangements considered molten salt as the storage medium. In 2014 Smith et. al. analysed a hypothetical 100 MW central receiver plant operating in central Australia with either a two tank molten salt, a thermocline or a phase change salt system [34]. The team utilised costs of 30.1, 20.6 or 18 USD/kWh for thermal storage in their modelling respectively. Thus it appears from literature over the last 10 years that a cost of between 10 and 80 USD/kWh is the cost range for thermal storage systems involving molten salts. Figure 12 shows the nominal material cost per kWh and the energy density for a range of thermal storage materials.

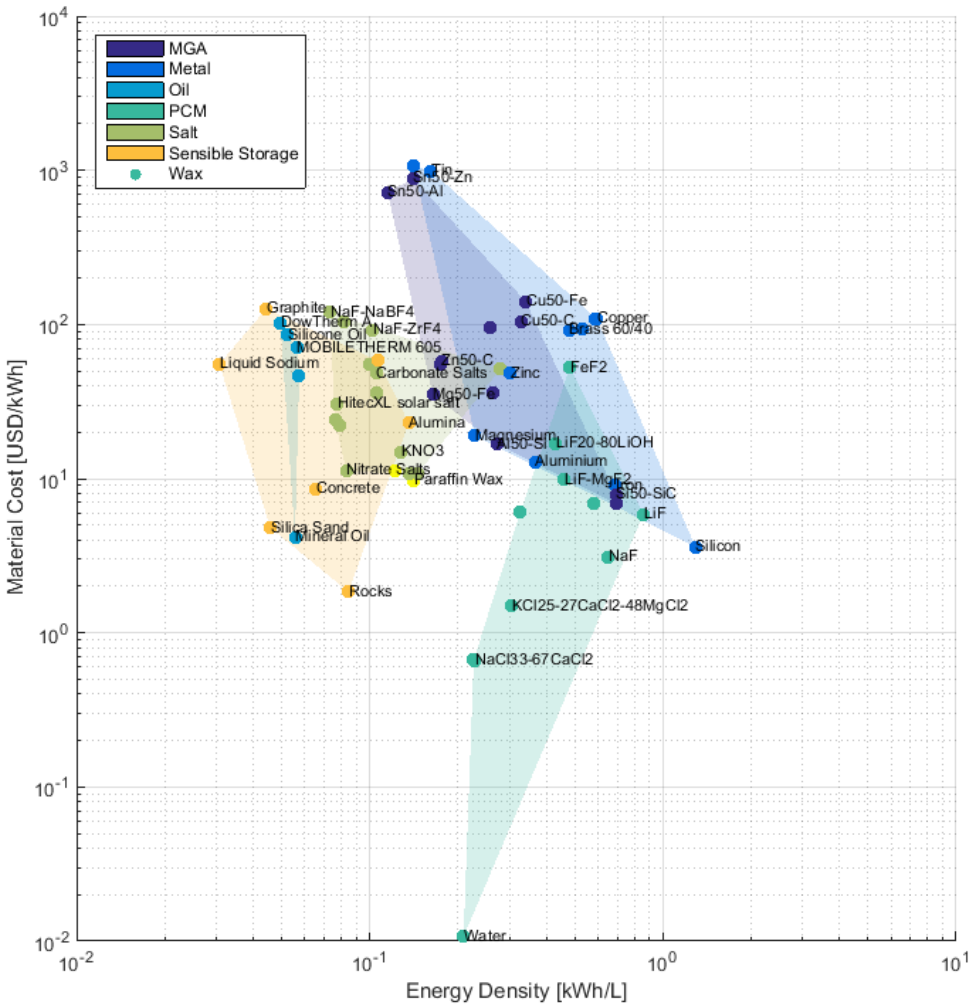

Figure 12 Nominal material cost plotted against energy density for a range of thermal storage materials.

Cost breakdown analyses for thermal storage systems are intuitively highly specific to the thermal storage material and the particular power cycle being augmented. A two tank molten salt system was investigated by Kuvari in 2013 [35] utilising the prior analysis of an IRENA report [36]. The Authors concluded that 49% of the net cost was borne by material costs whilst infrastructure made up the other 51%. Smith et. al. in 2014 broke the cost of

storage down between material cost and infrastructure (further categorised as piping, insulation, foundations and instrumentation) to be between 30 to 47% material price [34]. A feasibility study for concentrating solar thermal power in China written by Zhang and published as a thesis in 2009 places the material cost at around 35% of the total thermal storage cost [37]. Maintenance was not included in these analyses. Material cost for molten salt thermal storage solutions appears to take 30 to 50% of the total cost of deploying a system.

2.7. Homogenisation of Thermal Properties

A composite material generally has a much more complicated microstructure than a homogeneous material. When analysing these systems at a macroscopic scale (much larger than the microstructure), homogenisation of the constituent properties to an effective average is advantageous. Property homogenisation involves replacing the discontinuous microstructure of the composite with an equivalent homogenous system. Homogenisation of material properties has been an open field of research for centuries, including contributions from many renowned scientists such as Michael Faraday, James Maxwell and John Strutt (3rd Baron Rayleigh), who made significant contributions through the late 19th century [38, 39]. A great number of analytical and empirical methods were developed through the 20th century, before advances in computational resources allowed numerical methods to become widely used [40-43]. The applications of homogenisation theory encompass a great variety of scientific fields. It is little wonder that such a diversity of contributions have been made to the body of theory. When the benefits of composite materials (particularly strength to weight ratio) became well known during the 1960's research in the field significantly accelerated [41].

The models and theory discovered over time might be divided into *direct*, *bounding* and *empirical* approaches. This listing also suggests the order in which the theory developed. Analytical models presented rare and great leaps in understanding during the field's infancy. Once the complexity of the field was firmly grasped, researchers proceeded to define fundamental bounds to effective properties. Empirical models followed later when accurate information for specific (and perhaps commercial) composites was required in a more applied sense. The following introduction describes the progress of the field whilst the functions are presented in the following chapter.

Direct approaches to analytically determining effective conductivity might involve assuming an isolated local temperature field for an inclusion with an harmonic solution, attempting to solve the heat equation for a set of (potentially periodic) boundary conditions or applying statistical mean field theory to a structured or random distribution of particles. The approaches are varied and add to the mathematical richness of the field.

Dilute suspensions of different particle shapes were treated early on. It is quite likely that Lorentz developed the first solution for effective conductivity in dilute spherical inclusions during 1870 [44]. Maxwell discussed the same phenomenon through his seminal treatise on electromagnetism in 1873 [38]. The models developed by Maxwell were applied to the thermal case by Eucken in 1940 [45]. A similar case was discussed by Lorenz in 1880 for unidirectional aligned cylinders [46]. A distinct derivation resulting in a similar theory was given by Clausius in his 1879 book [47]. The simplifying assumption of dilute concentrations enabled the physicist to isolate a single particle's local temperature field. Ellipsoidal inclusions were investigated later by Fricke in 1924 [48] and others (including varying orientation) later in the 20^{th} century [49, 50]. These studies were inherently limited

to low concentrations of inclusions, neglecting interesting behaviour where particles begin to physically touch (or percolate) at higher volume fractions.

To account for the considerable divergence of effective conductivity about the percolation volume fraction, a number of approaches were attempted. Ordered media involving periodic morphological patterns were investigated by some. John Strutt (3rd Baron Rayleigh) analysed effective polarisation for systems of spheres on a cubic array in 1892 [39]. Meredith and Tobias further analysed this case with experimental data in 1960 [51]. Other structured packings of spheres were considered by Sangani and Acrivos in 1983 [52].

An effective medium theory was proposed by Bruggeman in 1935 to account for the influence of percolation on conductivity [53]. This method analysed the influence of two or more arbitrarily located inclusions in random media. Landauer developed and extended the theory in 1952. [54]. In 1973 Kirkpatrick derived a modified form of Landauer's model by investigating networks of resistors in different cubic structures [55].

During the 1960s many attempts were made to better account for varying microstructural features and their dominant influence on conductivity. A number of correlation functions were developed to better mathematically identify microstructural features. Torquato developed a general formulation to statistically characterise composites with distributed inclusions in 1982 [56]. Many modern models utilise some form of the correlation functions developed by Torquato [57].

Keller introduced a distinct theorem based on reciprocity in 1963 [58] for superconducting unilateral cylinders with arbitrary cross sections and later with arbitrary

conductivity in 1964 [59]. Schulgasser simplified the proofs somewhat in 1992 [60]. The work was extended to general 3d shapes by J.A. del Rio et. al. in 1998 [61].

Variational bounding seeks to identify limitations to what the effective properties of a composite can be, given some restrictions. Wiener identified fundamental variational bounding for a variety of composite properties in 1912 [62]. Acknowledging these bounds were the arithmetic and harmonic weighted averages, a geometric average was suggested by Lichteneker in 1926 [63]. In 1962 Hashin and Shtrikman published a seminal paper introducing a more restricted set of 'Wiener type' bounds for effective magnetic permeability (and by analogy thermal conductivity) for composites [64]. Eventually termed the Hashin-Shtrikman bounds, the restriction applied to macroscopically homogeneous and isotropic multiphase composites. Other similar bounds were proposed separately by Brown and Beran in 1965 [65, 66]. Where composites are formed of constituents with dissimilar conductivity bounding approaches generally yield a large range for the homogeneous property.

The author of this thesis began developing the concept of microstructural efficiency in an attempt to generalise morphological dependency. The method was first outlined in a numerical paper analysing the effective conductivity of Miscibility Gap Alloys [67]. Two papers were subsequently written describing how the microstructural efficiency varied for structured packings of spheres and cubes [68] and for random packings of spheres (unpublished).

It is clear from the number of new effective conductivity models being developed each year that homogenisation of material properties is still an open field. It draws together many fields of physical science and varies from engineering applications to pure

mathematics. Applications exist in any field involving composite materials and as such will be an open field of research as new morphologies, materials and means of determining properties are discovered.

2.8. The Lattice Monte Carlo Method

The Monte Carlo method was first developed as a means of predicting neutron trajectories during nuclear fission in the United States during World War II [69, 70]. It was named this by Nick Metropolis who with his colleagues Edward Teller, John von Neumann, Stanislaw Ulam and Robert Richtmyer developed the first techniques and algorithms of Monte Carlo type simulation [71]. The method is computationally demanding and only became widely used in a large number of fields as computational power became accessible. Early classic papers utilising the Monte Carlo method include modelling of order-disorder in BCC lattices by Flinn and McManus in 1961 [72] and annealing of vacancies in an FCC lattice (with recombination) by Mehrer in 1969 [73, 74] amongst others.

The Lattice Monte Carlo method refers to a random walk upon a lattice where the direction and probability of a successful jump are driven by random number generation. The lattice method was originally utilised to monitor tracer diffusion in complex materials [75]. The process was subsequently adapted to model heat transfer in composites closely matching experimental results [69]. Many complex geometries have been investigated including cellular metals [76, 77], random and structured lattices of spheres [68] and other composites [78]. Phase change materials have been modelled with the method providing an alternative for finite element and difference methods [79]. Heat transfer via convection in

laminar flow has also been investigated using Lattice Monte Carlo analysis reproducing an expected boundary layer [80].

The Lattice Monte Carlo method for heat transfer modelling appears to be utilised more and more as computational resources becomes more powerful. The method has been adapted to complex heat transfer situations and even more complex cases are likely to be investigated. There exists potential for novel analysis into generalised optimisation and uncertainty of the procedure. Finally combining heat transfer and atomic diffusion models is a logical next step in the field.

2.9. Lifetime Properties of Alloys

Research into the long term behaviour of immiscible alloys undergoing thermal cycling is not well represented in the literature. Metallic composites of immiscible metals are uncommon in practical applications as they do not show desirable mechanical properties or reduce the cost of alloy manufacture. Where they have been utilised they generally would not undergo thermal cycles through the melting temperature of an embedded constituent. In fact the natural microstructure for an immiscible alloy cast would see the higher melting temperature phase distributed within the lower temperature constituent.

An attempt at utilising a copper-nickel coated sphere system with and without an inhibiting layer was made by Marouka and his colleagues in 2002 [81]. The inhibiting layer of graphite or ruthenium was not capable of separating the two completely miscible constituents resulting in failure after a single cycle for most samples. Recently a CuMgSi ternary alloy was encapsulated in stainless steel compatible with molten sodium. The

ternary alloy was found to interact and degrade the encapsulating material due to silicon diffusion after a single thermal cycle [82].

An analogue in the literature appears to be in attempts to harden metallic materials through dispersing particles of a second phase. Strunz and colleagues found that larger particles of lead would grow preferentially to smaller particles in an aluminium matrix, typical of Ostwald ripening and approach a spherical shape during cycling above and below the melting temperature of lead (327°C) [83].

Some work has also been performed where very small particles were of interest. Particles of lead under 100 nm in an aluminium matrix were monitored with a Scanning Electron Microscope *in situ* whilst thermal cycles were undertaken [84]. The shape hysteresis of the lead particle was equated to the surface energy and it was found that for single crystals very little anisotropy in surface energy was apparent. Other work has been done in microgravity for alloys with a liquid-liquid miscibility gap [85]. Otherwise a great deal of literature exists discussing the heat treatment and associated microstructural change of different alloys common in engineering applications. An introductory textbook like ‘Physical Metallurgy Principles’ describes the principles of crystallisation and melting of binary alloys [86].

CHAPTER 3: THEORETICAL AND COMPUTATIONAL METHODS

This section of the thesis is concerned with providing scientific background to the research in succeeding sections. The relevant thermodynamic, kinetic, transport, chemical and structural fields are introduced. Given this theoretical basis a rigorous definition of miscibility gap alloys is made. Homogenisation of thermal properties is discussed next before numerical methods of extracting that information are presented. The physics behind modelling microstructural evolution is then presented with the enabling numerical techniques explained. The chapter is concluded with a discussion of the strengths and limitations of the methods used.

3.1. Physics of Thermal Storage

An energy storage system is required to efficiently store energy in a volume, absorb or deliver it when required and last for an appreciable time span. The physics necessary to adjudicate on whether a material can achieve these requirements is broad, spanning the fields of thermodynamics, kinetics, transport phenomena, chemistry and solid mechanics.

3.1.1. Equilibrium

Fundamental to the idea of storing thermal energy in a material is the notion of equilibrium. Processes in nature tend to act to maximise entropy [87]. How a system acts to achieve this depends on how the system is in contact with the environment and is best explained through considering equation 1:

$$dS = \frac{1}{T}\left(dU + pdV - \sum_i \mu_i dN_i\right) \qquad 1.$$

Here dS is an infinitesimal change in entropy, T is temperature, dU is an infinitesimal change of internal energy, P is pressure, dV is an infinitesimal change in volume, μ_i is the chemical potential of the ith species and dN_i is an infinitesimal change in the number of moles of that species.

Each infinitesimal term on the right hand side of the equation represents a quantity that may be exchanged. Each exchanged quantity has a related governing variable. If two systems are brought together they will exchange quantities until the two systems have identical governing variables. This concept is best demonstrated through the following examples:

1) Two systems brought into thermal contact will exchange internal energy until they are at the same temperature.
2) Two systems brought into mechanical contact will exchange volume until they are at the same pressure.
3) Two systems brought into diffusive contact will exchange particles until they are at the same chemical potential.

Of course these interfaces may occur separately or in combination. Regardless, at equilibrium all combinations of governing variables are the same. Of most interest to the study of Miscibility Gap Alloys are thermal and chemical equilibrium.

A thermal storage system in thermal contact with a power cycle will exchange heat until it comes into thermal equilibrium (is at the same temperature) with the power cycle fluid. Thus, if the desire is to provide heat to a power cycle, the thermal storage material must be at a higher temperature than the fluid. How temperature is related to internal energy within the material is of major interest as well as the rate at which heat may be

exchanged within the material and through the thermal interface. These phenomena are discussed in the following section.

When two objects at the same temperature and pressure but containing different species are brought into diffusive contact, particles will be exchanged until chemical potential is uniform throughout the combined system. Chemical potential is dependent on temperature and if the temperature of the system is altered the chemical equilibrium may be upset. Particles must diffuse until the chemical potential is again uniform. Approaching chemical equilibrium may require mixing or de-mixing of species resulting in morphological detail. Chemical potential also varies with pressure though the pressures required to see major changes are not obtainable in Miscibility Gap Alloy operation. The temporal rate at which species can diffuse is important in Miscibility Gap Alloy evolution and will be discussed in §3.1.3.

3.1.2. Thermal Properties

An energy storage system is required to efficiently store energy in a volume and absorb or deliver it when required. These requirements involve properties of both steady state and transient nature. Maximising the energy stored in a volume whilst still maintaining a fast charge and discharge capacity is an optimisation problem with a range of solutions specific to particular cases.

When a thermal storage system is considered, these requirements may be met through a combination of material properties and storage system design. The steady state or equilibrium material properties designate how much energy might be stored in a volume. The transient properties in combination with the heat exchanger control how fast the system may charge or discharge to a cycle.

The equilibrium properties of interest in a thermal storage device define the amount of storage available in a volume or mass. They are specific heat capacity, density and latent heat of transition.

Specific heat capacity is an intensive property which may be ambiguously defined as the amount of heat needed to raise a kilogram of a material by one degree in temperature. That is:

$$c = \frac{\Delta Q}{m \Delta T} \qquad 2.$$

Here c is specific heat capacity, ΔQ is an amount of heat, m is mass and ΔT is a change in temperature.

A more precise definition should describe how heat is entering the system. This heat could be entering whilst the system is held at constant volume or constant pressure. In the first case, the heat transferred is all absorbed as internal energy, the heat capacity at constant volume (c_V) is defined as:

$$c_V = \left(\frac{\Delta u}{\Delta T}\right)_V = \left(\frac{\partial u}{\partial T}\right)_V \qquad 3.$$

Here Δu is a change in mass specific internal energy and ∂u is an infinitesimal change.

In the latter case where volume is unconstrained, compression or expansion work may also occur. This is accommodated as:

$$c_p = \left(\frac{\Delta u + p\Delta v}{\Delta T}\right)_p = \left(\frac{\partial u}{\partial T}\right)_p + p\left(\frac{\partial v}{\partial T}\right)_p = \left(\frac{\partial h}{\partial T}\right)_p \qquad 4.$$

Where v is mass specific volume and ∂h is an infinitesimal change in enthalpy.

For a solid or liquid the rate of change of volume with temperature at constant pressure is very small and can be neglected in most cases [87]. Generally for solids the method of heating (constant volume or pressure) does not make a large difference, thus the

subscript will be dropped and a single value quoted. This thesis is mostly concerned with solids and liquids and thus heat capacity here is equivalent in the isochoric and isobaric cases.

Specific heat capacity is temperature and pressure dependent. In a solid the temperature dependence is very pronounced near absolute zero [87], however, at room temperature and above a solids heat capacity is only weakly temperature dependent. Heat capacity in solids and liquids is only very weakly dependent on pressure and may be neglected for the purposes of this thesis.

Density (ρ) refers to the ratio of mass present in a system to the volume displaced by it. Density is an intensive property and is defined as:

$$\rho = \frac{m}{V} \qquad 5.$$

For a solid or liquid the density is only weakly temperature and pressure dependent [88] provided the material does not undergo a change in phase (ie. the material does not melt, freeze or undergo a crystalline transition).

Where a material does undergo a phase transition a certain amount of energy is absorbed or released. This energy is associated with breaking, joining or altering of bonds. Solid to liquid (melting) and liquid to solid (freezing) are of most concern to the materials discussed in this thesis, though solid to solid transitions are also encountered. Here atomic bonds are those being broken, reformed or altered. Whilst a phase change is occurring, any heat injected to (or rejected from) the material will contribute to (or detract from) the breaking of bonds. Thus, given enough time for heat diffusion to achieve thermal equilibrium, no sensible heating can occur whilst a phase change is occurring. Hence a phase change in a pure substance takes place at a constant temperature.

The amount of energy required to achieve a phase change is called the latent heat of transition (λ). Usually it is normalised to mass, creating an intensive property. Specifically for melting and freezing this energy is called the latent heat of fusion. The temperature at which this phase change occurs is the freezing or melting temperature and depends on the specific phase transition in a specific material and weakly on pressure. The variation is not large enough to be of importance for the small pressure changes encountered in the materials discussed in this thesis, thus the melting temperature is considered independent of pressure.

An extremely important property in the analysis of thermal storage media is energy density (ρ_e). This property describes the amount of thermal energy that may be stored in a volume for a temperature change. It is given by:

$$\rho_e = \left(\Delta T c_p + \lambda\right)\rho \qquad 6.$$

It is obvious here that the only parameter not inherent to a material is the selection of the operating temperature range. It is prudent to quote an operating temperature range when describing thermal storage material properties to ensure that the capacity is not exaggerated for typical uses.

The properties discussed hitherto are equilibrium properties and are defined for a system that has achieved local equilibrium. Heat transfer can occur through conduction, convection and radiation. When a thermal transient within an opaque solid is of interest the properties of thermal conductivity and diffusivity are salient. The two are related by:

$$\alpha = \frac{k}{\rho c_p} \qquad 7.$$

Here α refers to thermal diffusivity and k to thermal conductivity.

Thermal conductivity is the proportionality between heat flux through a unit area over a temperature differential covering a unit distance:

$$\dot{Q}=k\frac{A\Delta T}{\Delta x} \quad 8.$$

Here $\dot{Q}$ is heat transfer per unit time (in Watts), A is an area normal to the change in x coordinate Δx.

Thermal conductivity should in general be treated as a 2nd rank tensor. The above equation more generally is:

$$\vec{q}=\underline{k}\nabla\vec{T} \quad 9.$$

Thermal conductivity is temperature and pressure dependent. The conductivity of solid metals tends to decrease with increasing temperature above room temperature [89]. Some metals experience a solid-solid phase change on heating, resulting in an abrupt change of thermal conductivity (e.g. iron transforms from body centred cubic (bcc) to a face centred cubic (fcc) crystal structure at 910 °C). Upon melting thermal conductivity will essentially halve in most metals. Increasing the molten metal temperature from here will generally see a slight increase in conductivity [90] before decreasing again as the liquid temperature increases. Liquid thermal conductivities are generally insensitive to pressure unless the material is near its critical point [89].

Thermal diffusivity is the proportionality between the temporal rate of change of temperature to the spatial Laplacian (∇^2) of temperature in a homogeneous material. That is:

$$\frac{\partial T}{\partial t}=\alpha\nabla^2 T \quad 10.$$

In a heterogeneous material where diffusivity is a function of position, the relationship is:

$$\frac{\partial T}{\partial t} = \nabla \cdot (\alpha \nabla T) \quad 11.$$

Thermal diffusivity might be thought of as the ratio of a materials capacity to conduct thermal energy to its capacity to store it [89]. Thermal diffusivity tends to decrease with temperature for solid metals. It increases for most liquid metals as temperature increases near the melting point [91] before decreasing (similar to thermal conductivity behaviour).

Thermal effusivity (e) is an interesting property which gives a measure of the rate at which a material can absorb heat from a thermal reservoir in conductive contact. It is a very relevant parameter for surface heating and cooling processes [92]. Thermal effusivity is defined as:

$$e = \sqrt{k \rho c_p} \quad 12.$$

Multiplying energy density by thermal effusivity gives a useful parameter for comparing both the thermal storage and charge/discharge properties of a thermal storage material. Effusive energy density ($\rho_{e,eff}$) is herein defined as:

$$\rho_{e,effusive} = \rho_e e \quad 13.$$

The units of this property, $J^2 s^{0.5} m^{-5} K^{-1}$ are a little unusual consisting of the product of a volumetric energy and square root term, nevertheless it is a useful comparative parameter.

3.1.3. Chemical Properties

Miscibility Gap Alloys rely on mixtures of distinct phases arranged in a particular microstructure (see Figure 8). Phases in a metallurgical sense refer to particular arrangement of atoms; typically [93]:

1) solid solutions with variable composition and a crystal structure,
2) intermetallic compounds with a distinct composition and crystal structure or
3) liquids with variable composition but no crystal structure.

At equilibrium the phase with the lowest Gibb's Free Energy for the temperature, pressure and composition will exist. Gibb's Free Energy (G) for a pure element in a particular phase is defined as:

$$G=U-TS+pV \tag{14.}$$

For solids and liquids under atmospheric pressures, the pressure term may be neglected [93]. The Gibb's free energy for the pure elemental phase is then equivalent to the Helmholtz Free Energy (F):

$$G\sim F=U-TS \tag{15.}$$

If data is available for a number of different phases over a temperature range for a pure element the equilibrium phase may be determined. Whichever phase has the minimum Gibb's free energy at a temperature will be the equilibrium phase. The following figure shows the Gibbs Free Energy for a number of pure iron phases. It can be seen that for temperatures below 1185 K the most stable phase is bcc in crystal structure, above this temperature but below 1667 K the fcc structure is most stable. Between 1667 K and 1811 K the most stable phase is again bcc before the liquid phase becomes most stable above 1811 K (the melting temperature).

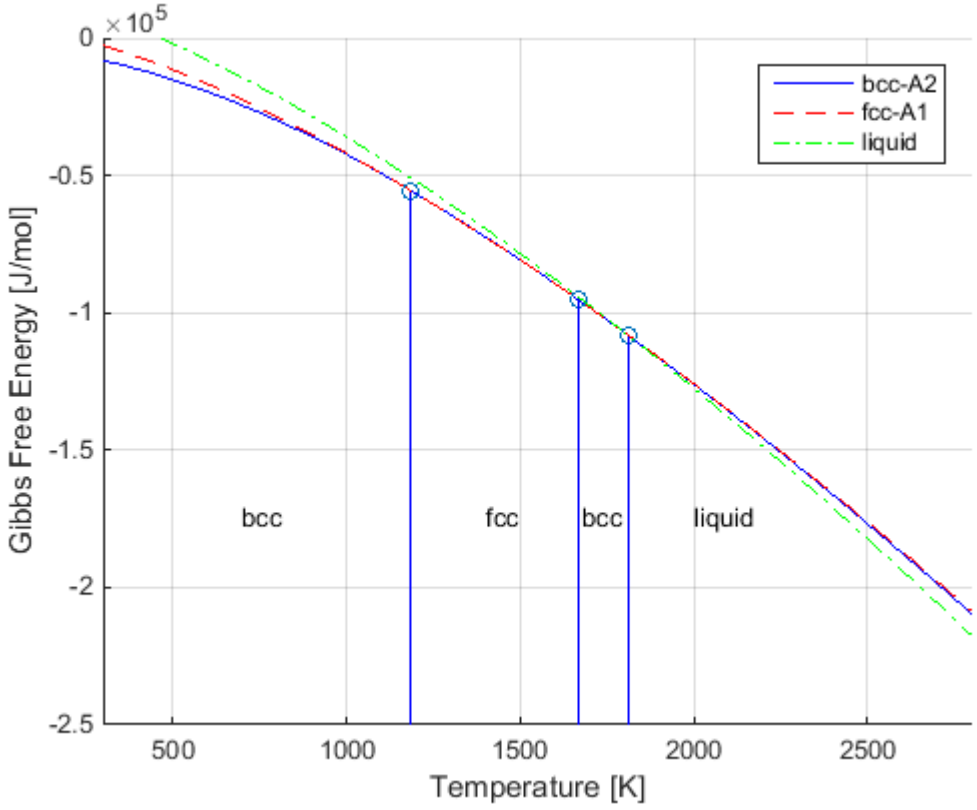

Figure 13 Gibbs free energy for pure iron phases from 300 to 2800 K.

When different pure materials are mixed, the Gibbs Free Energy of each phase depends on both composition and temperature. The Gibb's Free Energy for a solution phase ϕ (either solid solution or liquid) of composition described by vector $\vec{x}=(x_1,x_2,...,x_N) : \sum_i^N x_i = 1$ at a temperature T is described by the general equation [94]:

$$G^{\phi}(T,\vec{x}) = G_{Ref}(\vec{x}) + G_{Ideal\ Mixing}(T,\vec{x}) + G_{Excess\ Mixing}(T,\vec{x}) \quad 16.$$

The first term is a reference Gibb's Free Energy given by:

$$G_{Ref}(\vec{x}) = \sum_i x_i\, G_i^{\phi} \quad 17.$$

The second term is an ideal mixing term.

$$G_{\text{Ideal Mixing}}(T,\vec{x}) = RT\sum_{i} x_i \ln x_i \qquad 18.$$

The final term takes into account non-regular terms and may be modelled in a number of different ways. Modern computational thermodynamics methods (CALPHAD) evaluate the excess mixing term according to [94]:

$$G_{\text{Excess Mixing}}(T,\vec{x}) = \sum_{i}^{n}\sum_{j=i+1}^{n+1} x_i x_j \left[\Omega_{ij}^{0} + \Omega_{ij}^{1}(x_i - x_j) + \Omega_{ij}^{2}(x_i - x_j)^2 + \ldots\right] \qquad 19.$$

The Ω terms' exponent refers to an equation index which does not usually exceed two.

For binary alloys the Gibb's Free Energy for each stable phase may be plotted against composition for a particular temperature. Similar to the previous procedure, whichever phase has the lowest Gibbs free energy at a composition is the equilibrium phase. It may be the case that two phases will display local minima at different compositions. The lowest energy state for intermediate compositions is neither one phase nor the other, but a distinct mixture of the two. The energy of the two phase mixture is simply an atomic fraction weighted average of the Gibbs free energies of each phase at a common tangent (equal chemical potential) and hence the two phase region appears as a straight line joining the two different phase curves.

A phase diagram is a convenient means of showing the equilibrium phases over a temperature and concentration range for binary alloy. A number of Gibbs free energy - composition curves are obtained over a range of temperatures and the minimum phases (or two phase regions) noted [93]. This is demonstrated in

Figure 14.

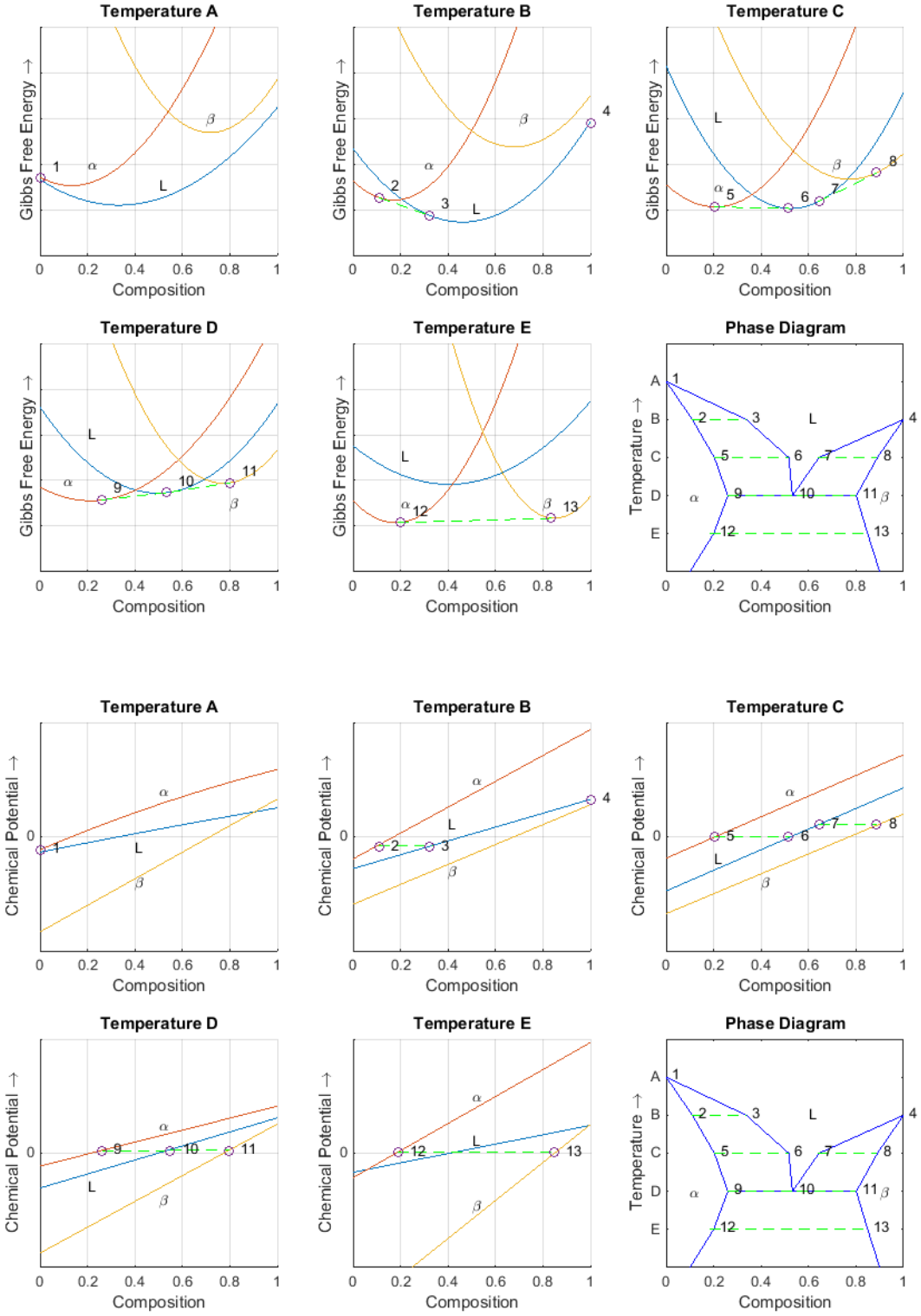
Temperature A
Temperature B
Temperature C
Temperature D
Temperature E
Phase Diagram
Gibbs Free Energy →
Chemical Potential →
Temperature →
Composition
α
β
L
1
2
3
4
5
6
7
8
9
10
11
12
13
A
B
C
D
E
0
0.2
0.4
0.6
0.8
1

Figure 14 An example of several Gibbs Free Energy and Chemical Potential curves at different temperatures and their relationship to the topology of a phase diagram. The top left panel represents T_A on the phase diagram where the only stable phase is liquid (L). The top centre panel shows two stable phases, solid α (stable from 0 to x_3 in composition) and liquid at temperature T_B (stable from x_3 to 1 in composition). The top right panel shows three stable phases, α, liquid and β occurring at T_C stable from 0 to x_5, x_6 to x_7 and x_8 to 1 in composition respectively. As the system cools further in the bottom left panel to the eutectic temperature T_D the liquid phase ceases to be stable except at a single composition x_{10}, the α and β phases are stable from 0 to x_9 and x_{11} to 1 respectively. At the lowest temperature, T_E , in the bottom middle panel the system is composed of solid α and β phase with stable compositions 0 to x_{12} and x_{13} to 1 respectively.

A miscibility gap is essentially any two phase region upon a phase diagram. Systems that are useful as Miscibility Gap Alloys display considerable immiscibility of the two solid phases (or solid and liquid phases) either side of the operating composition. They may be identified by inspecting the phase diagrams for different binary alloy combinations.

As discussed in §3.1.1, two systems brought into diffusive contact will exchange particles until they achieve uniform chemical potential. In a binary system chemical potential is the first derivative of Gibb's Free Energy with respect to composition. This derivative is over the Gibb's Free Energy for the equilibrium phases at a temperature and pressure.

$$\mu_i = \frac{\partial G}{\partial x_i}\Big)_{T,P} \qquad 20.$$

Here x refers to composition.

The rate at which the system may proceed towards steady state is controlled by the capacity for atoms to move through different phases. The mechanism by which atoms diffuse depends upon which phase they are within. In a solid, atoms predominantly diffuse through either an interstitial or vacancy mechanism. If the solute has an appreciably smaller size than the solvent the dominant mechanism is interstitial. If the atom sizes are comparable a vacancy mechanism is predominant. Diffusion in a liquid is much more rapid

than in a solid as no definite crystal structure exists and all atoms move with much more freedom [95].

The rate at which species diffusion occurs, similar to heat diffusion, is proportional to the diffusivity multiplied by the spatial Laplacian of chemical potential in a homogeneous material.

$$\frac{\partial c_i}{\partial t} = D\nabla^2\mu_i \qquad 21.$$

Here c_i is the concentration of the ith species.

In a heterogeneous material where diffusivity is a function of space, binary composition and temperature the relationship is:

$$\frac{\partial c_i}{\partial t} = \nabla\cdot\left(\widetilde{D}(\vec{r},x_i,T)\nabla\mu_i\right) \qquad 22.$$

Here $\widetilde{D}$ is an interdiffusion coefficient.

Diffusivity is commonly measured by applying a film of radioactive isotope of the diffusing species to the surface of the host of interest. The depth to which it penetrates over time can be used to calculate the tracer diffusivity of species. However, this diffusion coefficient is only valid for a very dilute solution and hence may not be utilised in equation 22. Generally tracer diffusivities are quoted for a solvent and solute with an Arrhenius type equation:

$$D = D_0 e^{-\frac{Q}{RT}} \qquad 23.$$

Here Q is an activation energy, D_0 is a base diffusivity and R is the universal gas constant.

An interdiffusion coefficient is dependent on composition and hence may be utilised in equation 22. Tracer diffusion coefficients can be converted to an interdiffusion

coefficient through Darken's equation for a binary alloy (below for two arbitrary species A and B):

$$\widetilde{D}(x_A)=x_B D_A(x_A)+x_A D_B(x_A) \quad (24.)$$

This requires knowledge of the tracer diffusivity at all possible compositions in the binary alloy. Where a two phase region is encountered on the phase diagram a volume weighted average of the two relevant phases can be used as an approximation of the effective tracer diffusivity.

In some cases it may be beneficial to adjust equation 21 to use a spatial laplacian of concentration rather than chemical potential. If this is the case, then the thermodynamic biasing can be handled by modifying the interdiffusion coefficient by a thermodynamic factor, ϕ.

$$\widetilde{D}'(x_A)=\left(x_B D_A(x_A)+x_A D_B(x_A)\right)\phi \quad (25.)$$

$$\phi=\frac{x_A x_B}{RT}\frac{\partial(\mu_A-\mu_B)}{\partial x_A} \quad (26.)$$

$$\frac{\partial c_i}{\partial t}=\nabla\cdot\left(\widetilde{D}'\nabla c_i\right) \quad (27.)$$

The thermodynamic factor is positive through solutions (generally less than twenty) decreasing to zero in a two phase region. This model is often referred to as Fickian diffusion. Where diffusion of species occurs through a stable solution without altering the composition significantly the thermodynamic factor can be approximated as unity. Unfortunately for the modelling of morphological evolution it can only describe diffusion, not nucleation and morphological evolution.

Nucleation of one phase from another is a matter of balancing the reduction in bulk Gibb's Free Energy of the system against the increased energy of maintaining an

interface. Interface energy is proportional to the surface area of the phase nucleating whilst the reduction in bulk Gibb's Free Energy is proportional to the volume. There exists a critical surface area to volume ratio below which a nucleated phase is thermodynamically favourable to maintenance of a single phase solution. Once a stable phase has formed it will continue to grow until the local region is depleted of solute. The rate of growth depends on both the rate of diffusion of solute to and across the interface.

The evolution of material morphology is governed by the tendency for systems to maximise their entropy and minimise their potential energy. If the potential's dependence on both bulk volumetric Gibbs Free Energy and interface energy is known then nucleation and morphological evolution may be described. The Cahn-Hilliard free energy is one such thermodynamic potential [96, 97]:

$$G_{CH}\left(\vec{x}(\vec{r})\right)=\frac{1}{\rho}\int_{V} G\left(\vec{x}(\vec{r})\right)+\frac{1}{2}\kappa\nabla^{2}\vec{x}(\vec{r})\ dV \qquad 28.$$

Here ρ is the molar density of the mixture, G refers to the homogeneous free energy for the system and $\kappa\nabla^2\vec{x}(\vec{r})$ is a gradient energy. The chemical potential for the Cahn-Hilliard free energy is, through the calculus of variations, then:

$$\mu_{CH}=\frac{\delta G_{CH}\left(\vec{x}(\vec{r})\right)}{\delta\vec{x}(\vec{r})}=\mu\left(\vec{x}(\vec{r})\right)-\kappa\nabla^{2}\vec{x}(\vec{r}) \qquad 29.$$

Diffusion then proceeds as per equation 21 to minimise fluctuations in chemical potential. This involves proceeding towards local minima in Gibbs Free Energy and minimising interface energy. The following partial differential equation is known as the Cahn-Hilliard equation:

$$\frac{\partial x_i}{\partial t}=\nabla\cdot\left(\widetilde{D}(\vec{r},x_i,T)\nabla\left(\mu\left(c_i(\vec{r})\right)-\kappa\nabla^{2}c_i(\vec{r})\right)\right) \qquad 30.$$

The Cahn-Hilliard equation may be used to predict changes in composite morphology due to diffusive and interfacial phenomena. Unfortunately the equation is generally impossible to solve analytically and extremely computationally intensive when numerically solved. It is unsuitable for simulating very long chemical diffusion processes such as those encountered in Thermal Storage cycling.

Another approach involves assuming a simplified morphological arrangement and simulating how it changes in size through a number of thermal cycles. The approach to equilibrium composition of solid and liquid during each cycle can be estimated using the Fickian methods described earlier. A known amount of material can be simulated dissolving into the liquid through melting and being rejected through resolidification. The morphology may then grow or shrink according to the transport of material. A critical threshold might be encountered in a characteristic length that represents a percolation threshold or the morphology might cease to exist in favour of a more stable arrangement. This simplified model lacks the morphological detail of the Cahn Hilliard method described previously, however it is practical to solve and provides limiting cases to the lifetime of thermal storage materials through diffusion cycling.

3.1.4. Homogenisation of Equilibrium Properties

Morphological detail within a composite may occur at a variety of scales. If the largest detail is at a much smaller scale than that at which an observation is to take place, the local influence of the detail on material properties may be ‘smoothed out’ to an *effective* average. The size at which the observation is large enough might be called a representative volume [41].

Material properties may be categorised as equilibrium or non-equilibrium properties. Equilibrium properties may be homogenised on mass, volume or molar fractions without consideration of the configuration of the phases. Transient properties depend on the morphology of the composite in addition to the relative amount of each phase. Properties of prime relevance to this study are matter density, heat capacity, thermal conductivity/diffusivity and atomic diffusivity.

The effective density ($\bar{\rho}$) of a composite is the volume weighted average of the constituent material densities. This can be shown through conservation of mass (the derivation is given in appendix B). As mentioned earlier, density is weakly temperature and pressure dependent. The effective density for a composite composed of n-constituents each with density ρ_i and volume fraction φ_i is:

$$\bar{\rho} = \sum_{i=1}^{n} \rho_i \varphi_i \qquad 31.$$

Heat capacity may be homogenised in a similar manner. Instead of a volume weighted average, a mass weighted average is required. This can be shown from conservation of sensible heat energy and is described in appendix B. For a composite of n-constituents, each with heat capacity $c_{p,i}$ and mass fraction ψ_i, the effective specific heat capacity ($\bar{c_p}$) is:

$$\bar{c_p} = \sum_{i=1}^{n} \psi_i c_{p,i} \qquad 32.$$

Similarly the effective latent heat of fusion ($\bar{\lambda}$) is simply the mass fraction of material undergoing a phase change multiplied by the mass normalised latent heat of transformation. For a single phase (the ith) undergoing a phase change:

$$\bar{\lambda}=\lambda_i\psi_i \quad 33.$$

Mass fraction and volume fraction are related through:

$$\psi_i=\frac{\varphi_i\rho_i}{\bar{\rho}} \quad 34.$$

Composites often have some unavoidable porosity introduced through the manufacturing method. Typically it is less than 5% by volume for a metallic composite formed through powder metallurgy. The homogenisation described above is modified to account for porosity by assuming that the pores contribute negligible mass. This is appropriate for composites formed of materials with densities much greater than gases at atmospheric pressures. With this justified simplification the modified matter density for a porous composite is given by:

$$\bar{\rho}_{\text{porous}}=(1-\varphi_{\text{pores}})\sum_{i=1}^{n}\rho_i\,\varphi_i \quad 35.$$

Interestingly the effective heat capacity is unaffected by porosity as it is normalised on mass rather than volume. The energy density of a porous binary composite where one phase is undergoing a phase change is then:

$$\bar{\rho_e}=(1-\varphi_{\text{pores}})\bar{\rho}\left(\Delta T\bar{c_p}+\bar{\lambda}\right) \quad 36.$$

The effective equilibrium properties of composite porous thermal storage materials undergoing a phase change are thus defined in terms of their constituent properties, volume fractions and porosity

3.1.5. Homogenisation of Non-Equilibrium Properties

Homogenisation of non-equilibrium properties like thermal conductivity requires consideration of the composite morphology. The homogenisation of non-equilibrium properties is not trivial and leads to complex and very interesting solutions.

There exist a multitude of analytical and empirical methods of homogenising thermal conductivity as described in the literature review. It appears in modern literature that generally a select group of analytical methods (namely the Weiner bounds, the Hashin Shtrikman bounds, the Maxwell-Eucken methods and the effective medium theory) are introduced and examined before more material specific semi-analytical or empirical methods are analysed. Several review articles exist categorising the available methods and rating their validity against a particular class of composites [41, 42, 98].

The Weiner bounds represent the highest and lowest possible effective conductivity for a composite provided conduction is the only heat transfer mechanism [99]. These bounds hold for any material structure and are very useful for normalisation. The bounds may also be known as the series and parallel models. This terminology appears inconsistent when referring to the upper and lower bounds, some authors following the convention of resistors in parallel [42, 67], whilst others consider conductors in parallel [99]. A more rigorous definition might be the arithmetic and harmonic volume weighted averages of conductivity, where the arithmetic is the higher. The upper and lower Weiner bounds are given in equations 37 and 38.

$$\bar{k}_{Arith} = \sum_{i=1}^{n} k_i \varphi_i \qquad 37.$$

$$\bar{k}_{Harm} = \frac{1}{\sum_{i=1}^{n} \varphi_i / k_i} \qquad 38.$$

The Weiner bounds are not a good estimate of the actual effective conductivity of a composite. The upper bound physically represents a parallel tensor component of conductivity in a series of parallel plates. The lower bound represents the perpendicular

tensor component in this configuration. The Weiner bounds serve mostly as a point of reference and a validity check.

The geometric mean lies between the Weiner bounds and is also commonly used as a reference point for effective conductivity measurements. The geometric mean is given by equation 39:

$$\bar{k}_{Geom} = \prod_{i=1}^{n} k_i^{\varphi_i} \qquad 39.$$

This estimate at effective conductivity is still just a method of averaging and does not take into account the morphology of a composite beyond the relative volume of constituents.

The best estimate possible for the effective conductivity of macroscopically homogeneous and isotropic binary composites without knowledge of the microstructure will fall within the Hashin-Shtrikman bounds. The upper and lower bounds are:

$$\bar{k}_{HK,Upper} = k_1 + \frac{\varphi_2}{\frac{1}{k_2 - k_1} + \frac{\varphi_1}{3k_1}} \qquad 40.$$

$$\bar{k}_{HK,Lower} = k_2 + \frac{\varphi_1}{\frac{1}{k_1 - k_2} + \frac{\varphi_2}{3k_2}} \qquad 41.$$

Here the subscript 1 refers to the distributed phase and 2 to the matrix phase. Maxwell developed a significant theory on electrical conduction through heterogeneous materials during the late 19th and early 20th century [38]. The work has been utilised by many authors and applies to many phenomenological transport problems. The theory is based on a number of non-interacting spherical inclusions contained within a much larger sphere. By equating the contribution of each small spheres' potential field to the hypothetical containing sphere, an estimate of an effective conductivity could be made.

Eucken in 1940 adapted the work of Maxwell to thermal phenomena. [45] For a binary composite the model is:

$$\bar{k}_{ME,Inclusion}=\frac{k_1\varphi_1+k_2\varphi_2[3k_1/(2k_1+k_2)]}{\varphi_1+\varphi_2[3k_1/(2k_1+k_2)]} \quad 42.$$

The model is valid for sparse inclusions (<50% volume fraction) within a matrix. Composites must also be macroscopically isotropic for prediction using the Maxwell-Eucken model. This model still does not account for geometric parameters beyond the implicit derivation on spherical inclusions.

The Maxwell-Eucken model may be utilised for low conductivity inclusions (omissions) through simple modification of equation 42:

$$\bar{k}_{ME,0mission}=\frac{k_2\varphi_2+k_1\varphi_1[3k_2/(2k_2+k_1)]}{\varphi_2+\varphi_1[3k_2/(2k_2+k_1)]} \quad 43.$$

Effective medium theory assumes that the net influence on overall potential gradient caused by microstructural features is zero when averaged over a sufficiently large volume [99]. The effective mean field theory was first proposed by Bruggeman in 1935 [53]:

$$\varphi_1\frac{k_1-\bar{k}_{EMT}}{k_1+2k_{EMT}}+\varphi_2\frac{k_2-\bar{k}_{EMT}}{k_2+2k_{EMT}}=0 \quad 44.$$

The reciprocity theory developed by Keller [59] was adapted to estimate the effective thermal conductivity of a two phase composite by Del Rio et. al. [61]. The theory does not assume any particular shape of inclusion and is most valid for materials that are isotropic in two dimensions.

$$\bar{k}_{Rec}=k_1\frac{1+\varphi_2\left(\sqrt{\frac{k_2}{k_1}}-1\right)}{1+\varphi_2\left(\sqrt{\frac{k_1}{k_2}}-1\right)} \quad 45.$$

A simple model that considers a specific morphology is the Halpin-Tsai theoretical model [42, 100]. It is most appropriate for filaments of uniform cross-sectional area running in parallel through a matrix. The parallel and lateral components of the effective conductivity tensor are separately considered. The parallel component is assumed to be the series volume (or area in this case) weighted average. The transverse components take into account the shape of the filament. The effective isotropic conductivity through this model is:

$$\bar{k}_{HT}=\frac{2}{3}\left(\frac{1+\xi\gamma\varphi_1}{1-\gamma\varphi_1}\right)+\frac{1}{3}(\varphi_1 k_1+(1-\varphi_1)k_0) \qquad 46.$$

Here the additional coefficients are:

$$\gamma=\frac{\frac{k_1}{k_0}-1}{\frac{k_1}{k_0}-\xi}$$

$$\xi=\begin{cases}\sqrt{3}\log\left(\frac{a}{b}\right) & \text{for a plate of width a and height b}\\ 1.0 & \text{for square or circular fibres}\end{cases}$$

Each of these models estimates an effective conductivity for a particular or range of morphologies. The arithmetic and harmonic means have clear geometrical representations; that of parallel and normal conduction through parallel plates. The geometric mean is more difficult to define; it shows no sudden change in efficiency due to percolation but more of a gradual shift. Material with high surface area to volume fraction will touch at lower volume fractions and increase in microstructural efficiency more gradually than more spherical particles. It is thought that the geometric mean represents morphologies of these distributed particles best. The Hashin-Shtrikman bounds are appropriate for a range of macroscopically homogeneous and isotropic binary composites. The Maxwell-Eucken models require dilute

composites of ideally spherical particles. Very fine morphological detail can be well represented through both the effective medium and reciprocity models. Effective medium theory will predict a percolation threshold at around 50% volume fraction. These representations are schematically summarised in Figure 15.

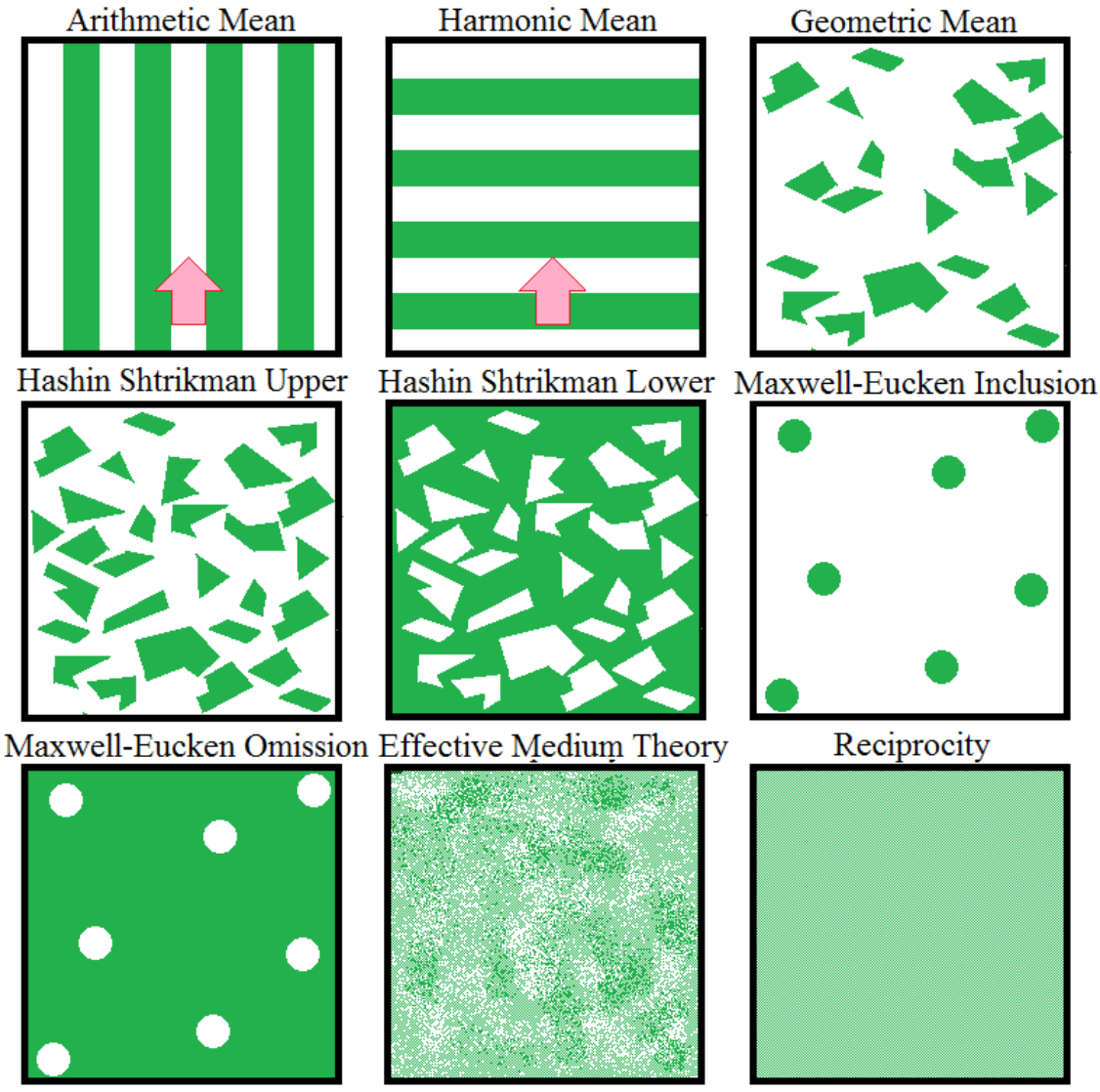

Figure 15 Schematics of morphologies appropriate for each of the microstructural efficiency models presented in the previous figure. Here green represents the high conductivity phase whilst white represents the poorer conductor.

Microstructural Efficiency was developed by the candidate as a means of better quantifying the impact of morphology on a binary composites effective conductivity [67, 68]. A two dimensional function of volume fraction and conductivity ratio (k_{dis}/k_{mat}) is created for each morphology of interest where the result is a fraction of the upper Weiner bound. Given the two dimensional function, the effective conductivity can be back calculated regardless of the morphology. The empirical functions are determined experimentally or numerically and recorded for each morphology of interest. It will be shown later (§4) that the onset of percolation for a morphology dominates effective thermal conductivity behaviour.

Homogenisation problems are frequent in the literature and often are discussed with reference to a very specific material or subset of materials. As such a great deal of work has been done developing empirical models that yield very accurate estimates for effective properties for a small set of composites. As Miscibility Gap Alloys are a recent invention there does not exist an empirical model specifically developed for the case, however the spherical distribution is common to a lot of the theoretical models introduced previously. Thus the focus of this thesis is more on how the materials compare to theoretical models.

The introduction of porosity to effective transient properties is intuitively more complex than its application to equilibrium properties. If it is assumed that the porosity shows identical morphology in both the inclusion and matrix phase then the procedure of homogenisation can be undertaken twice, first for pores of negligible conductivity in each constituent then for the two modified constituents. Assuming a distribution of spherical pores with low volume fraction allows the use of a number of models for the first step. The

Maxwell Eucken omission model is selected for this work. The second stage must utilise the model appropriate for the morphology of the greater inclusion and matrix phases.

The homogenisation field contains a huge volume of work based on both experiment and theory. Most modern contributions to the field are very accurate and specific to particular composites but lack the level of generality that early researchers provided. Through the introduction of microstructural efficiency, previous results may be combined with new experiments. This increases the range of prediction for each theory and highlights the underlying physical mechanism controlling the conductivity behaviour.

3.1.6. Other Material Properties

The predominant function of Miscibility Gap Alloys is as a thermal storage medium. Thus special attention was given to thermal and chemical properties. It is necessary also to consider thermo-mechanical and mechanical properties for actual implementation of the materials. The following section briefly introduces thermal expansivity, stiffness and compliance, yield and ultimate strength.

Thermal expansion of materials is an important phenomenon. It may be considered a thermo-mechanical property (and was not included in §1.21). The amount that a material expands due to a change in temperature is described by a coefficient of expansion. This coefficient of expansion is a second rank tensor relating strain to temperature change [101]:

$$\vec{\varepsilon} = \underline{e}\Delta T \qquad 47.$$

Effective thermal expansion coefficient for a composite is a morphology dependent property.

A material subjected to external forces will be in a state of stress. The deformation of the body, or the strain state, is proportional to this stress if the material is below a yield stress. The proportionality between stress and strain is handled through the fourth rank stiffness and compliance tensors (unfortunately the convention is stiffness $\underline{C}$ and compliance $\underline{S}$).

$$\vec{\sigma}=\underline{C}\vec{\varepsilon} \quad (48.)$$

$$\vec{\varepsilon}=\underline{S}\vec{\sigma} \quad (49.)$$

The stiffness and compliance of a material are morphology dependent and are often evaluated for composites.

Most metallic materials will only behave elastically up to around 0.005 strain. Beyond this strain the material plastically deforms and will not return to its original state on removal of the external force. Yield strength for a material describes the stress at which this occurs and is commonly used as a critical constraint in engineering design. Aluminium may have a yield strength as low as 50 MPa whilst some high strength steels exceed 2400 MPa [102].

There exists a tensile stress at which a material can no longer plastically deform and will break. This stress is called the ultimate strength. Metals will plastically deform considerably before failing whist brittle materials will not plastically deform much before breaking. Understanding how the materials in a miscibility gap alloy are likely to fail gives insight into how the morphology of a system might progress through thermal cycling.

3.2. The Lattice Monte Carlo Method for Thermal Diffusion

The Lattice Monte Carlo numerical method proved to be a very powerful tool for analysing the thermal characteristics of Miscibility Gap Alloys and more general composites. The following section introduces the theory of Lattice Monte Carlo analysis, describes two algorithms utilised by the candidate before explaining how and to what extent it may be implemented.

3.2.1. Theory of the Lattice Monte Carlo Method for Thermal Diffusion

Heat diffusion is a random process that can be represented by random walks of 'heat' particles. The Einstein-Smoluchowski equation describes the thermal diffusivity of a system in a number of dimensions based on an ensemble average of such heat particles:

$$\alpha = \frac{\langle r^2 \rangle}{2dt} \qquad 50.$$

A Lattice Monte Carlo simulation models random walks of particles representing quanta of heat energy on a lattice. In a composite the probability that a heat particle will step is proportional to the relative conductivity and thermal inertia (the product of heat capacity and density) of the material. At any point of time in the simulation, the number of heat particles upon a node is proportional to the energy and hence temperature of the surrounding discrete volume of material.

The simulation may be utilised as a transient solution to a boundary condition problem, as a steady state solution to a boundary condition problem or as a means to solving the Einstein-Smoluchowski equation above. As a transient and steady state solver

for boundary condition problems, the Lattice Monte Carlo method is relatively inefficient (compared to traditional Finite Difference discretisation)[3]. The method is quite common for homogenising material properties and is the manner in which the candidate has used the Lattice Monte Carlo method.

3.2.2. Lattice Monte Carlo Method for Transient Thermal Diffusion

Transient thermal diffusion requires the inclusion of thermal inertia to a Lattice Monte Carlo simulation. This additional probability to overcome for a successful jump acts to increase the length of a simulation by both increasing the number of jump failures and computational time. The algorithm may be represented in a flow chart like that shown in Figure 16.

[3] This is a general observation. Lattice Monte Carlo methods may be quite appropriate and indeed more efficient for particular boundary condition problems involving complex morphology with many interfaces.

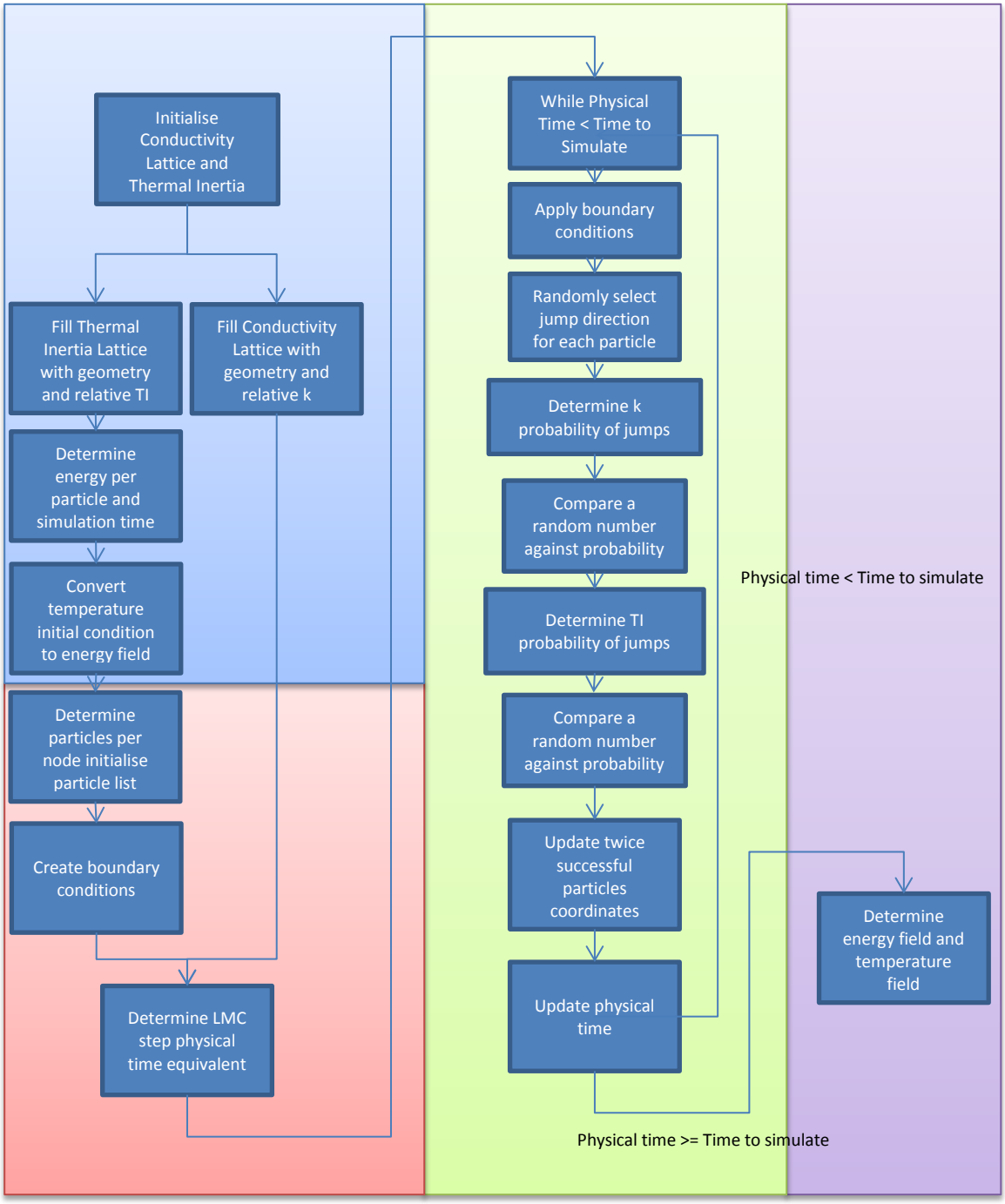

Figure 16 Flow diagram of a Lattice Monte Carlo method for transient thermal diffusion with isothermal thermal properties. The top left shaded region represents the initialisation phase, the bottom left represents the particle list initialisation, the central region is the simulation phase whilst the right hand region is post processing.

The algorithm naturally breaks into four distinct processes (as indicated with shaded regions on Figure 16). The first requires initialisation of the domains, this includes initialising and normalising the conductivity and thermal inertia topological information. The particle list must be initialised next. This includes calculating the quantum of energy each virtual particle shall possess by discretising the initial energy field (calculated from the initial temperature field and the thermal inertia field), before stacking the particles upon each node of the energy profile to achieve the desired initial temperature profile. The relationship between physical time and Lattice Monte Carlo step is calculated at this stage. The simulation phase follows where particles are created and destroyed to maintain boundary conditions whilst they randomly walk guided only by the thermal inertia and conductivity lattices. Once the desired time interval has been simulated, the final energy field and hence temperature field may be determined.

3.2.3. Lattice Monte Carlo Method for Steady State Thermal Diffusion Algorithm

The algorithm for a steady state Lattice Monte Carlo method is much simpler and efficient than that for transient diffusion. At steady state a composite system with periodic boundaries as the only boundary conditions will have achieved a uniform temperature field. Thus, thermal inertia may be ignored and the random walk is guided only by the thermal conductivity lattice.

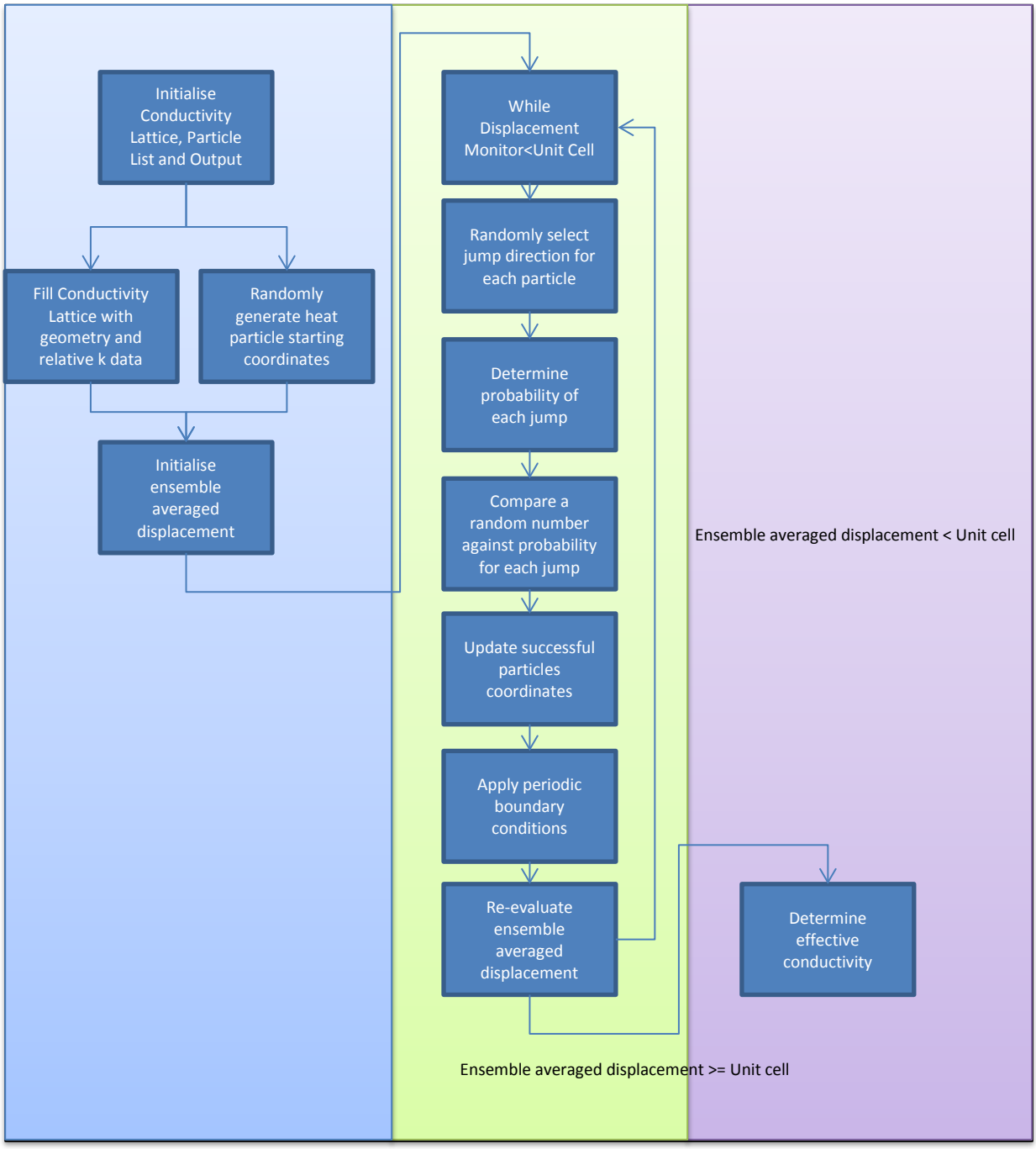

Figure 17 Flow diagram of a Lattice Monte Carlo method for steady state thermal diffusion with isothermal thermal properties. The left shaded region represents the initialisation phase, the central region is the simulation phase whilst the right region is post processing.

In the initial phase particles are randomly seeded over the initial lattice representing an isothermal state with unit thermal inertia everywhere. A simulation loop is then entered where particles randomly walk with a jump probability proportional to the harmonic average between current and target node conductivities. The ensemble averaged squared displacement is determined after each time step. Once this exceeds twice the periodic cell size, the particles are likely to have adequately explored the domain. The simulation stops at this point and the effective conductivity is evaluated from the number of time steps and diffusion length mentioned.

A demonstrative implementation of this algorithm is provided in electronic form on the attached compact disk. The algorithm is implemented in MATLAB® language and is labelled SA1_Lattice_Monte_Carlo_Main.m.

3.2.4. Uncertainty in the Lattice Monte Carlo Method for Thermal Diffusion

A statistical uncertainty exists for any random walk algorithm. A histogram of the displacement of a large number of particles undergoing random walks after a large number of time steps would appear to have a normal distribution. This is because a random walk is controlled by the central limit theorem. The variance of the normal distribution is related to diffusivity and the time of the process as:

$$\sigma^2 = 6\alpha t \tag{51.}$$

Thus if the uncertainty in α is taken as the standard deviation of the normal distribution (the square root of the variance) the dependence is:

$$\Delta\alpha = \frac{1}{\sqrt{6t}} \tag{52.}$$

A model microstructure need not be an exact geometrical representation of a sample's real microstructure to give accurate numbers for effective thermal conductivity. It may be prohibitively expensive and time consuming to establish complete three dimensional geometry of samples through the technique of Micro Computed Tomography scanning. A much more efficient option for obtaining three dimensional geometry may be to 'grow' a representative morphology through a random microstructure generation algorithm. The candidate published a journal article demonstrating morphology growth and how it introduced uncertainty for Sn-Al and Cu-Fe Miscibility Gap Alloys [67], the details are not discussed here for the sake of brevity.

Sources of uncertainty also lie within the discretisation of a morphology for Lattice Monte Carlo Analysis. The size of the elements used in the analysis must be small enough to capture morphological details that influence the effective conductivity estimation. These details might be the curvature of a surface or the fine interface between two close particles. Whether a result is independent of the size of the elements (or equivalently the resolution of the mesh) may be proved by establishing mesh independence. This may be achieved by repeating a Lattice Monte Carlo simulation for progressively smaller elements until the output of the simulation is consistent. It was found that 10 nodes across the base radius of the inclusion would consistently yield a mesh independent result.

The final major source of uncertainty in the use of Lattice Monte Carlo Analysis for the effective conductivity of composites is a result of the use of periodic boundaries. The volume of composite simulated must be large enough to be characteristic of the whole medium. Periodicity independence may be established in a similar manner to mesh independence. The volume of a composite simulated is gradually increased whilst Lattice

Monte Carlo simulations are performed upon it until the standard deviation in the result is constant. It was found that a cubic volume with dimensions above 16 times the base inclusion radius would yield results independent of the periodic volume.

As discussed earlier in §3.1.5 the effective thermal diffusivity is related to the effective conductivity and thermal inertia. As the effective thermal inertia is a simple mass weighted average of constituent properties, a Lattice Monte Carlo simulation need only provide an effective conductivity. Simulation time can be minimised by assigning the thermal inertia of each constituent in a composite to be unity.

3.2.5. Use of the Lattice Monte Carlo Method to Homogenise Miscibility Gap Alloy Material Properties

The Lattice Monte Carlo method is appropriate for homogenising the thermal conductivity (and diffusivity) of Miscibility Gap Alloys. Provided that the molten constituent is of typical powder dimensions (<7 mm radius) the transport of heat through the bulk will be completely dominated by conduction [67]. Morphologies typical of Miscibility Gap Alloys are easily grown for direct correlation and comparison. It will be seen later that a more general method can be utilised where typical Miscibility Gap Alloy morphologies are modelled for a range of volume fractions and conductivity ratios to allow easy estimation of effective conductivity for changing temperature and morphology of the materials.

3.3. Longevity Analysis of Thermal Storage

Miscibility Gap Alloys are intended to be a very long term and stable solution to the problem of thermal energy storage. Thus it is prudent to analyse the long term behaviour of the alloys as they are cycled and maintained at temperatures near the melting point of the distributed phase. The equilibrium microstructure of a miscibility gap alloy is a result of several competing thermal, mechanical and chemical phenomena. These phenomena are strongly dependent on the constituent materials, manufacture, and particular thermal cycle of the alloy. As with any type of 'many cycle' analysis of an engineering problem methods must be devised to accelerate or account for prohibitively long direct experiments.

3.3.1. Diffusion Dominated Aging

Diffusion dominated aging occurs in Miscibility Gap Alloys where a non-negligible solubility exists in the distributed or matrix phases at the upper operating temperature. Alloys involving graphite matrices do not show considerable solubility and are unlikely to age due to this mechanism. The Mg-Fe and Si-SiC systems also show negligible solubility. However, the Sn-Al and Cu-Fe systems have a strong potential to age though diffusion.

In the following discussion the matrix phase will be referred to as the alpha phase and be dominated by A atoms. The distributed phase is referred to as the beta phase and is dominated by B atoms. For example in the Sn-Al system the alpha phase is Face Centred Cubic and dominated by aluminium (A) atoms whilst the Body Centred Tetragonal phase is referred to as beta and is dominated by tin atoms (B).

As discussed in §3.1.1 two bodies brought into diffusive contact will exchange atoms until chemical equilibrium is obtained. The atomic composition for chemical

equilibrium is described by the boundary of a two phase region on a phase diagram. For example pure tin placed in contact with pure aluminium at 200 °C will exchange atoms until the tin rich beta phase has composition (0.993 mol fraction Sn, 0.007 mol fraction Al) and the aluminium rich alpha phase has composition (0.00002 mol fraction Sn, 0.99998 mol fraction Al). Cooling from this temperature to 100 °C will alter the equilibrium compositions to (0.9987 mol fraction Sn, 0.0013 mol fraction Al) and (8.257×10^{-6} mol fraction Sn) respectively. Thus changing the temperature of a binary system will alter the equilibrium composition of the phases and hence drive a flux of atoms.

Movement of atoms is achieved through diffusion, the rate of which is also temperature dependent. The diffusivity of aluminium atoms in tin at 200 °C is 1.7×10^{-14} m^2/s whilst at 100 °C it is 8.5×10^{-16} m^2/s. As described in §3.1.3 the diffusivity dependence on temperature is modelled very well by an Arrhenius relationship.

Most drastic changes occur in solubility and diffusivity when a component melts. In the Sn-Al example the solubility of aluminium in tin rich beta phase increases from 0.0101 mol fraction Al to 0.0196 mol fraction Al through melting, a 94% increase. The diffusivity also jumps from 3.44×10^{-14} m^2/s to 2.34×10^{-10} m^2/s, an increase of four orders of magnitude. The opposite step is observed on freezing with a sudden drop in solubility and in diffusivity.

A sudden reduction in diffusivity and change in solubility of the minor component leads to a ‘freezing’ of the beta phase composition. In all systems analysed in this thesis except Cu-Fe, this leads to an unstable solid solution. As the temperature is further reduced the Gibbs Free Energy of the unstable solid solution increases. At a certain degree of undercooling the system will spontaneously decompose to equilibrium beta phase with new

nuclei of alpha phase. The size of the alpha crystals nucleated is dependent on the rate of cooling with smaller crystals formed for faster cooling rates. The process of nucleating crystals of alpha phase within the beta phase results in gradual percolation of the Miscibility Gap Alloy morphology, eventually leading to failure.

As described in the Introduction, simulation of the precipitation of material in a melt is an extremely involved process occurring over a very short time (μs) and distance scale (nm). Given thermal cycles occur on the order of hours to days the Cahn-Hilliard model is inappropriate for determining the life cycle of a Miscibility Gap Alloy through diffusion dominated aging. Instead of simulating exactly the geometry of nuclei, one can assume the arrangement and analyse instead the flow of material through the composite during each thermal cycle.

The model utilised in this work assumes that precipitates will form a single sphere of alpha phase at the centre of a spherical shell of beta phase which in itself lies within a shell of alpha matrix. The diffusion of atoms through the shell is simulated using simplified methods (given in §3.1.3) to establish how close to equilibrium the fusible phase is after the heating and cooling cycles are complete. The approaches to equilibrium are then fed to a simple growth-decay model where the number of moles of each species is monitored through each thermal cycle using the methods derived in Appendix D. The algorithm is summarised in Figure 18.

A demonstrative implementation of this algorithm is provided in electronic form on the attached compact disk. The algorithm is implemented in MATLAB® language and is labelled SA2_Lattice_Monte_Carlo_Main.m. The script requires a number of functions to operate which are also provided on the compact disc.

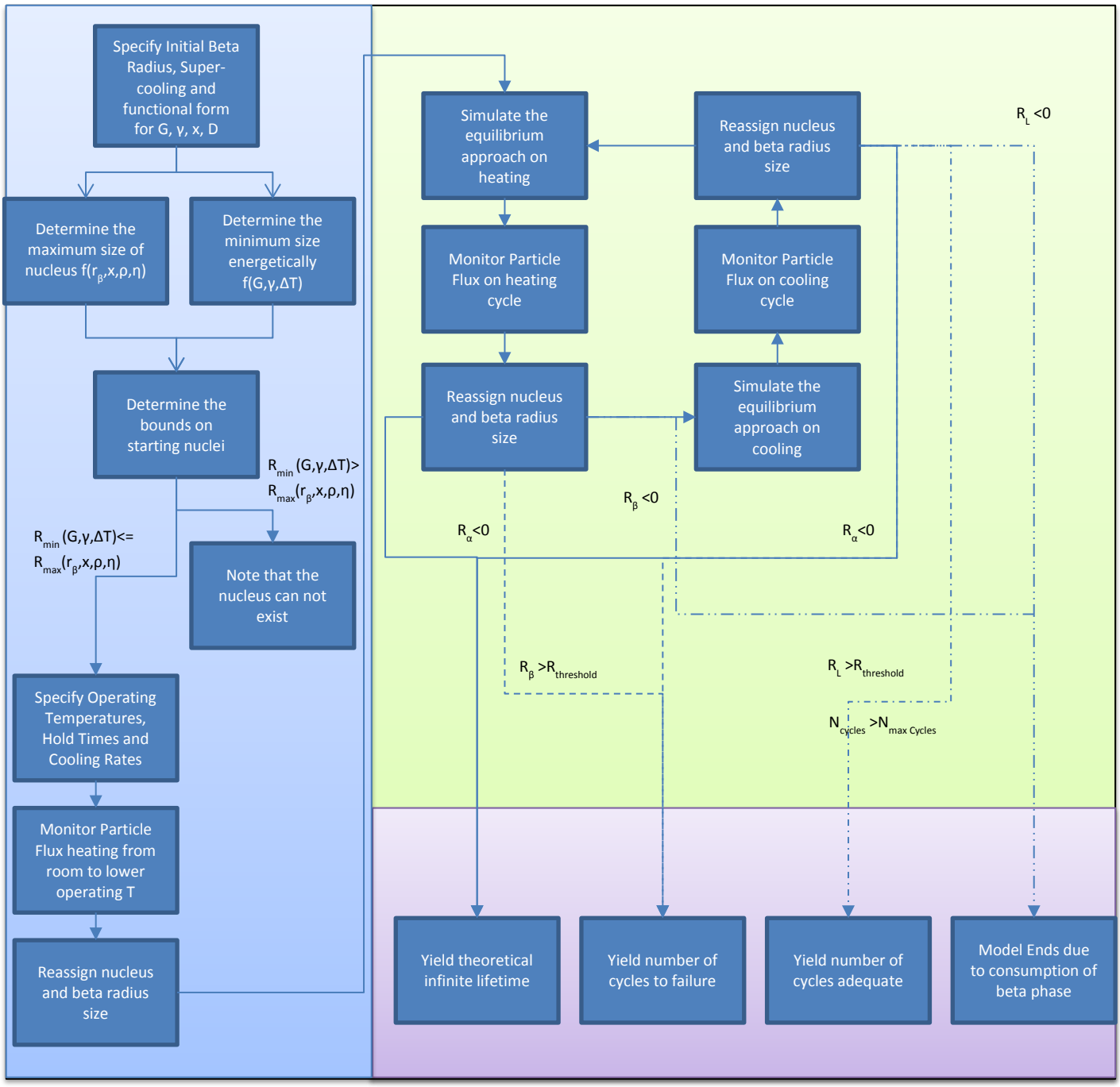

Figure 18 Flow Chart of Thermal Cycling model.

If a nucleus of alpha phase is to form on changing temperature the system must satisfy two requirements:

1) The beta phase must trap material and form an unstable solution
2) The resultant spherical nucleus must be large enough to be energetically favourable

This suggests that small powder sizes of beta phase with low operating temperatures may not have enough dissolved material for a stable nucleus to form. So the effect is expected for large powders undergoing elevated manufacturing and cycling temperatures where a great deal of material may be dissolved.

The minimum energetically favourable nucleus size may be determined from knowledge of the Gibbs Free Energy of the nucleating phase as compared to the unstable solution and the surface energy between the two. The surface energy of most metals in contact with other metals is on the order of 1 J/m^2 [103], and the allowable nucleus is generally on the order of a few micrometres. The following equation relies on the assumption that the nucleus will be spherical:

$$r^* = -\frac{2\gamma_\alpha^{eq}}{G_\alpha^{eq} + G_\beta^{eq}\frac{\rho_\alpha^{eq}}{\rho_\beta^{eq}}\frac{x - x_\alpha^{eq}}{x_\beta^{eq} - x} - G_\beta(T,x)\frac{\rho_\alpha^{eq}}{\rho_\beta(T,x)}\left(1 + \frac{x - x_\alpha^{eq}}{x_\beta^{eq} - x}\right)} \qquad 53.$$

Here r^* is the minimum stable nucleus radius, γ_α^{eq} is the surface energy of the alpha phase at equilibrium, G_α^{eq} is the Gibb's Free Energy of the alpha phase at equilibrium on a volumetric basis, G_β^{eq} is the Gibb's Free Energy of the beta phase at equilibrium on a volumetric basis, ρ_α^{eq} is the molar density of the alpha phase at equilibrium, ρ_β^{eq} is the molar density of the beta phase at equilibrium, x is the current composition, x_α^{eq} is the composition

of the alpha phase at equilibrium, x_{β}^{eq} is the composition of the beta phase at equilibrium, $G_{\beta}(T,x)$ is the Gibb's Free Energy of the unstable solution and $\rho_{\beta}(T,x)$ is the molar density of the unstable solution.

Any diffusion event may be modelled using the equations derived in Appendix D. The specific events occurring when modelling thermal cycling of Miscibility Gap Alloys are explained below with the required adaption of the equations from the Appendix.

1) Heating of pure materials to the manufacturing temperature at a specified heating rate and holding at the manufacturing temperature for a time.

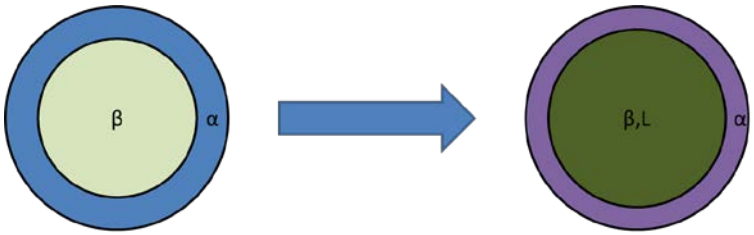

Room temperature β powder and α matrix at specified composition

High temperature β phase and α matrix at calculated composition

Step one involves taking a pure (or other composition) powder that forms the beta phase at a specified radius. The sphere of material is heated to the manufacturing temperature. During this heating ramp the beta phase will begin to dissolve the surrounding alpha matrix to approach the equilibrium composition. The system is allowed to soak at the manufacturing temperature for some time allowing further A atoms to dissolve into the beta phase. The equilibrium approach is found by simulating diffusion through a sphere of beta as the boundary condition and diffusivity change as a function of temperature (which is a function of time according to the heating ramp). The boundary condition is set to the equilibrium composition for the beta phase at the system temperature through the

simulation. After the ramp and hold have been simulated the amount of material that dissolved into the system is compared to that required to reach equilibrium, this ratio is the equilibrium approach (η).

$$\eta = \frac{n - n_{in}}{n_{eq} - n_{in}} \qquad 54.$$

Here n is the number of moles at the end of the diffusion simulation, n_{in} is the original number of moles and n_{eq} is the number of moles if the simulation had proceeded to equilibrium. Equilibrium approach is generally between 0 and 1 for most diffusion events.

The composition of the beta phase at the manufacturing temperature is found from:

$$x_{\beta,Manu} = \frac{x_{\beta,RT}\left(x_{\alpha,RT} - x_{\beta,Manu,eq}\right) + x_{\alpha,RT}\eta_{H,Manu}\left(x_{\beta,Manu,eq} - x_{\beta,RT}\right)}{x_{\alpha,RT} - x_{\beta,Manu,eq} + \eta_{H,Manu}\left(x_{\beta,Manu,eq} - x_{\beta,RT}\right)} \qquad 55.$$

Here $x_{\beta,Manu}$ is the composition of the beta (or liquid) phase after manufacturing heating, $x_{\alpha,RT}$ is the composition of the alpha phase at room temperature, $x_{\beta,Manu,eq}$ is the equilibrium composition at the manufacturing temperature for the beta (or liquid) phase, $\eta_{H,Manu}$ is the equilibrium approach on manufacturing heating, $x_{\beta,RT}$ is the composition of the beta phase at room temperature.

For the systems and manufacturing conditions investigated in this thesis this composition will always be a stable solid or liquid solution[4]. The number of moles of the manufacturing temperature beta phase is:

$$n_{\beta,Manu} = n_{\beta,RT}\frac{\left[x_{\alpha,RT} - x_{\beta,Manu,eq} + \eta_{H,Manu}\left(x_{\beta,Manu,eq} - x_{\beta,RT}\right)\right]}{x_{\alpha,RT} - x_{\beta,Manu,eq}} \qquad 56.$$

Here $n_{\beta,RT}$ is the number of moles in the beta phase at room temperature (prior to heating).

[4] If it is necessary to model nucleation on heating the general equations of appendix D are still valid.

The radius is found from the number of moles above, the molar density and the volume of a sphere:

$$r_{\beta,Manu} = \sqrt[3]{\frac{3}{4\pi}\frac{n_{\beta,Manu}}{\rho_{\beta,Manu}}} \qquad 57.$$

2) Cooling of the system from the manufacturing temperature to room temperature at a specified cooling rate.

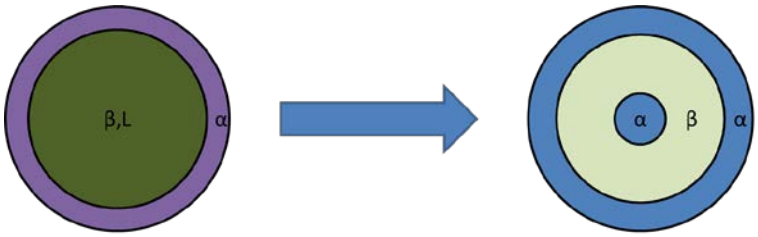

High temperature β phase and α matrix at calculated composition

Room temperature β phase, α matrix and potential α nucleus at calculated composition

Step two involves cooling the beta phase from the manufacturing temperature, likely creating a nucleus of alpha phase. Starting from the composition and number of moles found in step one, the composition of the beta phase at room temperature will be:

$$x_{\beta,RT} = \frac{x_{\beta,Manu}\left(x_{\alpha,Manu} - x_{\beta,RT,eq}\right) + x_{\alpha,Manu}\eta_{C,Manu}\left(x_{\beta,RT,eq} - x_{\beta,Manu}\right)}{x_{\alpha,Manu} - x_{\beta,RT,eq} + \eta_{C,Manu}\left(x_{\beta,RT,eq} - x_{\beta,Manu}\right)} \qquad 58.$$

Here $x_{\alpha,Manu}$ is the composition of the alpha phase at the manufacturing temperature, $x_{\beta,RT,eq}$ is the equilibrium composition at room temperature for the beta phase, $\eta_{C,Manu}$ is the equilibrium approach on cooling from the manufacturing temperature.

This composition is very likely to fall within a two phase region due to the freezing phenomenon described previously. In this introduction it is assumed that this will

occur. The number of moles of the beta phase shell and alpha phase nucleus are found from:

$$n_{\beta,RT}=\frac{n_{\beta,Manu}}{x_{\alpha,RT,eq}-x_{\beta,RT,eq}}\left\{\left(x_{\alpha,RT,eq}-1\right)\left[x_{\beta,Manu}-\eta_{C,Manu}\left(x_{\beta,Manu}-x_{\beta,RT,eq}\frac{x_{\alpha,RT,eq}-x_{\beta,Manu}}{x_{\alpha,RT,eq}-x_{\beta,RT,eq}}\right)\right]\right.$$
$$\left.+x_{\alpha,RT,eq}\left[\left(1-x_{\beta,Manu}\right)+\eta_{C,Manu}\left(x_{\beta,Manu}-1-\left(x_{\beta,RT,eq}-1\right)\frac{x_{\alpha,RT,eq}-x_{\beta,Manu}}{x_{\alpha,RT,eq}-x_{\beta,RT,eq}}\right)\right]\right\} \quad 59.$$

$$n_{\alpha,RT}=\frac{n_{\beta,Manu}}{x_{\alpha,RT,eq}-x_{\beta,RT,eq}}\left\{\left(x_{\alpha,RT,eq}-1\right)\left[x_{\beta,Manu}-\eta_{C,Manu}\left(x_{\beta,Manu}-x_{\beta,RT,eq}\frac{x_{\alpha,Manu,eq}-x_{\beta,Manu}}{x_{\alpha,Manu,eq}-x_{\beta,RT,eq}}\right)\right]\right.$$
$$\left.+x_{\alpha,RT,eq}\left[\left(1-x_{\beta,Manu}\right)+\eta_{C,Manu}\left(x_{\beta,Manu}-1-\left(x_{\beta,Manu}-1\right)\frac{x_{\alpha,Manu,eq}-x_{\beta,Manu}}{x_{\alpha,Manu,eq}-x_{\beta,RT,eq}}\right)\right]\right\} \quad 60.$$

The radius is found from the number of moles above, the molar density and the volume of a sphere:

$$r_{\beta,RT}=\sqrt[3]{\frac{3}{4\pi}\left(\frac{n_{\alpha,RT}}{\rho_{\alpha,RT}}+\frac{n_{\beta,RT}}{\rho_{\beta,RT}}\right)} \quad 61.$$

$$r_{\alpha,RT}=\sqrt[3]{\frac{3}{4\pi}\frac{n_{\alpha,RT}}{\rho_{\alpha,RT}}} \quad 62.$$

3) Heating of the system to the lower operating temperature at a heating rate.

Room temperature β phase, α matrix and potential α nucleus at calculated composition

Lower operating temperature β phase, α matrix and potential α nucleus at calculated composition

Step three is an intermediate step bringing the sample from room temperature to the lower operating temperature. The systems analysed here will have a low operating temperature below the melting temperature of the beta phase. It is assumed that initialising the system will lead to a stable solid solution in both phases. At this point in the model the composition of the beta and alpha phases are:

$$x_{\beta,Low}=\frac{n_{\beta,RT}x_{\beta,RT}\left(x_{\alpha,Low,eq}-x_{\beta,Low,eq}\right)(1-\eta_{In})+n_{\alpha,RT}x_{\beta,RT}\eta_{In}\left(x_{\alpha,Low,eq}-x_{\alpha,RT}\right)\left(1+\frac{r_{\beta,RT}^2}{r_{\alpha,RT}^2}\right)}{n_{\beta,RT}\left[x_{\alpha,Low,eq}-x_{\beta,Low,eq}+\eta_{In}\left(x_{\beta,Low,eq}-x_{\beta,RT}\right)\right]+n_{\alpha,RT}\eta_{In}\left(x_{\alpha,Low,eq}-x_{\alpha,RT}\right)\left(1+\frac{r_{\beta,RT}^2}{r_{\alpha,RT}^2}\right)} \quad 63.$$

$$x_{\alpha,Low}=\frac{n_{\alpha,RT}x_{\alpha,RT}+\eta_{In}\left[x_{\alpha,Low,eq}\frac{n_{\beta,RT}\left(x_{\beta,RT}-x_{\beta,Low,eq}\right)+n_{\alpha,RT}\left(x_{\alpha,RT}-x_{\beta,Low,eq}\right)\left(1+\frac{r_{\beta,RT}^2}{r_{\alpha,RT}^2}\right)}{\left(x_{\alpha,Low,eq}-x_{\beta,Low,eq}\right)\left(1+\frac{r_{\beta,RT}^2}{r_{\alpha,RT}^2}\right)}-n_{\alpha,RT}x_{\alpha,RT}\right]}{n_{\alpha,RT}+\eta_{In}\left[\frac{n_{\beta,RT}\left(x_{\beta,RT}-x_{\beta,Low,eq}\right)+n_{\alpha,RT}\left(x_{\alpha,RT}-x_{\beta,Low,eq}\right)\left(1+\frac{r_{\beta,RT}^2}{r_{\alpha,RT}^2}\right)}{\left(x_{\alpha,Low,eq}-x_{\beta,Low,eq}\right)\left(1+\frac{r_{\beta,RT}^2}{r_{\alpha,RT}^2}\right)}-n_{\alpha,RT}\right]} \quad 64.$$

Here $n_{\beta,RT}$ is the number of moles in the beta phase after manufacturing, $n_{\alpha,RT}$ is the number of moles in the alpha nucleus after manufacturing, $x_{\alpha,Low,eq}$ is the equilibrium composition of the alpha phase at the lower operating temperature, $x_{\beta,Low,eq}$ is the equilibrium composition of the beta phase at the lower operating temperature, η_{In} is the equilibrium approach on initialisation.

The new number of moles of beta and alpha phase are found from:

$$n_{\beta,Low}=\frac{n_{\beta,RT}\left[x_{\alpha,Low,eq}-x_{\beta,Low,eq}+\eta_{In}\left(x_{\beta,Low,eq}-x_{\beta,RT}\right)\right]+n_{\alpha,RT}\eta_{In}\left(x_{\alpha,Low,eq}-x_{\alpha,RT}\right)\left(1+\frac{r_{\beta,RT}^2}{r_{\alpha,RT}^2}\right)}{x_{\alpha,Low,eq}-x_{\beta,Low,eq}} \quad 65.$$

$$n_{\alpha,Low}=\frac{n_{\beta,RT}\eta_{In}\left(x_{\beta,RT}-x_{\beta,Low,eq}\right)+n_{\alpha,RT}\left[x_{\alpha,Low,eq}-x_{\beta,Low,eq}+\eta_{In}\left(x_{\alpha,RT}-x_{\alpha,Low,eq}\right)\right]\left(1+\frac{r_{\beta,RT}^2}{r_{\alpha,RT}^2}\right)}{\left(x_{\alpha,Low,eq}-x_{\beta,Low,eq}\right)\left(1+\frac{r_{\beta,RT}^2}{r_{\alpha,RT}^2}\right)} \quad 66.$$

The radii of the shell and nucleus are then:

$$r_{\beta,Low}=\sqrt[3]{\frac{3}{4\pi}\left(\frac{n_{\alpha,Low}}{\rho_{\alpha,Low}}+\frac{n_{\beta,Low}}{\rho_{\beta,Low}}\right)} \quad 67.$$

$$r_{\alpha,Low}=\sqrt[3]{\frac{3}{4\pi}\frac{n_{\alpha,Low}}{\rho_{\alpha,Low}}} \quad 68.$$

Generally the equilibrium approach will be quite low for this operation and the composition will not vary much from the room temperature values.

4) Heating the system from the lower operating temperature to the upper operating temperature at a heating rate and holding.

Lower operating temperature β phase, α matrix and potential α nucleus at calculated composition

Higher operating temperature liquid phase, α matrix and potential α nucleus at calculated composition

This step is the first in each cycle and involves heating the system from the lower operating temperature to the upper operating temperature and holding there for a set period of time. Part of the nucleus is expected to dissolve into the beta phase though this is not always the case. At this stage of the model the composition of the alpha nucleus and beta shell are found similar to the previous step:

$$x_{\beta,High}=\frac{n_{\beta,Low}x_{\beta,Low}\left(x_{\alpha,High,eq}-x_{\beta,High,eq}\right)(1-\eta_H)+n_{\alpha,Low}x_{\beta,Low}\eta_H\left(x_{\alpha,High,eq}-x_{\alpha,Low}\right)\left(1+\frac{r_{\beta,Low}^2}{r_{\alpha,Low}^2}\right)}{n_{\beta,Low}\left[x_{\alpha,High,eq}-x_{\beta,High,eq}+\eta_H\left(x_{\beta,High,eq}-x_{\beta,Low}\right)\right]+n_{\alpha,Low}\eta_H\left(x_{\alpha,High,eq}-x_{\alpha,Low}\right)\left(1+\frac{r_{\beta,Low}^2}{r_{\alpha,Low}^2}\right)} \quad 69.$$

$$x_{\alpha,High}=\frac{n_{\alpha,Low}x_{\alpha,Low}+\eta_H\left[x_{\alpha,High,eq}\frac{n_{\beta,Low}\left(x_{\beta,Low}-x_{\beta,High,eq}\right)+n_{\alpha,Low}\left(x_{\alpha,Low}-x_{\beta,High,eq}\right)\left(1+\frac{r_{\beta,Low}^2}{r_{\alpha,Low}^2}\right)}{\left(x_{\alpha,Low,eq}-x_{\beta,Low,eq}\right)\left(1+\frac{r_{\beta,Low}^2}{r_{\alpha,Low}^2}\right)}-n_{\alpha,Low}x_{\alpha,Low}\right]}{n_{\alpha,Low}+\eta_H\left[\frac{n_{\beta,Low}\left(x_{\beta,Low}-x_{\beta,High,eq}\right)+n_{\alpha,Low}\left(x_{\alpha,Low}-x_{\beta,High,eq}\right)\left(1+\frac{r_{\beta,Low}^2}{r_{\alpha,Low}^2}\right)}{\left(x_{\alpha,High,eq}-x_{\beta,High,eq}\right)\left(1+\frac{r_{\beta,Low}^2}{r_{\alpha,Low}^2}\right)}-n_{\alpha,Low}\right]} \quad 70.$$

Here $x_{\alpha,High,eq}$ is the equilibrium composition of the alpha phase at the high operating temperature, $x_{\beta,High,eq}$ is the equilibrium composition of the liquid phase at the high operating temperature and η_H is the equilibrium approach on heating.

If the alpha and beta phases are stable the procedure continues as it did for step 3. The new number of moles of beta and alpha phase are found from:

$$n_{\beta,High}=\frac{n_{\beta,Low}\left[x_{\alpha,High,eq}-x_{\beta,High,eq}+\eta_H\left(x_{\beta,High,eq}-x_{\beta,Low}\right)\right]+n_{\alpha,Low}\eta_H\left(x_{\alpha,High,eq}-x_{\alpha,Low}\right)\left(1+\frac{r_{\beta,Low}^2}{r_{\alpha,Low}^2}\right)}{x_{\alpha,High,eq}-x_{\beta,High,eq}} \quad 71.$$

$$n_{\alpha,High}=\frac{n_{\beta,Low}\eta_H\left(x_{\beta,Low}-x_{\beta,High,eq}\right)+n_{\alpha,Low}\left[x_{\alpha,High,eq}-x_{\beta,High,eq}+\eta_H\left(x_{\alpha,Low}-x_{\alpha,High,eq}\right)\right]\left(1+\frac{r_{\beta,Low}^2}{r_{\alpha,Low}^2}\right)}{\left(x_{\alpha,High,eq}-x_{\beta,High,eq}\right)\left(1+\frac{r_{\beta,Low}^2}{r_{\alpha,Low}^2}\right)} \quad 72.$$

The radii of the shell and nucleus are then:

$$r_{\beta,High}=\sqrt[3]{\frac{3}{4\pi}\left(\frac{n_{\alpha,High}}{\rho_{\alpha,High}}+\frac{n_{\beta,High}}{\rho_{\beta,High}}\right)} \quad 73.$$

$$r_{\alpha,High}=\sqrt[3]{\frac{3}{4\pi}\frac{n_{\alpha,High}}{\rho_{\alpha,High}}} \quad 74.$$

However if an unstable solution occurs the system will decompose. If either the alpha or beta phases are unstable then the number of moles of the new nucleus and shell are found from the following two equations:

$$n_{\beta,High}=\frac{x_{\alpha,High,eq}\left(n_{\alpha,High,uns}+n_{\beta,High,uns}\right)-n_{\beta,b,High,uns}-n_{\alpha,b,High,uns}}{x_{\alpha,High,eq}-x_{\beta,High,eq}} \quad 75.$$

$$n_{\alpha,High}=\frac{x_{\beta,High,eq}\left(n_{\alpha,High,uns}+n_{\beta,High,uns}\right)-n_{\beta,b,High,uns}-n_{\alpha,b,High,uns}}{x_{\beta,High,eq}-x_{\alpha,High,eq}} \quad 76.$$

These equations become extremely large and tedious if $x_{\alpha,High,eq}$, $n_{\alpha,High}$, and $n_{\beta,High}$ are substituted for the low temperature number of moles, composition equilibrium approach and radii. Thus they are left in terms of the unstable molar terms.

5) Cooling from the higher operating temperature to the lower operating temperature at a cooling rate and holding.

Higher operating temperature liquid phase, α matrix and potential α nucleus at calculated composition

Lower operating temperature β phase, α matrix and potential α nucleus at calculated composition

Step five models cooling from the high operating temperature to the low operating temperature. The nucleus is expected to grow on this step in most systems undergoing diffusion aging. The composition of the alpha nucleus and beta shell are found from:

$$x_{\beta,Low}=\frac{n_{\beta,High}x_{\beta,High}\left(x_{\alpha,Low,eq}-x_{\beta,Low,eq}\right)(1-\eta_C)+n_{\alpha,High}x_{\beta,High}\eta_C\left(x_{\alpha,Low,eq}-x_{\alpha,High}\right)\left(1+\frac{r_{\beta,High}^2}{r_{\alpha,High}^2}\right)}{n_{\beta,High}\left[x_{\alpha,Low,eq}-x_{\beta,Low,eq}+\eta_C\left(x_{\beta,Low,eq}-x_{\beta,High}\right)\right]+n_{\alpha,High}\eta_L\left(x_{\alpha,Low,eq}-x_{\alpha,High}\right)\left(1+\frac{r_{\beta,High}^2}{r_{\alpha,High}^2}\right)} \quad 77.$$

$$x_{\alpha,Low}=\frac{n_{\alpha,High}x_{\alpha,High}+\eta_C\left[x_{\alpha,Low,eq}\frac{n_{\beta,High}\left(x_{\beta,High}-x_{\beta,Low,eq}\right)+n_{\alpha,High}\left(x_{\alpha,High}-x_{\beta,Low,eq}\right)\left(1+\frac{r_{\beta,High}^2}{r_{\alpha,High}^2}\right)}{\left(x_{\alpha,High,eq}-x_{\beta,High,eq}\right)\left(1+\frac{r_{\beta,High}^2}{r_{\alpha,High}^2}\right)}-n_{\alpha,High}x_{\alpha,High}\right]}{n_{\alpha,High}+\eta_C\left[\frac{n_{\beta,High}\left(x_{\beta,High}-x_{\beta,Low,eq}\right)+n_{\alpha,High}\left(x_{\alpha,High}-x_{\beta,Low,eq}\right)\left(1+\frac{r_{\beta,High}^2}{r_{\alpha,High}^2}\right)}{\left(x_{\alpha,Low,eq}-x_{\beta,Low,eq}\right)\left(1+\frac{r_{\beta,High}^2}{r_{\alpha,High}^2}\right)}-n_{\alpha,High}\right]} \quad 78.$$

If the alpha and beta phases are stable the procedure continues as it did for step 3. The new number of moles of beta and alpha phase are found from:

$$n_{\beta,Low}=\frac{n_{\beta,High}\left[x_{\alpha,Low,eq}-x_{\beta,Low,eq}+\eta_C\left(x_{\beta,Low,eq}-x_{\beta,High}\right)\right]+n_{\alpha,High}\eta_C\left(x_{\alpha,Low,eq}-x_{\alpha,High}\right)\left(1+\frac{r_{\beta,High}^2}{r_{\alpha,High}^2}\right)}{x_{\alpha,Low,eq}-x_{\beta,Low,eq}} \quad 79.$$

$$n_{\alpha,Low}=\frac{n_{\beta,High}\eta_C\left(x_{\beta,High}-x_{\beta,Low,eq}\right)+n_{\alpha,High}\left[x_{\alpha,Low,eq}-x_{\beta,Low,eq}+\eta_C\left(x_{\alpha,High}-x_{\alpha,Low,eq}\right)\right]\left(1+\frac{r_{\beta,High}^2}{r_{\alpha,High}^2}\right)}{\left(x_{\alpha,Low,eq}-x_{\beta,Low,eq}\right)\left(1+\frac{r_{\beta,High}^2}{r_{\alpha,High}^2}\right)} \quad 80.$$

The radii of the shell and nucleus are then:

$$r_{\beta,Low}=\sqrt[3]{\frac{3}{4\pi}\left(\frac{n_{\alpha,Low}}{\rho_{\alpha,Low}}+\frac{n_{\beta,Low}}{\rho_{\beta,Low}}\right)} \quad 81.$$

$$r_{\alpha,Low}=\sqrt[3]{\frac{3}{4\pi}\frac{n_{\alpha,Low}}{\rho_{\alpha,Low}}} \quad 82.$$

However if an unstable solution occurs the system will decompose. If either the alpha or beta phase is unstable then the number of moles in the new nucleus and shell are found from the following two equations:

$$n_{\beta,Low}=\frac{x_{\alpha,Low,eq}\left(n_{\alpha,Low,uns}+n_{\beta,Low,uns}\right)-n_{\beta,b,Low,uns}-n_{\alpha,b,Low,uns}}{x_{\alpha,Low,eq}-x_{\beta,Low,eq}} \quad 83.$$

$$n_{\alpha,Low}=\frac{x_{\beta,Low,eq}\left(n_{\alpha,Low,uns}+n_{\beta,Low,uns}\right)-n_{\beta,b,Low,uns}-n_{\alpha,b,Low,uns}}{x_{\beta,Low,eq}-x_{\alpha,Low,eq}} \quad 84.$$

As before, these equations become extremely large if $x_{\alpha,Low,eq}$, $n_{\alpha,Low}$, and $n_{\beta,Low}$ are substituted for their respective functional forms. They are left in this form for the sake of brevity.

Steps 1 to 3 model the manufacturing and initial heating of the material. Steps 4 and 5 represent a thermal cycle. Through repetition of steps 4 and 5 any desired number of thermal cycles may be simulated. Given that thermal storage in a solar power plant or air heater generally operate with a daily cycle the lifetime in days is roughly equivalent to the number of cycles. For a 20 year design life around 7300 cycles must be completed without failure.

During cycling the nucleus may dissolve, grow to a stable size or grow indefinitely. The beta shell surrounding the nucleus will grow or shrink to accommodate and may itself be consumed by the matrix. If the beta shell grows to exceed the percolation threshold for the morphology of the MGA then the system has failed and the lifetime of the material has been realised. The percolation threshold for various packings are given in Table 2:

Table 2 Threshold radius for beta phase growth before matrix percolation occurs. The volume fraction threshold is also provided for each packing type. Here φ refers to the volume fraction of the distributed phase.

Packing Type	Radial Threshold	Volume Fraction Threshold
Cubic	$r_{threshold}=r_{\beta,Initial}\sqrt[3]{\frac{\pi}{6\varphi}}$	$\varphi_{threshold}=\frac{\pi}{6}\cong 0.52$
Body Centred Cubic	$r_{threshold}=r_{\beta,Initial}\sqrt[3]{\frac{\pi\sqrt{3}}{8\varphi}}$	$\varphi_{threshold}=\frac{\pi\sqrt{3}}{8}\cong 0.68$
Face Centred Cubic	$r_{threshold}=r_{\beta,Initial}\sqrt[3]{\frac{\pi}{3\sqrt{2}\varphi}}$	$\varphi_{threshold}=\frac{\pi}{3\sqrt{2}}\cong 0.74$
Random Close Packing	$r_{threshold}=r_{\beta,Initial}\sqrt[3]{\frac{0.63}{\varphi}}$	$\varphi_{threshold}=\cong 0.63$
General Form	$r_{threshold}=r_{\beta,Initial}\sqrt[3]{\frac{\varphi_{threshold}}{\varphi}}$	

If the beta shell is consumed into the matrix solid solution it will be redistributed through each thermal cycle. This does not necessarily imply that the morphology will be percolating. For the sake of this model if the beta phase is consumed the system is considered to have failed.

Ideally any nucleus created through manufacture will dissolve during thermal cycling and hence be unable to damage the morphology. The nucleus may disappear through thermal cycling provided the system dissolves more of the nucleus than it redeposits each cycle. This will occur if:

1) the starting nucleus is so small that it may be completely dissolved in the heating portion of the first cycle and be unable to nucleate on cooling

2) equilibrium is achieved on both heating and cooling as the surface to area ratio alone then drives diffusion
3) equilibrium approach on heating and cooling is sufficient to provide net flux of material from the nucleus to the matrix

If none of the above occur then the nucleus will grow indefinitely or stagnate. Stagnation will occur if the equilibrium approach increases to a point such that the same volume of material dissolved from the nucleus each cycle is redeposited. In the worst case the dissolved material from the nucleus will never equal the amount deposited and the nucleus will theoretically grow indefinitely. Summarising the processes:

Table 3 Summary of the possible outcomes of the simulation process.

Situation	Implication	Occurring in
The nucleus formed on manufacturing dissolves instantly.	The distributed phase **will not** lose encapsulation through cycling.	Small distributed phase with manufacturing temperature exceeding cycling temperature range.
Net flux of atoms *from the nucleus* to the matrix.	The distributed phase **will not** lose encapsulation through cycling.	Moderate distributed phase with manufacturing temperature exceeding cycling temperature range.
Balanced flux of atoms between nucleus and matrix.	The distributed phase **will not** lose encapsulation through cycling.	Moderate distributed phase with manufacturing temperature similar to cycling temperature range.
Net flux of atoms *to the nucleus* from the matrix.	The distributed phase **will** lose encapsulation through cycling.	Large distributed phase with large temperature amplitude on cycling.
Consumption of the beta shell by the matrix.	The distributed phase **will** lose encapsulation through cycling.	High solubility of the melting element in the solid matrix phase.

The number of cycles at which failure occurs (and whether it will occur at all) may be approximated using the model described above for a particular radial threshold and

thermal cycle. The predictions for each MGA of interest are presented in §6.1 for likely thermal cycles and starting morphologies.

The model described above simplifies the extremely complicated physics behind aging of Miscibility Gap Alloys through diffusion processes, thereby making some estimate of lifetime possible in a reasonable time frame. The use of concentric spheres deviates significantly from real morphologies, however this assumption should provide the most conservative estimate of Miscibility Gap Alloy life. Treating the matrix as infinite simplifies estimates for Miscibility Gap Alloys with negligible solubility of B atoms in the matrix but also limits the model. The model derived in this thesis provides some insight into the expected lifetime of the materials though by no means should be used as a substitute for physical experiments.

3.3.2. Thermo-Mechanical Aging

Given the materials involved in Miscibility Gap Alloys have non-negligible thermal expansion coefficients, a thermal gradient will introduce a strain field through the material. Complicating this is the potential miss-match between the expansion coefficient of the metallic phases in the alloy and the potential for volume change on melting or freezing. The matrix is expected to yield during sintering and the first few thermal cycles. Yielding is generally through plastic deformation in metallic matrix alloys and small brittle fractures in graphite matrices.

The stresses involved in heating and cooling in Miscibility Gap Alloys can be approximated with a concentric sphere model. Here only the mismatch in thermal expansion coefficients and the volume change on phase change contribute to the stresses

(assuming no thermal gradient exists). The peak radial and tangential stress may be determined and compared to the yield stress of the matrix material. The radial and tangential stresses may be determined from [104]:

$$\sigma_R = \frac{E_I c_{11}}{1-2\nu_I} - \frac{2E_I c_{12}}{1+\nu_1}\frac{1}{r^3} - \frac{2E_I}{1-\nu_I}\frac{1}{r^3}\int_0^r \varepsilon_{free,I} r^2 dr \text{, for } 0<r\leq r_I \quad 85.$$

$$\sigma_R = \frac{E_M c_{21}}{1-2\nu_M} - \frac{2E_M c_{22}}{1+\nu_M}\frac{1}{r^3} - \frac{2E_M}{1-\nu_M}\frac{1}{r^3}\int_{r_I}^r \varepsilon_{free,M} r^2 dr \text{, for } r_I<r<\infty \quad 86.$$

$$\sigma_T = \frac{E_I c_{11}}{1-2\nu_I} - \frac{E_I c_{12}}{1+\nu_I}\frac{1}{r^3} - \frac{E_I \varepsilon_{free,I}}{1-\nu_I} + \frac{E_I}{1-\nu_I}\frac{1}{r^3}\int_0^r \varepsilon_{free,I} r^2 dr \text{, for } 0<r\leq r_I \quad 87.$$

$$\sigma_T = \frac{E_M c_{21}}{1-2\nu_M} - \frac{E_M c_{22}}{1+\nu_M}\frac{1}{r^3} - \frac{E_I \varepsilon_{free,M}}{1-\nu_M} + \frac{E_I}{1-\nu_M}\frac{1}{r^3}\int_{r_I}^r \varepsilon_{free,M} r^2 dr \text{, for } r_I<r<\infty \quad 88.$$

Here E_I refers to the Young's Modulus of the inclusion, ν_I refers to the Poisson's ratio of the inclusion, ε_{free} is the unconstrained linear coefficient of thermal expansion, E_M is the Young's Modulus of the matrix, ν_M is the Poisson's ratio of the matrix and r_I is the radius at which the interface between inclusion and matrix exists.

Boundary conditions of a pinned centre point, constant displacement and normal stress at the interface and zero pressure at the external surface allow the coefficients to be found from the following:

$$\begin{bmatrix} 0 & -\frac{2E_I}{1+\nu_I} & 0 & 0 \\ r_I & \frac{1}{r_I^2} & -r_I & -\frac{1}{r_I^2} \\ \frac{E_I}{1-2\nu_I} & -\frac{2E_I}{1+\nu_I}\frac{1}{r_I^3} & \frac{-E_M}{1-2\nu_M} & \frac{2E_M}{1+\nu_M}\frac{1}{r_I^3} \\ 0 & 0 & \frac{E_M}{1-2\nu_M} & \frac{-2E_M}{1+\nu_M}\frac{1}{r_M^3} \end{bmatrix} \begin{bmatrix} c_{11} \\ c_{12} \\ c_{21} \\ c_{22} \end{bmatrix} = \begin{bmatrix} 0 \\ -\frac{1+\nu_I}{1-\nu_M}\frac{1}{r_I^2}\int_0^r \varepsilon_{free,I} r^2 dr \\ \frac{2E_I}{1-\nu_I}\frac{1}{r_I^3}\int_0^r \varepsilon_{free,I} r^2 dr \\ \frac{2E_M}{1-\nu_M}\frac{1}{r_M^3}\int_{r_I}^{r_M} \varepsilon_{free,M} r^2 dr \end{bmatrix} \quad 89.$$

The unconstrained linear coefficient of thermal expansion is related to the linear coefficient of thermal expansion:

$$\varepsilon_{free} = \int_{T_0}^{T} \alpha(T)\,dT \qquad 90.$$

The linear coefficient of thermal expansion is a function on temperature and takes into account the volume change on phase change. The Von-Mises yield criterion might then be used to establish whether plastic deformation will occur and at what temperature.

For the materials of interest in this thesis the Young's Modulus, Poisson's ratio, linear coefficient of thermal expansion and volume change on melting are provided below:

Table 4 Material properties appropriate for analysing a concentric sphere model with expansion coefficient mismatch and volume change on phase change.

Material	Young's Modulus [GPa]	Poisson's Ratio [diml]	Linear Coefficient of Thermal Expansion [μm/μm °C]	Volume Change on Melting [m^3_l/m^3_s]	Yield Strength [MPa]	Reference
Aluminium	72-89	0.32-0.36	16.5-24		50-330	[102]
Brass	90-110	0.34-0.35	17-20.7	1.113	95-500	[102]
Copper	112-148	0.34-0.35	16.9-18	1.113	30-350	[102]
Graphite	3-17	0.17-0.23	13-16		14-34	[105, 106]
Iron	80-138	0.26-0.28	11-12.5		140-420	[102]
Magnesium	44.4	0.3	26.1	1.094	20	[102, 107]
Silicon	140-155	0.21-0.22	2-3.2	0.873	160-180	[102]
SiC	400-460	0.16-0.18	4-4.8		400-610	[102]
Tin	41-45	0.32-0.34	22.5-23.5	1.040	7-15	[102]
Zinc	90-107	0.25-0.33	23-28	1.085	75-166	[102]

Yielding of the matrix need not imply that the Miscibility Gap Alloy has failed as the matrix may still encapsulate the molten phase. Repeated straining of the matrix even below the yield strength might encourage cracks to propagate in brittle matrices though repeated thermal cycles may continually anneal the material and prolong its lifetime. Most metallic materials are capable of significant plastic deformation and are unlikely to fail though they may yield. This form of failure would be best tested physically and conclusions drawn from experiments.

3.3.3. Chemical Reaction Aging

Ideally Miscibility Gap Alloy thermal storage systems should be isolated from the environment in all manner except thermally. However, this is difficult to achieve in practice. The metals involved in Miscibility Gap Alloys may be prone to oxidation at elevated temperatures. Furthermore, the contact of metals with dissimilar reduction potentials can create an unintentional galvanic cell if an electrolyte to act as a charge carrier is present. This cell may even be capable of electrolysing water to give hydrogen and oxygen whilst significant oxidation of one of the constituents occurs.

Pure metals (neglecting gold) and carbon will oxidise when exposed to oxygen in the atmosphere. The rate at and extent to which the metal will oxidise is a complex problem which involves a balance between the equilibrium energy reduction from reaction and the kinetics of the reaction (both diffusive and energetic). A clean surface of metal exposed to air will form a layer of oxide taking many different possible forms. The layer may be close packed and block further attack, interspersed with cavities and pores which allow oxygen to pass or have grain boundaries which offer faster diffusion paths for oxygen than the bulk oxide [108]. Given the many parameters affecting the growth of an oxide on an exposed Miscibility Gap Alloy, a single parameter is not sufficient as a comparative measure to the likelihood of life time reduction due to oxidation, instead a more holistic consideration of the particular matrix is given in §6.2.

Particularly reactive metals (potassium, sodium, lithium and calcium etc.) will react directly with water to form a metal oxide and hydrogen. Magnesium will react directly with steam to produce magnesium oxide and hydrogen. This is the only material considered that will react directly with water. Acidic environments will attack aluminium, iron,

magnesium, zinc and tin, though an acidic environment would be uncommon in typical Miscibility Gap Alloy operation.

Galvanic corrosion is an electrochemical process whereby an anode is oxidised preferentially to a cathode in direct electrical contact bridged by an electrolyte. The rate of corrosion of the anode is much faster than if it were immersed alone in the same electrolyte. The likelihood of a Galvanic cell forming may be inferred by analysing the standard electrode potential of the constituents reacting with a particular ion in the electrolyte. Given the enormous number of potential ions that might be dissolved in water bridging a Miscibility Gap Alloy phase boundary, individual analysis is inappropriate for the scope of this thesis. Instead, a more general corrosion potential chart can be analysed like that of Figure 19. Here the electrolyte is sea water which contains many different ions. Differences greater than 200 mV often suggest galvanic corrosion is possible [109] and the more anodic material will have an accelerated corrosion. If the difference is particularly large it may be possible to directly electrolyse the water adjacent to the metal couple producing hydrogen and oxygen gas.

The likelihood of oxidation or galvanic corrosion should be extremely small for Miscibility Gap Alloys implemented with adequate preparation. The alloys should always have a layer of either pure matrix material or an inhibiting layer between the composite and the atmosphere and also the working fluid. The work undertaken regarding chemical reaction in §6.2 this thesis provides scientific support to this intuitive (and perhaps obvious) requirement.

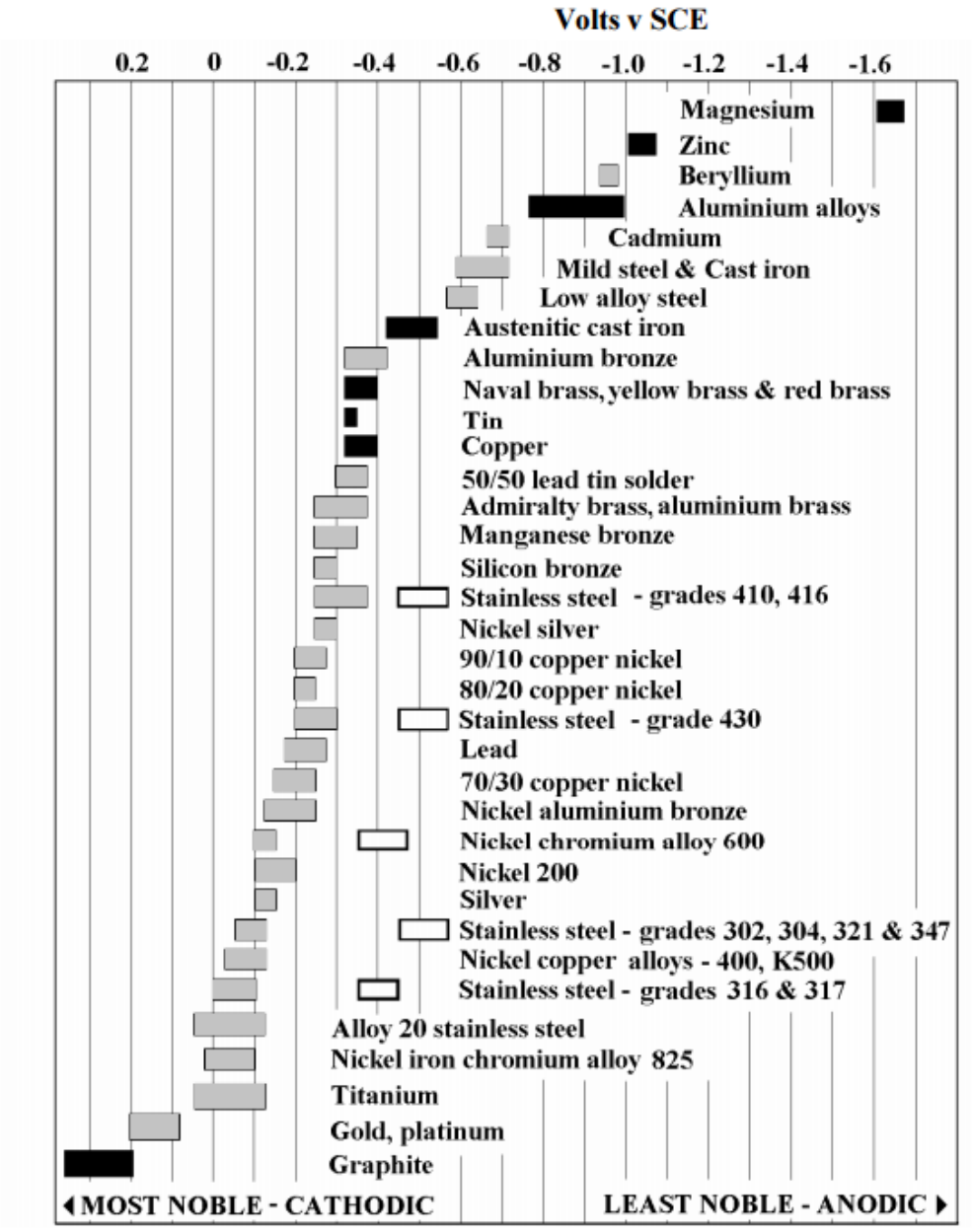

Figure 19 Corrosion potentials in flowing sea water at ambient temperature. The unshaded symbols show ranges exhibited by stainless steels in acidic water such as may exist in crevices or in stagnant or low velocity or poorly aerated water. The more Noble materials at the left side tend to be cathodic and hence protected; those at the right are less Noble and tend to be anodic and hence corroded in a galvanic couple [109].

3.4. Modelling the Economics of Miscibility Gap Alloys

To complete the analysis required in actually implementing a Miscibility Gap Alloy thermal storage system a discussion of the cost is necessary. The following section outlines

how the capital and running costs involved in utilising Miscibility Gap Alloys may be estimated.

3.4.1. Capital Costs

The capital costs of installing a Miscibility Gap Alloy based thermal storage solution may be separated into three broad categories. Material costs involve purchasing the raw material in a powder form. Manufacturing costs are incurred during processing of the raw material into a Miscibility Gap Alloy. Infrastructure costs include heat exchangers, encapsulation, insulation and piping necessary to utilise the storage medium. These costs can be normalised against unit thermal energy stored to provide a scalable estimate of capital cost.

Costing thermal storage systems is a considerable task as material prices are rarely quoted in academic literature and, if regularly traded, may vary according to international demand. Nevertheless, a cost can be calculated to within a practical uncertainty.

Manufacturing costs of Miscibility Gap Alloys depend on the processes involved in their creation. It is assumed in this thesis that powder metallurgy is the manufacturing method.

The infrastructure costs involved in creating an MGA system may be separated into three subcategories; encapsulation, insulation and piping:

1. Encapsulation concerns the immediate skin surrounding the Miscibility Gap Alloys and the atmosphere. The skin was taken as either steel, stainless steel or a ceramic depending on the system. Some Miscibility Gap Alloys require a low oxygen atmosphere which necessitated an air tight surrounding with a carbon dioxide or argon atmosphere.

2. Insulation was required for all systems to efficiently store heat without loss to the environment. Some Miscibility Gap Alloys are for very high temperature operation and consequently required Alumino-silicate type insulation.

3. Very little piping is required to transfer heat energy to (and from) the very thermally effuse MGAs.

The estimated range of infrastructure prices for MGAs was determined by costing each element mentioned above on a volumetric basis before conversion to an energy basis.

3.4.2. Running Costs

One of the chief advantages of Miscibility Gap Alloys is their low running costs. Unlike salts and thermal oils, the alloys do not require pumping to achieve adequate heat transfer. Maintenance of the system involves repairing cracks in the encapsulation surface and removing any oxidation that has occurred. Descaling of heat transfer pipes might be considered a maintenance cost belonging to the power cycle rather than the storage system.

The alloys are expected to last an extremely long time with a design lifetime of ideally greater than twenty years. The dominant aging mechanisms of each system are discussed in §6 and some have greater degradation potential due to use and exposure. The materials are extremely recyclable providing a great potential for capital cost recuperation through salvage at the end of the design lifetime.

3.4.3. Cost Modelling

The following equations may be used to obtain a cost per unit energy stored. The manufacturing costs are based on cost modelling within the CES Database [102]. Powder metallurgy techniques assumed in this article have typical unit sizes from 50 mm to 250

mm cubic dimensions, thus very large storage blocks will be composed of a number of items (N_{item}). Each item has an associated mass (m_{item}). An overall utilisation factor is included in the material cost index to account for wasted material during production ($u_{Mat\ Uti}$). The dies used in the manufacture are assumed to cost an amount (c_{Tool}) and will last a finite number of items, this is the tool life ($N_{Tool\ life}$). The number of items produced in a batch (N_{Batch}) should be high enough such that the expense of purchasing tools is not wasted. Capital costs of equipment ($c_{Capital}$) are converted to a cost per hour by dividing by the write off time ($\Delta t_{Write\ off}$) over which the cost is recovered (typically several years). In powder metallurgy processes it is likely that this equipment can be used for multiple projects (the cost is not solely dedicated to the current MGA production). The equipment is unlikely to run continuously so the write off time is modified by a time utilisation or load factor ($u_{Load\ factor}$). Other overheads including operator wages, energy and land rates are covered with a cost per time ($c_{Overhead}$). A production rate (r_{Prod}) then converts the overhead and capital cost per time to cost per item. The cost per item may then be converted to a cost per unit energy stored by dividing by the volume of the item and the energy density.

$$c_{Material} = \frac{1}{V_{item}\rho_e}\frac{m_{item}(c_1\psi_1 + c_2\psi_2)}{u_{Mat\ Uti}} \quad 91.$$

$$c_{Tooling} = \frac{1}{V_{item}\rho_e}\frac{c_{Tool}}{N_{Batch}}\left(1 + \frac{N_{Batch}}{N_{Tool\ life}}\right) \quad 92.$$

$$c_{Capital,Overhead} = \frac{1}{V_{item}\rho_e}\frac{1}{r_{Prod}}\left(c_{Overhead} + \frac{c_{Capital}}{\Delta t_{Write\ Off} u_{Load\ Factor}}\right) \quad 93.$$

Infrastructure costs may be evaluated as discussed in the previous section on a per system basis. The maintenance costs are also on a per item basis where different procedures

occur with a cost ($c_{Maint,i}$) and frequency (f_i). These costs may be converted to a per energy stored basis by dividing by the system volume and energy density.

$$c_{Infrastructure} = \frac{1}{V_{system}\rho_e}\left[l_{pipe}c_{Pipe} + A_{Surface}\left(c_{Encap} + c_{Insul}\right) + V_{Atmo}c_{Atmo}\right] \quad 94.$$

$$c_{Maintenance} = \frac{1}{V_{system}\rho_e}\Delta t_{Design\ Life}\sum_{1}^{n} c_{Maint,i}f_i \quad 95.$$

Salvage benefits are evaluated as a proportion of the material costs initially occurred (it is assumed that the commodity price of the materials will include inflation after the design lifetime is complete).

$$c_{Salvage} = sc_{Material} \quad 96.$$

Finally all these costs may be added to yield an estimate at the total cost per kWh of thermal storage.

$$c_{Total} = c_{Material} + c_{Tooling} + c_{Capital,Overhead} + c_{Infrastructure} + c_{Maintenance} - c_{Salvage} \quad 97.$$

There is variation in all the costs and parameters associated with the implementation of a Miscibility Gap Alloy thermal storage system. It is thus prudent to present bounds on the cost per kWh thermal energy stored rather than a definite figure. The bounds may be calculated using a maximum possible error approach.

In addition to the variation in cost, Miscibility Gap Alloys may exist at any volume fraction below the percolation threshold of the distributed phase. The economic analysis may be repeated for many different volume fractions of constituents. This yields bounds for energy density in addition to cost per unit energy stored. Thus on a plot of energy normalised cost against energy density a two dimensional area is presented for each Miscibility Gap Alloy.

3.4.4. Economic Comparison

The cost of thermal storage implementations may be compared in a number of ways. The most obvious property for comparison is the cost per unit thermal energy stored. Units of United States Dollar per kilowatt hour [USD/kWh] are utilised in this thesis. Plotting the cost per kWh against the energy density or the effusive energy density then allows the optimal design solution to be selected. An example is shown in Figure 20 for the Copper-Iron system.

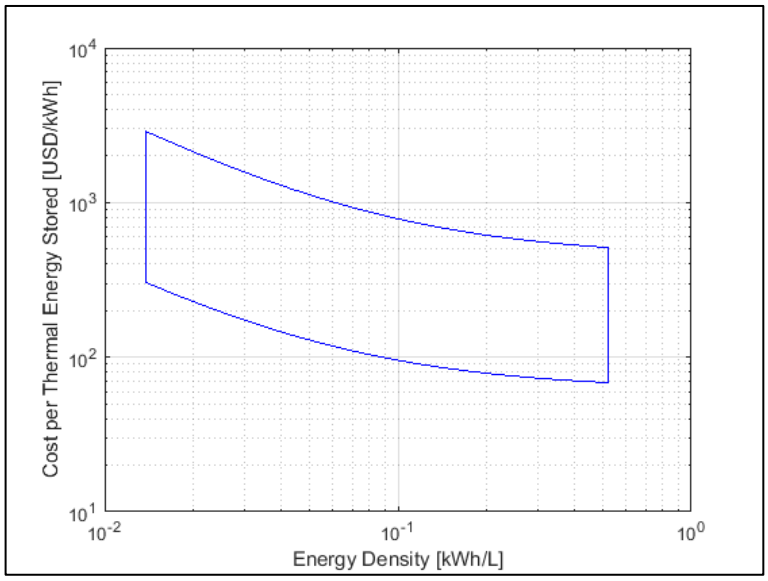

Figure 20 Cost of thermal energy storage plotted against energy density for the Cu-Fe system over a range of volume fractions. This example includes 100 °C of sensible heat and models a central receiver implementation. Due to large variation in commodity price and system manufacture costs the potential range of costs can be significant.

Where the implementation and maintenance schedule of a particular thermal storage material is unknown the additional (non-material) costs may be inferred from literature. This allows comparison of thermal storage media in a more thorough and holistic way than comparison purely on material cost. One of the chief advantages of a Miscibility Gap Alloy

thermal storage system is the cost reduction in infrastructure and hence it is necessary to make a comparison on more than material price alone.

CHAPTER 4: THE CONCEPT OF MICROSTRUCTURAL EFFICIENCY

The specific morphologies found in Miscibility Gap Alloy samples required a homogenisation step to accurately characterise their effective thermal conductivity. The candidate found this process to be highly specific to morphology which may change through manufacturing method, or with thermal cycling. A concept called microstructural efficiency was developed to describe the morphology dependence of the effective conductivity of a composite. The theory, results and potential extensions of the concept are outlined in this chapter.

4.1. Microstructural Efficiency

Microstructural efficiency is a convenient property for quantifying the overall impact of morphology on the effective isotropic conductivity of a composite ($\bar{k}_{iso}$). The microstructural efficiency (η_μ) is defined as the ratio of effective isotropic conductivity to the volume weighted series average of the constituent conductivities.

$$\eta_\mu = \frac{\bar{k}_{iso}}{\sum_{i=1}^{n} \varphi_i k_i} \qquad 98.$$

Here φ_i refers to the volume fraction and k_i refers to the conductivity of the ith species.

This simple relationship provides a link between the actual effective conductivity and the conductivity of constituent materials. If the microstructural efficiency is available then the effective isotropic conductivity can be easily calculated.

$$\bar{k}_{iso} = \eta_\mu \sum_{i=1}^{n} \varphi_i k_i \qquad 99.$$

The effective isotropic conductivity may be determined through measurement, or through analytical and numerical means. If an effective conductivity measurement can be delivered fast and accurately then a reference base of microstructural efficiencies can be

built for different morphologies. This enables a materials scientist to predict the effective conductivity for a composite with a variety of morphologies or conductivity ratios.

4.2. Microstructural Efficiency of Analytically Tractable or Estimable Morphologies

Many analytical and empirical models exist predicting the effective conductivity of specific morphologies and materials as discussed in §3.1.4. These models can be used directly to produce microstructural efficiency information.

4.2.1. Parallel Plates

The peculiar case of parallel plate morphology does have an exact analytical solution for effective conductivity. The tensor components for this morphologies conductivity are the Weiner bounds. Where the laminates are stacked in the x-direction (and the heat flux vector is of the form [x,y,z]), the tensor is:

$$\underline{k}_{\text{Parallel Plates}} = \begin{pmatrix} \bar{k}_{\text{Harm}} & 0 & 0 \\ 0 & \bar{k}_{\text{Arith}} & 0 \\ 0 & 0 & \bar{k}_{\text{Arith}} \end{pmatrix} \quad 100.$$

Given the effective isotropic conductivity is equal to the trace of the conductivity tensor divided by dimensionality (d), the microstructural efficiency for parallel plates can be derived exactly. That is:

$$\bar{k}_{\text{iso}} = \frac{\text{tr}(\underline{k})}{d} \quad 101.$$

$$\eta_{\mu} = \frac{\bar{k}_{\text{iso}}}{\bar{k}_{\text{ser}}} \quad 102.$$

Writing this as a direct function of volume fraction and conductivity (r_{Inc}/r_{Mat}) ratio for both two and three dimensional cases gives:

$$\eta_\mu(\varphi_1,r)=\frac{1}{3}\left(2+\frac{1}{(\varphi_1+(1-\varphi_1)r)(\varphi_1+(1-\varphi_1)/r)}\right) \qquad 103.$$

This two dimensional function is shown as a contour plot in Figure 21. It has general behaviour which is observed in all morphologies. A high efficiency ridge is apparent through conductivity ratios about unity. The high conductivity ridge widens for more extreme volume fractions. In the parallel plate morphology, the behaviour is symmetric about this unity conductivity ratio and about 50% volume fraction.

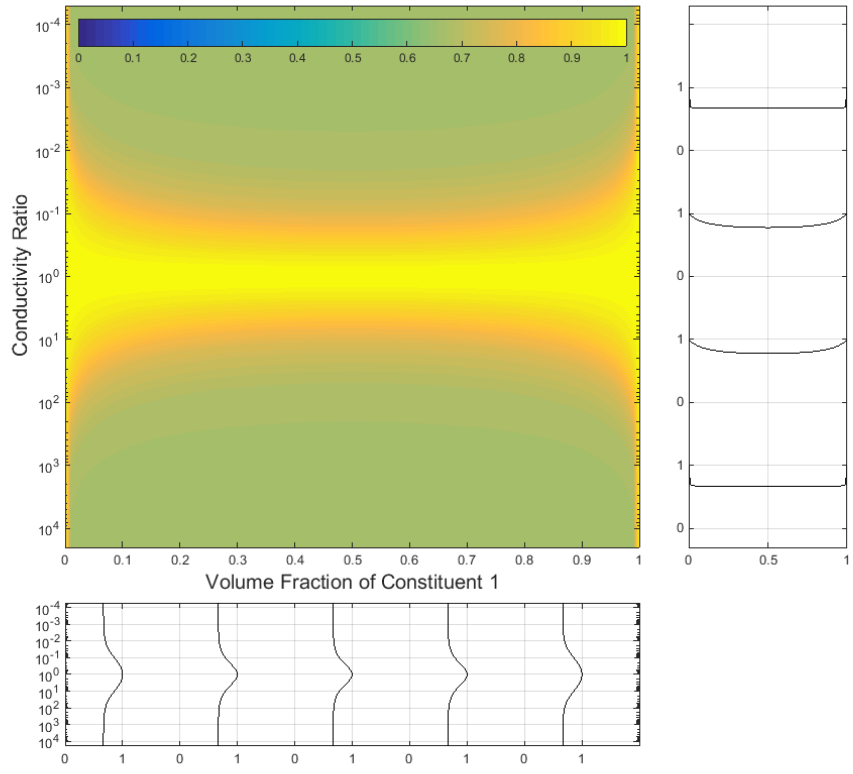

Figure 21 Microstructural efficiency for a system of parallel plates. Note the symmetric behaviour and lower limit of two thirds. The top of this chart represents a more conductive matrix phase, the bottom represents a more conductive distributed phase. The 2d charts to the right and below are anchored at η_μ=1 in conductivity ratio or volume fraction.

4.2.2. Sparse, Macroscopically Isotropic Morphologies

The Maxwell-Eucken and Bruggeman models are useful in predicting the effective isotropic thermal conductivity of sparse distributions of spherical inclusions within a matrix. The microstructural efficiency may be calculated directly for these two models. Care must be taken to acknowledge the constraints of the models, particularly the requirement for sparse dispersions. Figure 22 and Figure 23 show the microstructural efficiency behaviour for the Maxwell and Bruggeman models respectively.

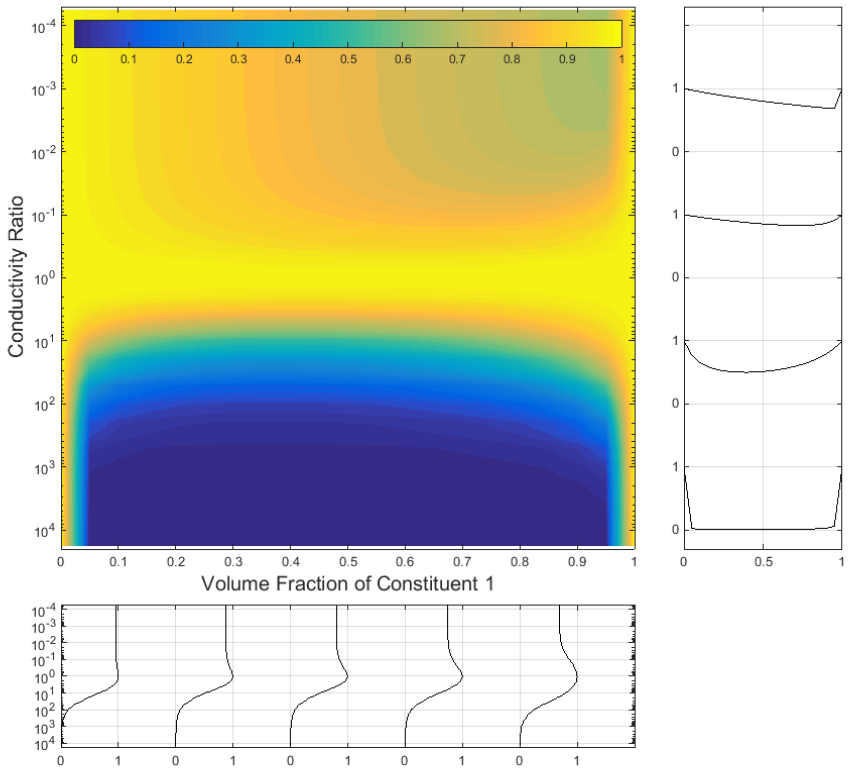

Figure 22 Microstructural Efficiency predicted by the Maxwell-Eucken model of equation 4. The top of this chart represents a more conductive matrix phase, the bottom represents a more conductive distributed phase. The 2d charts to the right and below are anchored at η_{μ}=1 in conductivity ratio or volume fraction.

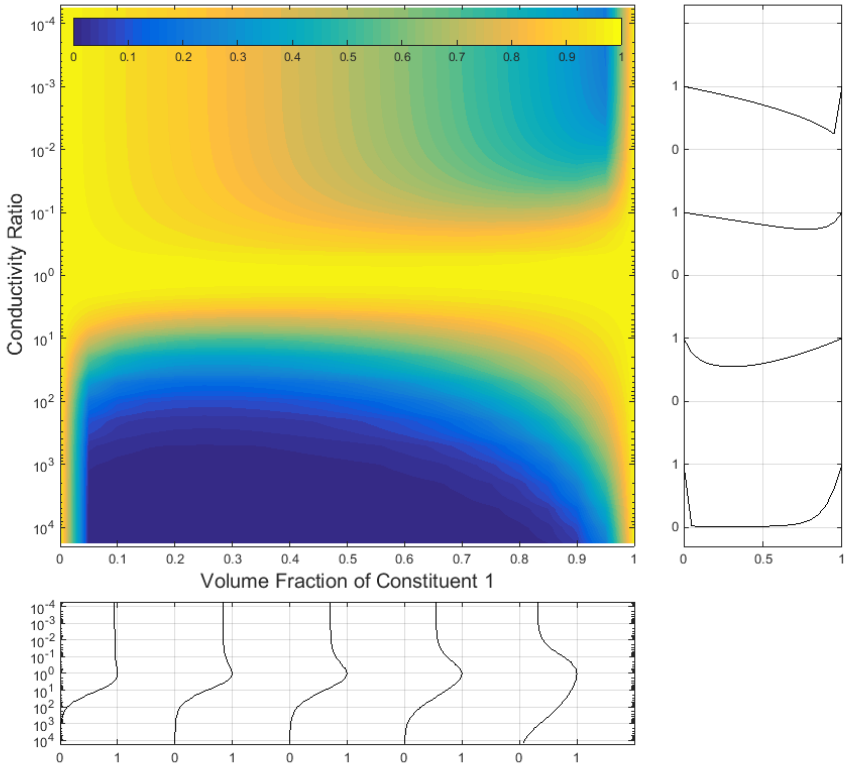

Figure 23 Microstructural Efficiency predicted by the Bruggemann model of equation 5. The top of this chart represents a more conductive matrix phase, the bottom represents a more conductive distributed phase. The 2d charts to the right and below are anchored at η_μ=1 in conductivity ratio or volume fraction.

The Maxwell-Eucken model predicts a gradual drop in efficiency to a minimum of two thirds on the low conductivity ratio (high conductivity matrix - top) side. For high conductivity ratios (high conductivity inclusions - bottom) the efficiency is nearly zero for all but extreme volume fractions near zero and unity. The Maxwell-Eucken model is limited in validity to moderate volume fractions (~50%). The Bruggeman model behaves similarly on the low conductivity ratio side with a minimum of near zero instead of two thirds. The high conductivity ratio side shows an increased efficiency for moderate conductivity ratios and high volume fractions over the Maxwell-Eucken model.

These models indicate how percolation of distributed spheres influences the effective conductivity. The top half describes a high conductivity matrix. Heat easily moves through the matrix and only begins to become blocked when volume fractions are high enough for chains of low conductivity inclusions to form. On the bottom of these charts the matrix is now more insulating and heat can't flow effectively until the inclusions manage to touch and form chains of high conductivity material.

4.2.3. Sparse, Prismatic Morphologies

Prismatic morphologies involve composites that have a constant morphology in one dimension. Only a cross section normal to this dimension is required to define the complete microstructure.

A simple model that considers a specific prismatic morphology is the Halpin-Tsai theoretical model [42, 100]. It is most appropriate for filaments of uniform cross-sectional area running in parallel through a matrix. Figure 24 displays the microstructural efficiency for the effective conductivity predicted by this model. The model predicts identical efficiency for both square and circular fibres.

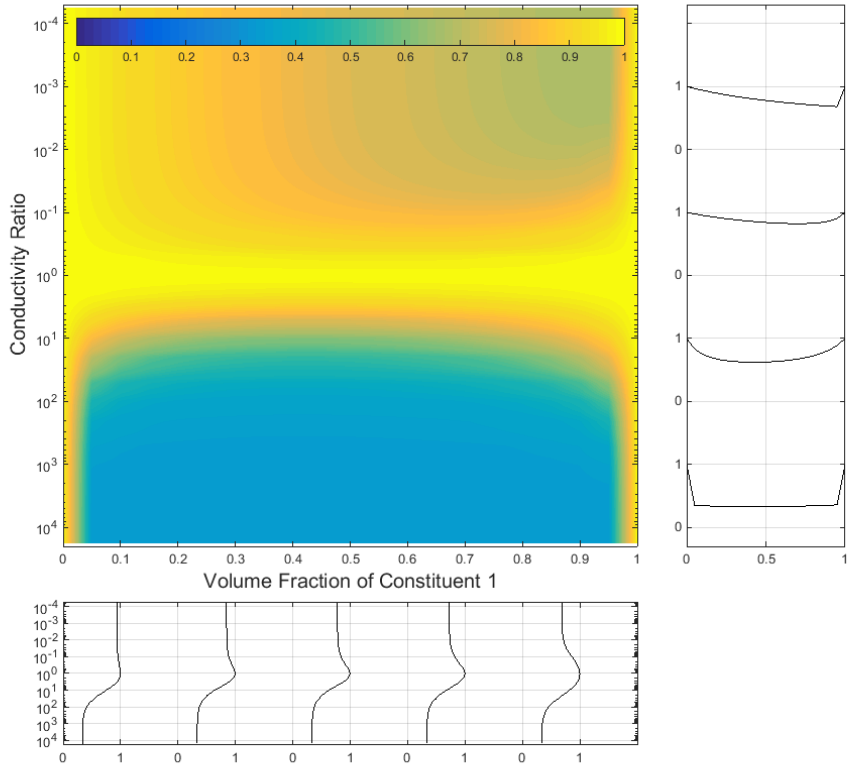

Figure 24 Microstructural Efficiency predicted by the Halpin-Tsai model of equation 6. The top of this chart represents a more conductive matrix phase, the bottom represents a more conductive distributed phase. The 2d charts to the right and below are anchored at η_μ=1 in conductivity ratio or volume fraction.

The microstructural efficiency behaviour of the Halpin-Tsai model is similar to that predicted by the Maxwell-Eucken model. For low conductivity ratios the efficiency drops with increasing volume fraction to a minimum of around two thirds. For high conductivity ratios the efficiency is of a similar shape but with a minimum of one third instead of zero. The limit of one third is a result of the prismatic morphology. The direction parallel to the fibre axes will always yield the series average conductivity.

4.2.4. Summary of Microstructural Efficiency of Analytical and Empirical Models

The microstructural efficiency for a number of the models mentioned in §3.1.5 are shown in Figure 25. The arithmetic mean is of course the limiting case that all others are normalised against. The harmonic mean leads to the lowest possible efficiency for the composite. The geometric mean is quite similar to the reciprocity model, though the former predicts higher efficiency for low volume fractions of poor conductivity inclusions. The Hashin-Shtrikman upper and lower bound give efficiencies extremely similar to the Maxwell-Eucken inclusion and omission models. The effective medium theory is the only model here to predict percolation across the conductivity ratio range. The contour charts below consider solely the functional form and thus are asymptotic to zero where as a parallel plates morphology (which has both arithmetic and harmonic averages) is instead asymptotic to two thirds.

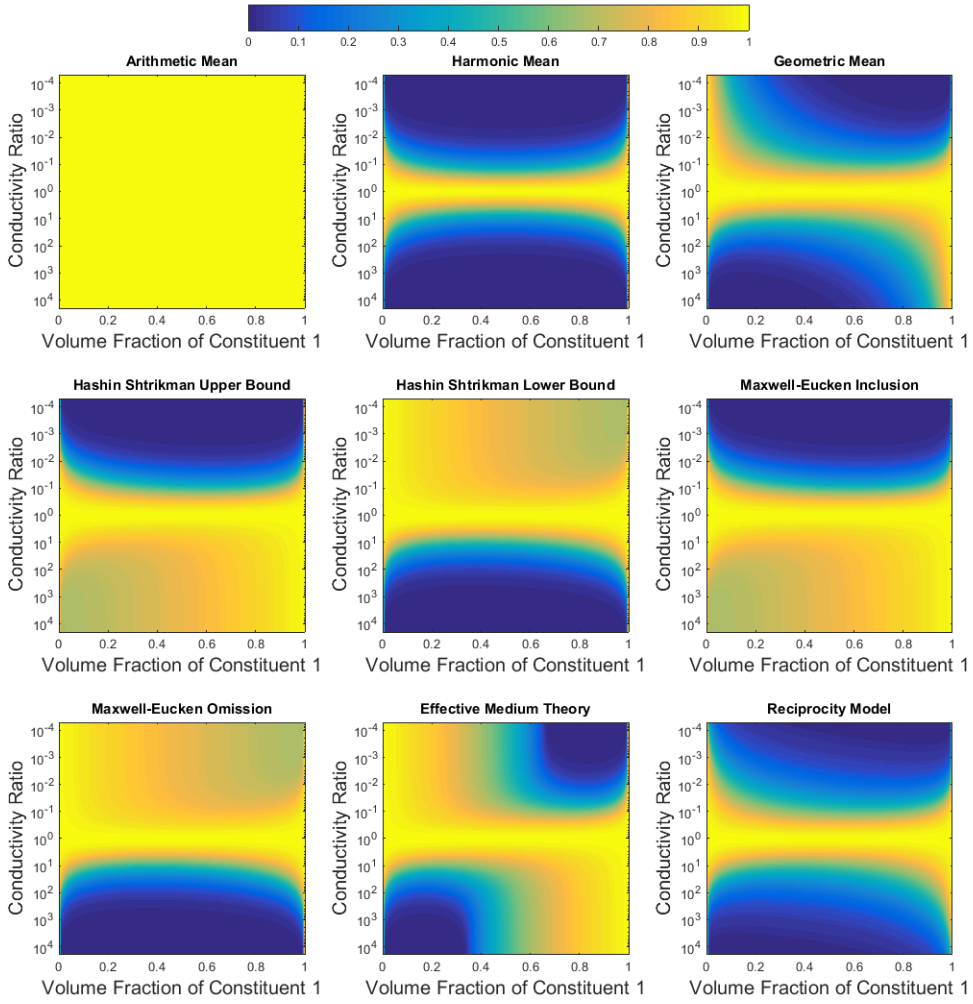

Figure 25 Microstructural Efficiency of a number of theoretical models. Conductivity ratio below 1 implies a high conductivity matrix and is plotted on the top half of each chart. High conductivity inclusions have conductivity ratios greater than one and are plotted on the bottom half of each chart.

4.3. Microstructural Efficiency of Prismatic Morphologies

Where a microstructure is highly regular in one Cartesian component, the effective conductivity may be established through consideration of only a cross section. The dimension with constant morphology will have a tensor component of effective conductivity that corresponds to the series average weighted on area fraction. This

contributes to ensuring the minimum efficiency of any prismatic morphology is one third. The morphologies of §4.3 are analysed using Lattice Monte Carlo analysis.

4.3.1. Structured Packing of Square Prisms

A square cross section corresponds to an infinitely long rectangular prism. This representation might be imagined as a number of long prisms all stacked parallel. Many different configurations are possible through variation of location and orientation of the square cross sections. Two different structured cases are discussed below.

If the edges of a single square cross section are parallel to square periodic boundaries, a square packed rectangular prism morphology is modelled. This type of morphology is of interest due to the lack of a percolation volume fraction. The periodic inclusion does not connect to a neighbouring inclusion until a volume fraction of 100% is achieved. Thus a continuous matrix exists for all binary volume fractions. Figure 26 below displays the cross section for 9 base cells.

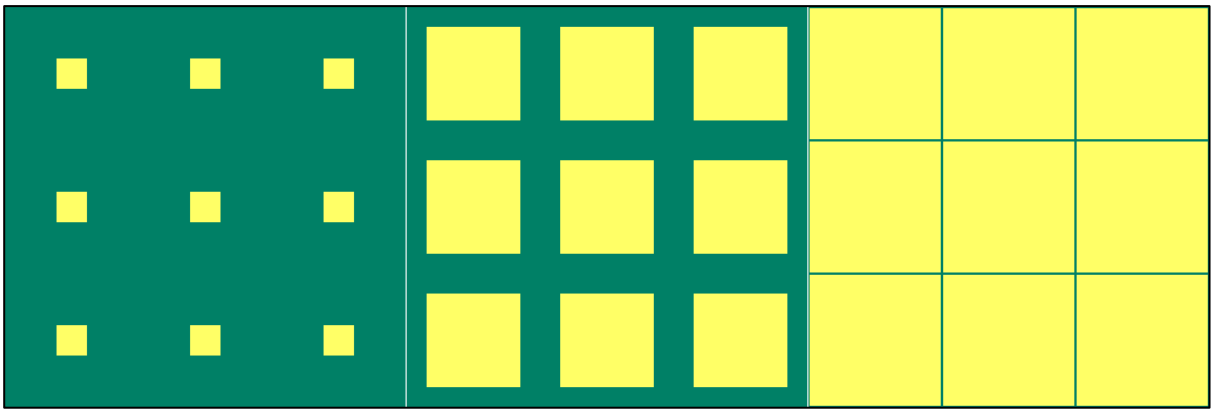

Figure 26 Cross sections of square packed square prisms. Volume fraction is increasing from left to right.

The microstructural efficiency is shown in Figure 27.The top half (high conductivity matrix – top) of the chart displays a higher microstructural efficiency. This intuitive result is due to the presence of a continuous high conductivity matrix. Even as the inclusion concentration approaches unity, the microstructural efficiency stays relatively high as the matrix remains continuous. The limiting case of two thirds is similar to that of parallel plates and is a result of two completely percolating high conductivity tensor components existing at all volume fractions.

The lower half (high conductivity inclusion – bottom) of the chart shows more symmetrical behaviour against volume fraction with much lower microstructural efficiency than the top half. For low volume fractions and high conductivity ratio, the limiting case of one third is approached. On this side of the chart the matrix is the poor conductor and acts to restrict lateral heat transfer.

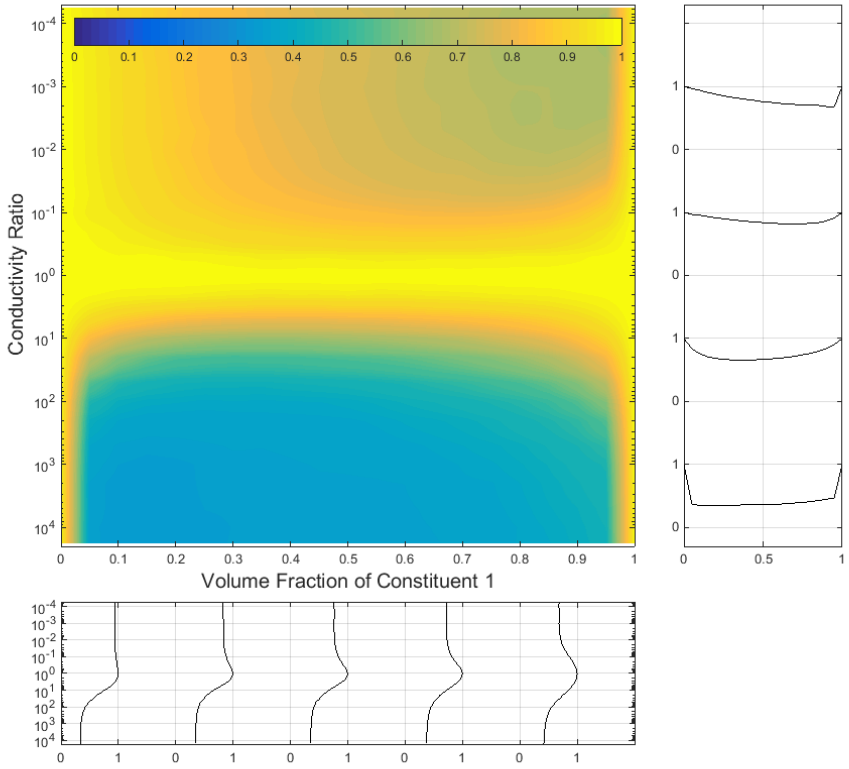

Figure 27 Microstructural efficiency of square prisms square packed. Note the high microstructural efficiency for low conductivity ratios over a range of volume fractions. The top of this chart represents a more conductive matrix phase, the bottom represents a more conductive distributed phase. The 2d charts to the right and below are anchored at η_{μ}=1 in conductivity ratio or volume fraction.

If the edges of a single square cross section are at 45° to the periodic boundaries, a square packed diamond prism morphology is achieved. This type of morphology differs from the previous in that a continuous chain of inclusion occurs for volume fractions above 50%. This occurrence strongly affects the effective conductivity and hence the microstructural efficiency.

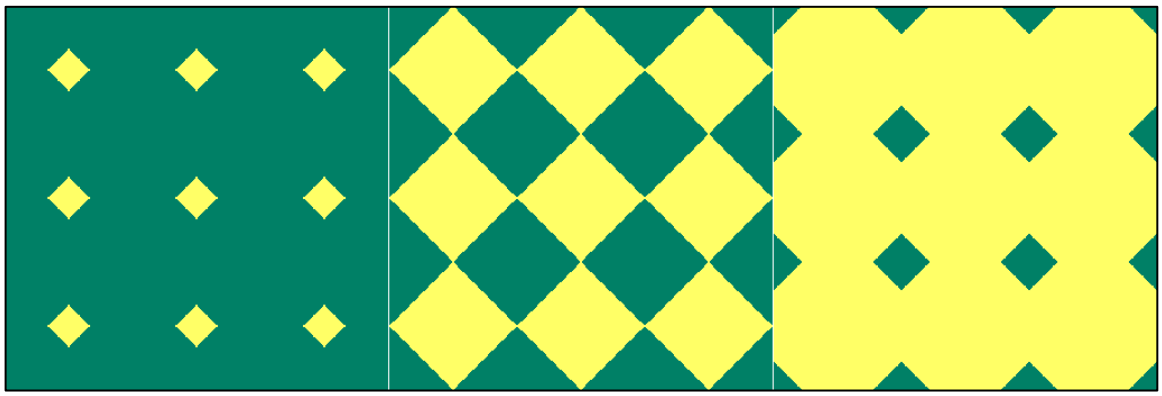

Figure 28 Cross sections of square packed diamond prisms. Volume fraction is increasing from left to right.

The microstructural efficiency behaviour of square packed diamonds is diagonally symmetric. High efficiencies occur for low conductivity ratios below 50% volume fraction and for high conductivity ratios above 50%. The morphology for volume fractions above 50% are the inverse of those below 50%. This drives the symmetry observed in the microstructural efficiency contour chart (Figure 29).

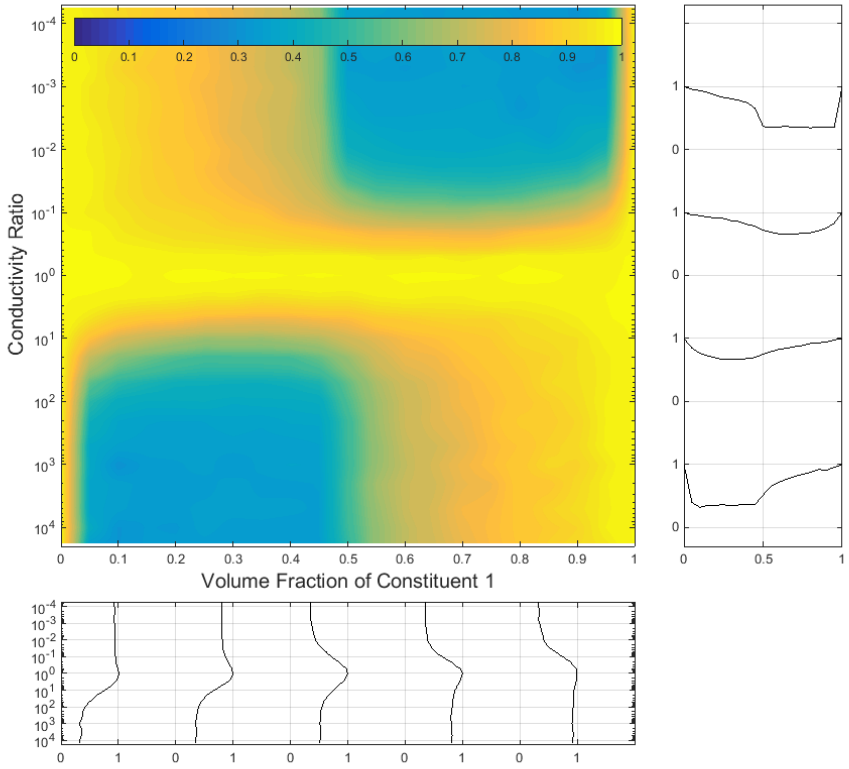

Figure 29 Microstructural efficiency of diamond prisms square packed. This map was simulated with 10 000 particles and has a higher uncertainty than the others. The top of this chart represents a more conductive matrix phase, the bottom represents a more conductive distributed phase. The 2d charts to the right and below are anchored at η_μ=1 in conductivity ratio or volume fraction.

The orientation of the square prism cross section to the periodic boundaries clearly has a significant influence on the microstructural efficiency behaviour. No known analogue occurs in three dimensions.

The behaviour observed for the two cases involving square cross sections is well predicted by the Halpin-Tsai model shown in Figure 24 for low to moderate volume fractions (<50%). For high volume fractions the model continues to predict square packed prisms well, but fails to account for the onset of percolation in the diamond morphology. Clearly the analytical model does not account for percolation.

4.3.2. Structured Packing of Cylinders

Cylinders must percolate at a volume fraction less than unity when arranged in square periodic boundaries (they do not tessellate). For square packed cylinders this percolation volume fraction occurs at exactly $\pi/4$ (~79%). Cylinders on a hexagonal lattice are of interest as they present the densest packing possible [110]. Here the percolation limit of volume fraction sits at exactly $\pi/\sqrt{12}$ (~91%). Cross sections of these cylinder morphologies are shown in Figure 30 and Figure 31.

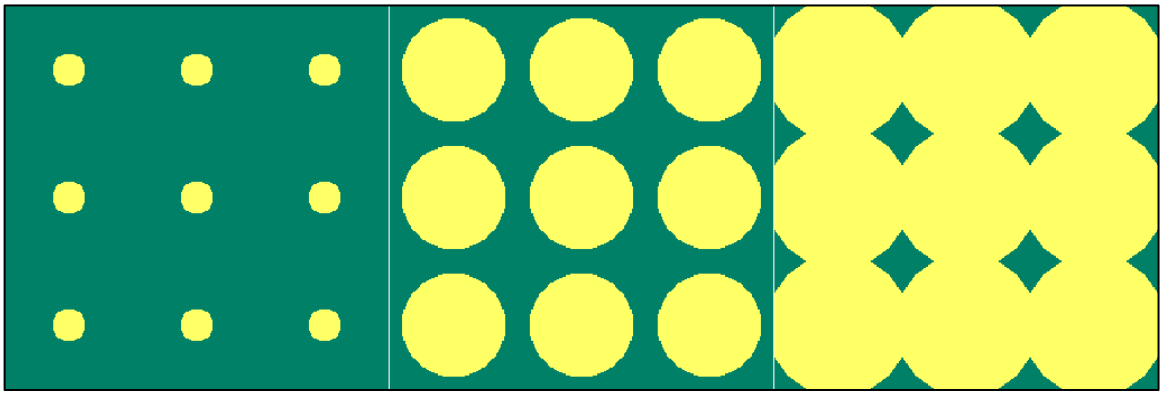

Figure 30 Cross sections of square packed cylinders. Volume fraction is increasing from left to right.

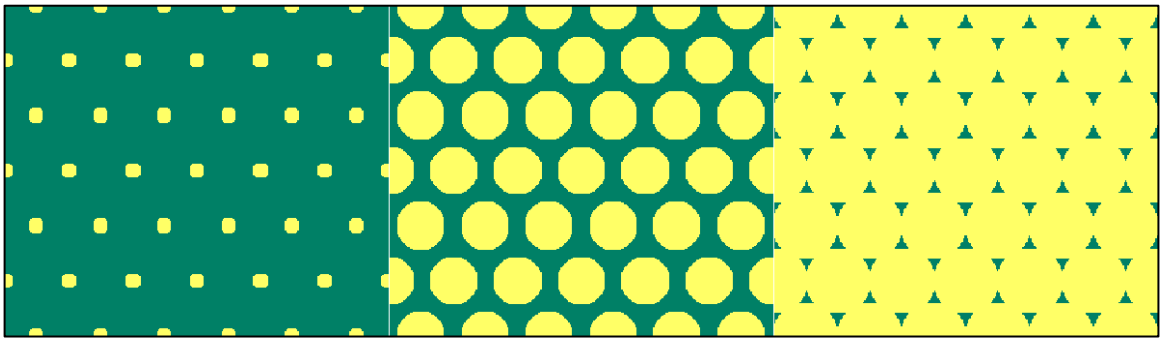

Figure 31 Cross sections of hexagonally packed cylinders. Volume fraction is increasing from left to right.

The microstructural efficiency for square packed and hexagonally packed cylinders is influenced by the onset of percolation for high volume fractions. There is a drastic decrease in efficiency for low conductivity ratios (high conductivity matrix – top) at volume fractions of 79% and 91% for the square packed and hexagonally packed cases respectively. At these volume fractions the cylinders touch laterally, creating a continuous chain of poor conductor that now *laterally encapsulates* the original matrix material. The efficiency experiences a sharp increase at these critical volume fractions when the inclusion is the higher conductor (high conductivity inclusions – bottom). This intuitive result is due to the formation of a continuous high conducting phase. The behaviour is captured in the contour charts of Figure 32 and Figure 33.

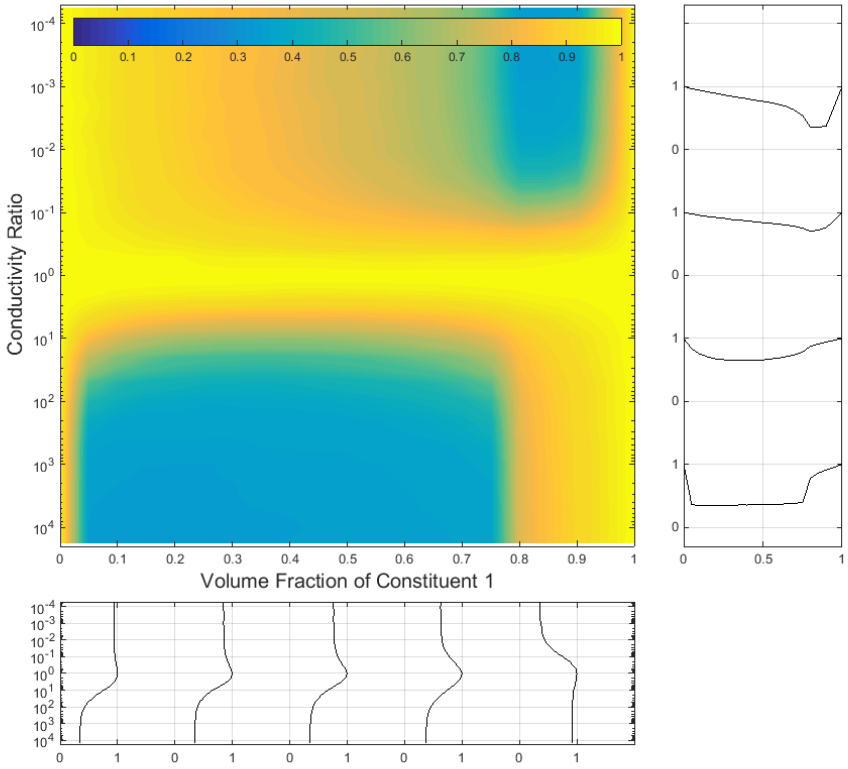

Figure 32 Microstructural efficiency of square packed cylinders. The percolation threshold occurs at a volume fraction of ~79%. The top of this chart represents a more conductive matrix phase, the bottom represents a more conductive distributed phase. The 2d charts to the right and below are anchored at η_{μ}=1 in conductivity ratio or volume fraction.

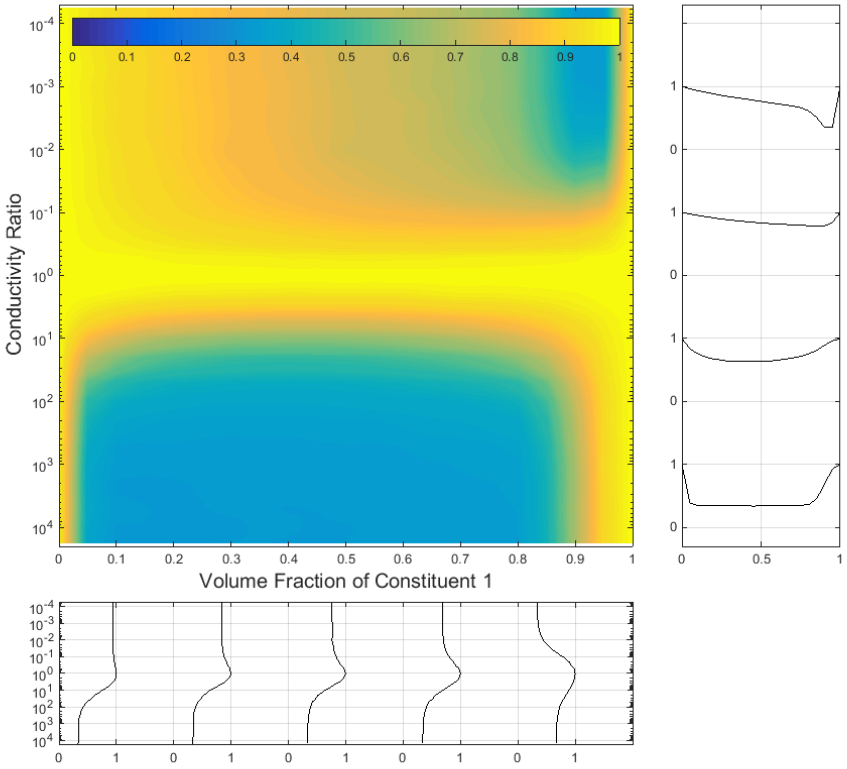

Figure 33 Microstructural efficiency of hexagonally packed cylinders. The percolation threshold occurs at a volume fraction of ~91%. The top of this chart represents a more conductive matrix phase, the bottom represents a more conductive distributed phase. The 2d charts to the right and below are anchored at η_{μ}=1 in conductivity ratio or volume fraction.

The behaviour observed for the two cases is well predicted by the Halpin-Tsai model for low to moderate volume fractions (<50%). The simulated and calculated efficiencies are very similar with less than 3% difference between simulated and calculated results over conductivity ratios below unity. For high volume fractions (>50%) the model fails to account for the onset of percolation in the cylinder based morphologies.

4.4. Microstructural Efficiency of Three Dimensional Morphologies

The microstructural efficiencies of three dimensional morphologies may vary from zero to unity as no unidirectional assumptions are required. The most commonly researched three dimensional morphology is surely that of different packings of spheres. How the conductivity of arrangements of spheres vary is of academic and practical interest as the system has many physical analogues in a variety of fields of study. It is of prime interest in the study of Miscibility Gap Alloys as the starting materials are generally near spherical powders distributed through an ideally continuous matrix. The section starts with a discussion of the microstructural efficiency of cubes in structured arrangements before moving to structured and random distributions of spheres. The morphologies of §4.4 are analysed using Lattice Monte Carlo analysis.

4.4.1. Structured Packing of Cubes

Many engineering materials may be simplified as having structured morphologies in three dimensions. Primitive cubic packed cubes are, as an analogue to square packed prisms, an interesting case. Again the microstructure does not percolate until 100% volume fraction is achieved, though this time the matrix completely encapsulates the inclusion in *all* directions. An array of primitive cubic packed cubes is shown in Figure 34.

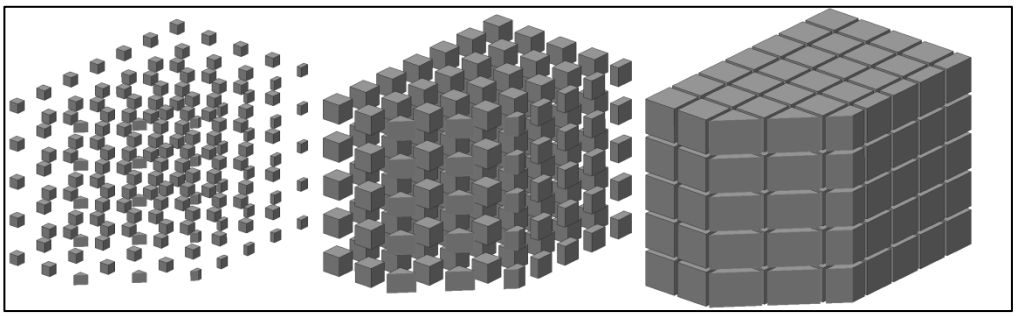

Figure 34 Primitive cubic packing of cubes. Volume fraction is increasing from left to right.

Primitive cubic packed cubes do not experience percolation and hence Figure 35 does not display any step change in microstructural efficiency. The behaviour is very similar to that of square packed square prisms. For low conductivity ratios the efficiency is high (greater than two thirds) for all volume fractions. Any conductivity ratio above 100 yields an efficiency of essentially zero over all non-trivial volume fractions. This is a result of the continuous and completely encapsulating matrix providing thermal resistance to heat flux in any direction. The Maxwell-Eucken model (§3.1.5) predicted a nearly identical microstructural efficiency to that simulated for primitive cubic packed cubes.

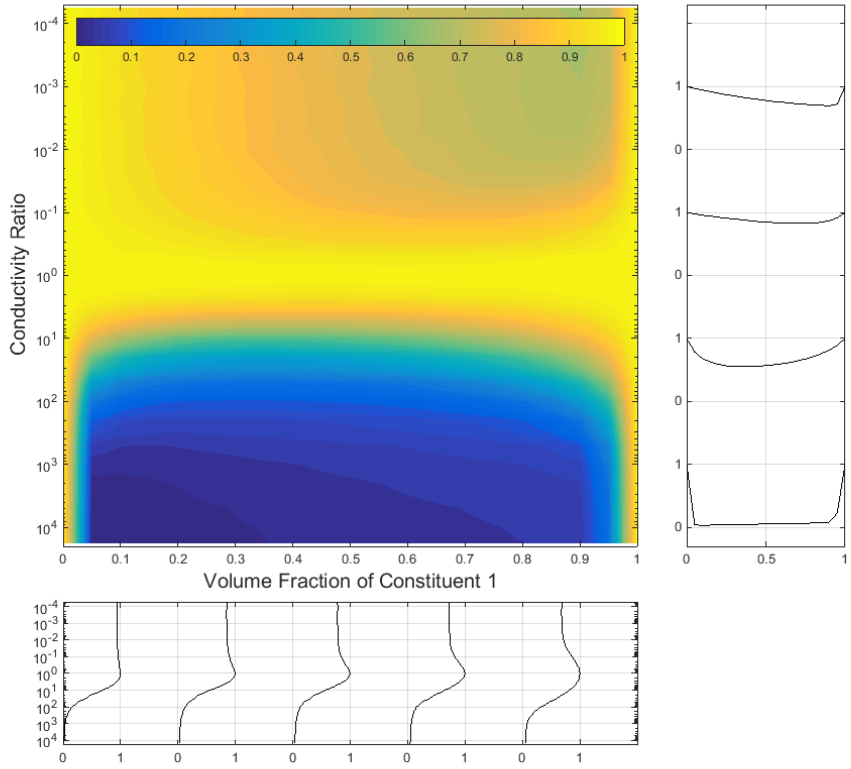

Figure 35 Microstructural efficiency of primitive cubic packed cubes. The top of this chart represents a more conductive matrix phase, the bottom represents a more conductive distributed phase. The 2d charts to the right and below are anchored at η_μ=1 in conductivity ratio or volume fraction.

4.4.2. Structured Packing of Spheres

Primitive cubic packed and face centred cubic spheres are a commonly analysed system analytically. Examples of these morphologies are shown in Figure 36 and Figure 37. The percolation threshold for the packings are $\pi/6$ (~52%) and $\frac{\pi}{3\sqrt{2}}$ (~74%) volume fraction respectively. Above these thresholds both the inclusion and matrix percolate. At the very high volume fraction of ~96.5% the matrix ceases to percolate for both structured sphere morphologies.

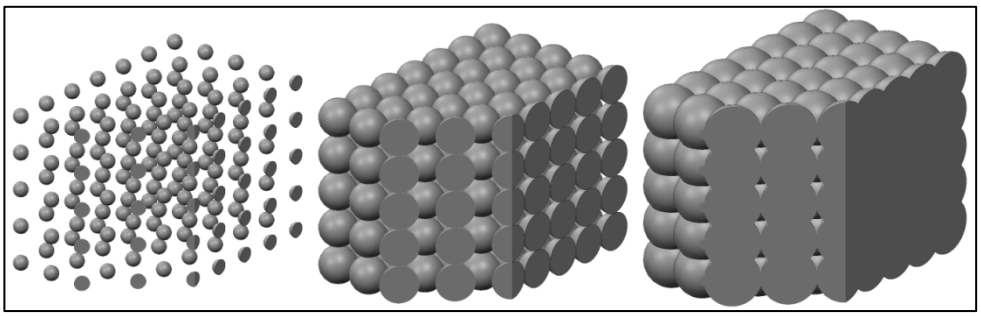

Figure 36 Primitive cubic packing of spheres. Volume fraction is increasing from left to right.

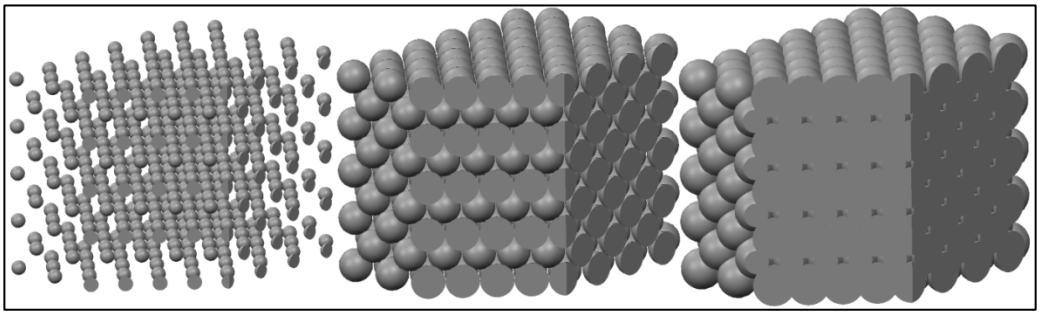

Figure 37 Face centred cubic packing of spheres. Volume fraction is increasing from left to right.

Both primitive cubic and face centred cubic packed spheres experience a notable change in microstructural efficiency at their respective percolation volume fractions. For low conductivity ratios the efficiency drops with volume fraction to a minimum of near zero occurring around 96.5% (the volume fraction at which the original matrix is isolated). For high conductivity ratios (>100) the microstructural efficiency does not increase from near zero until the respective percolation threshold occurs, after which a nearly logarithmic increasing trend is observed. The associated microstructural efficiencies are shown in Figure 38 and Figure 39.

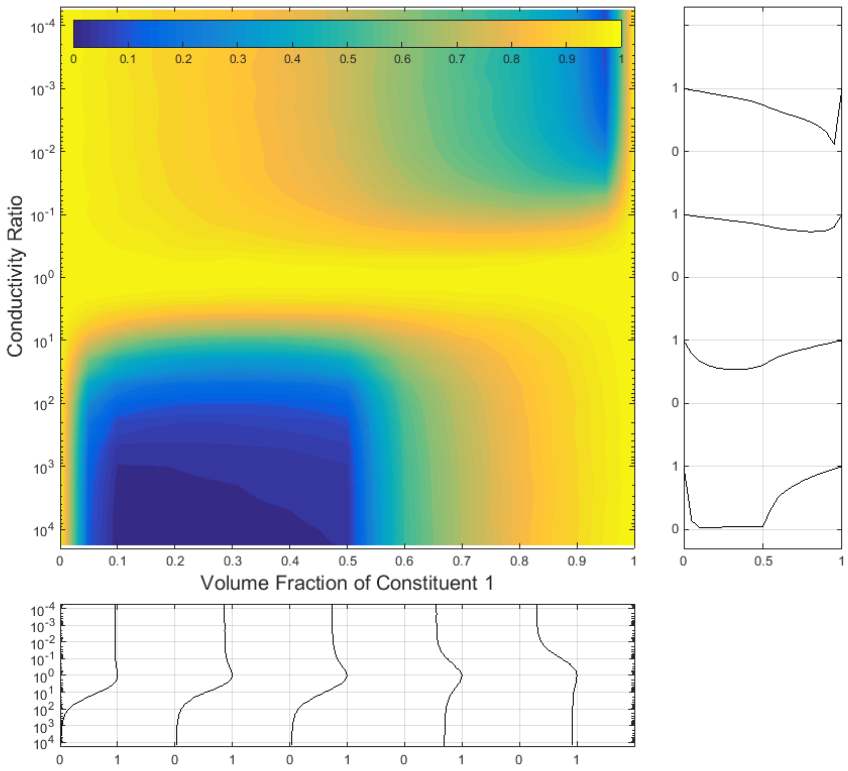

Figure 38 Microstructural Efficiency of primitive cubic packed spheres. The percolation threshold occurs at a volume fraction of ~52%. The top of this chart represents a more conductive matrix phase, the bottom represents a more conductive distributed phase. The 2d charts to the right and below are anchored at η_{μ}=1 in conductivity ratio or volume fraction.

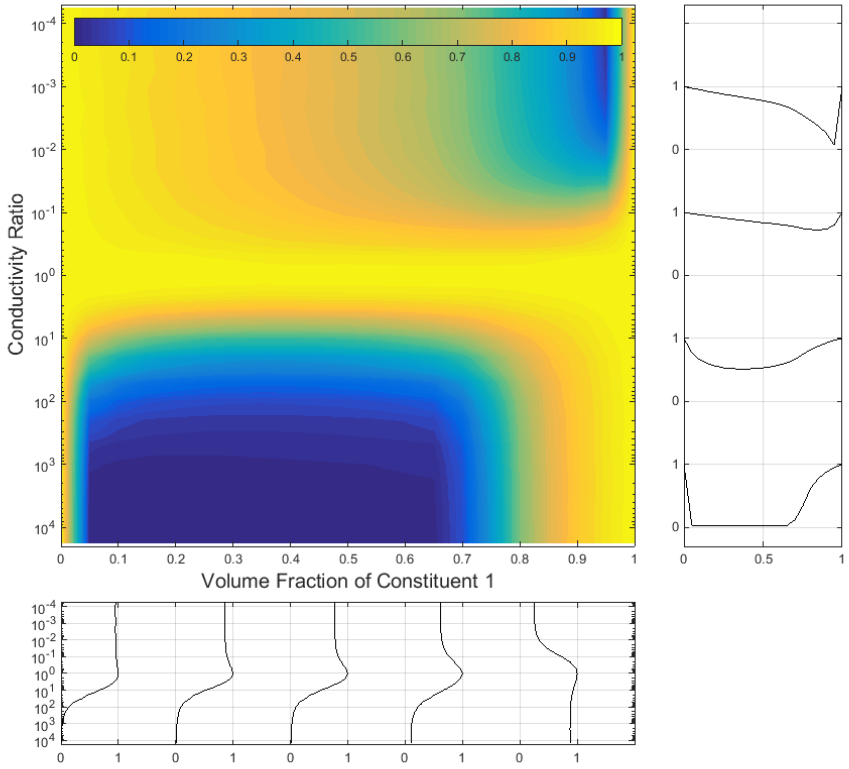

Figure 39 Microstructural Efficiency of face centred cubic packed spheres. The percolation threshold occurs at a volume fraction of ~74%. The top of this chart represents a more conductive matrix phase, the bottom represents a more conductive distributed phase. The 2d charts to the right and below are anchored at η_μ=1 in conductivity ratio or volume fraction.

4.4.3. Random Packing of Spheres

To best represent dense random distributions of spheres likely to occur in powder based metallurgy a discrete element algorithm was implemented for morphology generation. The selected framework was the open source code YADE[5]. Here a number of spheres were randomly seeded in a 3d space with small random velocities. The periodic

[5] Yade is an extensible open-source framework for discrete numerical models, focused on Discrete Element Method [111] V. Šmilauer, Welcome to Yade - Open Source Discrete Element Method, 2009, https://yade-dem.org/doc/..

boundaries of the cube were gradually brought in as the spheres were allowed to interact without deforming. The location, radii of the spheres and ensemble averaged hydrostatic stress were exported at regular intervals of volume fraction.

Binary cubic grids were then discretised from the YADE output and fed to a Lattice Monte Carlo algorithm. The conductivity ratio was varied from 5×10^{-5} as before and the effective isotropic conductivity recorded. This conductivity was then divided by the volume weighted series average of the conductivities to yield the microstructural efficiency for the morphology, conductivity ratio and volume fraction.

The statistical distribution of radii is of interest along with the spatial distribution of the spheres. Three cases were analysed; two Gaussian distributions of standard deviation 0.2 (Figure 41) and 0.4 (Figure 42) mean radii and a monodisperse system (Figure 43). The distributions of diameter of the particle lists are shown in Figure 40.

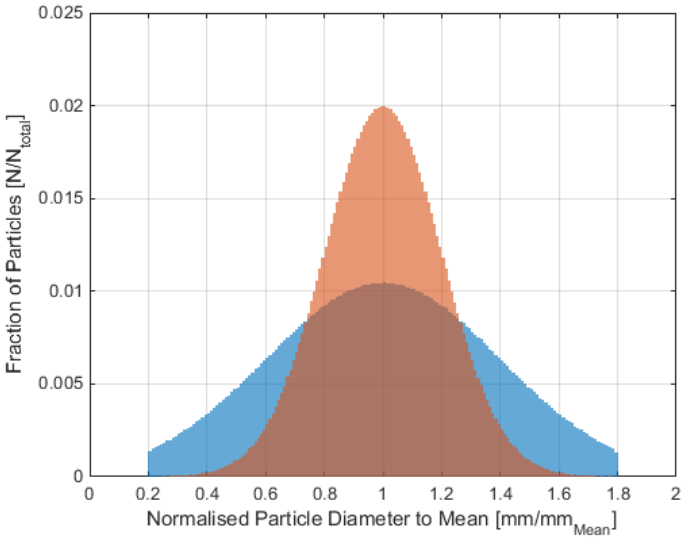

Figure 40 Distribution of particle diameter for the two Gaussian distributions used.

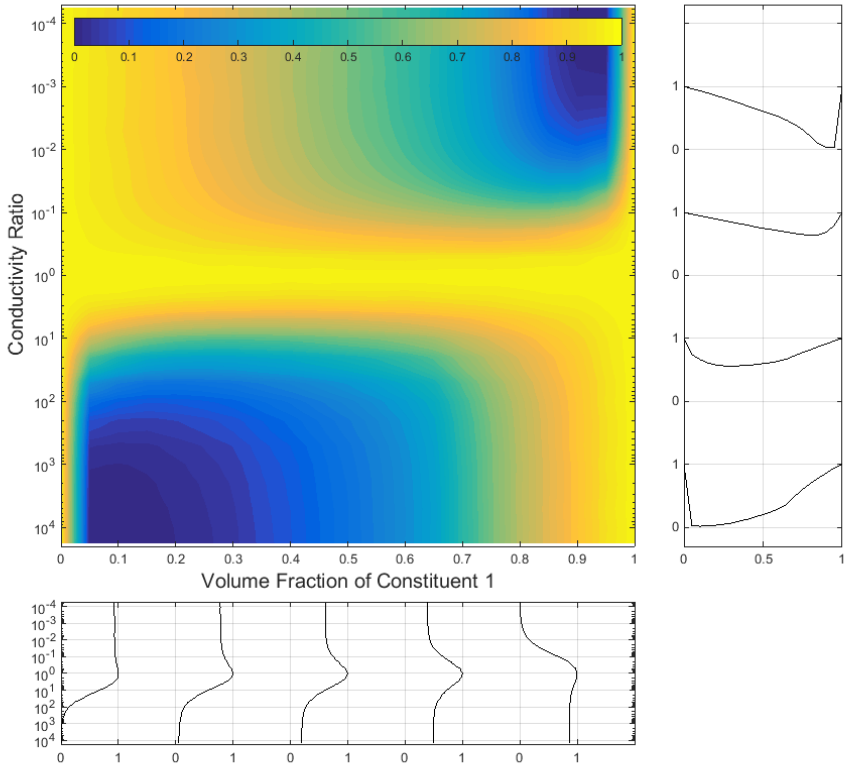

Figure 41 Microstructural Efficiency for randomly packed spheres with a Gaussian Distribution with a standard deviation 0.2 times the mean radius. The top of this chart represents a more conductive matrix phase, the bottom represents a more conductive distributed phase. The 2d charts to the right and below are anchored at η_μ=1 in conductivity ratio or volume fraction.

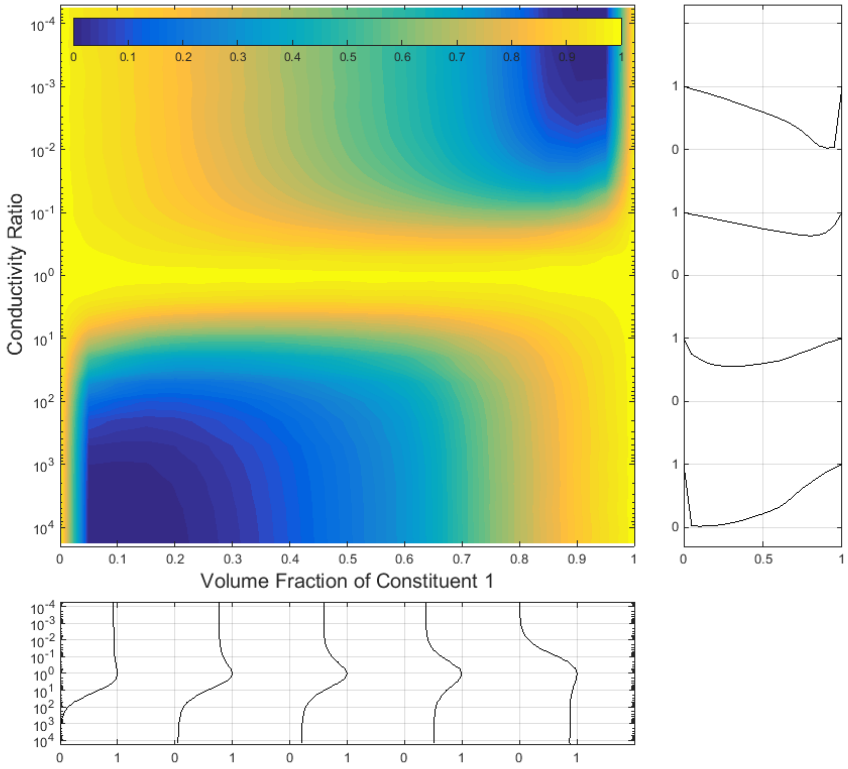

Figure 42 Microstructural Efficiency for randomly packed spheres with a Gaussian Distribution with a standard deviation 0.4 times the mean radius. The top of this chart represents a more conductive matrix phase, the bottom represents a more conductive distributed phase. The 2d charts to the right and below are anchored at η_{μ}=1 in conductivity ratio or volume fraction.

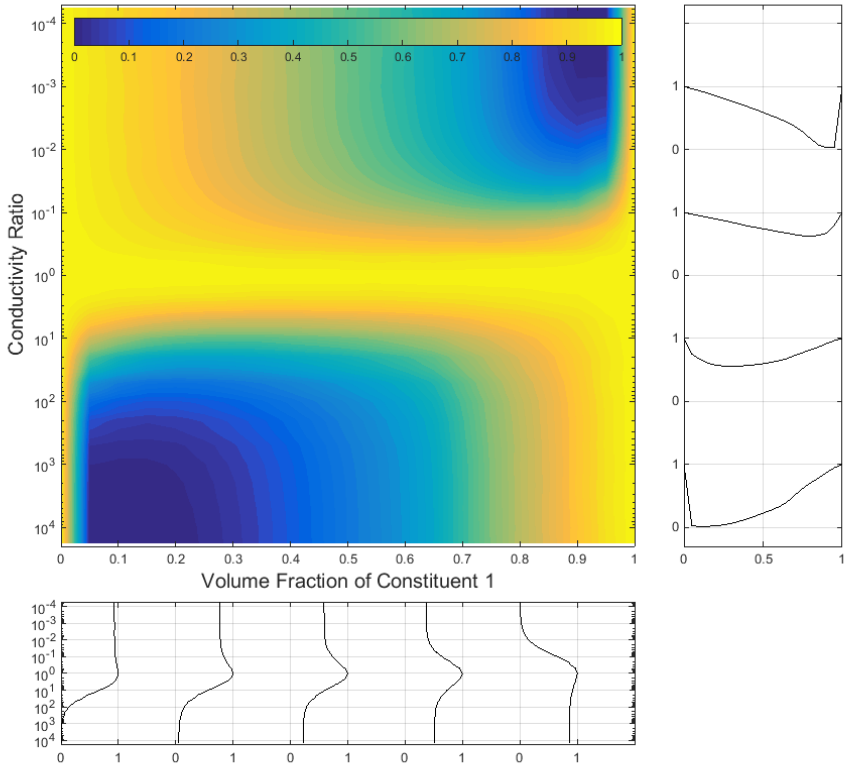

Figure 43 Microstructural Efficiency for monodisperse randomly packed spheres. The top of this chart represents a more conductive matrix phase, the bottom represents a more conductive distributed phase. The 2d charts to the right and below are anchored at η_μ=1 in conductivity ratio or volume fraction.

All three systems have very similar behaviour which is not well predicted by any analysed general model. The greatest contributor to the small variations between the packings and the poor general model prediction is the onset of percolation. Increasing the width of the Gaussian distribution of radii resulted in increasing the volume fraction percolation threshold slightly.

It is likely that having a distribution of particle radii would have a bigger influence where particles could jam within a container. The packing method performed in the above analysis utilised particles with frictionless contact. Provided an indicator for how ‘jammed’

a morphology is, the methodology could be applied again. This is beyond the scope of this thesis.

4.5. Discussion

Microstructural Efficiency is seen to be a very useful concept in reducing the complexity of homogenising thermal conductivity. Analysis of the efficiency reveals for metal-metal composites the arrangement of distributions below percolation has a very minor influence on thermal conductivity. As alluded to in §3.1.5 any transient property that may be modelled with diffusion may be treated in this manner. If a change in constituent properties, volume fraction or morphology is known to occur, the change in effective properties may be easily predicted by moving vertically, horizontally or between microstructural efficiency charts. It is hoped that in the future further direct validation will be performed on the method and its results might be used to find a closed form for effective properties of a binary composite.

Analysis of both the homogenisation models introduced in §3.1.5 and numerical simulation results suggest that composites with moderate conductivity ratios (>0.2, <5) and volume fractions below percolation vary very little between distributed morphologies. Augmentation of poorly conducting thermal storage materials through distributing high conductivity inclusions is seen to be disadvantageous. Instead a continuous matrix of augmenting material would be preferable (resulting in considerable manufacturing complexity and cost.

Though thermal conductivity is taken as the running example in this paper, analogies exist in other physical systems. Table 5 describes some analogues between

thermal conductivity and other common engineering situations. These properties are also resolvable with the methodology presented in this thesis.

Table 5 Similar transient properties involved in engineering situations.

Situation	Transient Property
Temperature Field	Thermal Conductivity
Electric Field	Electrical Conductivity
Concentration Field	Species Diffusivity
Electric Field applied on a Dielectric	Permittivity
Magnetic Field	Magnetic Permeability

During a thermal cycle of a Miscibility Gap Alloy the thermal conductivity of the constituents will change independently, likely resulting in substantial changes to the conductivity ratio. Changes in volume fraction are likely to occur in manufacture to achieve a particular energy storage requirement or just through small inconsistencies in production. Through thermal cycling the morphology is likely to change as interfacial energy is minimised and atoms are dissolved and deposited. The influence of these occurrences on effective conductivity can be easily estimated through moving vertically or horizontally upon a Microstructural Efficiency chart (demonstrated on Figure 44) and interpolating between two different charts representing the morphology before and after the predicted change.

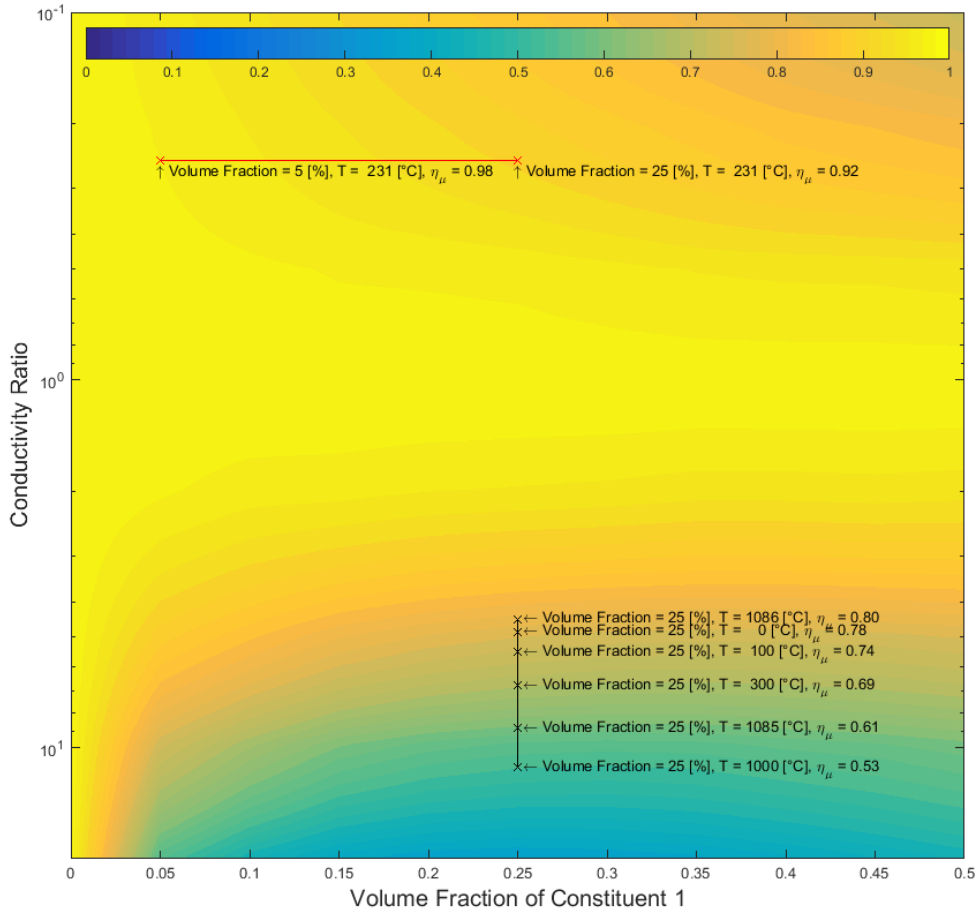

Figure 44 Changes in microstructural efficiency for a random monodisperse system as (black) Cu-Fe changes temperature (hence conductivity ratio) and (red) Sn-Al changes volume fraction.

It is hoped that the charts shown above and the discussion about them might lead to both direct experimental validation and perhaps a closed form solution for the surfaces produced numerically. Through new 3d printing technology it is thought that porous structures and filled composites, of both structured and randomly generated morphologies, might be created to further validate the work above for structures uncommonly found in literature. The multitude of surfaces generated above might also form a database for a researcher interested in furthering the field of property homogenisation.

CHAPTER 5: MANUFACTURING AND MATERIAL PROPERTIES OF MISCIBILITY GAP ALLOYS

This chapter provides the manufacturing methods involved in production of the Miscibility Gap Alloys discussed in later chapters. From the established manufacturing methods the range of porosity and morphologies is determined. Given the porosity and constituent material properties from literature the homogenised equilibrium properties of interest are calculated and presented comparatively (tabular information is provided in Appendix E). Knowledge of the morphology and transient properties from literature allows estimates of the transient properties to be made. Finally the energy density and effusive energy density may be calculated for each system and compared to other state of the art thermal storage materials.

5.1. Manufacturing Methods

5.1.1. Manufacture of Brass-Graphite Miscibility Gap Alloys

The current manufacturing method for Brass-Graphite MGAs was discovered by Mr. Nathan Morton, a mechanical engineering student of the University of Newcastle, Australia and later was improved Mr. Bastien Monnier, a materials engineering student from Université de Technologie Troyes, France improved the method. The Author gratefully acknowledges the contribution of these two students to the understanding of Miscibility Gap Alloy manufacture [112, 113].

Graphite powder is combined with sodium silicate binder (8.9% Na_2O, 28.7% SiO_2, 62.4% H_2O mass) at a mass fraction of 10% Sodium Silicate in a mortar and pestle. A brass powder of 200 μm is then added to the wet graphite and mixed in the mortar and pestle further. The mixed wet powder is pressed at 32 MPa before being dried at 80 °C for 72

hours. Another drying stage follows at 250 °C for 8 hours. The dry samples are then fired at 500 °C for 8 hours before stepping to 1100 °C for a further 8 hours. Densities of 91% to 95% of theoretical were obtained repeatedly [112]. A back scattered electron micrograph of the system's typical morphology is shown in Figure 45. The odd shape of the brass particles is a result of the powder production and not a result of the firing.

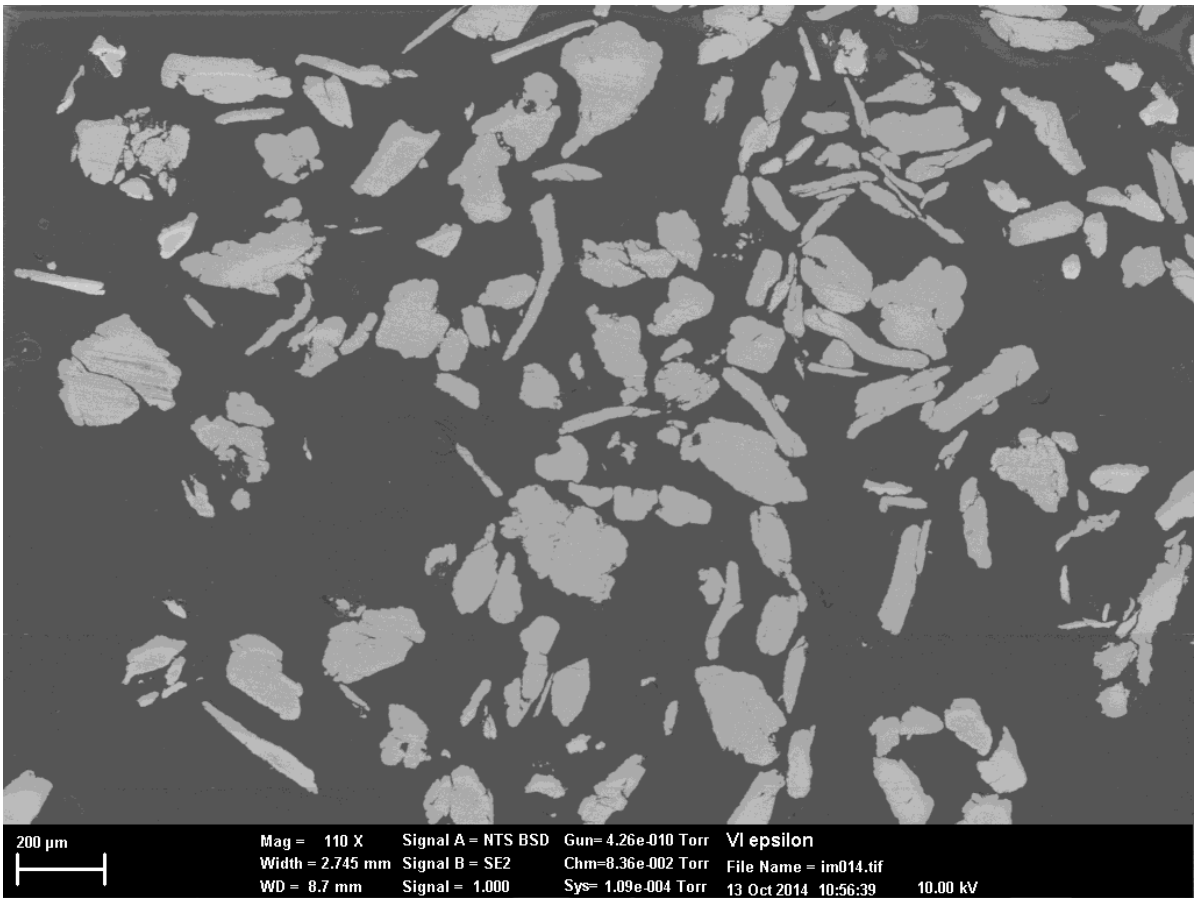

Figure 45 Back Scattered Electron Microscope image of the Brass-C System at 25% volume fraction [112] . The light distributed phase is brass whilst the dark matrix is graphite.

5.1.2. Manufacture of Copper-Graphite Miscibility Gap Alloys

The manufacturing process and proportion of theoretical densities obtained for Cu-C were identical to that of the Brass-C systems. Copper powder of 90 μm diameter was used. A scanning electron micrograph is shown in Figure 46 of the typical morphology for this system.

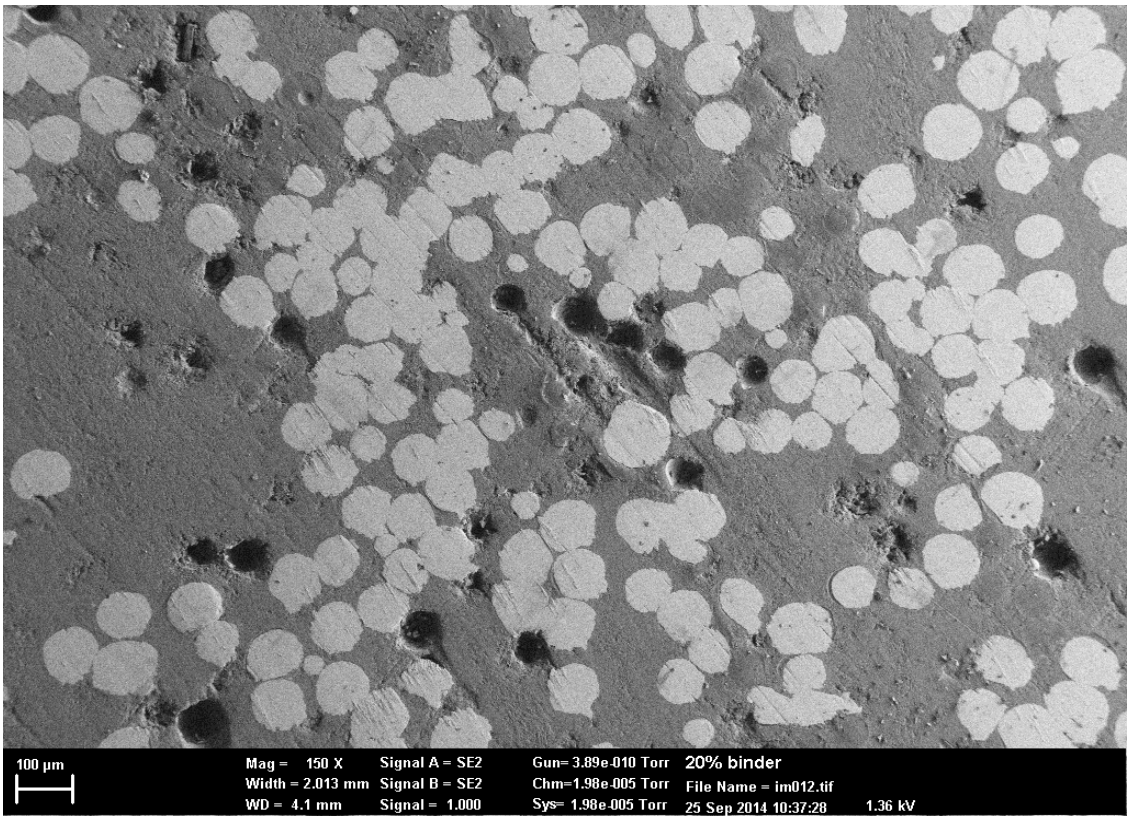

Figure 46 Scanning Electron Microscope image of the Cu-C system at 20% volume fraction [112]. The light distributed phase is copper whilst the dark phase is graphite. The large pores are a result of the polishing process in preparation for microscopy and are not a result of the manufacturing procedure.

5.1.3. Manufacture of Copper-Iron Miscibility Gap Alloys

Copper-Iron Miscibility Gap Alloys were relatively easy to manufacture. An iron matrix was found to sinter well at 1000°C (below the melting temperature of copper). The

copper powder shape was preserved on manufacture. Leakage of copper was observed on samples with volume fractions greater than 60%.

Iron powder of -300 mesh (<44 μm) was found to sinter well with -200 mesh (<90 μm) copper powder. The powders were mixed by hand in atmosphere and pressed into pellets with a pressure of 400 MPa. The Miscibility Gap Alloy sintered adequately with a 5°C/minute ramp from room temperature to a 1000°C 2 hour hold before a 5°C/minute ramp back to room temperature. The sintering operation was carried out in an atmosphere of Argon. Densities of 95% to 98% of theoretical were typical.

The typical morphology for Cu-Fe with the manufacturing method described above is shown for four different volume fractions in the optical microscope images below (Figure 47). The morphology is of the distributed spheres type.

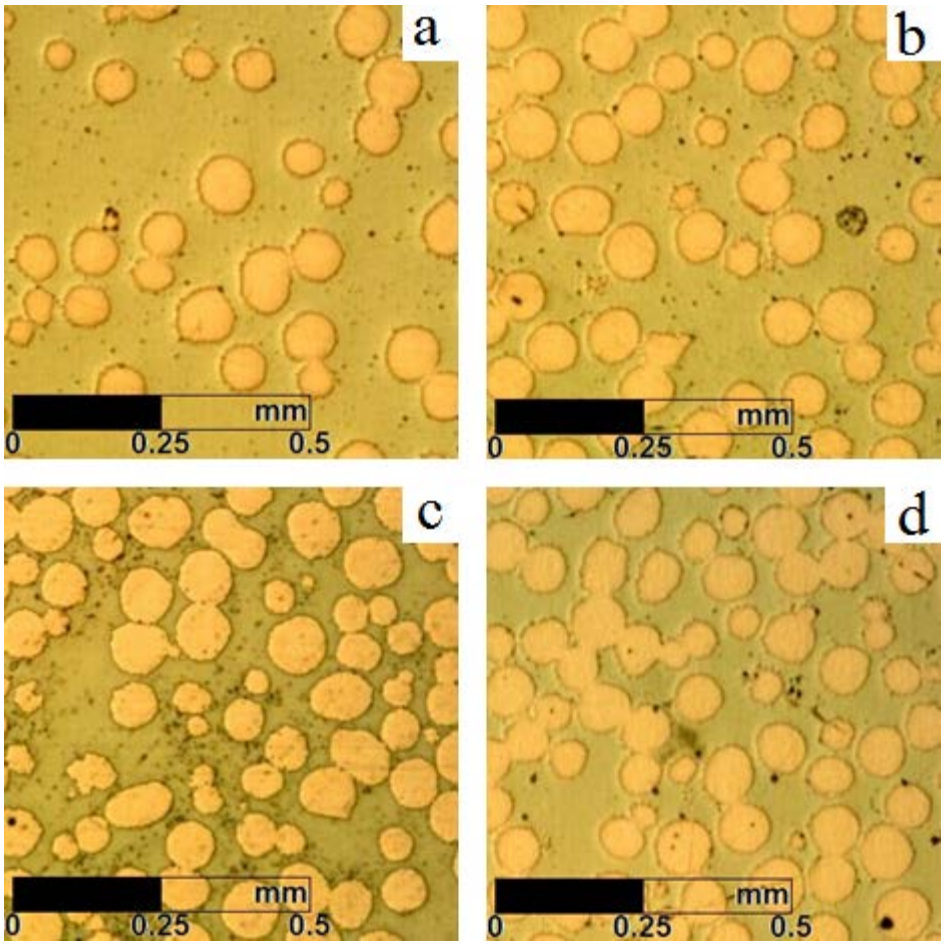

Figure 47 Optical microscope images of Cu-Fe Miscibility Gap Alloys with various volume fractions of copper. a) 20%, b) 40%, c) 50% and d) 60%. The light distributed phase is copper.

5.1.4. Manufacture of Magnesium-Iron Miscibility Gap Alloys

Magnesium-Iron Miscibility Gap Alloys were manufactured simply. An iron matrix was known to sinter well at 1000°C (from manufacture of Copper-Iron alloys). It was shown however that a much longer hold at the lower temperature of 600°C could adequately sinter this alloy. This hold temperature was below the melting point of magnesium (650°C) and hence the powder shape was preserved through sintering.

Iron powder of [-300] mesh was found to sinter well with [-200] magnesium powder. The powders were mixed by hand in atmosphere and pressed into pellets with a

pressure of 400 MPa. The Miscibility Gap Alloy sintered adequately with a 5°C/minute ramp from room temperature to a 600°C 10 hour hold before a 5°C/minute ramp back to room temperature. Sintering was carried out in an atmosphere of Argon. Densities of 95% to 98% theoretical were typical.

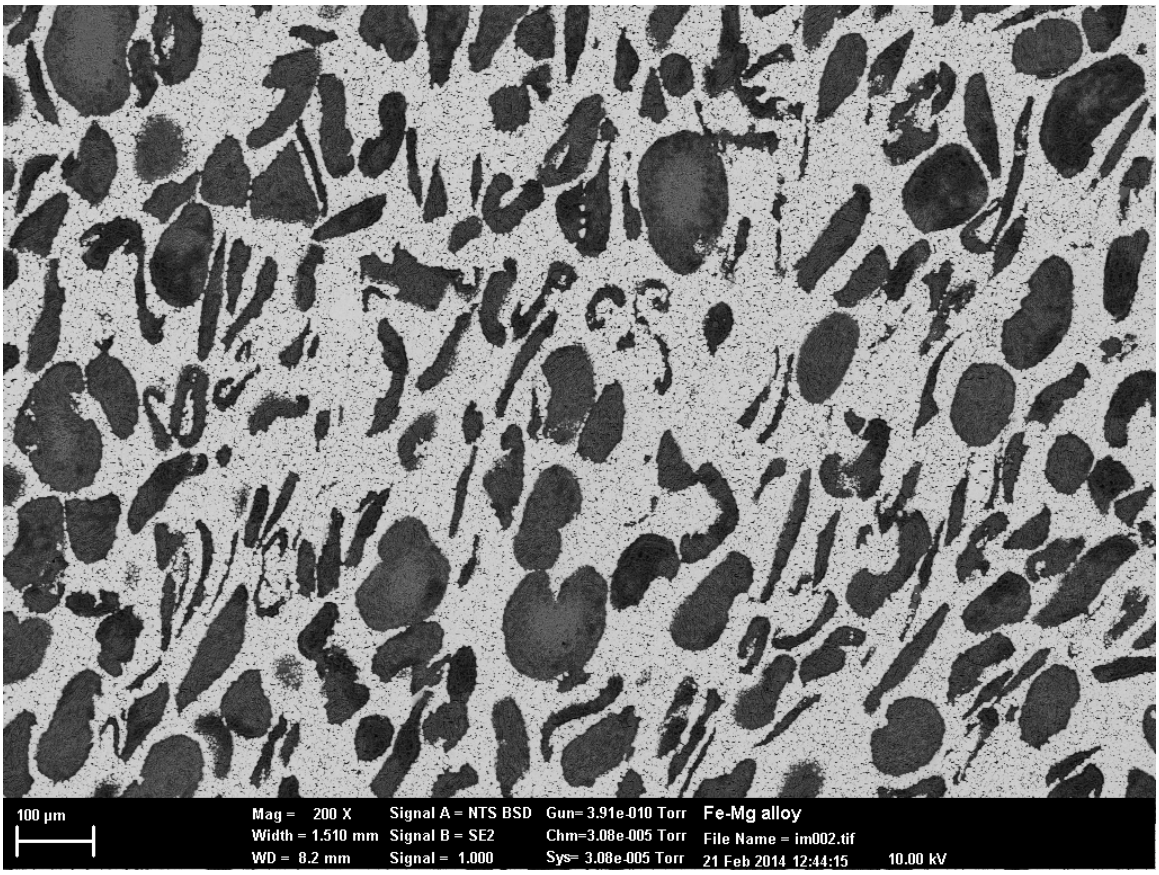

Figure 48 Back Scattered Electron Microscope image of Mg-Fe [29].

5.1.5. Manufacture of Silicon-Silicon Carbide Miscibility Gap Alloys

The current practise for manufacturing Silicon-Silicon Carbide MGAs was discovered by Mr. Peter Steel, a mechanical engineering undergraduate student of the University of Newcastle, Australia. The Author gratefully acknowledges Peter's contribution to the understanding of Miscibility Gap Alloy manufacture [114].

Silicon carbide is a very hard material and resists plastic deformation to a much greater degree than a metallic matrix. Thus the use of a binding agent was found to significantly improve the density of the samples. Peter Steel discovered that both the use of Sodium Silicate as a binder and additional free silicon and graphite to reaction bond the silicon carbide yielded higher density samples. Silicon carbide was combined with a mixture of graphite and silicon in a weight ratio of 3:1. The graphite and silicon mixture was mixed in a mortar and pestle at a 1:1 molar ratio (or 7:3 mass ratio). The Sodium Silicate binder was added to the matrix and silicon powders at a mass fraction of 0.3 and mixed by hand to a moist clumping mixture. This mixture was then pressed at 400 MPa. The green pellets were dried at 300 °C for 2 hours before being fired at 1440 °C under Argon for 2 hours. All heating and cooling ramps were at 5 °C/min. An example of the morphology is shown in Figure 49.

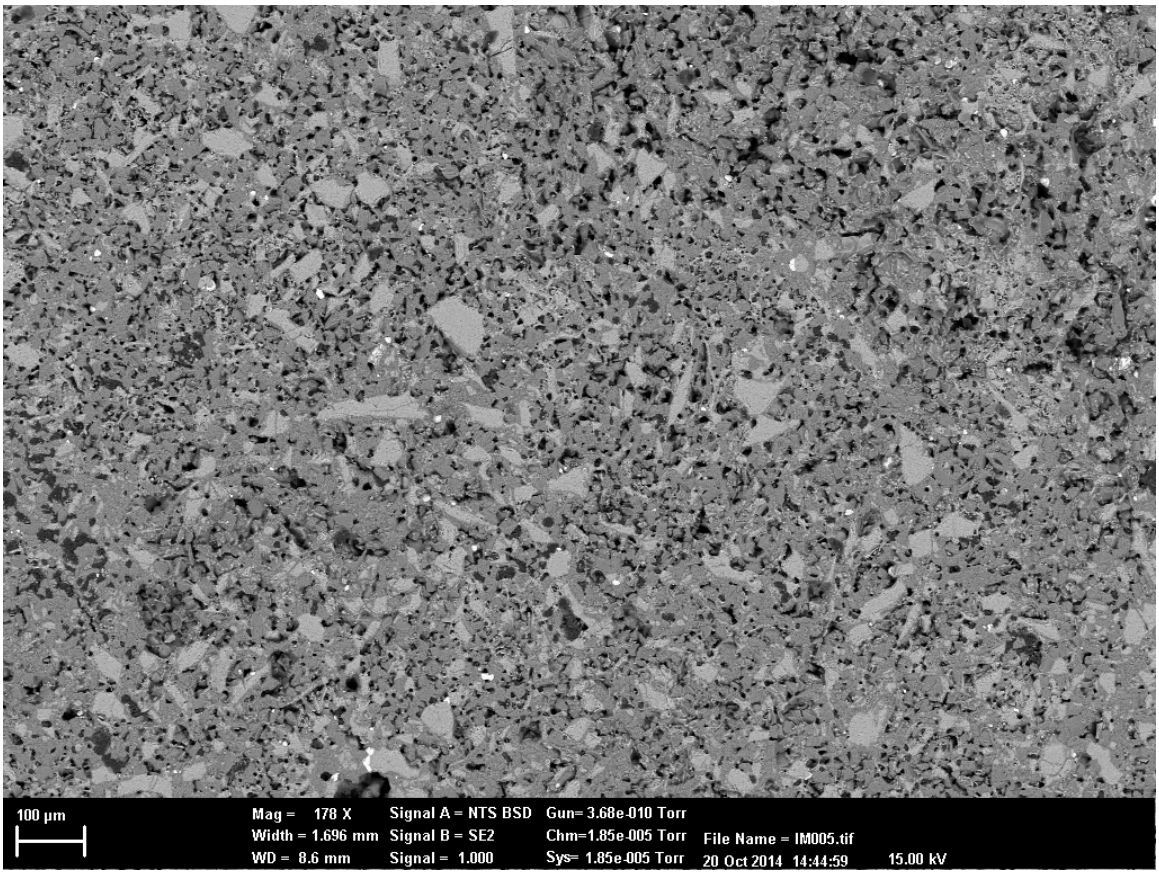

Figure 49 Back Scattered Electron Microscope image of Si-SiC system at 50% volume fraction [114]. The lighter phase is silicon whilst the darker phase is silicon carbide. Note the significant porosity (black phase) present throughout the sample.

5.1.6. Manufacture of Tin-Aluminium Miscibility Gap Alloys

Tin Aluminium samples were found to be simple to manufacture. Aluminium was found to consistently sinter above the melting temperature of tin. Leakage of tin was generally observed for tin volume fractions greater than 50%.

Aluminium powder (-400 mesh, <37 μm) was found to sinter well with -325 mesh (<44 μm) or 1mm tin shot when subjected to the following sintering conditions. Powders were mixed by hand in a mortar and pestle before being pressed into pellets with a pressure of 400 MPa. A 5°C/minute ramp from room temperature to a 500°C 2 hour hold before a 5°C/minute ramp down to room temperature was found to adequately sinter the Miscibility

Gap Alloy. The pellet was tightly wrapped in aluminium foil during sintering to minimise oxidation. Fully dense samples were consistently produced.

Morphologies for the Sn-Al system with various loadings of tin manufactured as described above are shown below in Figure 50. The morphologies could be either of a distributed particle or interstice filling type morphology (as described in §3.1.5)

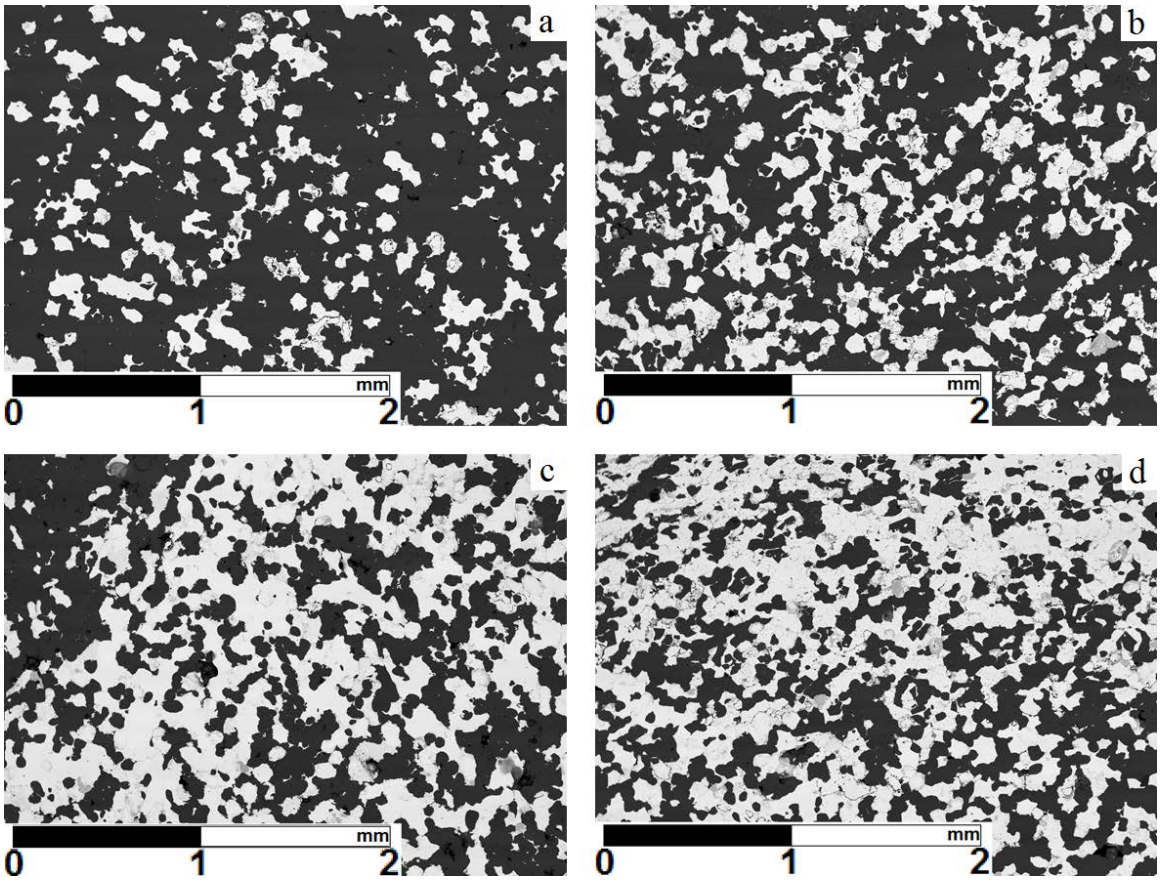

Figure 50 Scanning Electron Microscope images of Sn-Al Miscibility Gap Alloys with various volume fractions of tin. a) 20%, b) 40%, c) 50% and d) 60%. The lighter phase is Sn. Coarser Sn powder yielded better encapsulation of the Sn phase (see Figure 60 in §6.1).

It was found that aluminium crystals would form within the tin pockets when the samples were sintered at ~500 °C. These crystals were thought to grow upon thermal cycling and were the main motivation behind developing the growth-decay theory (introduced in §3.4.1 and undertaken in §6.1.1). The crystals were likely caused by the

increased solubility of Al in liquid Sn at the sintering temperature which subsequently nucleated when cooled. Figure 60 in §6.1 highlights the crystals in a Sn inclusion.

5.1.7. Manufacture of Zinc-Graphite Miscibility Gap Alloys

The current practise for manufacturing Zinc-Graphite MGAs was discovered by Ms. Melanie Jackson, a mechanical engineering student of the University of Newcastle. The Author gratefully acknowledges Melanie's contribution to the understanding of Miscibility Gap Alloy manufacture.

Graphite powder is combined with sodium silicate (8.9% Na_2O, 28.7% SiO_2, 62.4% H_2O mass) binder diluted with additional water (1:3 binder to water by mass) in an electric mixer for 30 seconds. Zinc powder is gradually mixed by hand into the binder and graphite mix. The entire mix is then blended for a further 30 seconds. The blended mixture is then pressed in a die to 84 MPa over a period of ~5 minutes. The green sample must then be dried at 80 °C until mass loss due to water evaporation ceases (~ 72 hours). The block is then surrounded in aluminium foil to achieve a low oxygen atmosphere and fired three times. The first firing is at 230 °C for 8 hours to remove any remaining water (this must proceed at the gentle heating rate of 2.5 °C/minute). The second firing is at 500 °C for 8 hours. The aluminium foil is then removed and the block surface cleaned before another firing at 500 °C for 8 hours. Zinc-Graphite samples were shown to achieve a consistent density of between 83.9% and 86% of theoretical.

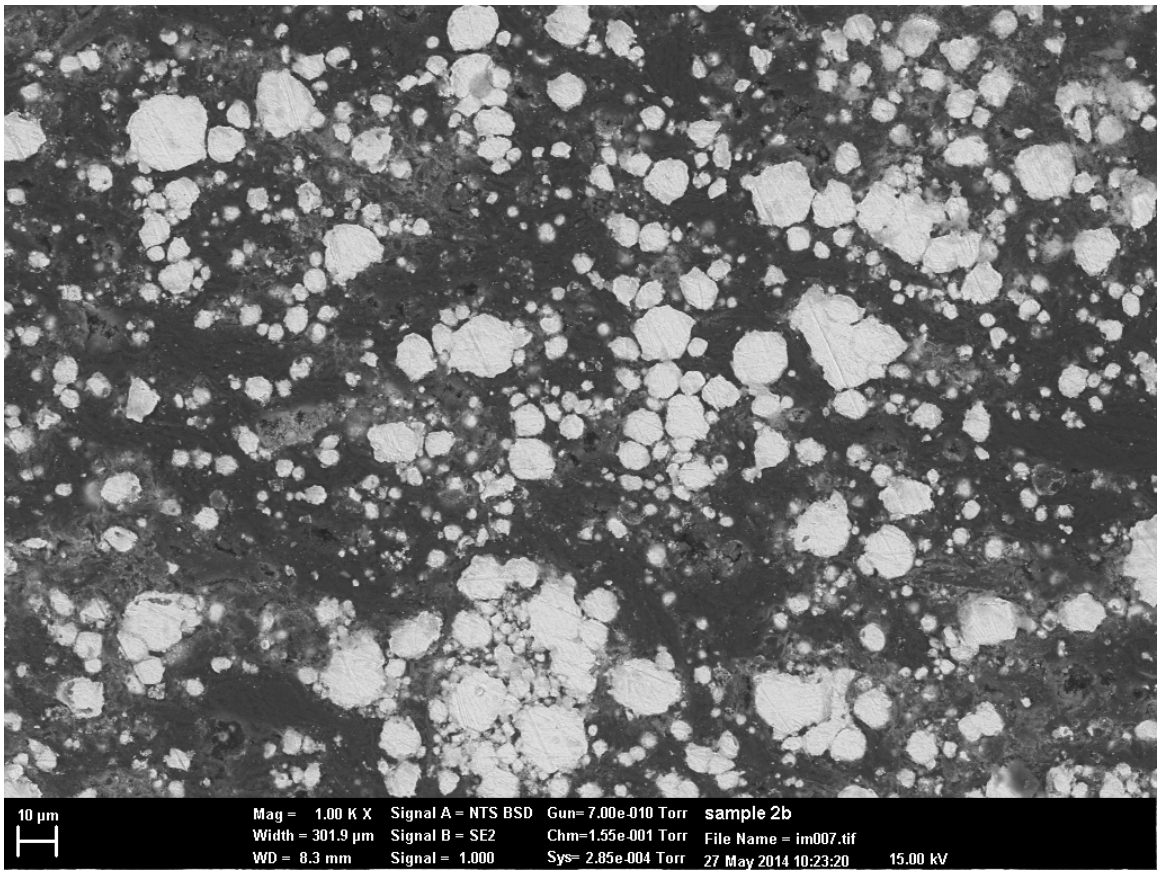

Figure 51 Back Scattered Electron Microscope image of Zn-C. The lighter phase is zinc, the darker phase is graphite.

5.1.8. Comparative Analysis of Manufacturing Methods

The manufacturing methods described in detail above are summarised in Table 6. These methods yield consistent results and require little specialised machinery. There exists significant scope for optimisation of manufacturing methods to minimise porosity, achieve high conductivity morphologies and prevent percolation through thermal cycling.

Table 6 Summary of manufacturing methods used in Miscibility Gap Alloy production in this thesis.

System	Distributed Powder Size [µm]	Matrix Powder Size [µm]	Binder	Mixing Method	Pressing Pressure [MPa]	Drying	Firing	Furnace Atmosphere
Brass-C	<200	<100	Sodium Silicate[1] 10% Mass	Mortar and Pestle	32	80 °C 72 hours, 250 °C 8 hours	500 °C 8 hours, 1100 °C 8 hours	Argon
Cu-C	<90	<100	Sodium Silicate[1] 10% Mass	Mortar and Pestle	32	80 °C 72 hours, 250 °C 8 hours	500 °C 8 hours, 1100 °C 8 hours	Argon
Cu-Fe	<90	<44	Nil	Mortar and Pestle	400	Nil	1000 °C 2 hours	Argon
Mg-Fe	<74	<44	Nil	Mortar and Pestle	400	Nil	600°C 10 hours	Argon
Si-SiC	<44	<100	Si+C[2] & Sodium Silicate[1] 10% Mass	Mortar and Pestle	400	300 °C 2 hours	1440 °C 2 hours	Argon
Sn-Al	<44	<37	Nil	Mortar and Pestle	400	Nil	500 °C 2 hours	Air
Zn-C	<44	<100	Sodium Silicate[3] 25% Mass	Electric Blender	84	80 °C 72 hours, 230 °C 8 hours	500 °C 8 hours, 500 °C 8 hours	Air

[1]8.9% Na_2O, 28.7% SiO_2, 62.4% H_2O mass

[2]Free silicon and graphite combined in 1:1 atomic or 3:7 mass to achieve reaction bonding

[3]2.2% Na_2O, 7.18% SiO_2, 90.6% H_2O mass

5.2. Discussion

The following section describes the influence of porosity and morphology on the homogeneous material properties of the alloys analysed.

5.2.1. Proportion of Theoretical Density

Brass-Graphite and Copper-Graphite Miscibility Gap Alloys were manufactured according to the methods developed by Bastien Monnier and Nathan Morton as described in §5.1.1-2. Densities of 90 to 95% theoretical were attained for alloys made using these methods.

Copper-Iron and Magnesium-Iron Miscibility Gap Alloys were found to be produced at 95 to 98% of theoretical density following the manufacturing methods outlined in the previous section. The malleability of the iron powder was thought to contribute to the very high density.

Following the manufacturing methods of Peter Steel samples at 71.8% of theoretical density was repeatable for a 50% volume fraction Si-SiC Miscibility Gap Alloy. This relatively low density is thought to be improvable with further study.

The manufacturing procedure described in §5.1.6 produced high quality Sn-Al samples. The density of these Miscibility Gap Alloys was essentially 100% of theoretical. The high malleability of the aluminium and tin powders is the main contributor to the extremely high density obtained.

Zinc-Graphite samples were shown to achieve a consistent density of between 83.9% and 86% of theoretical as seen through the work of Melanie Jackson. This relatively high porosity is a result of the drying process and decomposition process for the diluted Sodium Silicate binder. The gaseous species formed on decomposition leave pores in the

matrix. A consolidation step might be considered for these alloys if the matrix can maintain encapsulation and not fracture.

Table 7 summarises the proportion of theoretical density found for Miscibility Gap Alloys experimentally:

Table 7 Experimentally found percentage of theoretical density for Miscibility Gap Alloys discussed in this thesis.

System	Lower Limit [%]	Upper Limit [%]	Reference
Brass-Graphite	90	95	[112, 113]
Copper-Graphite	90	95	[112]
Copper-Iron	95	98	This work
Magnesium-Iron	95	98	This work
Silicon-Silicon Carbide	71.8	71.8	[114]
Tin-Aluminium	~100	~100	This work
Zinc-Graphite	83.9	86	[115]

Miscibility Gap Alloys involving metallic matrices were found to have the highest densities, whilst those involving graphite and silicon carbide were lower. Improvements in density are likely as the technology moves from the laboratory state to commercialisation. Sintered graphite and silicon carbide items are common in industry and achieve very high densities. Application of the hot pressing techniques used in industry would benefit the properties of Miscibility Gap Alloys involving these matrices.

5.2.2. Effective Conductivity

All systems analysed in detail through this thesis may be manufactured with a morphology representative of distributed spheres for the purpose of thermal conductivity homogenisation. Sn-Al manufactured with fine Sn and Al powder has shown a more percolating morphology. During manufacture for commercial use a coarser tin powder would be utilised with a finer aluminium powder to obtain the preferred distributed

morphology. The Maxwell-Eucken model is most appropriate for morphologies of this type.

The effective conductivity for volume fractions up to 50% averaged over the operating temperature range (50 °C either side of melting) are shown in Figure 52 and Figure 53. Over the volume fractions analysed the Sn-Al system is most conductive. The matrix constituent is high conductivity aluminium and forms a continuous chain for low volume fractions of tin. Copper based Miscibility Gap Alloys never see percolation of the distributed phase (nor would they be manufactured to as this destroys the Miscibility Gap Alloy Morphology). Thus even though one constituent has an extremely high conductivity, the poorer conductor completely encapsulates it.

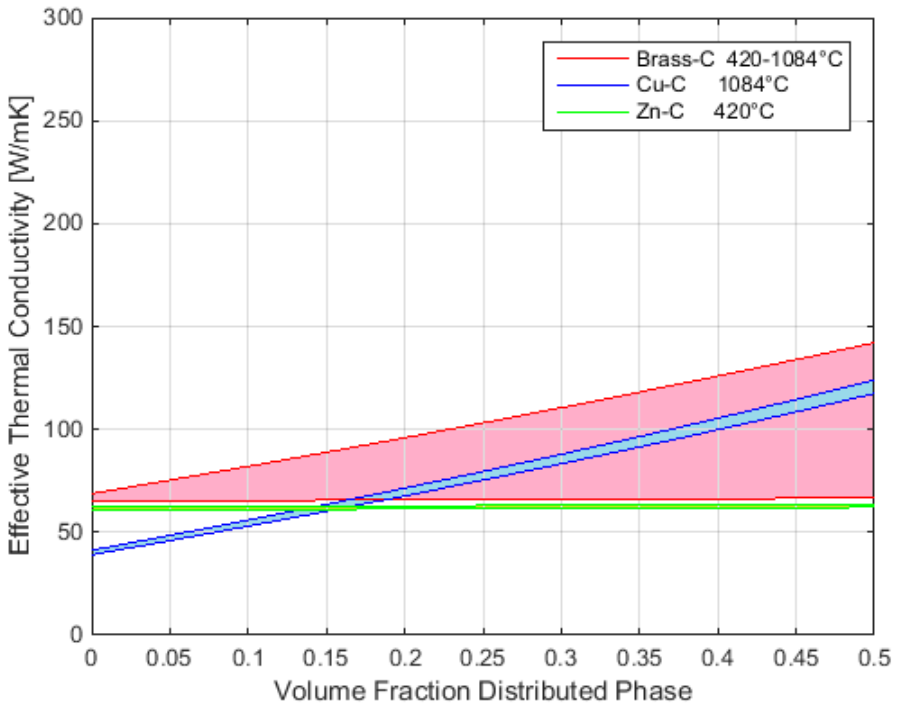

Figure 52 Effective conductivity ranges for Brass-C, Cu-C and Zn-C Miscibility Gap Alloys calculated with the Maxwell-Eucken model of equation 42.

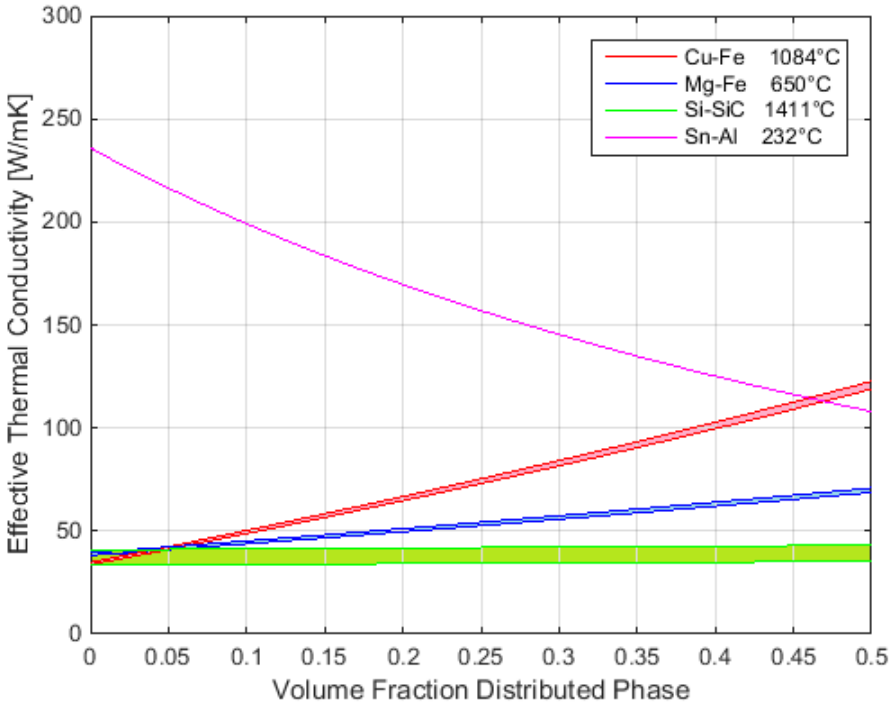

Figure 53 Effective conductivity ranges for Copper-Iron, Magnesium-Iron, Silicon-Silicon Carbide and Tin-Aluminium Miscibility Gap Alloys.

5.2.3. Energy Density

Energy density is calculated for a Miscibility Gap Alloy system with knowledge of the theoretical density and thermal properties of the constituents. Given that energy density relies only on equilibrium properties, the morphology of the alloy does not enter into calculations. The porosity determined through manufacturing experiments modifies the energy density.

The energy density for each system was calculated as a function of volume fraction for up to 50% of the fusible phase with upper and lower bounds according to the proportion of theoretical density described in the previous section. The ranges are plotted in Figure 54 and Figure 55. In each case sensible heating of 50 °C below and above the melting temperature is added to the latent heat. Sensible heat contributions to energy density were

found by integrating the heat capacity over the temperature range as described in §3.1.2. The average density over the 100 °C temperature range is utilised.

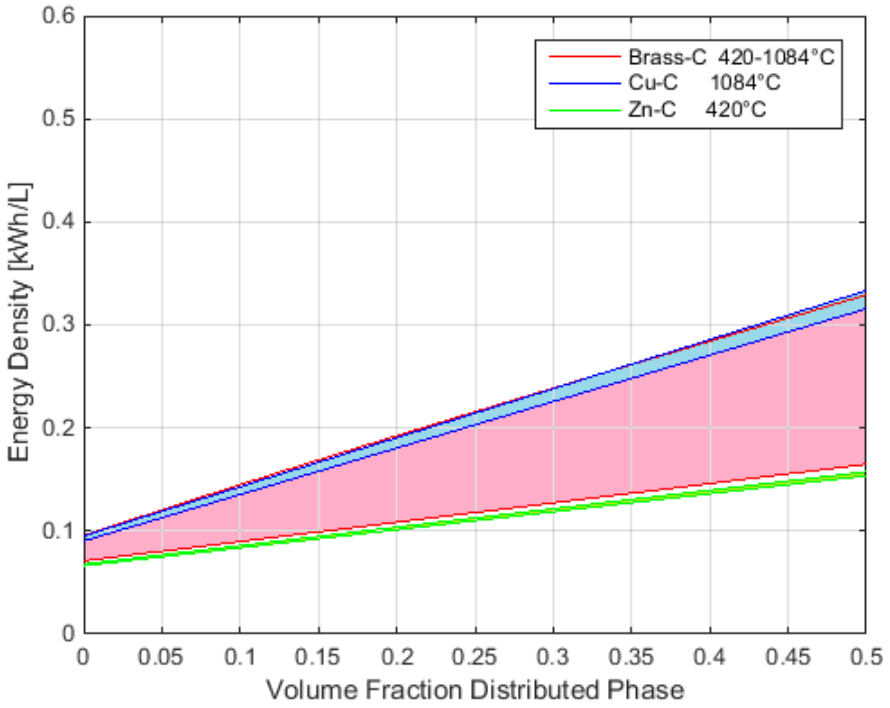

Figure 54 Porosity modified energy density range for Brass-Graphite, Copper-Graphite and Zinc-Graphite Miscibility Gap Alloys.

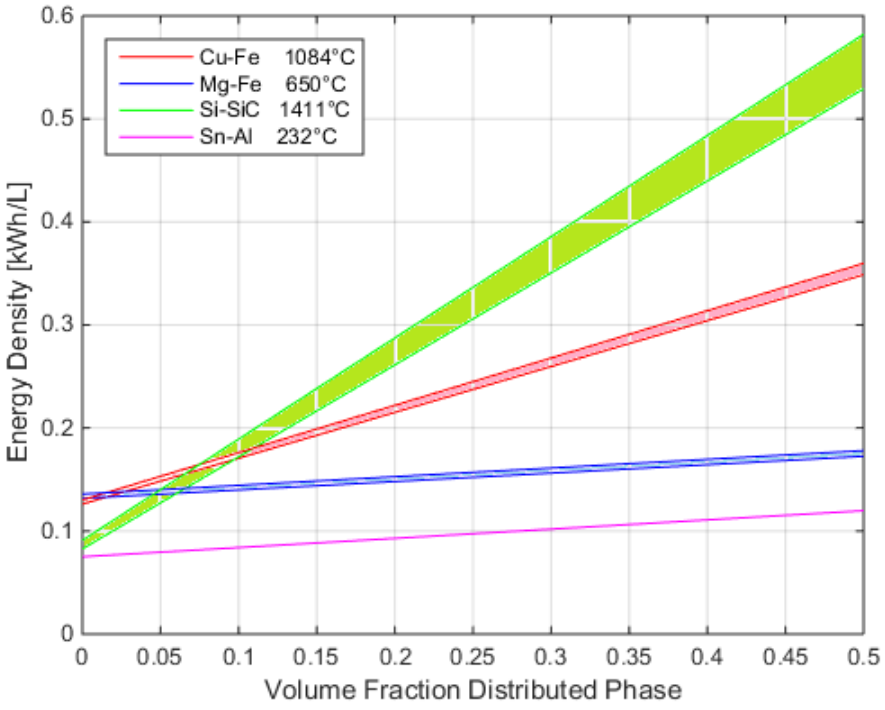

Figure 55 Porosity modified energy density range for Copper-Iron, Magnesium-Iron, Silicon-Silicon Carbide and Tin-Aluminium Miscibility Gap Alloys.

Of the Miscibility Gap Alloys discussed in this thesis, the most energy dense is Silicon-Silicon Carbide, followed by the copper and brass systems. Magnesium, zinc then tin systems follow in decreasing energy density. Silicon-Silicon Carbide was the most porous system yet still showed the greatest energy density for practical volume fractions. The ranges for the Brass-Graphite systems are significant, reflecting the variety of Brasses that can be utilised as a distributed phase. For the temperature amplitude of 50 °C and the systems studied all increased in energy density with volume fraction of the distributed phases.

Increased porosity involved in manufacturing the very hard Silicon Carbide matrix of Si-SiC does not decrease the energy density significantly. The very high heat of fusion of silicon is the main contributor to the high energy density of the system. Even at the current

modest level of manufacturing development for this system, this Miscibility Gap Alloy is still extremely energy dense.

The Brass-Graphite system has options for a variety of brasses that may be utilised as the distributed phase. For the purpose of brevity the heat capacity and heat of fusion of the intermediate phases on the Cu-Zn phase diagram have been linearly interpolated between pure copper and zinc. The bounds in this case do not just reflect uncertainty in the heat capacity, latent heat of fusion, density and porosity but extend from the lower bound of Zinc-Graphite to Copper-Graphite.

If the temperature amplitude of operation is significant then the sensible heat contribution to the energy density is also significant. If the matrix phase has a higher volumetric heat capacity than the distributed phase then it could be that increasing the volume fraction of distributed phase would not improve energy density. In the examples here with a temperature amplitude of 50 °C all of the Miscibility Gap Alloys discussed here improved in energy density with increasing volume fraction of the fusible phases.

To better quantify for the benefits of increased thermal conductivity, the energy density might be modified by the thermal effusivity of the system. Effusive energy density is simply the energy density multiplied by the thermal effusivity of the system. Thermal effusivity depends on both the equilibrium and transient thermal properties of the system and hence requires knowledge of the morphology. The effusivity in this thesis has been calculated with a homogenised conductivity using the Maxwell Eucken model of equation 42 with porosity taken into account.

In Figure 56 the nominal effusivity is plotted against energy density for a number of thermal storage materials. The chart indicates that Miscibility Gap Alloys achieve both a

high energy density and effusivity whilst salts, waxes and oils might achieve high energy density but are not very thermally effuse. This suggests that significant conductivity enhancing infrastructure will be required to charge and discharge the materials.

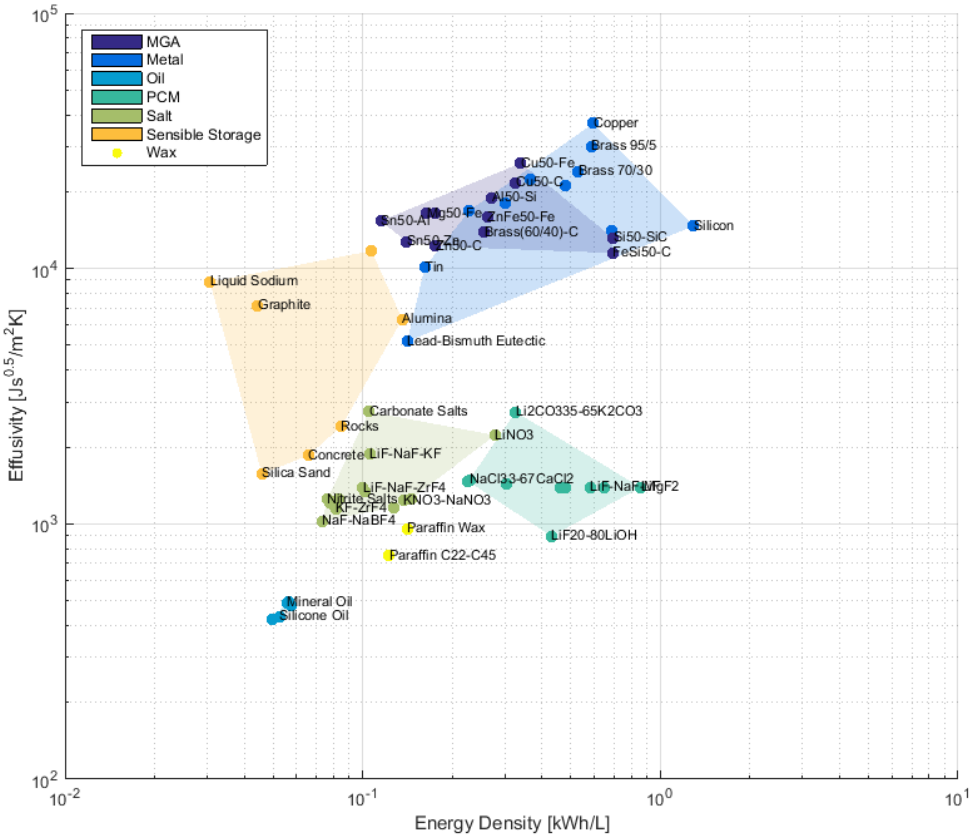

Figure 56 Effusivity plotted against energy density for a range of different thermal storage materials. Shaded regions represent the range typical for the set of materials.

As with energy density, effusive energy density depends on the distributed phase volume fraction in a Miscibility Gap Alloy. Figure 57 and Figure 58 show the range possible for each miscibility gap alloy over a range of volume fractions.

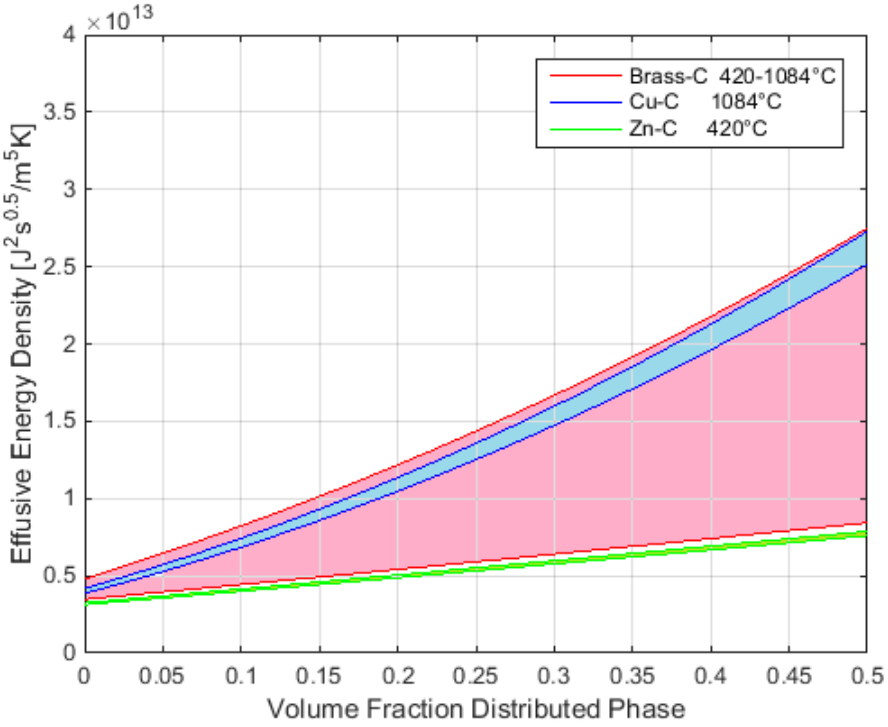

Figure 57 Effusive energy density for Brass-Graphite, Copper-Graphite and Zinc Graphite Miscibility Gap Alloys.

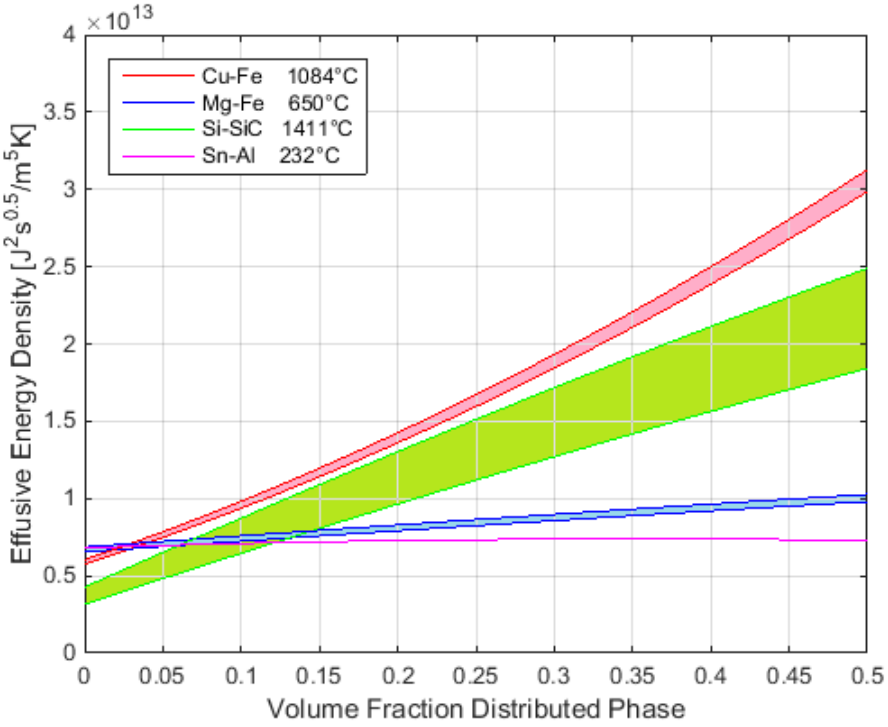

Figure 58 Effusive energy density for Copper-Iron, Magnesium-Iron, Silicon-Silicon Carbide and Tin-Aluminium Miscibility Gap Alloys.

Effusive energy density is highest for the Copper-Iron system, followed by the Silicon-Silicon Carbide system before Cu-C, Brass-C, Mg-Fe, Zn-C and Sn-Al. This is the same order as previously observed for unmodified energy density.

Effusive energy density shows both the benefits of high energy density and thermal effusivity through a single indicator. A high effusive energy density is achieved for a highly conductive and energy dense material. This is desirable for all thermal storage devices. Figure 59 plots the ranges of effusive energy density for a number of different thermal storage materials categorised as Miscibility Gap Alloys, Metals, Oils, Phase Change Materials, Salts, Sensible heat materials and Waxes.

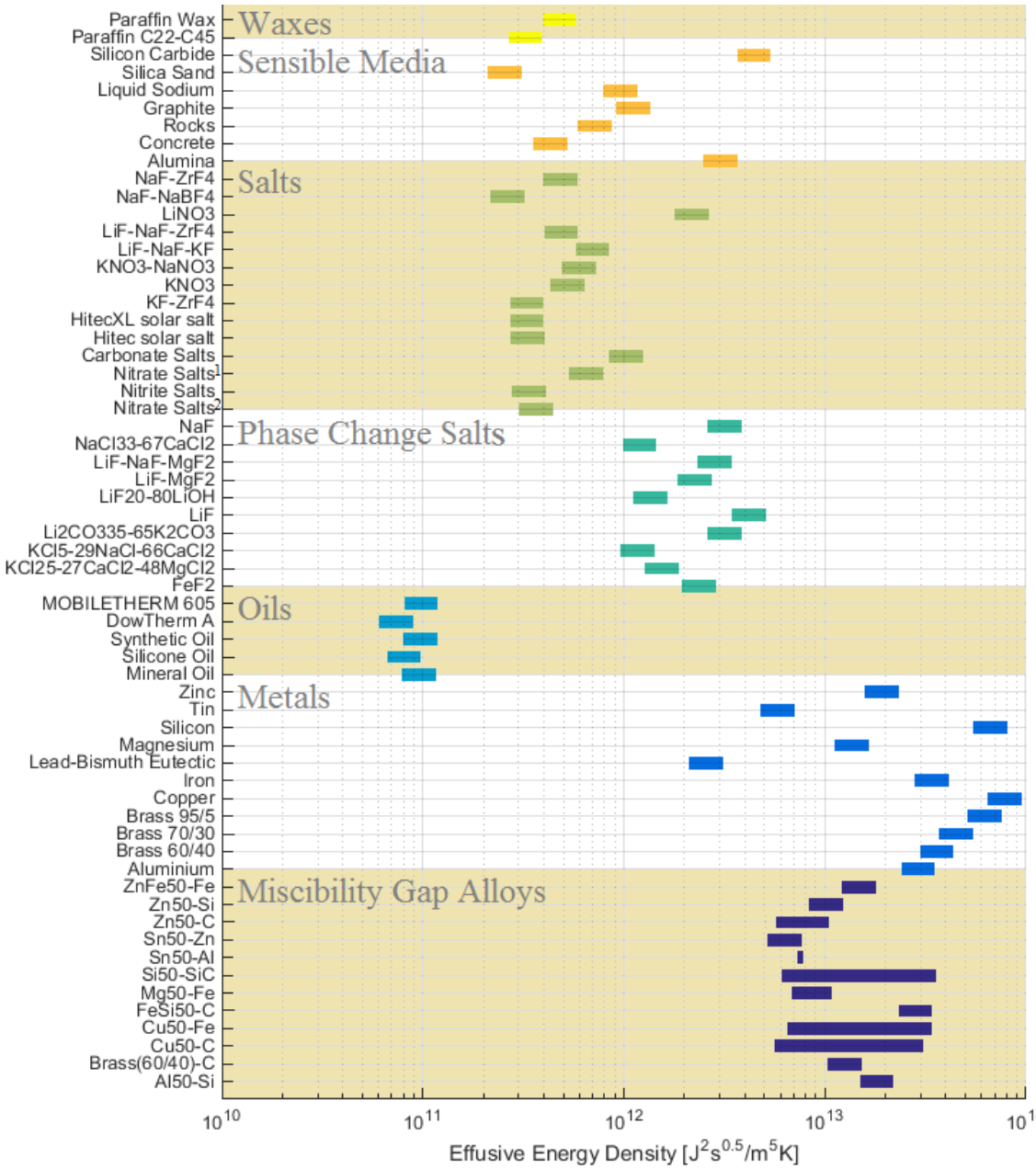

Figure 59 Ranges for effusive energy density of some common thermal storage materials. Uncertainty of 20 % was added to nominal values in literature. Miscibility Gap Alloy ranges span 0 to 50% volume fraction for alloys studied in this research.

The above chart shows that pure metals have the highest effusive energy density followed by Miscibility Gap Alloys, Phase Change Salts and some sensible heat media are next highest before waxes, salts and oils. The logarithmic horizontal axis is necessary for

plotting all the materials together but it must be noted that orders of magnitude differences exist between the materials. The best materials, pure metals, are difficult to implement in bulk due to unpredictable freezing kinetics and volume changes on phase transition. Miscibility Gap Alloys overcome these difficulties through having the fusible phase distributed as small particles within a rigid matrix that may deform to accommodate the melting/freezing transition. Of those analysed, Miscibility Gap Alloys are the most suitable group of materials for thermal storage when material properties are considered.

CHAPTER 6: LIFETIME ANALYSIS OF MISCIBILITY GAP ALLOYS

The lifetime of a Miscibility Gap Alloy refers to the number of thermal cycles it can undertake before becoming inoperable. An alloy may become inoperable through either percolation of the distributed phase or reaction of the constituent materials. The focus of the first section of this chapter is on how the systems may percolate through diffusion and mechanical effects. The second section describes the likelihood of chemical reactions occurring for the systems and how this may be prevented. The chapter concludes with a summary of the systems likely aging mechanism and lifetime prediction before discussing trends in aging mechanisms for future systems and the limitations of modelling.

6.1. Percolation Based Aging

A Miscibility Gap Alloy has a specific morphology where a lower melting temperature constituent is encapsulated by a higher melting temperature matrix. It has been observed experimentally that upon thermal cycling the Sn-Al and Cu-Fe systems form crystals of the matrix phase within the distributed phase (see Figure 60 and Figure 61). The mechanism behind this was thought to be due to diffusion of the matrix element, due to its relatively high solubility into the distributed liquid. The question as to whether these crystals would grow to force the liquid phase out as a shell (to eventually percolate) was of great interest for the lifetime of these alloys.

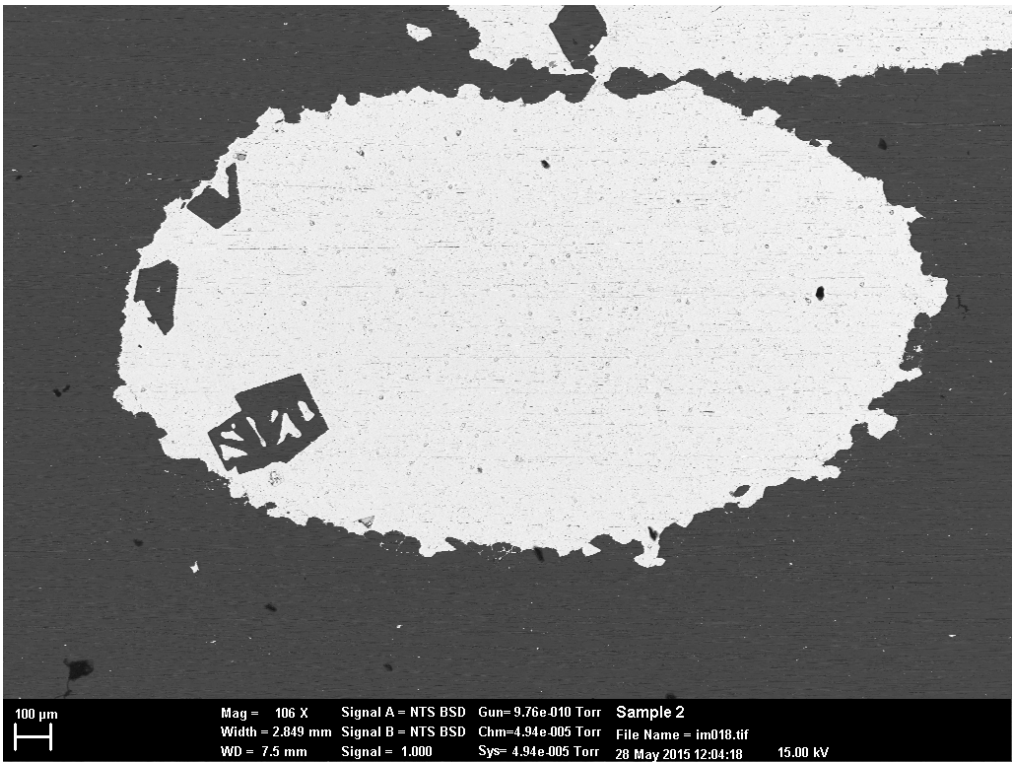

Figure 60 Back Scattered Electron image of aluminium crystals (darker phase) formed within a tin inclusion (lighter phase) after manufacturing at 500 °C.

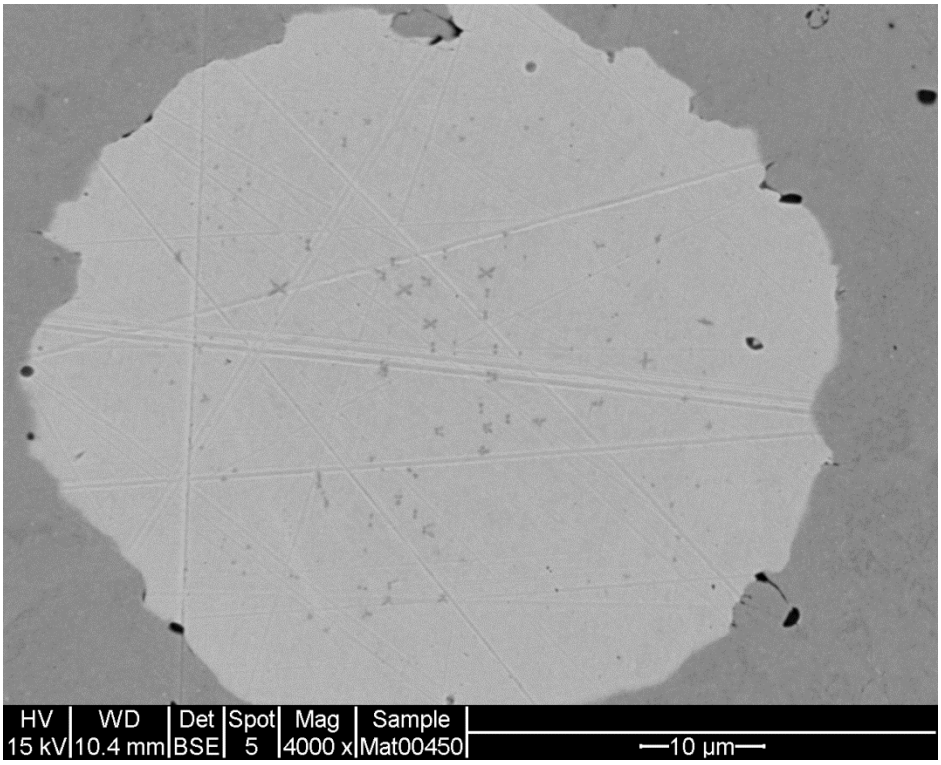

Figure 61 Back Scattered Electron image of iron (darker phase) crystallites forming in a copper (lighter phase) inclusion after heating above the melting temperature.

In contrast, crystals of graphite in the Brass-C, Cu-C and Zn-C systems were not observed experimentally. Similarly, the Fe-Mg and Si-SiC systems have not been seen to crystallise the matrix phase within the distributed phase. Comparison of the phase diagrams of these systems with those for Sn-Al and Cu-Fe indicates that the high equilibrium solubility of the liquid phase at the high operating temperature may be the cause. In Figure 62 below the phase diagrams of Sn-Al and Cu-Fe are compared with Cu-C which is typical of the graphite matrix systems.

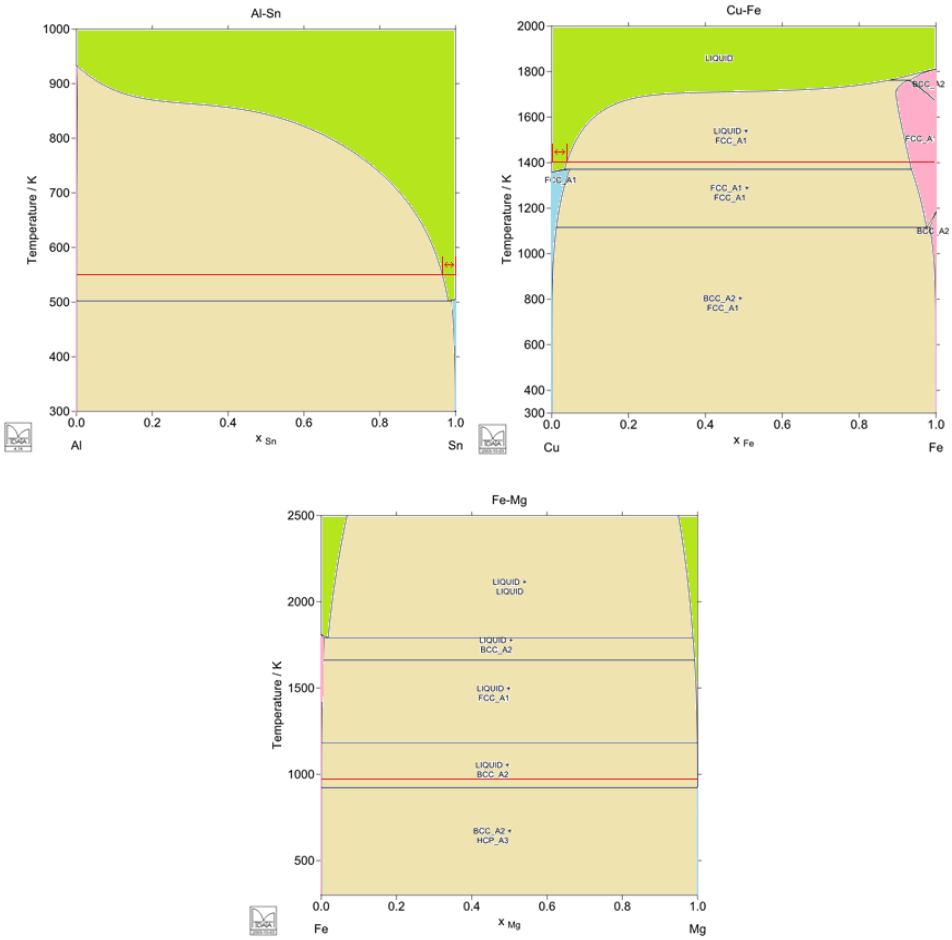

Figure 62 Coloured phase diagrams of Al-Cn, Cu-Fe and Fe-Mg. The red line indicates the highest operating temperature (50 °C above the melting temperature). Note the considerable solubility of the liquid phase in both the Sn-Al and Cu-Fe system when compared to the Mg-Fe system. Cu-Fe also displays considerable solubility of Cu in the Fe rich alpha phase.

At the high operating temperatures the Sn-Al and Cu-Fe systems have equilibrium solubility much higher than any of the other systems. The Cu-Fe system also shows a great deal of solubility of copper in the iron rich matrix phase. The following table describes the solubility at 10 and 50 °C above the melting temperature of the distributed phase in each system.

Table 8 Solubility of the liquid and high temperature alpha phase for each system 10 and 50 °C above the melting temperature.

System	Temperature Amplitude [°C]	High Operating Temperature [°C]	Solubility of A species in liquid [mol_A/mol_L]	Solubility of B species in solid alpha phase [mol_B/mol_α]
Cu-C	10	1095	$<8x10^{-6}$	[1]
	50	1135	$<8x10^{-6}$	[1]
Cu-Fe	10	1095	0.037	0.073
	50	1135	0.042	0.080
Mg-Fe	10	660	0.001	[1]
	50	700	0.001	[1]
Si-SiC	10	1424	$2.84x10^{-4}$	[1]
	50	1464	$3.97x10^{-4}$	[1]
Sn-Al	10	242	0.023	$5.11x10^{-5}$
	50	282	0.037	$1.05x10^{-4}$
Zn-C	10	430	[1]	[1]
	50	470	[1]	[1]

[1]Solubility is considered negligible.

The diffusion behaviour in the long term was modelled using the methods introduced in §3.4.1 for the Sn-Al and Cu-Fe systems. The remaining systems were not considered to experience considerable morphological changes through dissolution and deposition of the matrix phase.

6.1.1. Diffusion Modelling of the Sn-Al System

Tin-Aluminium binary alloys show non-negligible solubility of the beta and liquid phases about the melting temperature of tin (232 °C). The step change on melting beta phase acts to dissolve additional aluminium (~ 0.01 mol_{Al}/mol_β to ~ 0.02 mol_{Al}/mol_L at the

melting point). At very high temperatures the solubility of the liquid increases rapidly. The alpha phase is essentially pure aluminium for the temperature range of interest. The phase diagram is provided in Figure 63.

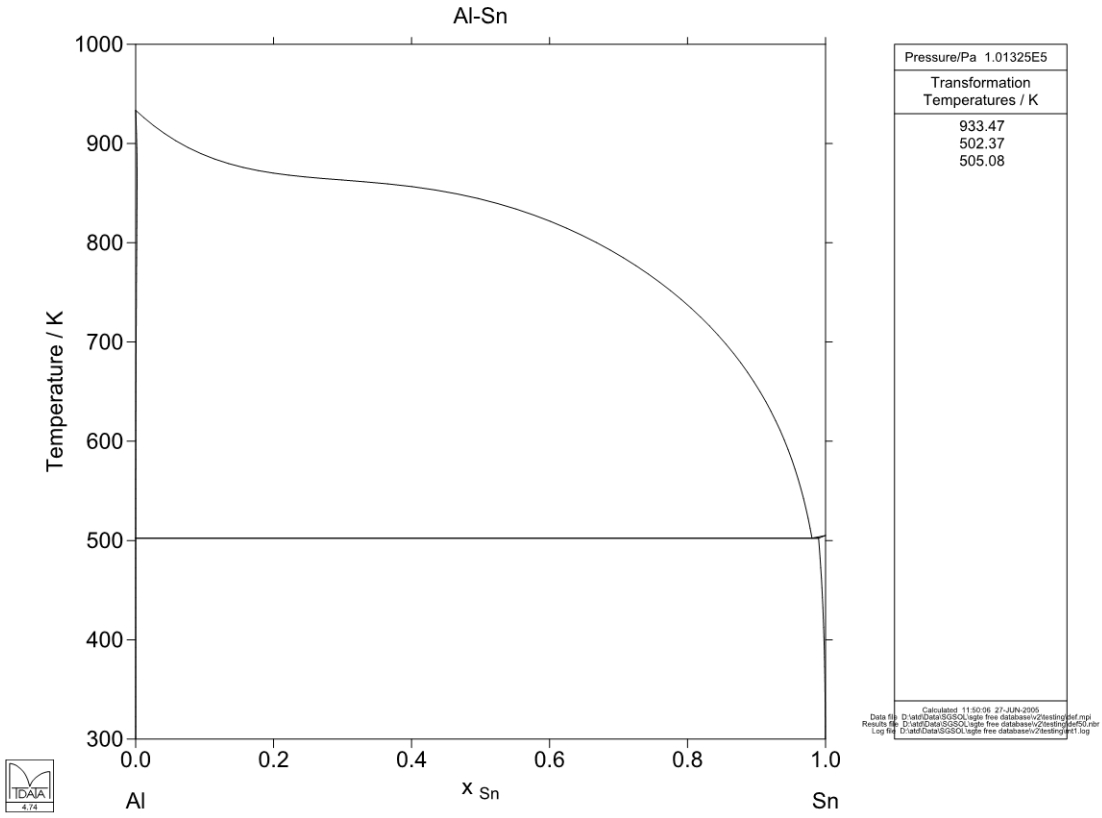

Figure 63 Phase Diagram for Sn-Al [116].

The Tin-Aluminium system shows a step change in solubility through freezing. The liquid is more soluble than the solid and hence when freezing excess aluminium may be trapped and will likely nucleate. The beta phase powder size (assumed constant), manufacturing and thermal cycling conditions under which nucleation and growth occurs is hence of prime importance.

Miscibility Gap Alloys composed of tin and aluminium have been successfully sintered under a range of temperatures. The lowest successful sintering operation was at

300 °C and sintering was regularly successful at 500 °C. These two temperatures form the bounds of interest for manufacturing simulation. Samples performed well with cooling rates from 0.2 °C/minute to quenching. Dendritic growth of alpha phase in the distributed beta phase was observed for quenched samples (Figure 64). Larger inclusions were evident for slower cooling rates. Cooling rates from manufacturing temperature to room temperature of 0.2 °C/min and 5°C/min are analysed.

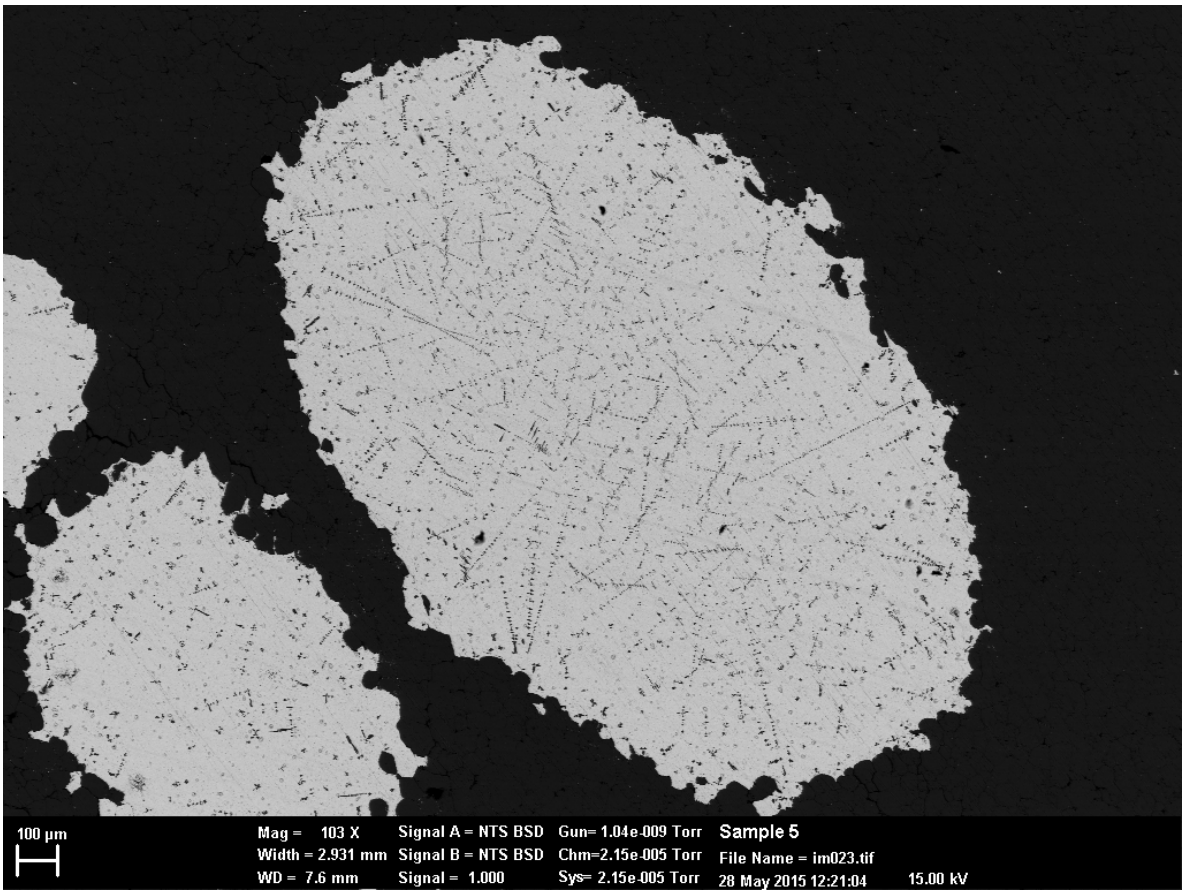

Figure 64 Dendritic aluminium crystals formed in tin pocket when quenched. The lighter phase is tin whilst the darker is aluminium.

Tin powders from 100 µm to 2 mm in radius are selected for the starting material. This is based on previous manufacture and the size to which the (ideally smaller) aluminium matrix powder can be obtained. Volume fractions of tin from 10 to 50% are inspected to cover the range below percolation in a Random Dense Packing arrangement of

spheres. Diurnal cycles with cooling and heating rates of 0.2 °C/minute are assumed for amplitudes about the melting point of 10 to 50 °C. The range of modelling parameters for growth-decay modelling are summarised in the table below:

Table 9 Range of parameters for Growth-Decay modelling of Sn-Al MGAs,

Property	Low Bound	High Bound	Units
Beta Phase Initial Radius	100	2000	μm
Volume Fraction	10	50	m^3_{Sn}/ m^3
Manufacturing Temperature	300	500	°C
Manufacturing Cooling Rate	0.2	0.2	°C/min
Operating Temperature Bounds	[222 – 242]	[182 – 282]	°C
Operating Heating/Cooling Rate	0.2	0.2	°C/min

The tracer diffusivities of tin and aluminium may be approximated with Arrhenius models for both self-diffusion and diffusion through the other constituent. The parameters utilised are shown in Table 10:

Table 10 Arrhenius parameters for Tracer Diffusion in Sn-Al systems

Solute	Solvent	D_0 Constant [cm^2/s]	Activation Energy [J/mol]	Reference
Tin	Solid Tin	$1.2x10^{-5}$	43 932	[117]
Tin	Liquid Tin	$22x10^{-5}$	19 121	[118]
Tin	Solid Aluminium	$4.5x10^{-5}$	114 500	[119]
Aluminium	Solid Tin	12.2	107 110	[120]
Aluminium	Liquid Tin	$1.9x10^{-3}$	21 757	[121]
Aluminium	Solid Aluminium	$2.2x10^{-4}$	144 400	[122]

A fixed surface energy of 1.143 J/m^2 for solid face centred cubic aluminium was presumed for analysis [103].

Manufacturing was simulated first in an attempt to determine whether the manufacturing conditions could be manipulated to prevent growth of nuclei. Heating the alloy above the melting temperature during sintering will create an excess of aluminium in the freezing beta phase. The beta phase may deposit the excess aluminium upon the matrix,

remain an unstable solid solution, or nucleate an alpha crystal. The size of the beta powder, the manufacturing temperature and the cooling rate were all seen to influence the behaviour. The composition behaviour for a 40[6], 100 and 500 μm radius powder during manufacturing is shown in Figure 65 for cooling rates of 0.2 and 5 °C/min.

During heating the tin rich beta phase reaches equilibrium with significant dissolved aluminium. The liquid is sufficiently diffuse for the powders analysed here to be at the equilibrium composition prior to freezing. Upon freezing, powders above 100 μm in radius nucleate an alpha crystal whilst those below are predicted to maintain an unstable solid solution to room temperature. The initial alpha nucleus radius is provided in Figure 66 (a) and (b) and shows that small nuclei will form for small powder sizes, low manufacturing temperatures and low cooling rates.

[6] The simulated 40 μm powder is likely to be challenging in manufacturing an effective Miscibility Gap Alloy but is of academic interest.

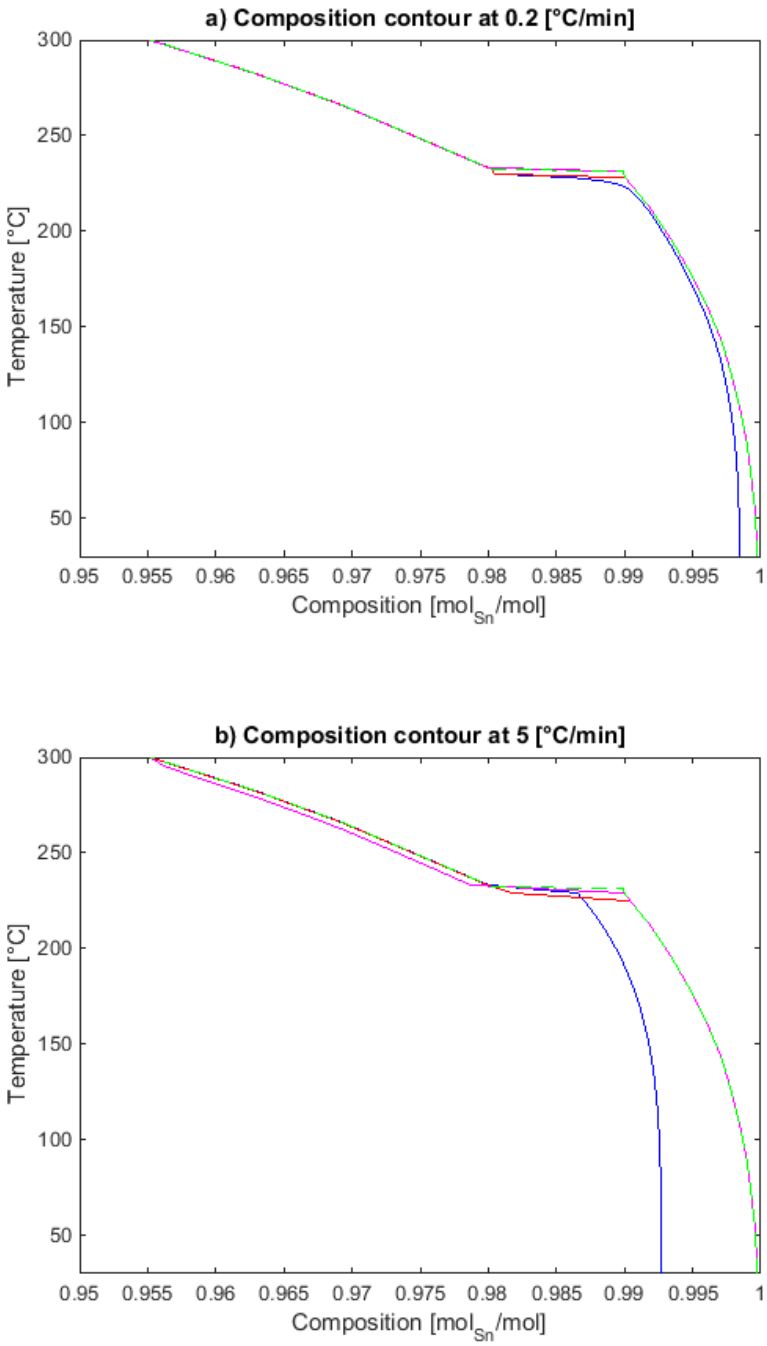

Figure 65 Composition contours for 40 (blue), 100 (red) and 500 (purple) µm radii powder undergoing a) 0.2 °C/min and b) 5 °C/min cooling rates. Note that the 40 µm powder is unable to nucleate internal alpha particles and is more unstable for higher cooling rates.

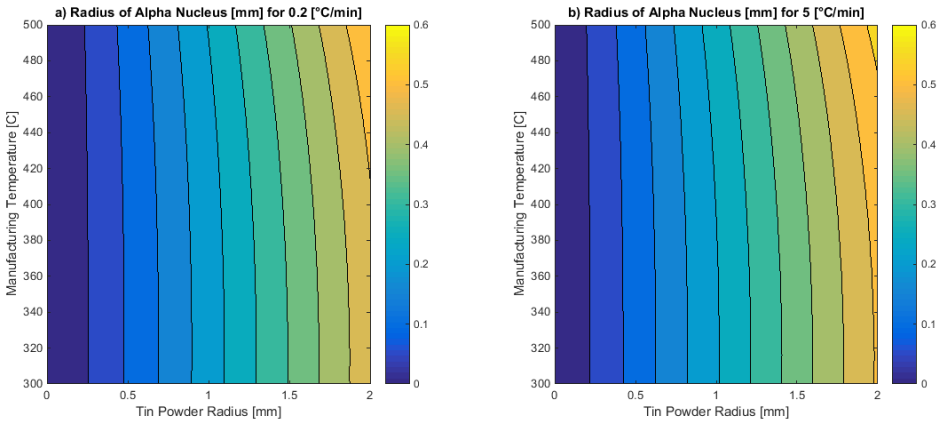

Figure 66 Simulation of manufacturing for Sn-Al Miscibility Gap Alloys. The radius of the alpha nucleus for a manufacturing temperature and tin powder size for 0.2 °C/min and 5 °C/min cooling rates.

Powder sizes below around 50 μm radius should not nucleate alpha phase for manufacturing temperatures below 500 °C and cooling rates slower than 5 °C. At this size the pocket is sufficiently small that a nucleus can't reach a stable size with the available dissolved material.

Thermal cycle modelling on the Sn-Al system revealed that growth and decay was dominated by the amplitude of the thermal cycle and the tin powder size. Increased amplitude resulted in a shorter lifetime as did increased tin powder radius. The initial size of the alpha nucleus had a very minor effect on the overall lifetime prediction. The composition and nucleus growth profiles for a typical thermal cycle at 100 μm and 500 μm radius powder are shown in Figure 67. The growth of the alpha nucleus is shown in Figure 68 for four different powder sizes and three different temperature amplitudes over many cycles.

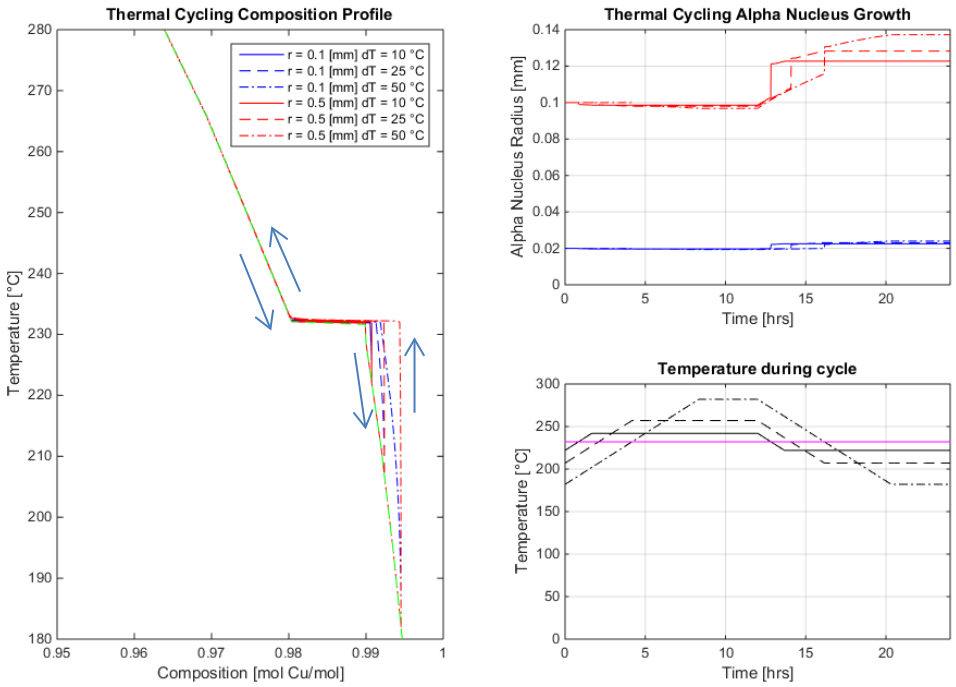

Figure 67 Composition and nucleus growth profiles for the Sn-Al system undergoing thermal cycles at 10, 25 and 50 °C temperature amplitudes. Note that smaller powder and amplitude result in a smaller increase in radius.

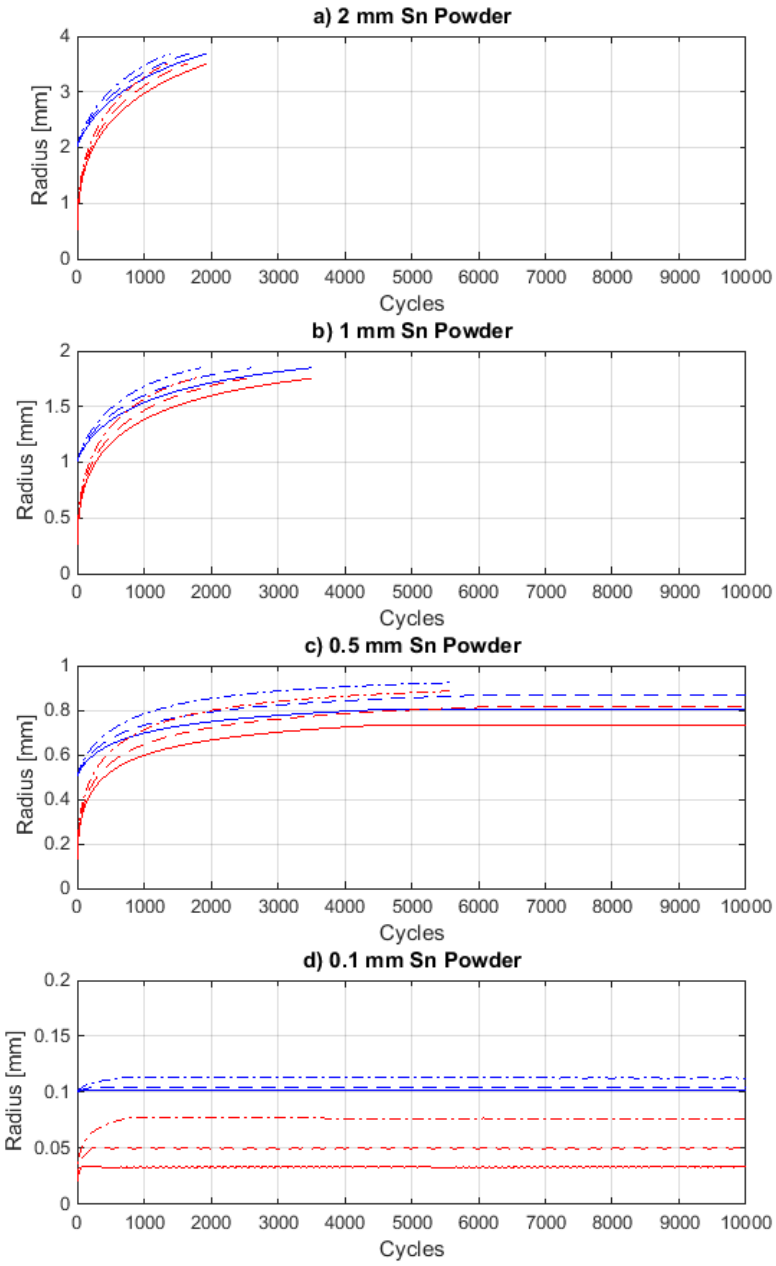

Figure 68 Unconstrained growth of the α nucleus for different powder sizes, cycle temperature amplitudes and manufacturing temperatures. The beta radius is represented by a blue line and the alpha radius by a red line. A solid line describes a 10 °C amplitude, a dashed line 25 °C and a dot-dash line 50 °C.

The cycle at which the beta radius exceeds the percolation threshold for a volume fraction and packing distribution describes the lifetime. For a packing distribution and an initial beta radius the lifetime as a function of volume fraction was found to be well described by an equation of the form:

$$N_{failure}(\varphi)=ae^{-b\varphi}+ce^{-d\varphi} \quad 104.$$

Where a, b, c and d are positive parameters that depend on the initial tin powder size and thermal cycle. No strong dependence on manufacturing temperature was found in the range analysed.

As the volume fraction approaches zero, cycles to failure approaches infinity whilst at the threshold of 0.63, all systems percolate instantly (the Sn powder is percolating after manufacture). The parameters for Sn-Al and random dense packing are shown below in Table 11. Where the alpha nucleus was found to not form or to not cause inversion in under 10000 cycles, the above equation is no longer relevant and the parameters are not provided in the table.

Table 11 Parameters to suit equation 103 describing the cycles to failure for different volume fractions. [1] For volume fractions of Sn below 50% and random dense packing these systems have a predicted lifetime greater than 10 000 cycles (~27 years).

Initial Tin Powder Radius [μm]	Thermal Cycle Amplitude [°C]	a [Cycles]	b [diml]	c [Cycles]	d [diml]
100	10	N/A[1]	N/A[1]	N/A[1]	N/A[1]
100	25	N/A[1]	N/A[1]	N/A[1]	N/A[1]
100	50	N/A[1]	N/A[1]	N/A[1]	N/A[1]
500	10	8321	9.45	994 741	38.07
500	25	6386	9.53	1 300 904	46.62
500	50	4306	9.37	1 102 917	55.75
1000	10	5602	9.60	715 417	59.80
1000	25	3935	9.01	466 166	58.28
1000	50	2906	8.71	419 302	61.69
2000	10	3218	8.16	52 331	43.79
2000	25	3326	8.89	384 774	68.96
2000	50	2328	8.15	105 881	53.56

The cycles to failure for 10, 25 and 50% volume fraction Sn-Al at different tin powder size are shown below in Figure 69. It can be seen that greater amplitude on thermal cycling and greater volume fraction results in lower lifetimes. Reducing the tin Powder size results in greater lifetime (theoretically infinite).

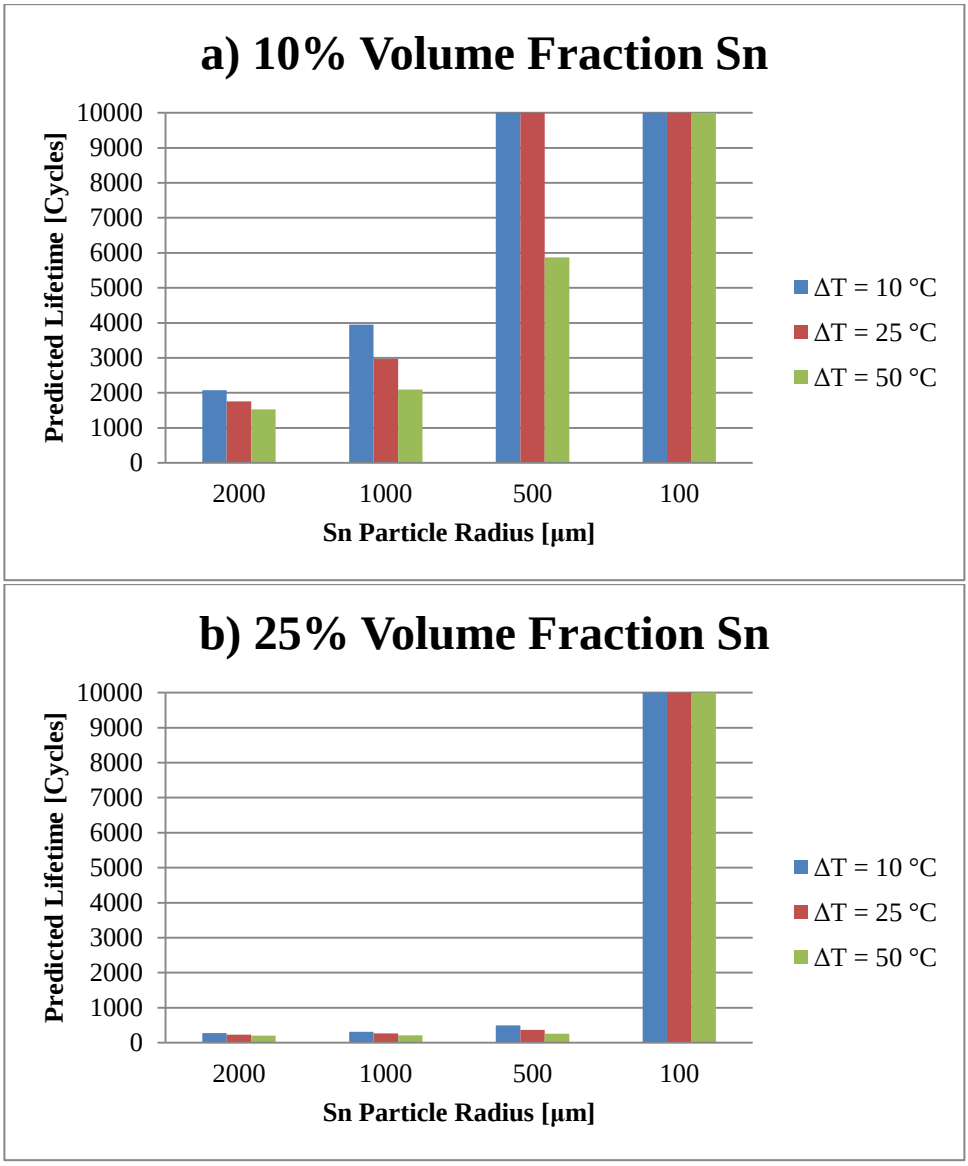

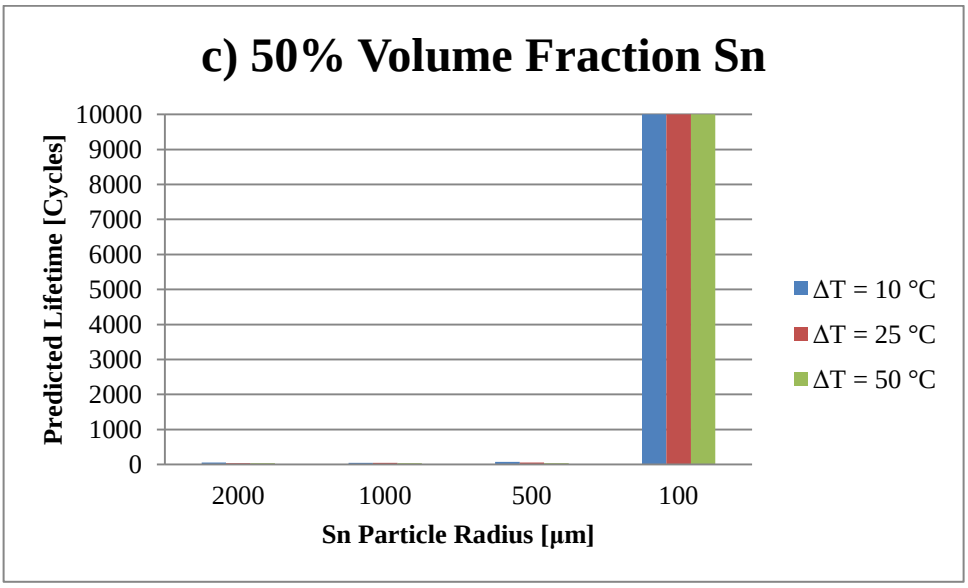

Figure 69 Cycles to failure for the Sn-Al system with different Sn Powder Radius and thermal cycle amplitude for: a) 10%, b) 25% and c) 50% volume fraction of Sn.

Under the set of computational assumptions made in this work, the relatively large decrease in solubility upon freezing repeatedly results in an excess of aluminium in the beta phase which can limit the lifetime of Miscibility Gap Alloys formed with large Sn particles. Even for very slow cooling rates and low thermal cycle amplitudes the material that must crystallise is still significant. Only for very small powders will the system not percolate in under 20 years of diurnal cycles. Therefore prior to the acquisition of experimental thermal cycling data, it is recommended that a powder size of less than 200 µm in diameter (> 80 Mesh) be utilised in Sn-Al Miscibility Gap Alloys.

6.1.2. Diffusion Modelling of the Cu-Fe System

The Copper-Iron system shows considerable solubility near the melting temperature of pure copper. A phase diagram describing this behaviour is provided in Figure 70. Prior to melting two fcc solid solutions are stable with saturation compositions of ~ 95.5% Cu (or 4.5% Fe) and 6.5% Cu molar fraction. Above the melting temperature a copper rich liquid

exists with a saturation composition of 96.6% Cu (or 3.4% Fe) and the previous fcc solid solution. The step change upon melting acts to reject iron from the liquid solution. The solubility then increases again with temperature, 10 °C above melting shows a solid phase of γ Fe (~7.3% Cu) and a copper rich liquid phase (~93% Cu). Due to the retrograde solubility between the eutectic and the solid beta phase (Cu rich) and the relatively large solubility of copper in the iron rich phase the cycling conditions will have a large impact on the growth of any alpha crystals within the beta pocket.

The significant solubility of copper in the iron rich face centred cubic phase around the melting temperature presents a constraint in the selection of volume fraction. For volume fractions below ~ 9.2% (equivalent to 7.3% Cu molar fraction) the matrix is capable of dissolving the entirety of the copper. This occurs only 10 °C above the melting temperature. Upon cooling the saturated alpha phase, copper will be rejected as beta phase crystals within the matrix, likely in a high energy region like an interface or grain boundary. The unpredictability of how the beta phase will be redistributed suggests that these low volume fractions should be avoided in manufacture.

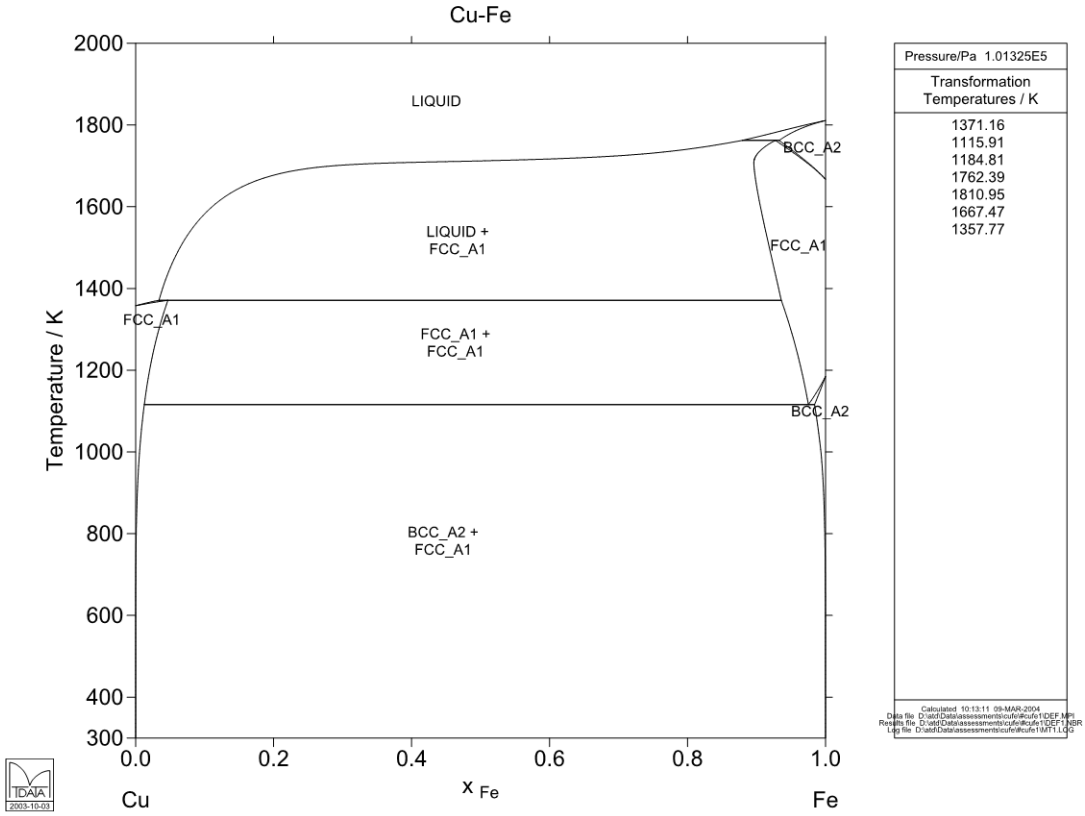

Figure 70 Phase Diagram for Cu-Fe [116].

Manufacturing conditions of the Cu-Fe Miscibility Gap Alloys are less extreme than the operating temperatures. They have been successfully sintered with temperatures of 600 to 1000 °C (this is below the melting temperature of Cu at 1085 °C) and holds of 2 hours. These temperatures form the bounds of interest for manufacturing simulation. Samples performed well with cooling rates from 0.2 °C/min to quenching. Cooling rates of 0.2 °C/min to 5 °C/min are analysed.

Diffusion modelling used copper powder from 100 μm to 2 mm in radius for the starting material. This is based on previous manufacture and the size to which the (ideally smaller) iron matrix powder can be obtained. Volume fractions of copper from 10 to 50%

are analysed during cycling. Diurnal cycles with cooling and heating rates of 0.2 °C/minute are assumed for amplitudes about the melting point of 10 to 50 °C. Modelling parameters for this range of growth-decay modelling are summarised in Table 12:

Table 12 Range of parameters for Growth-Decay modelling of Cu-Fe MGAs,

Property	Low Bound	High Bound	Units
Beta Phase Initial Radius	100	2000	μm
Volume Fraction	10	50	m^3_{Sn}/ m^3
Manufacturing Temperature	600	1000	°C
Manufacturing Heating Rate	0.2	0.2	°C/min
High Temperature Hold	120	120	min
Manufacturing Cooling Rate	0.2	5	°C/min
Operating Temperature Bounds	[1075 – 1095]	[1035 –1135]	°C
Operating Heating/Cooling Rate	0.2	0.2	°C/min

The tracer diffusivities of copper and iron are approximated with an Arrhenius function for both self-diffusion and diffusion through the other constituent. Only bulk diffusivities are considered in the model. The parameters utilised are shown in Table 13:

Table 13 Arrhenius parameters for Tracer Diffusion in Cu-Fe systems. Pure solid α iron is Body Centred Cubic and ferromagnetic to the Curie temperature at 771 °C before becoming paramagnetic, above 912 °C the Face Centre Cubic γ phase is stable.

Solute	Solvent	Constant [cm^2/s]	Activation Energy [J/mol]	Reference
Copper	Solid Copper	0.78	211 292	[123]
Copper	Liquid Copper	$1.46x10^{-3}$	40 627	[123]
Copper	Solid Iron (α ferromagnetic)	0.47	244 262	[124]
Copper	Solid Iron (α paramagnetic)	0.57	238 488	[124]
Copper	Solid Iron (γ)	0.19	272 378	[125]
Iron	Solid Copper	1.01	213 175	[126]
Iron	Liquid Copper	$3.5x10^{-3}$	51 630	[126]
Iron	Solid Iron (α ferromagnetic)	2.0	251 040	[127]
Iron	Solid Iron (α paramagnetic)	1.9	239 325	[127]
Iron	Solid Iron (γ)	0.18	269 868	[127]

A fixed surface energy of 2.41 J/m^2 for solid body centred cubic iron (α) was utilised [103].

The size of the nucleus upon manufacturing for the Copper-Iron system was calculated using the methods of §3.4.1 starting from materials at equilibrium. The particular

powder size and manufacturing temperature had an impact on the size of the nucleus formed initially. Cooling rate also had a strong influence on the size of the nucleus. Below are charts (Figure 71) showing the composition of the beta phase through manufacturing cycles with 40[7], 100 and 500 μm powder, various manufacturing temperatures and 0.2 °C/min and 5 °C/min cooling rates. Figure 72 shows the radius of the alpha nucleus for two cooling rates and a variety of manufacturing temperatures and powder sizes.

[7] Again the 40 μm case is challenging to machine but presents an interesting case in terms of kinetics.

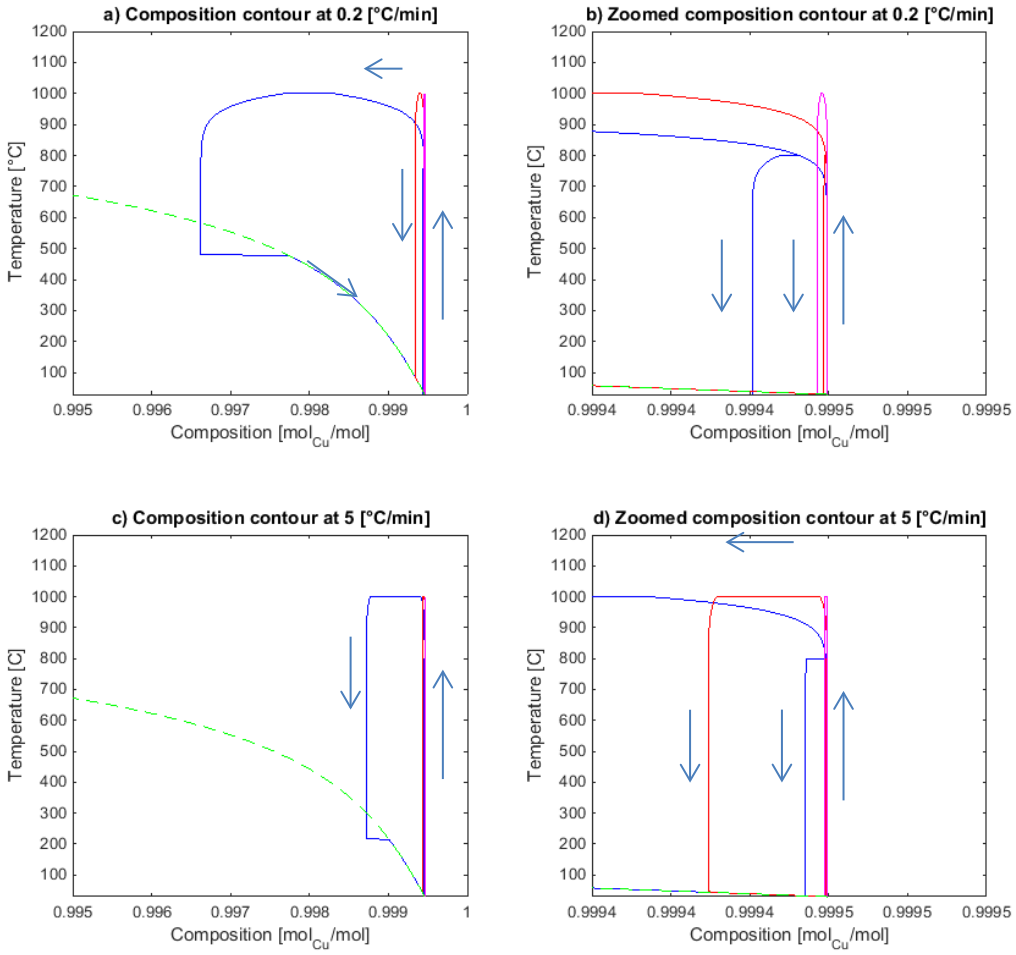

Figure 71 Composition plots of manufacturing Cu-Fe from equilibrium materials. The green dashed line is the phase boundary, the blue line is 40 µm radius powder, the red line is 100 µm radius powder and the magenta line is 500 µm radius powder. a) Show the contour for 0.2 °C/min whilst b) is zoomed to observe the contour at lower manufacturing temperatures. c) Show the contour for 5 °C/min whilst d) is again zoomed to observe the contour at lower manufacturing temperatures.

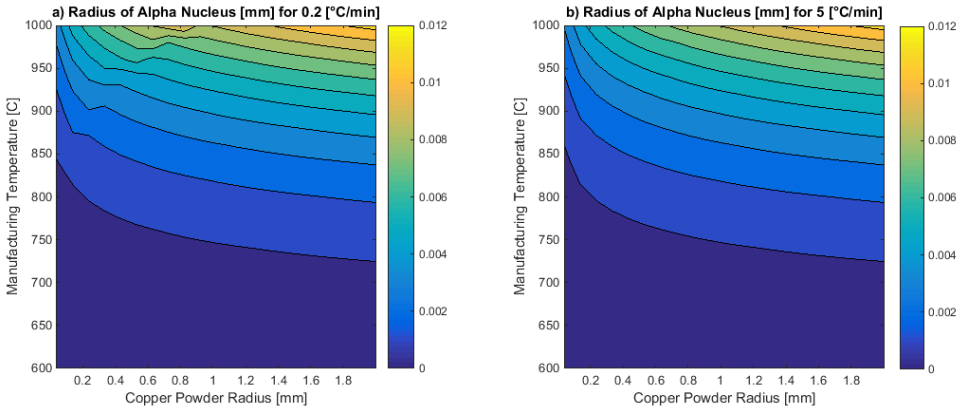

Figure 72 Simulation of manufacturing for Cu-Fe Miscibility Gap Alloys. The radius of the alpha nucleus for a manufacturing temperature and copper powder size for a) 0.2 °C/min and b) 5 °C/min cooling rates in mm.

Larger powder sizes led to greater nuclei size as did higher manufacturing temperatures. The nuclei size were much smaller than those formed in the Sn-Al system. This is due to the manufacturing conditions being below the copper melting temperature of 1085 °C. Even for small powders, the diffusivity is so low that the beta phase cannot achieve equilibrium. Upon cooling to the two phase boundary only a small amount of iron must be rejected.

Thermal Cycle modelling on the Cu-Fe system revealed the influence of retrograde solubility on melting beta phase and the high solubility of copper in the Alpha phase. The manufacturing temperature of the system (and hence the initial iron nucleus size) had little influence on the evolution, however the powder size and the temperature amplitude during cycling had significant effect. The composition and nucleus growth profiles for a typical thermal cycle at 100 μm and 500 μm radius powder are shown in Figure 73. The evolution of the beta and alpha phase radii are shown in Figure 74.

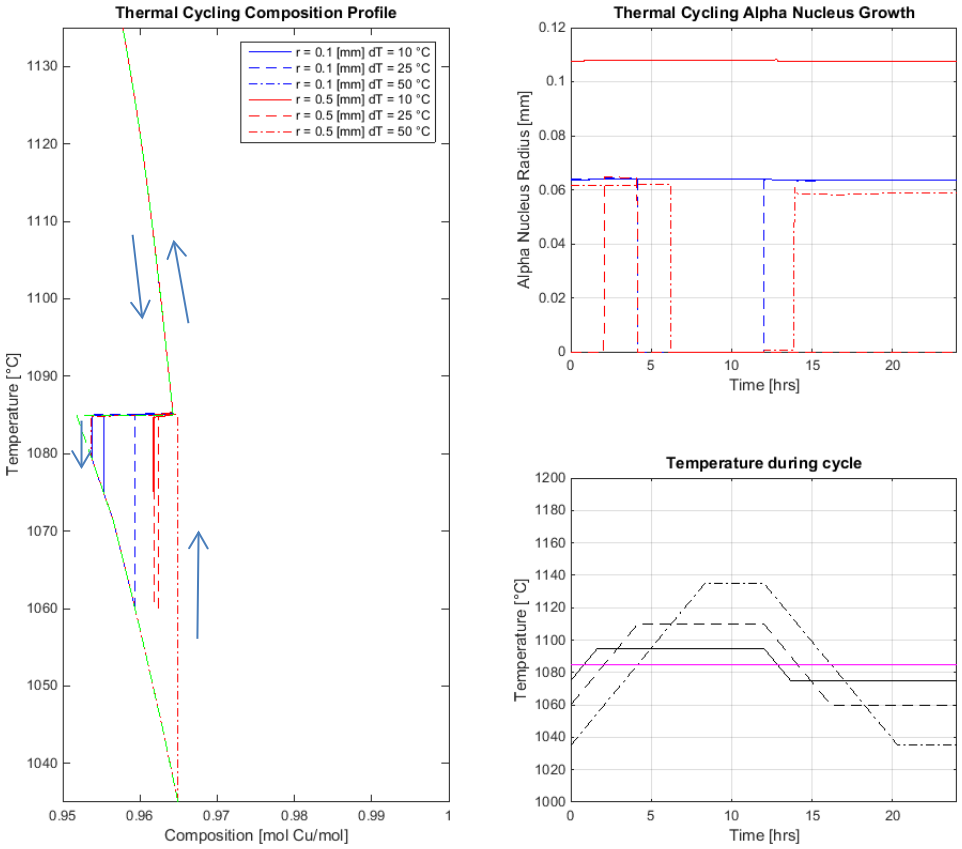

Figure 73 Composition and nucleus growth profiles for the Cu-Fe system undergoing thermal cycles at 10, 25 and 50 °C temperature amplitudes. Note that the 100 µm powder results in crystal growth on heating and cooling. This is a result of the increased kinetics allowing the stable solid solution to reach the solubility limit before the lower operating temperature, requiring nucleation. The 500 µm powder only nucleates on cooling for an amplitude of 50 °C.

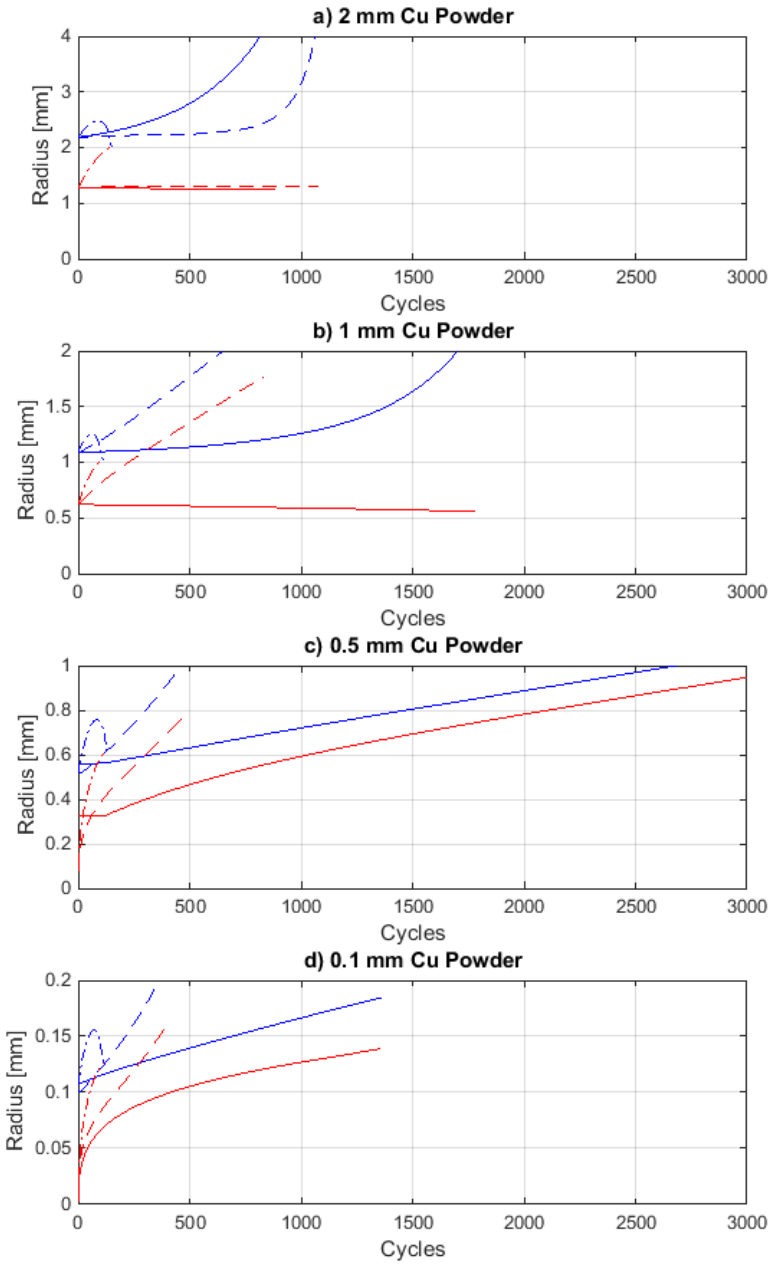

Figure 74 Evolution of Beta (blue) and Alpha (red) nucleus radius in Cu-Fe system during thermal cycling for a number of starting powder sizes, temperature amplitudes during thermal cycling and manufacturing temperatures. A solid line describes a 10 °C amplitude, a dashed line 25 °C and a dot-dash line 50 °C.

Cu-Fe Miscibility Gap Alloy morphology was modelled to either percolate after a number of cycles or see the Cu rich phase consumed by the matrix reservoir. Three categories of growth mechanism were identified which depended on the volume fraction, powder radius and the temperature amplitude of thermal cycling:

1) Microstructure percolation with decreasing alpha nucleus size.

This occurred for 1 and 2 mm powders with 10 °C temperature amplitudes. The beta radius was seen to increase as the initial alpha nucleus slowly decreased in radius. The cycle at which the beta radius exceeded the percolation threshold radius for a volume fraction was taken as the lifetime. The number of cycles to failure as a function of volume fraction for this mechanism was found to be well represented by a third order polynomial over the range 10 to 50 % volume fraction:

$$N_{failure}(\varphi)=a\varphi^3+b\varphi^2+c\varphi+d \quad (105.)$$

2) Microstructure percolation with increasing alpha nucleus size.

For high volume fractions, percolation tended to occur through this mechanism after very few cycles regardless of the temperature amplitude and volume fraction. For temperature amplitudes of 25 °C failure was due to this mechanism in all powders investigated. For small powders this failure mechanism occurred for 10 and 25 °C temperature amplitudes. The cycle at which the beta radius exceeded the percolation threshold radius for a volume fraction was taken as the lifetime. The number of cycles to failure as a function of volume fraction for this mechanism was found to be well represented by the following power law:

$$N_{failure}(\varphi)=A\varphi^B+C \quad (106.)$$

3) Consumption of the beta phase by the matrix

Consumption of the beta phase occurred for temperature amplitudes of 50 °C. The beta radius was found to increase with crystal growth to a peak value after which the crystal would continue to grow and the beta shell would be consumed. The peak radius achieved for the beta phase indicated the lowest bound in volume fraction for percolation through mechanism 3. All volume fractions lower than this volume were modelled to be consumed.

Figure 75 indicates which failure mechanism should be considered and Table 14 describes the parameters to be utilised in the equations (104 and 105) described above. An estimate is thus made for the lifetime of Cu-Fe Miscibility Gap Alloys based on their likely failure mechanism, initial copper powder radius, thermal cycle temperature amplitude and volume fraction. The cycles to failure for 10, 25 and 50% volume fraction Cu-Fe at different copper powder size are shown below in Figure 76.

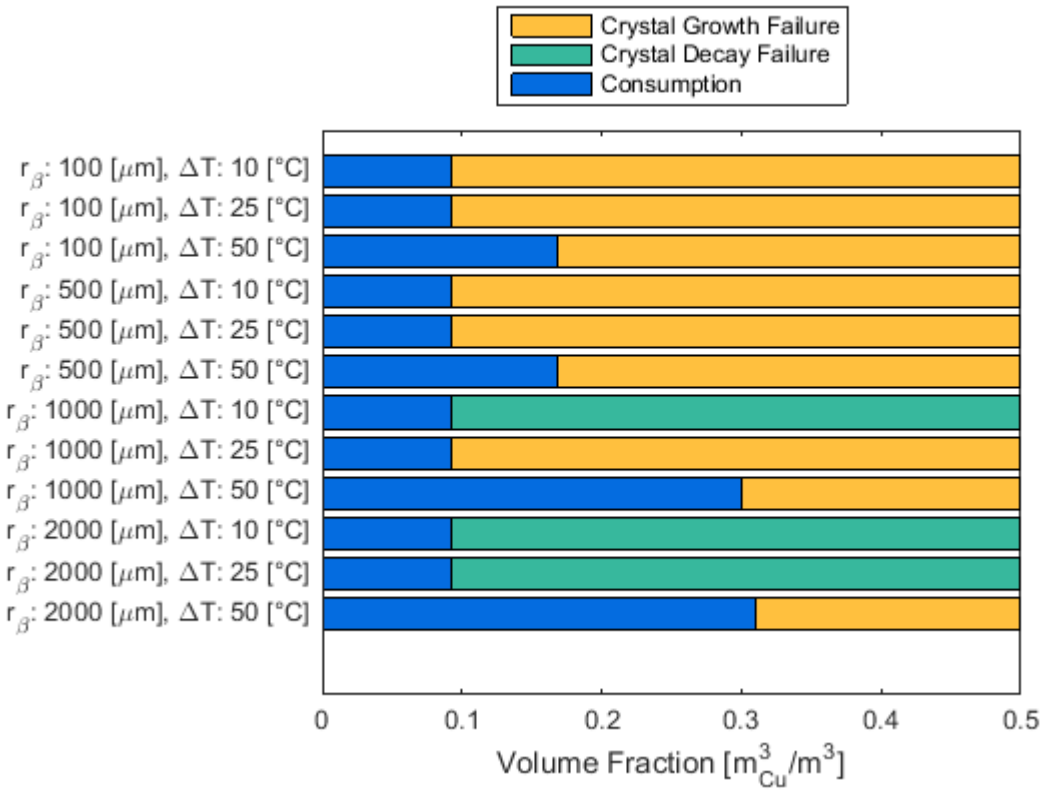

Figure 75 Failure mechanism for Cu-Fe systems. Below a volume fraction of 9.2 % Cu all systems will fail by consumption by the matrix. In general for the Cu-Fe system large powders fail with a decaying nucleus whilst small powders fail with growth of a nucleus.

Table 14 Parameters for curve fits to Cu-Fe lifetime predictions.

Initial Tin Powder Radius [μm]	Thermal Cycle Amplitude [°C]	Cycles to Failure by Consumption [Cycles]	Failure with crystal decay				Failure with crystal growth		
			a [Cycles]	b [Cycles]	c [Cycles]	d [Cycles]	A [Cycles]	B [Diml]	C [Cycles]
100	10	1[1]					662.1	–0.548	–973.6
100	25	1[1]					4965	–0.034	–5040
100	50	112					2.723	–1.795	–7.255
500	10	1[1]					1930	–0.396	–2548
500	25	1[1]					2234	–0.089	–2332
500	50	128					5.8	–1.555	–12.4
1000	10	1[1]	–8719	6410	–3784	2025			
1000	25	1[1]					1104	–0.223	–1221
1000	50	110					0.8607	–3.798	–10.92
2000	10	1[1]	–4770	4818	–2970	1074			
2000	25	1[1]	–4136	2732	–1144	1154			
2000	50	150					2.435	–3.365	–26.07

Crystals of alpha phase were modelled to decay for 1 mm radius powder cycled at 25 °C and 2 mm radius powder cycled at 10 or 25 °C. This did not necessarily lead to longer lifetime as the beta phase was still capable of consuming matrix material and growing through each thermal cycle.

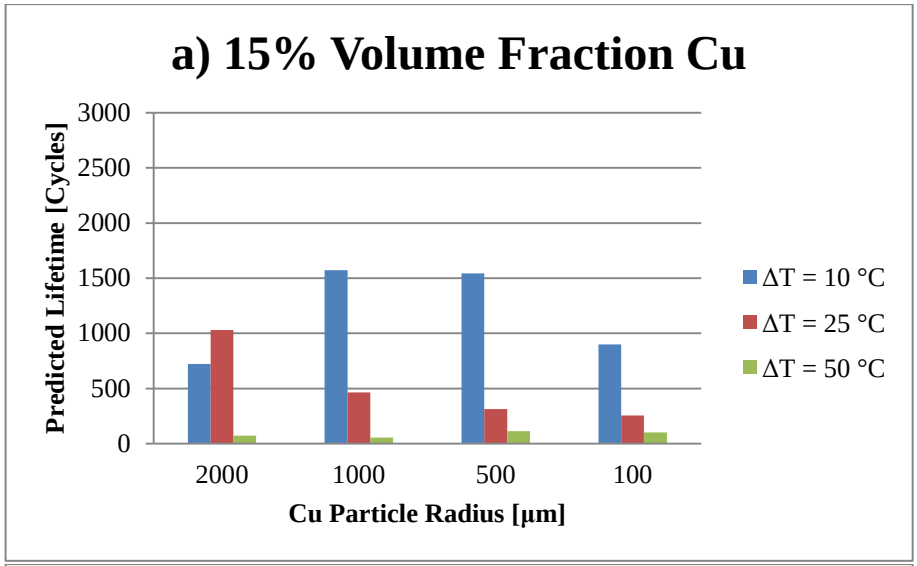

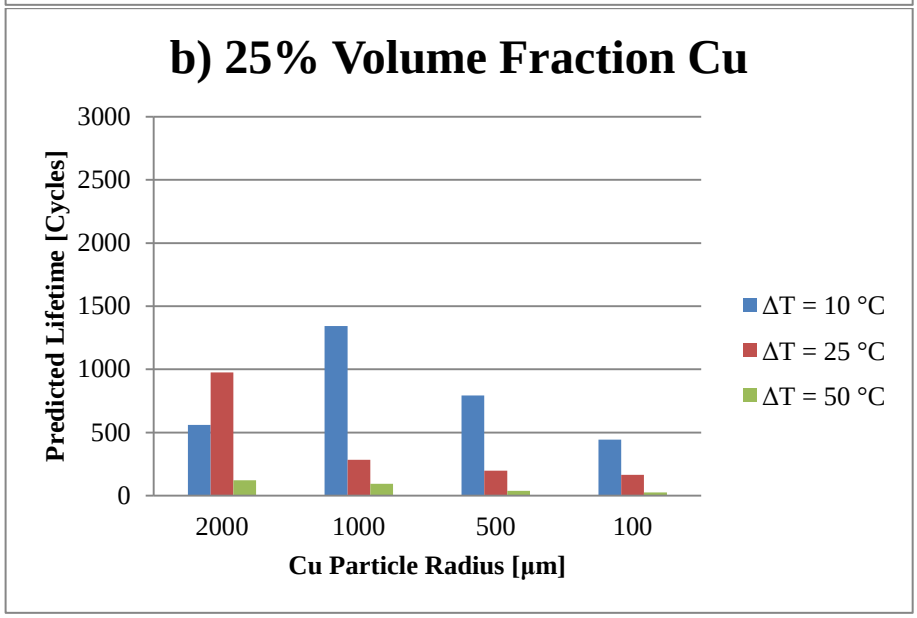

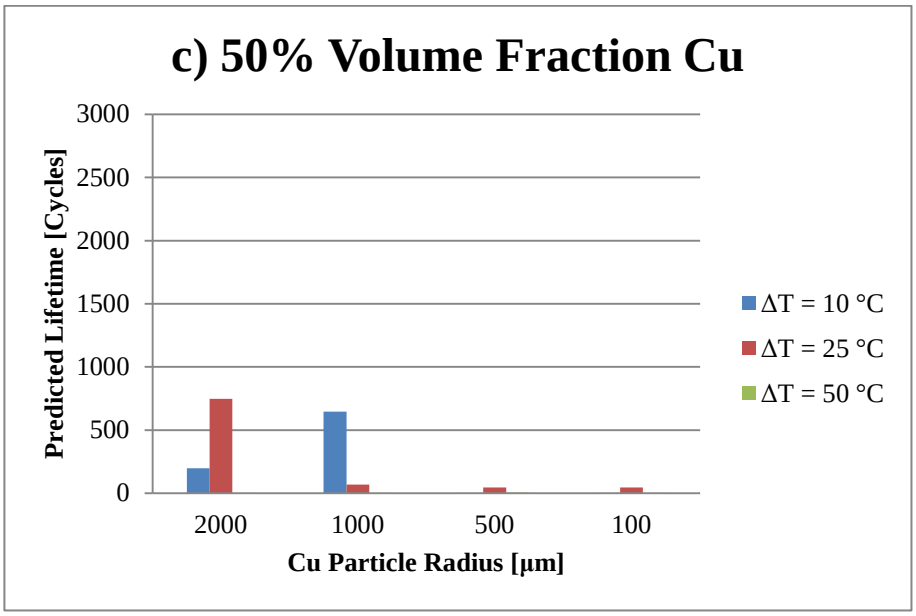

Figure 76 Cycles to failure for the Cu-Fe system with different Cu Powder Radius and thermal cycle amplitude for: a) 15%, b) 25% and c) 50% volume fraction of Cu. The 10% volume fraction case failed due to consumption by the matrix very rapidly so the 15% volume fraction case was preferred.

All other cases showed crystal growth with a rate strongly dependent on the temperature amplitude and powder size. Unlike in the Sn-Al system, smaller powders aren't necessarily optimal for all temperature amplitudes. Small powders (<100 µm radius) have adequate kinetics in a 10 °C amplitude cycle to approach equilibrium in the solid phase prior to the lower operating temperature. As cooling is still continuing and the kinetics are slowing further this case is likely to lead to additional nucleation. In the Cu-Fe system for a temperature amplitude of 10 °C there exists an optimum powder radius between 0.1 and 1 mm to maximise lifespan.

Larger powders are preferred for 25 °C temperature amplitudes whilst the 50 °C case results in rapid (~120 cycles) consumption of the copper regardless of the size. In reality the copper would nucleate elsewhere in the system provided the initial volume fraction were above the solubility limit of the alpha phase (if not a stable solid solution of

alpha would form over time consuming all distributed beta phase). This phenomenon is beyond the capacity of the developed theory as it requires the specification of the finite matrix volume.

This system was extremely challenging to model due to the retrograde solubility on freezing in the beta phase and the significant solubility of the constituents in the opposing binary phase. As such the outcomes of this modelling should be taken as a qualitative guide. Further development of the theory requiring specification of the system dimensions is necessary to capture the redistribution of copper through the alpha phase.

It must be emphasised at this point that in general Miscibility Gap Alloys should not suffer from diffusion dominated aging. The Sn-Al and Cu-Fe systems are peculiar in their relatively high solubility of phases.

6.1.3. Thermo-Mechanical Considerations of Morphology Inversion

The methods in §3.4.2 provide a means of estimating the stresses about an idealised inclusion of melting or freezing Miscibility Gap Alloy. It was found that nearly all systems will experience yield upon the first heating ramp from a zero stress state. The peak stress invariably occurred at the interface between the two materials and was dominated by the tangential components. The stress was independent of the size of the powder. Iron and aluminium matrices are likely to plastically deform at the interface when subjected to stresses above the yield. Silicon Carbide matrices will fail in a brittle fashion and this may contribute to the morphology evolution over the first few cycles. The peak Von Mises Stress for each system is tabulated below Table 15:

Table 15 Peak Von-Mises Stress ranges for the concentric sphere model of Miscibility Gap Alloys heated from room temperature to their peak operation temperature.

System		Peak Von Mises Stress Range [MPa]
Brass	Graphite	75-365
Copper	Graphite	75-435
Copper	Iron	1290-2435
Magnesium	Iron	890-1665
Silicon	Silicon Carbide	10300-11900
Tin	Aluminium	555-875
Zinc	Graphite	30-205

A Concentric Sphere model is a significant simplification in modelling mechanical aging of Miscibility Gap Alloys. It resembles Miscibility Gap Alloys manufactured below the melting point of their distributed phase but does not resemble the interstice filling type morphologies of those sintered above, nor does it account for two spheres nearby. In systems where the distributed phase flows into interstices between the sintering matrix particles during manufacture the morphology contains many stress concentrations not present in a distributed spheres morphology. At high volume fractions, distributed particles will be within a small distance from each other, so the matrix material separating the particles will experience a superposition of stress fields resulting in deformation to suit the combination.

Morphology evolution due to mechanical phenomena is best investigated experimentally. Detailed finite element models can be created to determine the stress field during thermal cycling and the geometry may be updated and re-meshed through analysis. The model would increase in complexity when accounting for liquid transport and recrystallisation mechanisms. The computational power to model this case would be significant and the uncertainty in the output would require significant experimental validation regardless.

6.2. Chemical Reaction Based Aging

Each system analysed in this thesis reacts differently with the environment. Corrosion due to oxidation at high temperature, reaction with water or galvanic effects are possible. The obvious recommendation for all alloys is to isolate them from the environment and provide an intermediate layer of matrix (or other) material between the composite and any working fluid. Potential oxidation of each of the matrix materials is considered before galvanic corrosion is briefly discussed.

6.2.1. Oxidation of Matrix Materials

The potential for each matrix phase to degrade due to reaction with Oxygen is significant due to the high operating temperatures of Miscibility Gap Alloys. The distributed phase should always be encapsulated by the matrix material, thus the oxidation behaviour of the distributed phase is not considered.

Graphite matrices will decompose in the presence of air and elevated temperatures to form gaseous CO or CO_2. Oxidation of graphite occurs for temperatures greater than 400 °C [128]. As the oxide is gaseous, no passivating layer may form and the graphite matrix will be consumed. All systems involving graphite operating above this conservative limit and will thus require a some passivating layer to prevent oxidation.

In contrast, iron forms three stable oxides: Wüstite (FeO), Magnetite (Fe_3O_4) and Hematite (Fe_2O_3). In typical atmospheric settings iron generally is corroded through the formation of hydrated oxides ($Fe_2O_3 \cdot nH_2O$) and oxide-hydroxides (FeO(OH), $Fe(OH)_3$) at the surface of the metal. Iron atoms readily diffuse through the oxide and hence the oxide

forms only a poor passivating layer. Iron corrosion will proceed until the metal is completely consumed given enough time under atmospheric conditions [129].

At the operating temperature of a Cu-Fe or Mg-Fe Miscibility Gap Alloy air in contact with the iron will contain little moisture and the oxide layer formed will be a combination of the three stable oxides mentioned above. Wüstite is not stable below 570 °C thermodynamically and thus will not appear for thermal cycles below that temperature. Above this temperature some combination of the three oxides will be formed [108]. Iron must be protected from attack by oxygen with some artificial passivating layer otherwise any Miscibility Gap Alloy involving iron will oxidise and degrade over time.

Silicon carbide has exceptional thermal and chemical stability at very high temperatures. When exposed to air at atmospheric pressure and room temperature it is prone to forming a thin layer of Silica (SiO_2) through passive oxidation. This thin layer protects the SiC below from further significant oxidation [130]. Common silicon carbide heating elements are rated up to 1315 °C in pure O_2 and up to 1600 °C in air [131, 132]. Oxidation of a silicon carbide matrix is unlikely to be the dominant aging mechanism in a Silicon-Silicon Carbide system undergoing thermal cycling.

Aluminium forms a passivating layer of Alumina at room temperature when a clean surface is exposed to air. This passivating layer is extremely stable up to 550 °C [133]. It is unlikely that a Sn-Al Miscibility Gap Alloy will be degraded by oxidation through thermal cycling.

6.2.2. Galvanic Corrosion of Miscibility Gap Alloys

Galvanic corrosion occurs commonly where dissimilar metals are bridged by an electrolyte. All Miscibility Gap Alloys are essentially dissimilar metals in contact and thus

all are to some degree susceptible to galvanic corrosion. Water from the environment (rain or tap water) is capable of acting as an electrolyte and should be kept apart from Miscibility Gap Alloys. Again, the simplest means of preventing galvanic corrosion is to provide an intermediate layer between the composite and the environment. Each system is discussed in brief below to indicate those with significant galvanic potential.

Brass-Graphite Miscibility Gap Alloys are prone to Galvanic corrosion as graphite is one of the most noble electrodes commonly used. The difference in corrosion potential is 0.6 to 0.8 V (as seen on Figure 19) suggesting corrosion will occur but water will not be electrolysed. These Miscibility Gap Alloys are likely to age due to accelerated galvanic corrosion of the brass if the metal boundary comes into contact with an electrolyte.

Copper-Graphite Miscibility Gap Alloys are prone to galvanic corrosion similar to the Brass-Graphite alloys. The difference in corrosion potential is again around 0.6 to 0.8 V (Figure 19) suggesting corrosion will occur but ruling out water electrolysis. The copper within these alloys will be oxidised in preference to the graphite at an accelerated rate if the interface is bridged by an electrolyte.

Iron and copper have differing corrosion potentials in many electrolytes. The difference is around 0.2 to 0.4 V in sea water (Figure 19). This suggests that accelerated corrosion of the more anodic iron will occur. The potential difference is not adequate to split water.

Magnesium-Iron Miscibility Gap Alloys are prone to Galvanic corrosion as magnesium is very anodic and iron is mildly noble. Mg-Fe Miscibility Gap Alloys are likely to age due to galvanic corrosion if they come into contact with an electrolyte during use.

The electrochemical properties of Silicon-Silicon Carbide cells are not well studied at this time. It is recommended that any phase boundaries should be kept free of electrolyte during use.

Aluminium will oxidise while tin is reduced if bridged by an electrolyte and the alumina layer removed. The corrosion potential in sea water is around 0.4 to 0.6 V (as seen on Figure 19) which should see accelerated corrosion of the more anodic aluminium. The potential difference is not adequate to split water. Sn-Al miscibility gap alloys should be kept apart from electrolytes during operation by ensuring the layer in immediate contact with water is aluminium.

Zinc-Graphite Miscibility Gap Alloys are extremely prone to Galvanic corrosion as zinc is one of the most anodic metals and graphite one of the most noble electrodes commonly used. These Miscibility Gap Alloys are extremely likely to age due to galvanic corrosion if they come into contact with ionised water during use and have the potential to electrolyse water bridging the metal boundary.

6.3. Discussion

The following section summarises the findings of lifetime analyses and discussed means of preventing aging.

6.3.1. Summary of Aging Mechanisms and Prevention Methods

The discussion and modelling presented up till now describes how each Miscibility Gap Alloy analysed in this thesis might degrade through its lifetime. Systems with substantial solubility (>0.02 molar fraction) either of matrix material in the inclusion or

inclusion material in the matrix are likely to percolate after a number of cycles due to diffusion. All systems are seen to experience significant stress during thermal cycling though the result of repeated annealing and straining are unknown. Each system has some capacity to react with air, water or an electrolyte. The following table summarises the significance of each aging mechanism for each analysed system.

Table 16 Different aging mechanism significance for analysed Miscibility Gap Alloys.

System	Diffusion Aging	Mechanical Aging	Oxidation	Galvanic Corrosion
Brass-C	Insignificant	Possible	Very Significant	Significant
Cu-C	Insignificant	Possible	Very Significant	Significant
Cu-Fe	Very Significant	Possible	Significant	Possible
Mg-Fe	Insignificant	Possible	Significant	Possible
Si-SiC	Insignificant	Possible	Insignificant	-
Sn-Al	Significant	Possible	Insignificant	Possible
Zn-C	Insignificant	Possible	Possible	Very Significant

Measures can be employed to prevent aging by each of these mechanisms. Diffusion aging can be minimised through selection of appropriate powder size, management of amplitude in thermal cycling and including diffusion barriers. Mechanical aging might be prevented through additional annealing stages in manufacture. Oxidation and galvanic corrosion can be avoided through adequate encapsulation of the material.

Modelling of diffusion aging in the Sn-Al and Cu-Fe systems revealed how selecting an optimum inclusion powder size for a thermal cycle could lead to longer periods before percolation occurred. The role of equilibrium approach also suggests that an inhibiting layer that limits diffusion between the species might increase lifespan. Tin powder dusted in a fine layer of graphite powder before being distributed in aluminium might be appropriate as an inhibiting layer. Carbon is inappropriate for the Cu-Fe system as small quantities of carbon are soluble in iron.

Exposing most materials to atmosphere at elevated temperatures is likely to result in some reaction occurring. It is recommended that all Miscibility Gap Alloys, regardless of their reactivity with air, be kept in some form of encapsulation from the environment. As most alloys also have some porosity which might allow infiltration of water and steam it is recommended that an impenetrable layer be present between Miscibility Gap Alloys and pressurised liquid or gas at all times. If the alloy is to provide thermal inertia to a steam power plant for example, a tube of dense matrix material should be in immediate contact with the working fluid, rather than the composite. An example of how a system might be protected is provided in Figure 77.

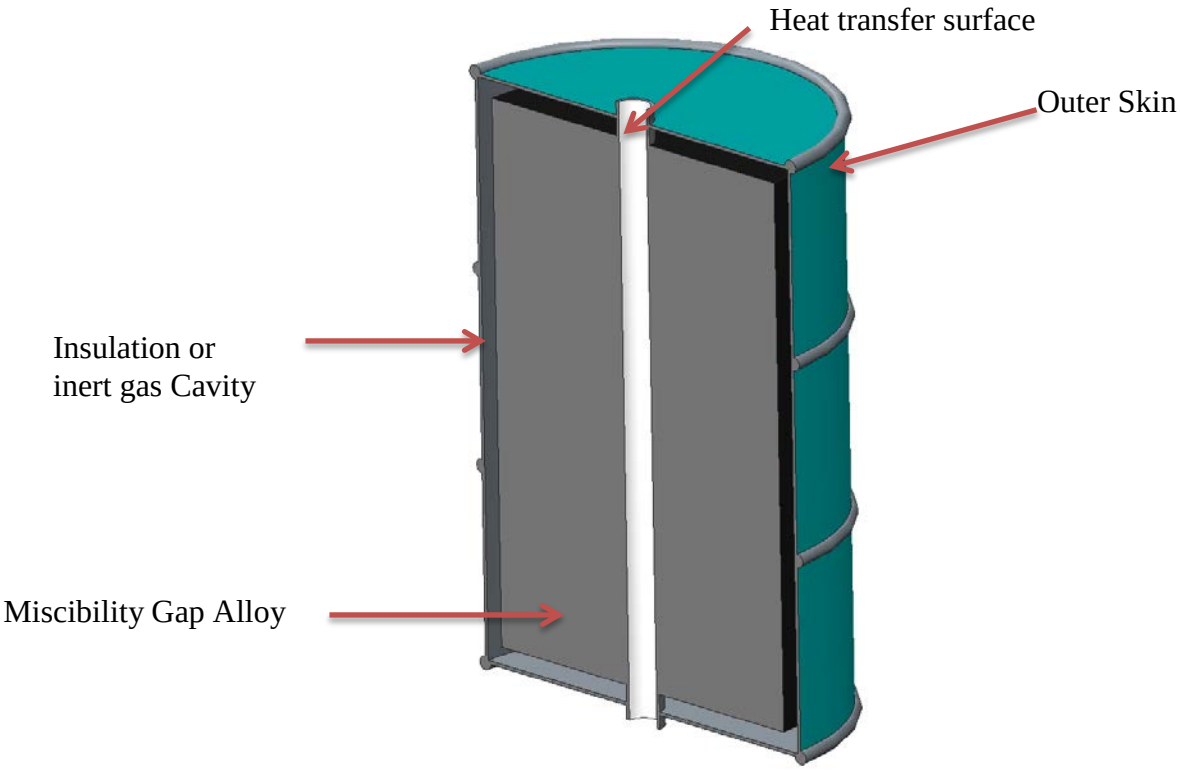

Figure 77 Demonstration of how a Miscibility Gap Alloy might be protected from chemical reaction aging.

6.3.2. Diffusion Modelling Limitations

The growth-decay model developed to estimate the lifetime of Miscibility Gap Alloys undertaking general thermo-temporal cycles with general manufacturing conditions is a good start in understanding the long term properties of the systems. The simplifications made are considerable though are justified in obtaining a bounding case for morphological evolution with the use of available computational resources.

As discussed in §3.4.1 the use of a Cahn-Hilliard based model for morphological evolution is very time intensive and reliant on data uncommon in literature. To capture the gradient between phases requires a very fine resolution spatially. For an explicitly time stepped model involving two del (∇) operations this requires a time step on the order of δx^4. If δx is in nm (the typical gradient between strongly immiscible solid phases) and typical mobility and gradient energy terms are used then δt is of the order of a second. It is unfathomable to simulate a cubic grid on the order of a millimetre discretised to this resolution nm ($1x10^{18}$ nodes) over years of time at one second per time step. Thus, even with phenomenal computational power, optimisation or simplification is still required.

Improvements can be made in meshing spatially and temporally for the Cahn Hilliard model. A cubic grid of isochoric elements is far from an optimised mesh for simulation. Tetrahedral meshes utilising varying volumes and regions of influence might be utilised to reduce the time required for simulation. Explicit time stepping is the least complex spatial discretisation possible. It is conditionally unstable for time steps exceeding a critical limit. Many alternatives exist that exploit unconditionally stable time stepping or utilise spectral methods. However, these methods are beyond the scope of this work.

Regardless of improvements in the numerical efficiency of the Cahn Hilliard model, accurate data is still required for the free and gradient energy terms being minimised. Accurate information for atomic mobility, Gibbs Free Energy and Surface Energy all functional on temperature and composition are still required. Through implementing CALPHAD methods the Gibbs Free Energy and the Surface Energy are calculable to a high degree of accuracy. Atomic mobility however still requires diffusion experiments which are uncommon through the entire composition range of binary alloys.

CHAPTER 7: ECONOMICS OF MISCIBILITY GAP ALLOY THERMAL STORAGE SYSTEMS

The following section describes the economic analysis of implementing a Miscibility Gap Alloy thermal storage system. Price estimates of materials are given in Appendix F whilst price estimates of infrastructure are given in Appendix G. Estimates are justified and then input to the cost model described in §3.5 yielding an estimated range of cost for each Miscibility Gap Alloy. A comparative analysis is then given demonstrating where Miscibility Gap Alloys are more cost effective than other thermal storage materials in use or proposed in the literature.

7.1. Capital Cost

The capital cost of implementing a thermal storage system might be broadly separated into material and infrastructure costs. Material costs may be determined with knowledge of the energy density, matter density and material cost on a mass basis. The raw material may require further manufacturing to be suitable as a thermal storage material, introducing an additional manufacturing cost. The infrastructure necessary for a thermal storage system is highly dependent on the physical state and material properties of the storage medium and the particular deployment.

7.1.1. Material Costs

Estimates of constituent material costs were made by analysing literature, trading websites and catalogues. A great range of material costs were found as prices varied from supplier to supplier. Appropriate ranges of cost were found and are described in Appendix

F. Figure 78 summarises the findings of this survey for materials involved in select Miscibility Gap Alloys.

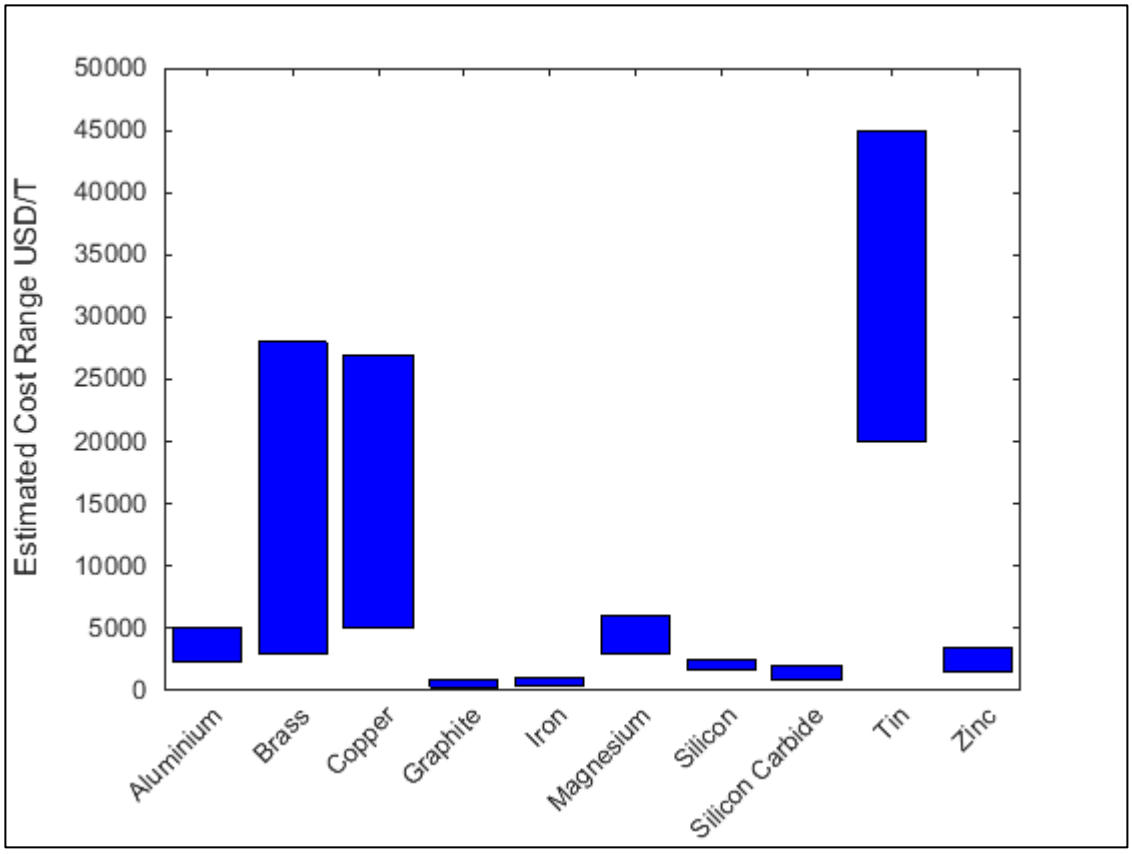

Figure 78 Relative estimated price range of constituent materials involved in some Miscibility Gap Alloys.

The figure above shows the considerable variation in cost between typical Miscibility Gap Alloy constituents. Alloys that involve copper or tin are likely to be much more expensive (on a mass basis) than those that utilise a less precious distributed phase.

Figure 79 shows a plot of nominal values of material cost for Miscibility Gap Alloys at 50% volume fraction with other thermal storage media against effusive energy density (introduced in §5.2). Note that Miscibility Gap Alloys have a range of costs per kWh but also show a very high effusive energy density.

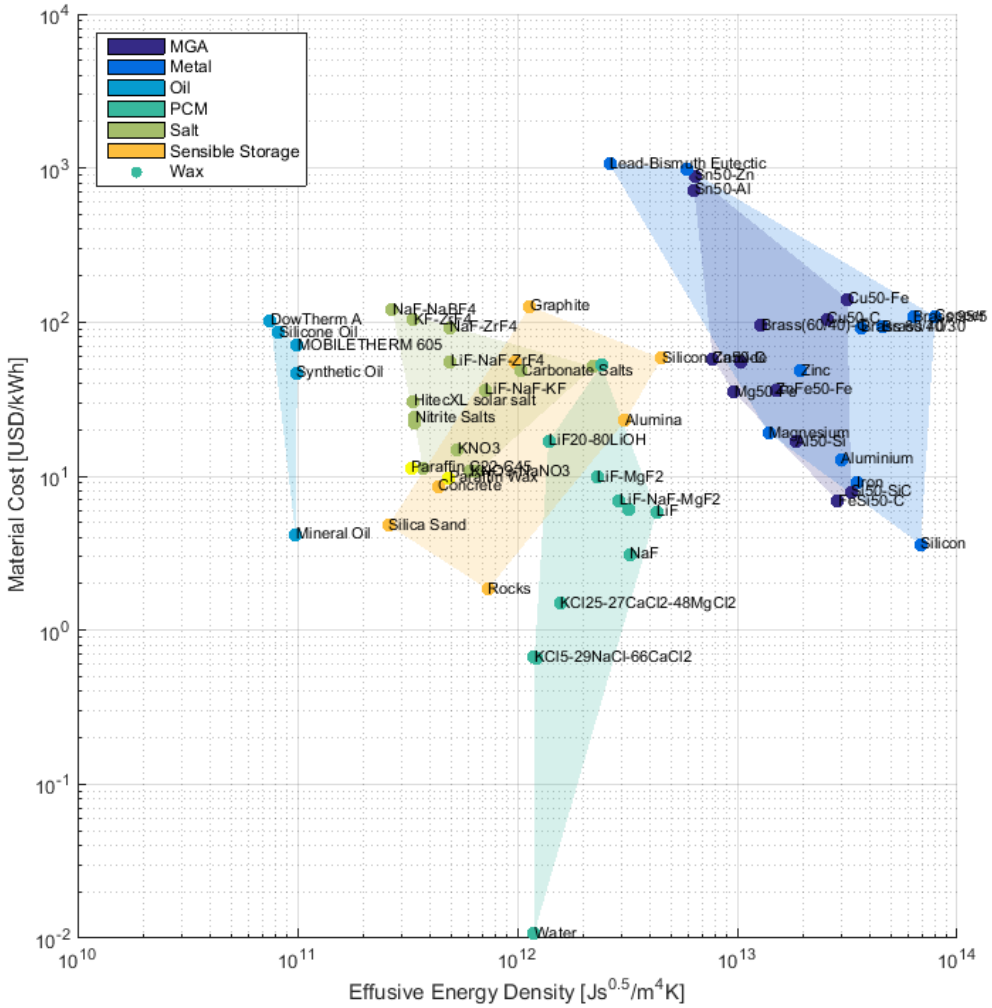

Figure 79 Nominal material cost plotted against effusive energy density for a range of thermal storage materials.

7.1.2. Manufacturing Costs

The cost of manufacturing Miscibility Gap Alloys must be considered when determining the total price of implementing a thermal storage system. All MGAs made thus far have been produced through powder metallurgy. Thus this manufacturing method was utilised in economic modelling. Typical bounds for material utilisation factors, capital

costs, write off times, overhead costs and load factors were taken from the CES database [102] and are summarised in Table 17. Here the unit of manufacture (item) is a single 50 mm ($125x10^3$ mm^3) cube piece of Miscibility Gap Alloy that would be subsequently joined to others to form a useful storage volume (deployment).

Table 17 Bounds for manufacturing costs taken from the CES database [102].

Material	Units	Symbol	Bounds
Mass Utilisation Factor	[Mass in Product/Mass Used]	$u_{Mat\ Uti}$	[0.9, 0.99]
Tool Cost	[USD/Tool set]	c_{Tool}	[5050, 16100]
Tool Life	[Items/Tool set]	$N_{Tool\ life}$	[10000, 50000]
Production Rate	[Items/hour]	r_{Prod}	[120, 1200]
Overhead Cost	[USD/hour]	$c_{Overhead}$	[100, 200]
Capital Cost	[USD]	$c_{Capital}$	[70600, 2830000]
Capital Write off Time	[Years]	$\Delta t_{Write\ Off}$	[5, 10]
Load Factor	[Time Producing/Time]	$u_{Load\ Factor}$	[0.4,0.6]

7.1.3. Infrastructure Costs

Infrastructure costs were dependent on both the particular deployment and the Miscibility Gap Alloy utilised. This was primarily a result of the operating temperature and capacity for oxidation of the matrix material. The recommended infrastructure elements for each MGA analysed in this article are shown in Table 18. For a barrel deployment (described in detail §8.1) the bulk encapsulating material is a 200 L barrel. An additional retrofitted shipping container cost is added per 96 barrels (the packing limit of 200L drums in a 20x8x8.5 ft. shipping container).

Table 18 Recommended infrastructure elements and price bounds for each Miscibility Gap Alloy of interest. Here MS refers to mild steel and SS refers to stainless steel. Atmosphere costs have units of [USD/m^3], Piping costs [USD/m], Encapsulation costs [USD/m^2] and Insulation costs [USD/m^2]. *Barrel implementation includes barrel encapsulation, foundation and shipping container costs.

MGA	Atmosphere		Piping		Encapsulation		Encapsulation*		Insulation	
Brass-C	Argon		SS Pipe		SS Sheet		SS Barrel		High Temp Min Wool	
	0.8	1.2	24	36	132	198	292	356	10	15
Cu-C	Argon		SS Pipe		SS Sheet		SS Barrel		High Temp Min Wool	
	0.8	1.2	24	36	132	198	292	356	10	15
Cu-Fe	Argon		SS Pipe		SS Sheet		SS Barrel		High Temp Min Wool	
	0.8	1.2	24	36	132	198	292	356	10	15
Mg-Fe	Air		MS Pipe		MS Sheet		Barrel		Min Wool	
	0	0	12	18	32	48	225	277	4	6
Si-SiC	Argon		Ceramic Pipe		Ceramic Coating		Ceramic Coated Barrel		High Temp Min Wool	
	0.8	1.2	48	72	264	396	850	1042	10	15
Sn-Al	Air		MS Pipe		MS Sheet		Barrel		Min Wool	
	0	0	2	18	32	48	225	277	4	6
Zn-C	Air		MS Pipe		MS Sheet		Barrel		Min Wool	
	0	0	2	18	32	48	225	277	4	6

Infrastructure prices were taken from a number of different resources. Atmosphere costs were assumed. Piping was costed from [134] with assumptions made for stainless steel and ceramic equivalents. Encapsulation costs were taken from [135] and ceramic coating cost was assumed. Barrel prices were found from [136], whilst shipping container costs were based on [137]. with an assumption on retrofitting cost. The slab was assumed to be rectangular 7x3 m in dimension and a depth of 1 m. Concrete with reinforcement was considered to cost 620 USD/m^3. Insulation prices were taken from [138]. An uncertainty of 20% was assumed for all costs.

7.1.4. Salvage Potential

The design lifetime of all three deployments was assumed to be twenty years. After this time it was assumed that a certain proportion of the material costs could be recovered as salvage. This was simply evaluated as a fraction of the initial cost as per Table 19. Conservative values were selected with considerable range as the price of recycled metals depends both on commodity price and whether a contractor is employed to undertake the work.

Table 19 Salvage proportion assumed for each Miscibility Gap Alloy system.

Miscibility Gap Alloy System	Salvage Fraction Bounds [USD recovered/USD material cost]
Brass-C	[0.0625,0.125]
Cu-C	[0.0625,0.125]
Cu-Fe	[0.125,0.25]
Mg-Fe	[0.125,0.25]
Si-SiC	[0.0625,0.125]
Sn-Al	[0.125,0.25]
Zn-C	[0.0625,0.125]

Salvage should be relatively simple for those MGAs involving two metallic constituents. The MGA must be heated to above the matrix constituents melting temperature. The two metals will then separate through their difference in density. Upon freezing the MGA should appear as two separate layers of metal, easily separated at the material boundary. Where the matrix required a binder (graphite and silicon carbide) the cost recoverable was assumed to be reduced as the matrix would require additional processing.

7.1.5. Net Capital Cost

The material cost of each alloy pair considered (both (a) without and (b) with the cost of manufacturing) per kilowatt hour of storage capacity are plotted in Figure 5. In this

plot, the horizontal axis displays the energy density (kWh/L) for varying volume fractions of the distributed phase. The vertical axis reflects the overall cost of the actual storage media. A wide spread exists in the cost per unit energy stored of different manufactured MGA storage media, with estimated values ranging from $3.0 USD/kWh for the Si-SiC system up to $1900 USD/kWh for Sn-Al. Since only material and manufacturing costs are considered here, it is assumed that the cost is independent of the particular deployment as long as the batch size is large enough to be economical.

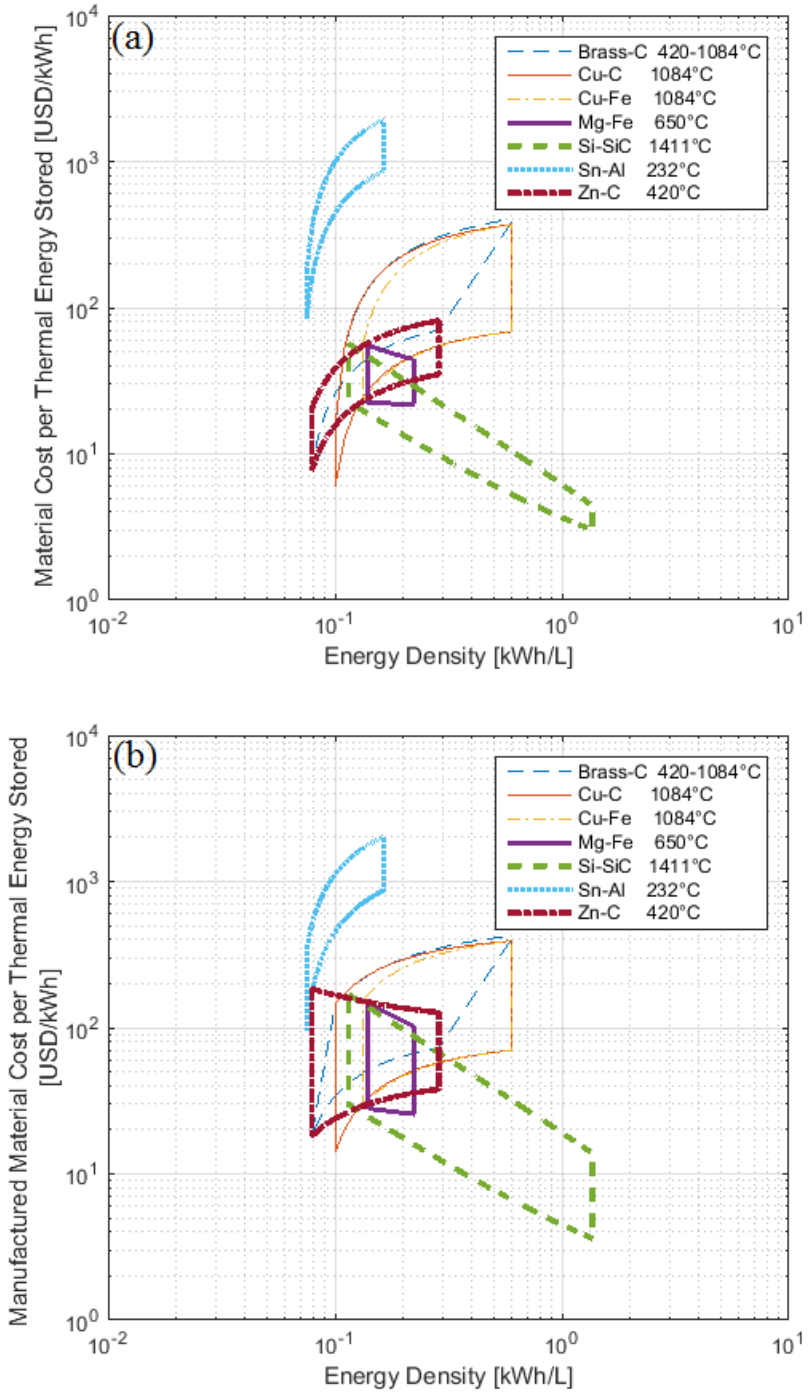

Figure 80 Plot of estimated (a) raw material and (b) manufactured material cost bounds against energy density for a number of Miscibility Gap Alloy combinations. In each plot, an operating temperature range of 100°C has been used to calculate energy density. The median operating temperature for each alloy system is displayed in the legend.

When infrastructure costs are considered as well, it can be observed that the overall system cost varies for each of the deployments considered in this study. Figure 81 contains plots of the overall cost of a storage system in USD against the energy storage capacity in kWh for each of the proposed MGA systems and for the three deployments previously mentioned.

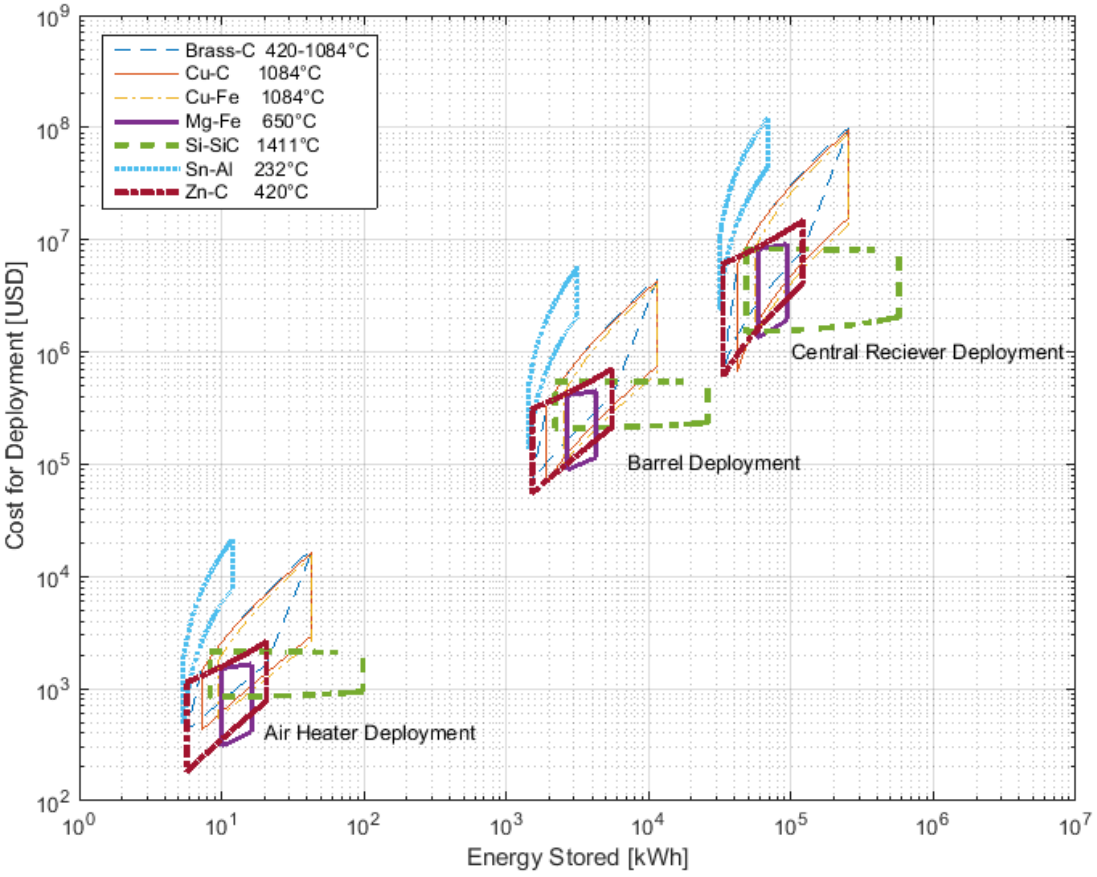

Figure 81 Total estimated cost of deployment plotted against stored energy for seven different Miscibility Gap Alloys in three different deployments.

The cost of deployment increases linearly with energy storage capacity across the three deployments considered. Thus to provide an overall costing figure independent of system size, the total cost of deployment can be normalised against energy stored for each deployment, and the resulting figures averaged. This data is portrayed in Figure 82, in which the capacity-normalised cost of storage averaged across all three deployments is plotted against energy density, in the same manner as Figure 80.

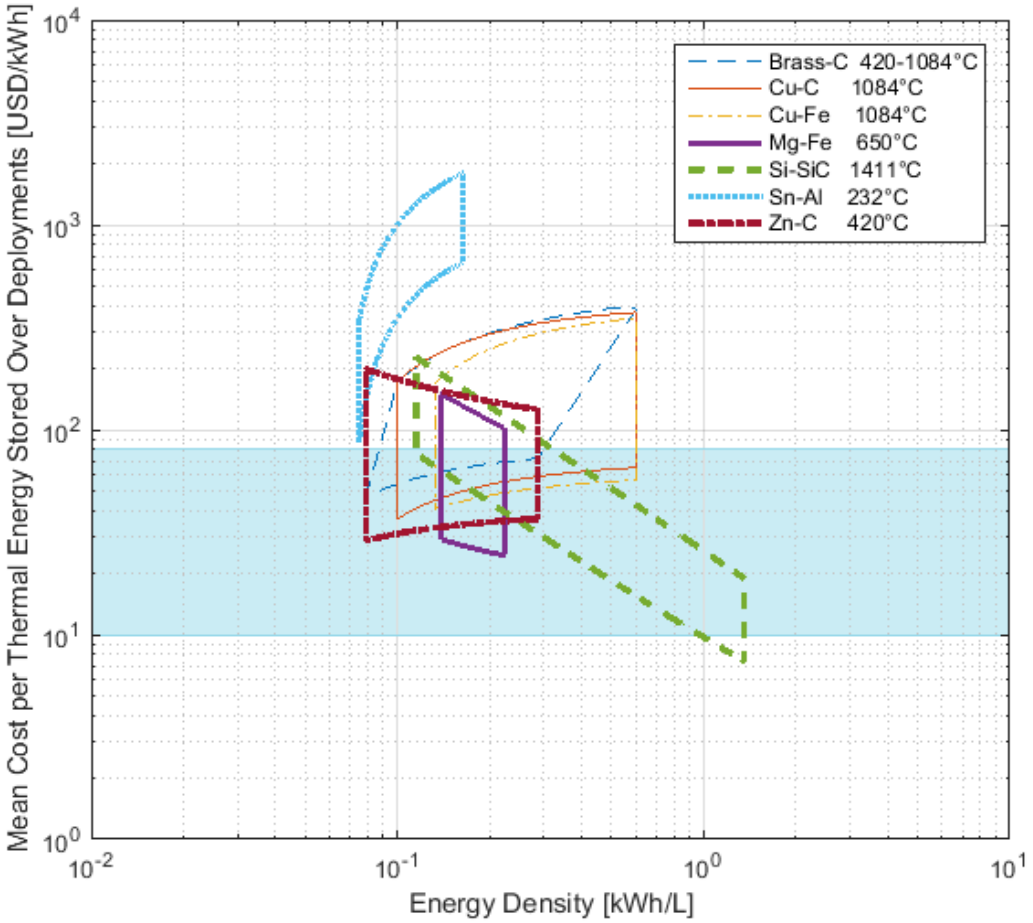

Figure 82 Mean cost per unit energy of storage over the three different deployments for the seven different Miscibility Gap Alloys. The shaded band indicates the cost per thermal energy stored commonly found in literature.

It can be seen from Figure 82 that the capital cost of Miscibility Gap Alloy thermal storage deployments are competitive with the price bounds established in the literature review of this thesis (shown in Figure 82 as the shaded 10-80 USD/kWh region) for most alloy systems. The most competitive systems of those discussed are Si-SiC and Mg-Fe, while the Sn-Al is the most expensive due to the high material cost of tin.

The breakdown of costs involved in implementing a Miscibility Gap Alloy thermal storage solution are dissimilar to molten salt implementations and to the general state of the art. MGA system costs are dominated by material and manufacturing costs (~50 to 90%) when compared to salts (30 to 50%). Figure 83 illustrates this by depicting the cost breakdown of a typical MGA storage system developed in this report to that of a typical Molten Salt system discussed in the introduction.

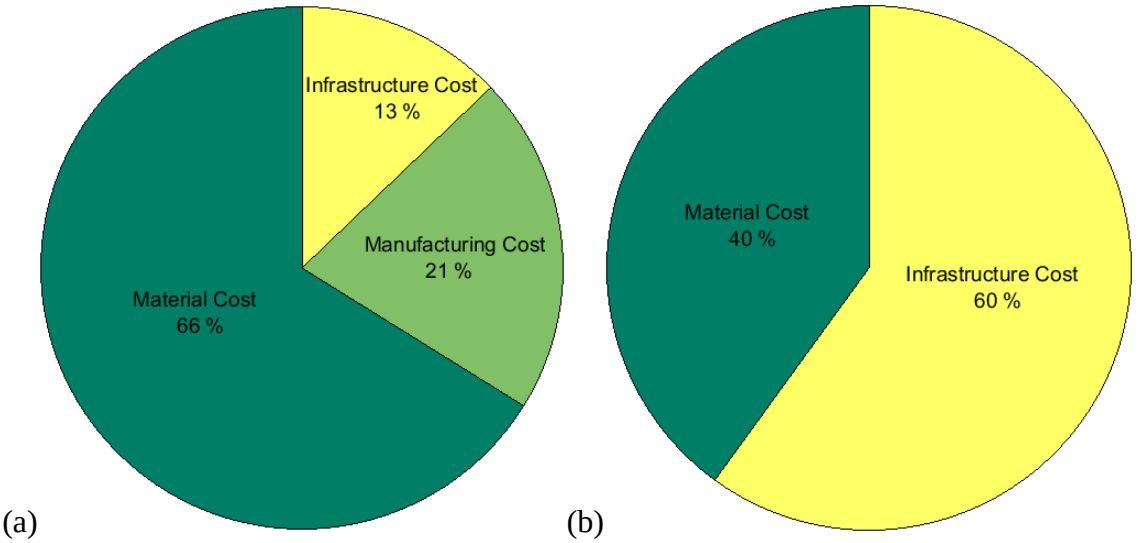

(a) (b)

Figure 83 Comparison of the typical cost breakdown for a) Miscibility Gap Alloys and b) Molten Salt thermal storage deployments.

7.2. On-going Cost

While the preceding section has demonstrated that MGA storage systems can be cost-competitive with mature storage technologies in terms of capital investment and salvage, the ongoing operation and maintenance costs have not been mentioned, nor has the material cycle life, all of which are necessary when factoring thermal storage into a Levelised Cost of Electricity (LCOE) figure for a CSP plant. In this regard, maintenance for a MGA thermal storage system is thought to be very minor involving recharging of the inert atmosphere to keep the exterior free of oxidation. Operating costs can be considered minor for these systems due to the high thermal conductivity of MGAs mitigating need for major pumping infrastructure. The design life of an MGA storage system is estimated to exceed 20 years of daily thermal cycling, after which salvage of storage materials is possible with an expected high recovery rate. The materials and infrastructure are not damaged by sub-cooling and are unlikely to ever experience localised over-heating due to their very high thermal diffusivity. For Miscibility Gap Alloy deployments on-going costs should not be a significant factor in Levelised Cost of Electricity calculations, especially in comparison to current alternatives.

7.3. Discussion

In the previous sections Miscibility Gap Alloys have been shown to be economically competitive with state of the art thermal storage materials. The total cost of the alloys is dominated by the cost of the constituent materials rather than manufacturing and infrastructure costs. Low infrastructure costs are one of the key benefits of Miscibility Gap Alloy thermal storage and this has been shown to be true for three different

implementations. The lifetime of alloys with strong immiscibility has been estimated in §6 to be very long without significant maintenance requirements. Additional relative benefits arise from the alleviation of pumping and heating costs associated with competing phase change materials.

The economic argument for Miscibility Gap Alloy thermal storage becomes stronger at higher temperatures. Elemental metals that melt at low temperatures (<450 °C) like mercury, gallium, tin, lead and bismuth are relatively expensive as they are not used at the volumes that higher melting temperature metals are. Miscibility Gap Alloys become most economical above 450 °C when zinc, magnesium and brass systems become available. At very high temperatures (~1440 °C) silicon systems become available with very low cost per kWh of storage. Very few competing thermal storage systems exist that operate at these temperatures. This temperature range suggests that Miscibility Gap Alloy thermal storage technologies are very appropriate for renewable energy applications involving steam Rankine Cycles and supercritical CO_2 Brayton or Stirling Cycles.

The extremely high conductivity of Miscibility Gap Alloy thermal storage implies that heat transfer will be limited only by convection to the working fluid (low Biot number storage). For poor conductors the difficulty in heat transfer is in moving heat through the storage material. To account for low conductivity thermal storage materials augmentation to the heat exchanger is required increasing cost and the effective volume of storage. Where the storage material is completely molten (oils and molten salts) a liquid-liquid heat exchanger must be used adding complexity and cost in operating a fluid circuit of corrosive or viscous material.

CHAPTER 7: ECONOMICS OF MISCIBILITY GAP ALLOY THERMAL STORAGE SYSTEMS

Very long lifetimes with little maintenance should be expected from Miscibility Gap Alloys. This may not be the case for other state of the art thermal storage materials that are degraded easily through overheating, dissolution of encapsulating material or stoichiometry imbalances through uneven cooling. Maintenance of the infrastructure in contact with storage materials is expected to be very minor for Miscibility Gap Alloy thermal storage.

CHAPTER 8: MISCIBILITY GAP ALLOY THERMAL STORAGE IMPLEMENTATIONS

This chapter presents a number of implementations for Miscibility Gap Alloy thermal storage starting with a simple domestic heater and increasing in scale to trough and ultimately power tower concentrated solar thermal power plants. These deployments are introduced in detail before they are critically evaluated. A number of novel implementations are then described in brief to conclude the chapter.

8.1. Air Heating

An air heater concept was introduced in the previous chapter (as an economic case study) where a household or small commercial enterprise might achieve space heating through converting off-peak electricity (e.g. surplus solar P.V.) to heat and storing this heat in a Miscibility Gap Alloy. A device involving Zinc-Graphite Alloy where 10 hours of storage at a maximum output of 10 kW could be achieved was designed (storing a total of 100 kWh). Here air would be drawn from the room with a small fan and blown over a series of Miscibility Gap Alloy blocks. The volumetric flow rate and the flow path could be controlled to achieve a particular heating load for an inflow of air.

The device is illustrated in Figure 84. It consists of an insulated shell in which blocks of Zn-C Miscibility Gap Alloy could be stacked to achieve the dimensions of 600x600x200 mm (72 L). The blocks are stacked within a caddy that can be easily inserted and removed. The shell is ducted to a fan with variable speed control and a set of backdraft shutters. Around the caddy are four shutters that can be manipulated by hand to adjust the air flow path over the surface of the blocks. Five different configurations are possible with

the shutters to maximise or minimise heat exchange surface area. The complete engineering drawings are shown in appendix I.

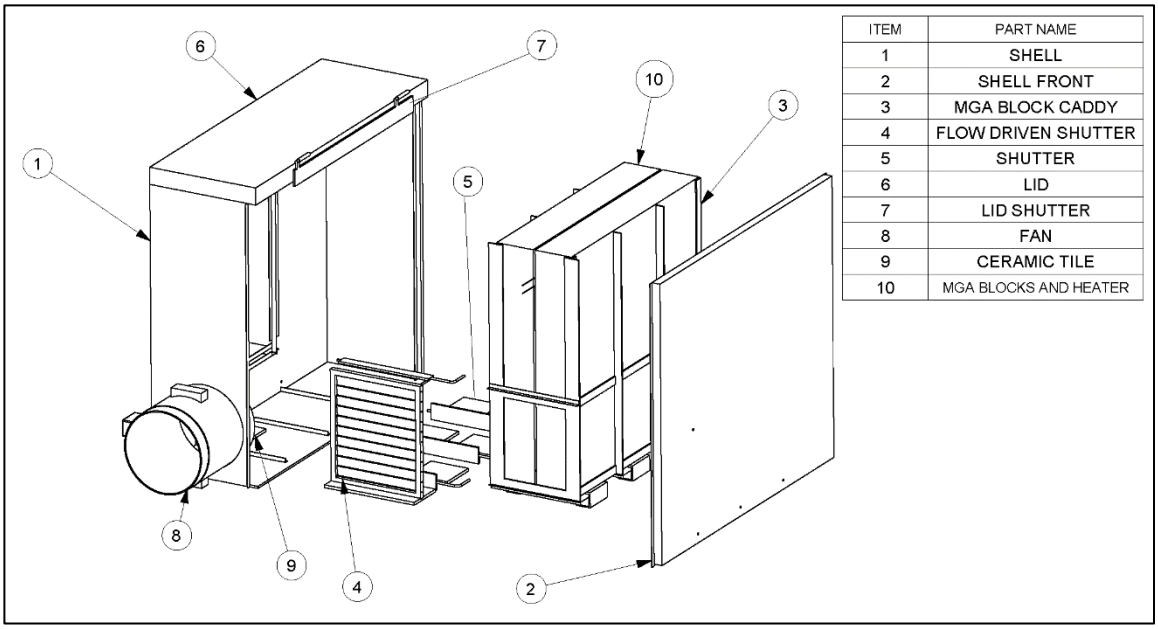

ITEM	PART NAME
1	SHELL
2	SHELL FRONT
3	MGA BLOCK CADDY
4	FLOW DRIVEN SHUTTER
5	SHUTTER
6	LID
7	LID SHUTTER
8	FAN
9	CERAMIC TILE
10	MGA BLOCKS AND HEATER

Figure 84 Exploded view of Air Heater design.

The discharge characteristics of the device for an inlet varying in temperature from 0 °C to 20 °C and a flow rate of 10 to 100 L/s were determined. The blocks were initialised at 470 °C and considered discharged when they reached 370 °C (50 °C below the melting temperature of zinc). If required there is still a great amount of sensible heat available down to room temperature. The outlet temperature[8] and time to discharge are shown as contour charts in Figure 85. The calculations are appended to appendix J.

[8] Here outlet temperature refers to the mean temperature at the outlet over the discharge time.

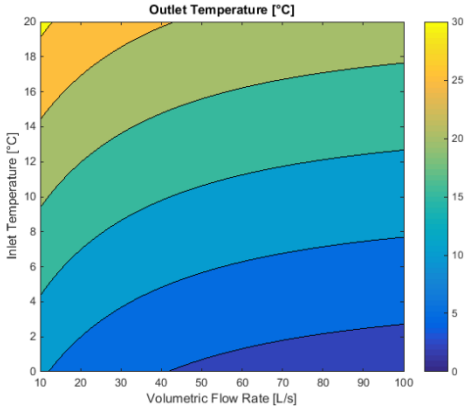

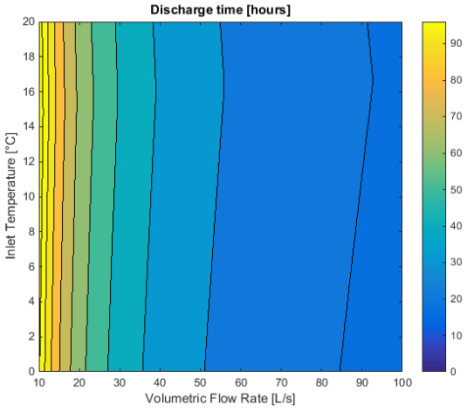

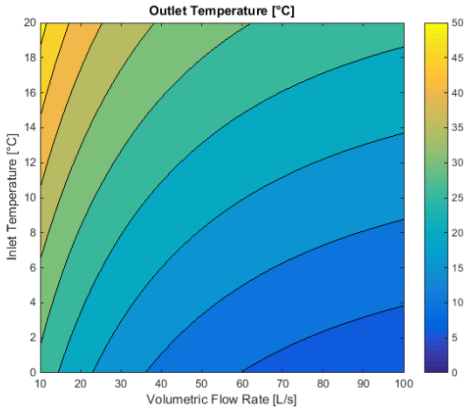

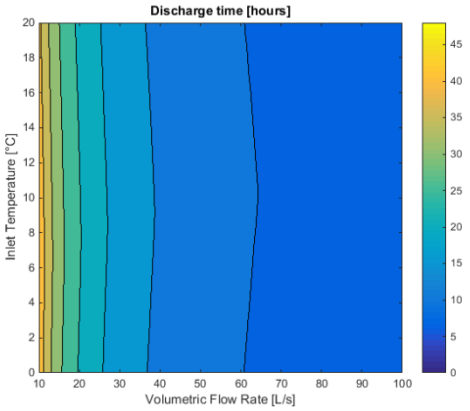

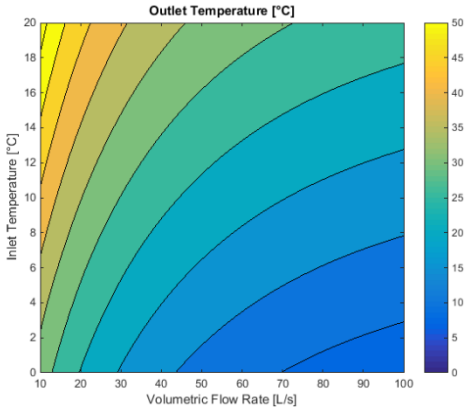

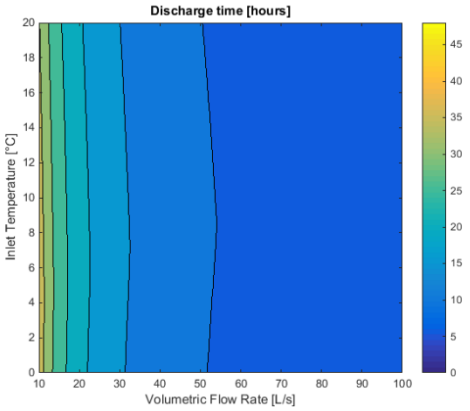

Outlet Temperature [°C]
Discharge time [hours]
Outlet Temperature [°C]
Discharge time [hours]
Outlet Temperature [°C]
Discharge time [hours]
Inlet Temperature [°C]
Volumetric Flow Rate [L/s]
0
2
4
6
8
10
12
14
16
18
20
10
20
30
40
50
60
70
80
90
100

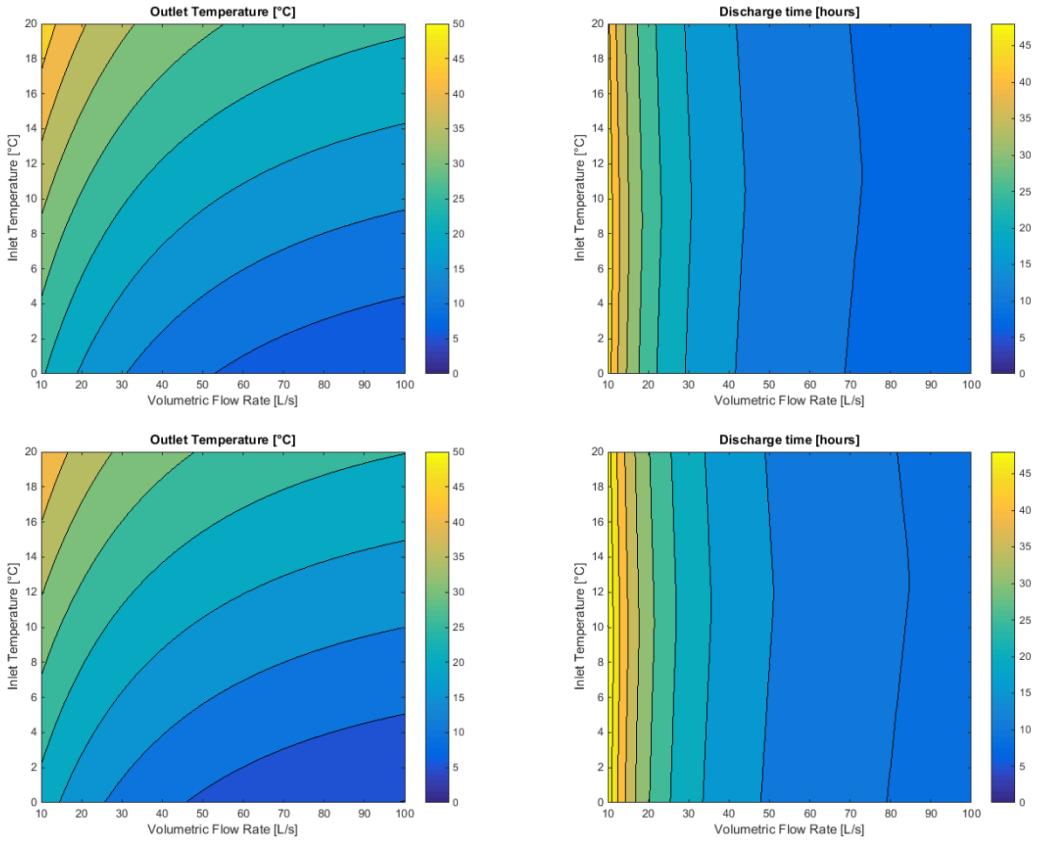

Figure 85 Theoretical discharge characteristics for the Air Heater device for 5 different operational configurations. From top to bottom: Bypass, Bypass closed & one shutter open, Bypass closed & two shutters open, Bypass closed & three Shutters open, All shutters open. Note that the Bypass charts have different limits.

With an inlet temperature of around 10 °C the air heater is predicted to be capable of delivering a comfortable supply of air at 23 °C at 20 L/s for around a day before being discharged. The extra control mechanisms do not have a significant impact on the delivery of warm air and could probably be simplified in subsequent revisions. Very high temperatures are possible with low flow rates (due to the ~420 °C heating source). It is possible that an air heater could be designed similarly to deliver very hot air for industrial processes like drying or even for cooking.

The design presented above may be improved in a number of ways in the next design stage. Through simplified controls and automation the device could be better adapted to a real world situation.

As mentioned previously the flow path controls lead to only minor differences in the output of the device. A two shutter design would likely achieve an adequate level of control provided the fan flow rate may still be varied. The shutters might also be actuated to allow automation of the flow path configuration.

The system could be automated to both minimise electric power consumption at peak price time and maintain an outlet temperature. The heating element should only be turned on if the air heater is at low charge and the cost of power is minimal. This could be programmed in to a simple controller to only consume off peak power or excess PV (if available) when the block temperature is low. The characteristics shown above could be used as the basis for a simple control algorithm where the fan speed and shutter configuration could be varied to achieve a comfortable outlet temperature.

8.2. Concentrated Trough Solar Thermal Power Plant

The chief motivator for much of this work has been to implement Miscibility Gap Alloys in Solar Thermal Power Plants. Concentrated Solar Troughs provide a means of focussing sunlight upon either a heat transfer fluid or directly on a working fluid. The fluid would then heat the thermal storage material or travel directly to the turbine. This arrangement is shown schematically in Figure 86. A highly adaptable method of using Miscibility Gap Alloys for thermal storage was developed for this case.

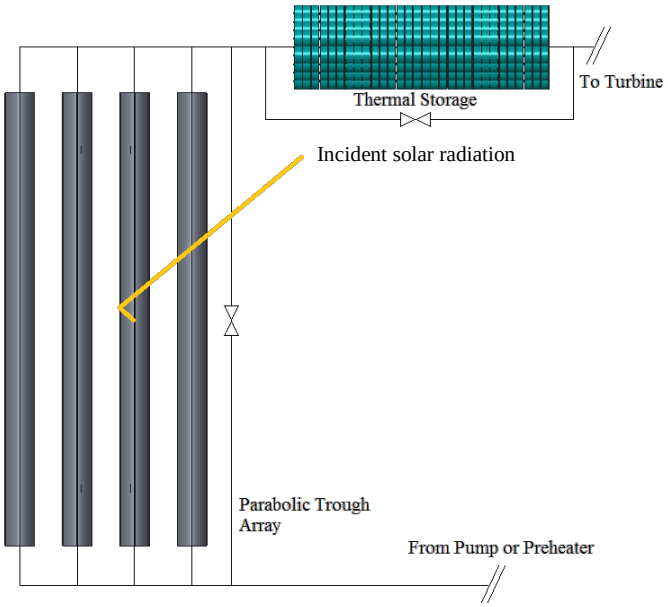

Figure 86 Schematic of how a thermal storage device might be implemented into a solar trough power plant.

The thermal storage device utilises 200 L (44 Gallon) steel or stainless steel drums as the outer encapsulation for a Miscibility Gap Alloy. Drums were chosen as they are a convenient volume and extensive infrastructure exists in transport and manufacture. As shown in Figure 87, a central pipe would carry the working fluid through each barrel and act as the heat exchange surface. Barrels would be placed on their side and arranged in an array of series and parallel blocks to achieve the required storage and discharge requirements of the particular power cycle (one configuration is demonstrated in Figure 88). The barrels may be placed in a shipping container which might be flooded with an inert gas if required. Table 20 summarises the energy stored per barrel for a number of different Miscibility Gap Alloys and common thermal storage materials.

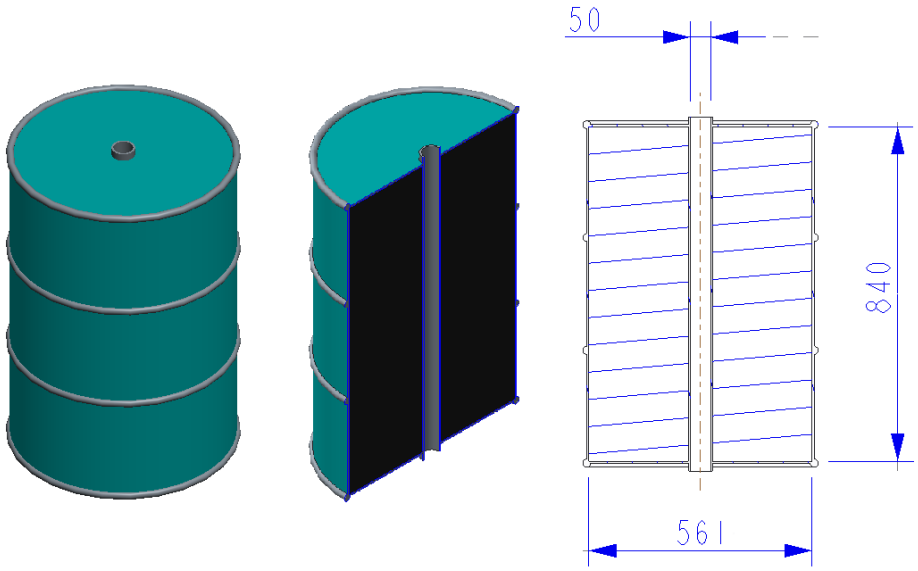

Figure 87 Barrel concept with rough dimensions.

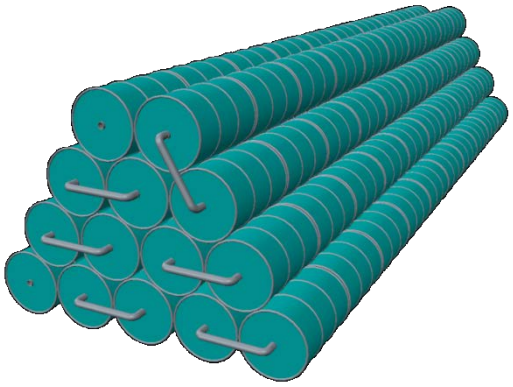

Figure 88 Array of storage barrels connected in series and stacked.

Table 20 Rated capacity per barrel for different materials (ΔT = 100 °C + latent heat).

Material	Rated Capacity [$kWh_{storage}$/Barrel]	Operating Temperature [°C]
Concrete	13.2	260-360
KNO_3 (sensible)	15	337-437
Sn-Al	24	180-280
KNO_3(54w)-$NaNO_3$	27.4	171-271
Mg-Fe	36.8	600-700
Zn-C	38	370-470
Brass-C	52	845-945
Cu-C	70.2	1035-1135
Cu-Fe	73.6	1035-1135
Si-SiC	148	1361-1461

High conductivity Miscibility Gap Alloys are particularly well suited to the single pipe design. Low conductivity materials like salts and concrete would require additional heat transfer area to effectively take advantage of a barrel storage system. Figure 89 shows the time to charge for four different materials. Here the film coefficient was calculated with the Dittus-Boelter equation [139] using 1 kg/s of steam at 25 bar and at the upper limit of the operating temperature listed in Table 20. The profile was determined with a transient axisymmetric finite element model utilising a convective boundary at the inner radius and insulated boundaries elsewhere.

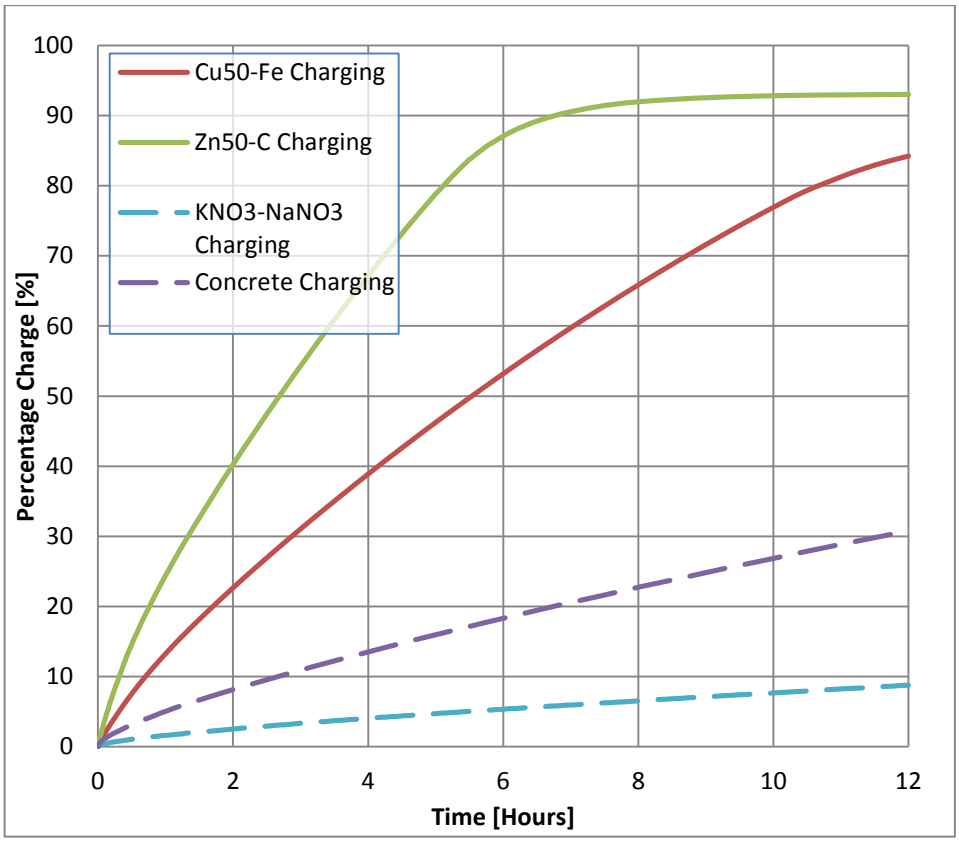

Figure 89 Charging curves for a single pipe barrel with differing material. Here conduction is the only method of heat transfer through the barrel. The film coefficient was assumed to be constant over the entire heat exchange surface of a single barrel [27].

Barrel storage may prove an adaptable and easily implemented method of thermal storage for systems that charge through a fluid though some limitations exist. The thin encapsulating layer of steel may need to be replaced with stainless steel or even include a ceramic coating for high temperature operation. Si-SiC would require a completely ceramic equivalent as the stainless would melt before the operating temperature was reached. The barrels are quite heavy when loaded with Miscibility Gap Alloy. Infrastructure established for the movement of oil filled barrels may not be able to support the up to 10 fold increase in mass (~170 kg for crude oil and ~ 1.7 Tonne for Cu-Fe) when repurposed. Potential miscibility or reaction between the barrel material and the Miscibility Gap Alloy

constituents might be an issue in the aluminium and graphite matrix systems. This may be mitigated through an inhibiting layer sprayed on the inner surface of the barrel before filling.

8.3. Concentrated Solar Tower Thermal Power Plant

In concentrated solar power tower plants, the sunlight is focussed onto a cavity which then provides heat to a transfer fluid. The transfer fluid may itself be the thermal storage medium or provide heat to a different material. It is proposed in this implementation that the cavity could be in itself a thermal storage material. Miscibility Gap Alloys are excellent candidates for a directly irradiated thermal storage device.

A material that is to absorb concentrated solar radiation must be a good absorber of the solar electromagnetic spectrum and thermally conductive to distribute heat away from the irradiated surface and ultimately to a working fluid. Miscibility Gap Alloys are usually encapsulated in either the matrix constituent or some shell material. Dull metals are reasonably effective at absorbing solar radiation but are improved significantly if coated with a high absorptivity surface. It is recommended that a surface coating be applied to the irradiated surfaces of a Miscibility Gap Alloy receiver. Thermal conductivity is extremely high in Miscibility Gap Alloys when compared to other thermal storage materials. Any sudden increase in solar power input will be distributed rapidly through the storage material without damaging it.

Graphite has been demonstrated to be an effective storage/receiver by Graphite Energy in Australia [140]. This concept is similar to that suggested for Miscibility Gap Alloy storage. Structural elements for a system involving the alloys would need to account

for the significant weight. An implementation whereby the focussed sunlight is directed towards a Miscibility Gap Alloy thermal storage block sitting on the ground might be preferred.

Figure 90 Existing graphite storage/receivers developed by Graphite Energy. These graphite systems could be doped with some distributed immiscible fusible phase to create a Miscibility Gap Alloy system with higher energy density [140].

Figure 91 Close up photograph of solar receiver utilising irradiated graphite [140].

8.4. Conventional Thermal Power Plant

Thermal inertia is also very useful in conventional power generation. Large turbines typical in coal, gas and nuclear power plants take a very long time to reach operating speeds. If an interruption occurs in the supply of steam such that the turbine must be taken offline, significant cost and delay in power generation may occur. Interruptions that stem from heating the working fluid may be minimised through a thermal storage medium in line with the working fluid.

Modern thermal power stations operate with super critical steam at high pressure (>22.1 MPa) and temperature (>650 °C) [88]. Miscibility Gap Alloys can be heated through the burning of fuels to very high temperatures. The operating temperatures of the copper, brass and silicon based systems are high enough to enable significant heat transfer to steam at the latter superheating stage whilst Mg-Fe and Zn-C are useful for boiling or initial superheating.

Introducing storage to a thermal power plant would allow for the switching of fuels whilst still maintaining steady power generation. A plant that utilised a combination of biomass, waste burning and coal for example could change burning temperature and heat transfer rates with minimal impact on the power cycle operation in the short term. A greater period would be available where the boiler need not be fired as preparations were made for the next fuel source.

8.5. Discussion

Miscibility Gap Alloy thermal storage has many applications in improving space heating, power generation and industrial processes. The particular application being augmented determines whether thermal storage is applicable and what type is optimal. The following discussion critically evaluates where thermal storage utilising Miscibility Gap Alloys in established technology is advantageous before introducing more novel uses.

Devices for storing energy for air heating do exist and achieve the desired outcome for short term domestic heating. Utilising Miscibility Gap Alloys allows for much greater energy density such that air heating could be maintained for a very long period. This lends itself to operation on photo voltaic cells that might be without sun for days to weeks with cloudy weather. The option to store at very high temperatures also provides air heating for cooking or other industrial processes (which might even be recycled after the process). Domestic settings in cool countries would benefit significantly from air heating with Miscibility Gap Alloys. Heating large spaces like offices and factories for long periods with excess PV might be the most suitable application of the technology in air heating.

Solar thermal power plants must utilise thermal storage if they are to operate continuously and Miscibility Gap Alloys have been shown in this work to be technologically and economically preferable to the state of the art. Low temperature systems utilising thermally fragile working fluids (Organic Rankine Cycles) might require intermediate heat transfer such that thermal decomposition does not occur on heat transfer surfaces. Steam, air or CO_2 power cycles can be in direct contact with Miscibility Gap Alloy thermal storage and thus require very little infrastructure for implementation. Heating very high temperature thermal storage materials may allow direct irradiation of the thermal

storage block. This may require a redesign of concentrated solar thermal systems, though it is expected the benefits would be significant. Retrofitting existing fuel based thermal power stations with storage may prove most advantageous where fuel supply was intermittent or varied.

8.6. Other Implementations

In situations where baseload power is not available from a large power station and electricity is generated from a variety of intermittent resources, thermal energy may provide a common means of storage. A combination of wind and solar resources in a small off grid town may be stored thermally without the need to convert the dc output of photo voltaic cells or transform the frequency of the wind resources. From the thermal storage a single Rankine cycle may be run with a steady electrical output frequency and amplitude.

Many industrial processes benefit from thermal inertia whether taking advantage of a steady heat transfer or in consuming off peak or intermittent power sources. Steam generation, drying and cement production are three examples where Miscibility Gap Alloys could improve the cost and efficiency of the process.

Steam Generation is important in many industrial processes and might benefit from boiling water through a heater including thermal inertia. Depending on the steam requirements, the appropriate Miscibility Gap Alloy would change. For low grade steam used in cleaning Sn-Al or Zn-C would be appropriate. For steam to be utilised in power generation or chemical reactions Mg-Fe, Cu-Fe or Cu-C might be better suited. A concept for a low grade steam generator is shown in Figure 92.

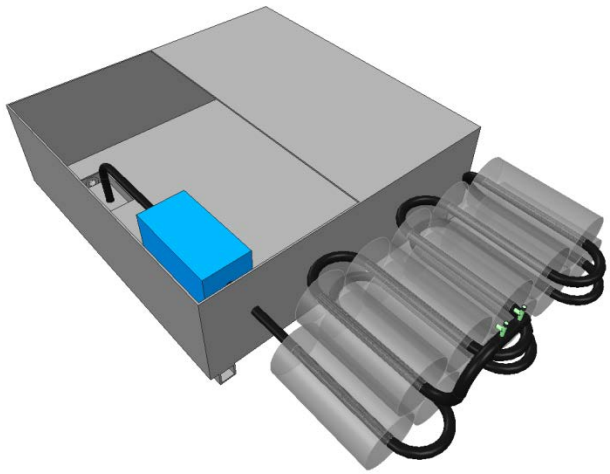

Figure 92 Concept sketch for a low grade steam generator. A reservoir to be filled with water sits next to a bank of Miscibility Gap Alloy barrels laid on their sides. The water is pumped through a tube which passes through the centre of each barrel in series before being extracted at the end of the pipeline. The barrels might be heated electrically during the day for cleaning processes in the evening.

Drying of food, timber products or waste products is common in industry. At a certain scale, drying might be better performed non-stop. If this were the case then a thermal storage system might be beneficial. Zinc-Graphite has a convenient operation temperature for heating air as demonstrated in §8.1. Forced or natural convection over or through an encapsulated block of Zn-C would provide a useful stream of hot air for drying processes.

Silicon-Silicon Carbide MGAs (1411°C operating temperature) operate at a useful temperature for providing thermal inertia to high temperature industry. A calcinating and/or fusion process in clinker production for cement manufacture requires temperatures of ~1500 °C whilst glass production needs furnace temperatures of ~ 1600 °C. Given cement and glass manufacture is extremely energy intensive, Miscibility Gap Alloy thermal storage has the potential to allow producers to maintain a high furnace temperature for continuous production whilst paying only off-peak rates for electricity or gas. Producers might also

consider implementing solar PV or concentrated thermal power to provide energy through the day to the storage material.

Many large ocean going vessels would benefit significantly from increased range. Only a fraction of the chemical energy available in the combusted fuel is converted to thrust for the ship. An additional power cycle to take advantage of the high temperature exhaust gases expelled after combustion could be utilised. These exhaust gases vary in flow rate and temperature depending on the requirements of the ship. Thermal storage utilising Miscibility Gap Alloys can capture the heat from the exhaust and transfer it to the secondary power cycle thus providing storage and effective heat transfer.

Wherever a material is required to be delivered at a specified temperature an opportunity exists for thermal storage materials. A potential use might be in 3d printing of polymers. A polymer must be delivered to a nozzle at a specified temperature such that the fluid flows and sets in a predictable manner. A small thermal storage system at a steady temperature might ensure consistency in printing and at a large scale lead to cost savings from consumption of off-peak power.

A huge variety of applications exist for Miscibility Gap Alloys. Due to their variable operating temperatures, durability, energy density, thermal conductivity and safety the materials are extremely competitive with existing methods. Their unique properties also open up new fields of application that have not had appropriate thermal storage solutions until now.

CONCLUSION

Thermal storage is a modern, globally relevant field with many contributions from myriad different fields of science and engineering. This thesis has introduced Miscibility Gap Alloys as a thermal storage material and contextualised where they fit within this field. Through development and analysis of a number of key indicators of thermal storage performance Miscibility Gap Alloys have been found to be favourable over the current state of the art in a number of applications.

A number of new Miscibility Gap Alloys were synthesised for the first time as part of this work. At initiation of the project only Cu-Fe and Sn-Al systems had successfully been manufactured. The Brass-Graphite, Copper-Graphite, Magnesium-Iron, Silicon-Silicon Carbide and Zinc Graphite systems were made and analysed.

Through integrating computer simulation, manufacturing experiments and review of literature the material properties of a number of potential Miscibility Gap Alloy thermal storage systems were estimated accurately. The range of porosity likely for each system as a result of the manufacturing process was found through experimentation and review of other researchers findings. This information enabled estimation of the equilibrium thermal properties through laws of mixtures and constituent data from literature. The composite thermal conductivity was then estimated accurately through analysis of sample microstructure and development of a Lattice Monte Carlo homogenisation algorithm. Generalisation of this process led to invention of Microstructural Efficiency as a homogenisation method.

The potential for Miscibility Gap Alloys to degrade over time was accounted for through the use of established solid mechanics and chemistry theory and through

development of a diffusional model. The materials are likely to undergo morphological changes due to mechanical effects initially as demonstrated through analysis of a simplified mechanical model. Through consideration of established chemical theory it was shown that the materials will require isolation from the environment to prevent long term corrosion. The developed diffusional model provided guidance on how degradation through diffusional morphological changes could be avoided. Experimental evidence is still required to further validate the theory.

With knowledge of how the alloys would behave in the long term, the economic case for Miscibility Gap Alloy thermal storage could be made. A number of implementations were envisioned and the cost per kWh of stored energy evaluated with consideration of material, manufacturing and infrastructure costs. Comparison to state of the art costs demonstrated that Miscibility Gap Alloys are economically favourable in many cases. Miscibility Gap Alloy systems utilising tin and copper were most expensive whilst those containing brass, silicon, magnesium and zinc were very cost effective.

Once the economic context of the materials was established a number of potential implementations were explored. A practical air heater was designed to take advantage of the Zn-C system and estimates of its performance proved adequate. Two adaptable implementations for concentrated solar power plants were described before a number of more exotic deployments discussed.

Miscibility Gap Alloys have been shown as a novel material that will enable a range of intermittent energy resources to be utilised continuously. This thesis has comprehensively demonstrated the alloys competitiveness in terms of the key indicators of

energy density, effusivity and durability for their cost whilst suggesting how the materials may be implemented.

RECOMMENDATIONS FOR FUTURE WORK

Analysis of New Binary, Ternary and Higher Order Miscibility Gap Alloys

Many exciting new Miscibility Gap Alloys have been identified during the candidate's tenure at the University of Newcastle. These include new low temperature binary systems like Cd-Al and Cd-Fe operating around 321 °C and higher energy density ternary systems of Al-Si-C (~0.5 kWh/L at 577 °C). As commercial opportunities arise alloys with distributed phases melting at the ventures requirements will be developed. The thermal properties, lifetime prediction and economics for specific applications of the new materials may be explored as in this thesis.

Analysis of Microstructural Efficiency Data to Yield a General Form

The transition of Microstructural Efficiency through percolation is potentially analogous to a thermodynamic phase transformation. Transformation from non-percolating to systems percolating in one dimension, two dimension and three dimensions can be considered as different phases of matter with different properties. Structured packings of monodisperse particles will experience such a 'phase change' at a definite volume fraction. Disperse particle sizes will result in a 'mushy' transformation as regions are jammed whilst others still are isolated (rattlers).

The stable phase of a monodisperse configuration/distribution might be described for a volume fraction through an energy term analogous to Gibb's Free Energy. Where a disperse system is encountered an additional parameter describing the different sizes (equivalent to species in a chemical sense) could be introduced.

Regardless of the physical analogues, the curve fitting procedure undertaken for phase diagrams could prove useful in establishing a functional form for Microstructural

efficiency data. A scientist familiar with CALPHAD procedures might find an interesting body of work here.

Incorporation of Further Morphologies into a Microstructural Efficiency Database

Many new composites are invented and described each year. Where composites of varying constituents share a morphology there exists an opportunity to combine the experimental or computational results through Microstructural Efficiency. Metal foams, aerogels, packed beds of particles, 3d printed morphologies and solid-gas reaction products are just a few examples of morphologies that may be studied through these methods.

Extension of Microstructural Efficiency to Incorporate Other Morphology Dependent Properties

Though thermal conductivity was considered throughout this thesis, Microstructural Efficiency may be used to characterise many analogous transient properties in composites. Table 5 (§4.5) describes a number of transient properties that might be considered. The charts developed through the thesis are universal amongst these properties, though the morphologies may not be typical of those encountered in different fields.

Extension to fourth order tensors, specifically elasticity, is thought to also be possible. Testing the response of a solid composite to different strain fields should enable homogenisation of the stiffness or compliance tensor. This might be best performed computationally. If the distribution of phases is macroscopically isotropic then the tensor might be reduced to a Young's modulus and Poisson's ratio (or Shear and Bulk modulus). The sudden change in rigidity upon melting for a Miscibility Gap Alloy could be captured in this way.

Adaption of Diffusion Model to Utilise Distribution of Nuclei Size and Account for Matrix Solution with Further Thermal Cycling Experimentation

The diffusion aging model developed in this thesis made the assumption that only a single nucleus could grow in the centre of the spherical beta phase pocket and that the matrix could be considered an infinite reservoir. These assumptions could be altered to better model the systems provided experimental data was available. The single sphere could be replaced with a distribution of nuclei sizes by considering the energy requirement for each and using a Boltzmann probability distribution. If the matrix size could be defined in a meaningful way generally the consumption of beta phase might be better considered in the long term behaviour.

Implement Miscibility Gap Alloys at a Commercial Scale

This thesis has established the information required to implement Miscibility Gap Alloys at a commercial level. Material properties have been accurately estimated such that capacity and infrastructure design may proceed. The expected lifetime of the materials is known and the economic case made for a number of different implementations. Designing a thermal storage device to the specifications of an industry partner may now proceed.

REFERENCES

[1] H. Paksoy, Preface, in: H.Ö. Paksoy (Ed.) Thermal Energy Storage for Sustainable Energy Consumption, Springer, 2007.
[2] D. Lew, N. Miller, K. Clark, G. Jordan, Z. Gao, Impact of High Solar Penetration in the Western Interconnection, National Renewable Energy Laboratory, 2010.
[3] E. Kisi, H. Sugo, D. Cuskelly, (2014), Alloys with inverse microstructures, 2012904737, http://www.google.com/patents/WO2014063191A1?cl=en.
[4] Retro Middle East: From camels to cosmopolitan - the changing Gulf landscape, in: Al Bawaba, 2013, http://www.albawaba.com/slideshow/gulf-modern-history-cities-513334.
[5] NASA/GSFC/METI/ERSDAC/JAROS, U.S./Japan ASTER Science Team, Brazil-Bolivia Border, NASA Jet Propulsion Laboratory, California Institute of Technology, 2008, http://www.jpl.nasa.gov/spaceimages/details.php?id=PIA16991.
[6] Key World Energy Statistics, International Energy Agency, 2015.
[7] S. Kreis, The Origins of the Industrial Revolution in England, The History Guide: Lectures on Modern European Intellectual History, 2011, http://www.historyguide.org/intellect/lecture17a.html.
[8] N. Forbes, B. Mahon, Faraday, Maxwell, and the Electromagnetic Field: How Two Men Revolutionized Physics, Prometheus Books, 2014.
[9] R. Munroe, Log Scale, (2013), https://xkcd.com/1162/.
[10] Desertec Foundation, Desertec Foundation, 2016, http://www.desertec.org/.
[11] C. Renfrew, Archeology Theories, Methods and Practice, Thames and Hudson Ltd, The United States, 1991.
[12] H. Knight, Umu-Ti, The Journal of the Polynesian Society, 75(3) (1996) 332-347.
[13] E. Morofsky, History of Thermal Energy Storage, in: H.Ö. Paksoy (Ed.) Thermal Energy Storage for Sustainable Energy Consumption Fundamentals, Case Studies and Design, Springer, 2007.
[14] R.H. Maskrey, W.J. Thayer, A Brief History of Electrohydraulic Servomechanisms, ASME Journal of Dynamic Systems, 141 (1978).
[15] B. Zalba, J. Marìn, L. Cabeza, H. Mehling, Review on thermal energy storage with phase change: materials, heat transfer analysis and applications, Applied Thermal Engineering, 23 (2003) 251-283.
[16] U. Herrmann, D. Kearney, Overview on Thermal Storage Systems, FLABEG, 2002.
[17] S. Khare, M. Dell'Amico, C. Knight, S. McGarry, Selection of materials for high temperature latent heat energy storage, Solar Energy Materials & Solar Cells, 107 (2012) 20-27.
[18] D. Laing, C. Bahl, T. Bauer, M. Fiss, N. Breidenbach, M. Hempel, High-Temperature Solid Media Thermal Energy Storage for Solar Thermal Power Plants, Proceedings of the IEEE, 100(2) (2012) 516-524.
[19] A. Sharma, V.V. Tyagi, C.R. Chen, D. Uddhi, Review on thermal energy storage with phase change materials and applications, Renewable and Sustainable Energy Reviews, 13 (2009) 318-345.
[20] R. Tamme, Optimised Industrial Process heat and Power Generation with Thermal Energy Storage, ECES, 2010.

[21] M.M. Farid, A.M. Khudhai, S.A.K. Razack, S. Al-Hallaj, A review on phase change energy storage: materials and applications, Energy Conversion and Management, 45 (2004) 1597-1615.
[22] M. Liu, W. Saman, F. Bruno, Review on storage materials and thermal performance enhancement techniques for high temperature phase change thermal storage systems, Renewable and Sustainable Energy Reviews, 16 (2012) 2118-2132.
[23] M.M. Kenisarin, High-temperature phase change materials for thermal energy storage, Renewable and Sustainable Energy Reviews, 14 (2010) 955-970.
[24] J.Q. Sun, R.Y. Zhang, Z.P. Liu, G.H. Lu, Thermal reliability test of Al-34%Mg-6%Zn alloy as latent heat storage material and corrosion of metal with respect to thermal cycling, Energy Conversion and Management, 48 (2007) 619-624.
[25] J.P. Kotzè, T.W.v. Backström, High Temperature Thermal Energy Storage Utilising Metallic Phase Change Materials and Metallic Heat Transfer Fluids, Journal of Solar Energy Engineering, 135 (2013) 1-6.
[26] P. Tatsidjodoung, N.L. Pierred, L. Luo, A review of potential materials for thermal energy storage in building applications, Renewable and Sustainable Energy Reviews, 18 (2013) 327-349.
[27] A.J. Rawson, H. Sugo, E. Kisi, Characterising Thermal Properties of Miscibility Gap Alloys for Thermal Storage Applications, in: Solar2014: The 52nd Annual Conference of the Australian Solar Council, Melbourne, Australia, 2014,
[28] H. Sugo, E. Kisi, D. Cuskelly, Miscibility gap alloys with inverse microstructures and high thermal conductivity for high energy density thermal storage applications, Applied Thermal Engineering, 51 (2013) 1345-1350.
[29] H. Sugo, D. Cuskelly, A. Rawson, E. Kisi, High Conductivity Phase Change Materials for Thermal Energy Storage - Miscibility Gap Alloys, in: Solar2014: The 52nd Annual Conference of the Australian Solar Council, Melbourne, Australia, 2014,
[30] R. Velraj, R. Seeniraj, B. Hafner, C. Faber, K. Schwarzer, Heat transfer enhancement in a latent heat storage system, Solar energy, 65(3) (1999) 171-180.
[31] H. Price, D. Kearney, Parabolic-Trough Technology Roadmap: A Pathway for Sustained Commercial Development and Deployment of Parabolic Trough Technology, SunLab/NREL and Keaney and Associates, 1999.
[32] J. Pacheco, S. Showalter, W. Kolb, Development of a molten-salt thermocline thermal storage system for parabolic trough plants, in: Solar Energy: The Power to Choose, Washington DC, 2001,
[33] C. Turchi, M. Mehos, C. Ho, G. Kolb, Current and Future Costs for Parabolic Trough and Power Tower Systems in the US Market, in: SolarPACES 2010, Perpignan, France, 2010,
[34] C. Smith, Y. Sun, B. Webby, A. Beath, F. Bruno, Cost analysis of high temperature thermal energy storage for solar power plant, in: Solar2014, Melbourne, Australia 2014, 2014,
[35] S. Kuravi, J. Trahan, D.Y. Goswami, M.M. Rahman, E.K. Stefanakos, Thermal energy storage technologies and systems for concentrating solar power plants, Progress in Energy and Combustion Science, 39(4) (2013) 285-319.
[36] IRENA, Concentrating Solar Power, 2012.

[37] W. Zhang, Concentrating Solar Power - State of the Art, Cost Analysis and Pre-Feasibility Study for the Implementation in China, Institut für Energiewirtschaft und Rationelle Energieanwendung, Stuttgart, Weinstadt, 2009.
[38] J.C. Maxwell, A Treatise on Electricity and Magnetism, 1st. ed., Clarendon Press, Oxford, 1873.
[39] L. Rayleigh, On the influence of obstacles in rectangular order upon the properties of a medium, Philosophical Magazine, 56 (1892) 481-502.
[40] R. Landauer, Electrical conductivity in inhomogeneous media, AIP Conference Proceedings, 40(1) (1978) 2-45.
[41] Z. Hashin, Analysis of Composite Materials - A Survey, Journal of Applied Mechanics, 50 (1983) 481-505.
[42] R.C. Progelhof, J.L. Throne, R.R. Ruetsch, Methods for Predicting the Thermal Conductivity of Composite Systems: A Review, Polymer Engineering and Science, 16(9) (1976) 615-625.
[43] J. Wang, J.K. Carson, M.F. North, D.J. Cleland, A new approach to modelling the effective thermal conductivity of heterogeneous materials, International Journal of Heat and Mass Transfer, 49 (2006) 3075-3083.
[44] H. Lorentz, The Theory of Electrons, 1868.
[45] A. Eucken, Allgemeine Gesetzmäßigkeiten für das Wärmeleitvermögen verschiedener Stoffarten und Aggregatzustände., Forschung., 11 (1940) 6-20.
[46] P. Furmañski, Heat conduction in composites: Homogenization and macroscopic behaviour, Applied Mechanics Reviews, 50(6) (1997) 327-356.
[47] R.J. Clausius, The Mechanical Theory of Heat, 1879.
[48] H. Fricke, Mathematical treatment of the electric conductivity and capacity of disperse systems, Physical Review, 24 (1924) 575-587.
[49] W. Davies, The dielectric constant of fibre composites, Journal of Physics D: Applied Physics, 7 (1974) 120-130.
[50] H. Hatta, M. Taya, Equivalent inclusion method for steady state heat conduction in composites, INternational Journal of Engineering Science, 24(7) (1986) 1159-1172.
[51] R.E. Meredith, C.W. Tobias, Resistance to potential flow through a cubical array of spheres, Journal of Applied Physics, 31(7) (1960) 1270-1273.
[52] A.S. Sangani, A. Acrivos, The effective conductivity of a periodic array of spheres, Proceedings of the Royal Society A: Mathematical, Physical and Engineering Sciences., 386(1791) (1983) 263-275.
[53] D.A.G. Bruggeman, Berechnung verschiedener physikalischer Konstanten von heterogenen Substanzen, Dielectrizitátkonstanten und Leitfähigkeiten der Mischkörper aus isotropen Substanzen, Annalen der Physik, 416 (1935).
[54] R. Landauer, The Electrical Resistance of Binary Metallic Mixtures, Journal of Applied Physics, 23(7) (1952) 779-784.
[55] S. Kirkpatrick, Percolation and Conduction, Reviews of Modern Physics, 45(4) (1973) 574-588.
[56] S. Torquato, G. Stell, Microstructure of two-phase random media. I. The n-point probability function, The Journal of Chemical Physics, 77 (1982) 2071-2077.
[57] S. Torquato, Random Heterogeneous Materials: Microstructure and Macroscopic Properties, in, Springer, New York, 2002, pp. 1333-1356.

[58] J.B. Keller, Conductivity of a Medium Containing a Dense Array of Perfectly Conducting Spheres or Cylinders or Nonconducting Cylinders, Journal of Applied Physics, 34(991) (1963).
[59] J.B. Keller, A Theorem on the Conductivity of a Composite Medium, Journal of Mathematical Physics, 5(4) (1964) 548-549.
[60] K. Schulgasser, A reciprocal theorem in two-dimensional heat transfer and its implications, International Communications in Heat and Mass Transfer, 19(5) (1992) 639-649.
[61] J.A.d. Rio, R.W. Zimmerman, R.A. Dawe, Formula for the conductivity of a two-component material based on the reciprocity theorem, Solid State Communications, 106(4) (1998) 183-186.
[62] O.H. Wiener, Physikalischen Klasse der Königlich Sächsischen Gesellshaft der Wisssenshaften, Abhandlungen der Mathematisch, 32 (1912).
[63] K. Lichtenecker, Phys. Z., 27 (1926).
[64] Z. Hashin, S. Shtrikman, A Variational Approach to the Theory of the Effective Magnetic Permeability of Multiphase Materials, Journal of Applied Physics, 33(10) (1962) 3125-3131.
[65] W.F. Brown, Dielectric constants, permeabilities and conductivities of random media, Transaction of the Society of Rheology, 9 (1965).
[66] M.J. Beran, Use of the variational approach to determine bounds for the effective permittivity in random media, Nuovo Cimento, 38 (1965).
[67] A.J. Rawson, H. Sugo, E. Kisi, T. Fiedler, Effective Conductivity of Cu-Fe and Sn-Al Miscibility Gap Alloys, International Journal of Heat and Mass Transfer, 77 (2014) 395-405.
[68] A.J. Rawson, E. Kisi, C. Wensrich, Microstructural Efficiency: Structured Morphologies, International Journal of Heat and Mass Transfer, 81 (2014) 820-828.
[69] I.V. Belova, G.E. Murch, T. Fiedler, A. Öchsner, The Lattice Monte Carlo Method for Solving Phenomenological Mass and Heat Transport Problems, diffusion-fundamentals, 4 (2007) 15.11-15.23.
[70] G.E. Murch, A.S. Nowick, Diffusion in Crystalline Solids, in: A.S. Nowick, G.G. Libowitz (Eds.) Materials Science and Technology series, Academic Press Inc., Sydney, 1984,
[71] H.L. Anderson, Metropolis, Monte Carlo, and the Maniac, in: Los Alamos Science, 1986, pp. 96-107,
[72] P.A. Flinn, G.M. McManus, Monte Carlo Calculation of the Order-Disorder Transformation in the Body-Centered Cubic Lattice, Physical Review, 124(1) (1961) 54-59.
[73] H. Mehrer, Zufallswege und Reaktionen atomarer Gitterfehler in Modellkristallen I. Die Simulationsmethode und ihre Andwndung auf die Ausscheidung von Leerstellen, Zeitschrift für Naturforschung A, 24 (1969) 358-367.
[74] H. Mehrer, Zufallswege und Reaktionen atomoarer Gitterfehler in Modellkristallen II Rekombination von Zwischengitteratomen und Leerstellen, Zeitschrift für Naturforschung A, 24 (1969) 367-376.
[75] C.H. Bennett, B.J. Alder, Persistence of vacancy motion in hard sphere crystals, Journal of Physics and Chemistry of Solids, 32(9) (1971) 2111-2122.

[76] T. Fiedler, I.V. Belova, G.E. Murch, Theoretical and Lattice Monte Carlo analyses on thermal conduction in cellular metals, Computational Materials Science, 50 (2010) 503-509.
[77] T. Fiedler, E. Solorzano, F. Garcia-Moreno, A. Öchsner, I.V. Belova, G.E. Murch, Lattice Monte Carlo and Experimental Analyses of the Thermal Conductivity of Random-Shaped Cellular Aluminium, Advanced Engineering Materials, 11(10) (2009) 843-847.
[78] T. Fiedler, A. Ochsner, N. Muthubandara, I.V. Belova, G.E. Murch, Calculation of the Effective Thermal Conductivity in Composites Using Finite Element and Monte Carlo Methods, Diffusion in Solids and Liquids II, 553 51-56.
[79] T. Fiedler, I.V. Belova, A. Öchsner, G.E. Murch, Lattice Monte Carlo Analysis of Thermal Diffusion in Multi-Phase Materials, in: Heat Transfer in Multi-Phase Materials, Springer, 2011, pp. 275-300.
[80] T. Fiedler, I.V. Belova, G.E. Murch, Lattice Monte Carlo analyses of thermal diffusion in laminar flow, in, http://hdl.handle.net/1959.13/932881.
[81] N. Maruoka, K. Sato, J.-i. Yagi, T. Akiyama, Development of PCM for Recovering High Temperature Waste Heat and Utilization for Producing Hydrogen by Reforming Reaction of Methane, ISIJ International, 42(2) (2002) 215-219.
[82] C.E. Andraka, A.M. Kruizenga, B.A. Hernandez-Sanchez, E.N. Coker, Metallic Phase Change Material Thermal Storage for Dish Stirling, Energy Procedia, 69 (2015) 726-736.
[83] P. Strunz, D. Mukherji, R. Gilles, T. Geue, J. Roesler, Investigation of metal-matrix composite containing liquid phase dispersion, in: 5th European Conference on Neutron Scattering, IOP Publishing, Prague, Czech Republic, 2012,
[84] H. Gabrisch, L. Kjeldgaard, E. Johnson, U. Dahmen, Equilibrium Shape and Interface Roughening of Small Liquid Pb Inclusions in Solid Al, Acta Materialia, 49 (2001) 4259-4269.
[85] C.P. Wang, X.J. Liu, I. Ohnuma, R. Kainuma, K. Ishida, Formation of Immiscible Alloy Powders with Egg-Type Microstructure, Science, 297 (2002) 990-993.
[86] R.E. Reed-Hill, R. Abbaschian, Physical Metallurgy Principles, Third ed., PWS-Kent, Boston, Massachusetts, 1992.
[87] D.V. Schroeder, An Introduction to Thermal Physics, Addison Wesley Longman, Sydney, 1999.
[88] M.J. Moran, H.N. Shapiro, Fundamentals of Engineering Thermodynamics, Second ed., John Wiley & Sons, New York City, NY, USA, 1993.
[89] F. Incropera, D. Dewitt, T. Bergman, A. Lavine, Fundamentals of heat and mass transfer, Wiley & Sons, Inc., Hoboken, NJ, USA, 2006.
[90] C.Y. Ho, R.W. Powell, P.E. Liley, Thermal Conductivity of the Elements, Journal of Physical and Chemical Reference Data, 1(2) (1972) 143.
[91] C.Y. Ho, R.W. Powell, P.E. Liley, Thermal Diffusivity of the Elements, Journal of Physical and Chemical Reference Data, (1972).
[92] J.A. Balderas-Lòpez, G. Gutièrrez-Juàrez, M.R. Jaime-Fonseca, F. Sànchez-Sinencio, Measurements of thermal effusivity of liquids using a conventional photoacoustic cell, Review of Scientific Instruments, 70(4) (1999) 2069-2071.
[93] H. Baker, ASM Metals Handbook: Phase Diagrams, 10th ed., ASM International, Ohio, 1992.
[94] N. Saunders, A.P. Miodownik, CALPHAD (Calculation of Phase Diagrams): A Comprehensive Guide, Pergamon, 1998.

[95] J. Crank, The Mathematics of Diffusion, 2 ed., Oxford University Press, London, 1975.
[96] J.W. Cahn, J.E. Hilliard, Free Energy of a Nonuniform System. I. Interfacial Free Energy, The Journal of Chemical Physics, 28 (1958) 258.
[97] J.W. Cahn, On spinodal decomposition, Acta Metallurgica, 9(9) (1961) 795-801.
[98] K.S. Reddy, K. P, Combinatory Models for Predicting the Effective Thermal Conductivity of Frozen and Unfrozen Food Materials, Advances in Mechanical Engineering, 2010 (2010).
[99] J.K. Carson, Prediction of the Thermal Conductivity of Porous Foods, Massey University, Palmerston North, New Zealand, 2002.
[100] J. Halpin, Primer on Composite Materials; Analysis, 2nd (Revised) ed., CRC Press, 1992.
[101] D.R. Lovett, Tensor properties of crystals, IOP Publishing, Bristol, 1989.
[102] Granta Design Limited, Granta CES 2015, in, 2015,
[103] L. Vitos, A.V. Ruban, H.L. Skriver, J. Kollár, The surface energy of metals, Surface Science, 411(1–2) (1998) 186-202.
[104] I. Stubna, S. Valovic, Linear thermal expansion of the two-phase ceramics.
[105] Entegris Inc., Properties and Characteristics of Graphite for the Semiconductor Industry, Entegris Inc.,, 2013.
[106] AZO Network, Carbon - Graphite Materials, 2015, http://www.azom.com/properties.aspx?ArticleID=516.
[107] Total Materia, Magnesium and Magnesium Alloys, 2006, http://www.totalmateria.com/Article138.htm.
[108] O. Kubaschewski, B.E. Hopkins, Oxidation of Metals and Alloys, Second ed., Butterworth & Co. (Publishers) LTD., London, 1962.
[109] Atlas Steels, Galvanic Corrosion, Atlas Steels,, 2010.
[110] H.-C. Chang, L.-C. Wang, A Simple Proof of Thue's Theorem on Circle Packing, arXiv Mathematics, (arXiv:1009.4322) (2010).
[111] V. Šmilauer, Welcome to Yade - Open Source Discrete Element Method, 2009, https://yade-dem.org/doc/.
[112] B. Monnier, Investigation of Miscibility Gap Alloy Thermal Storage Materials, University of Technologie Troyes, Newcastle, 2015.
[113] N. Morton, MGA PCMs in High temperature TES applications, University of Newcastle, Newcastle, 2014.
[114] P. Steel, Optimising high temperature high energy density Silicon-Silicon Carbide thermal energy storage medium for practical application, University of Newcastle, Newcastle, 2014.
[115] M. Jackson, Design and construction of miscibility gap alloy high energy density thermal storage demonstration apparatus, University of Newcastle, Newcastle, 2014.
[116] National Physical Laboratory, MTDATA – Phase Diagram Software from the National Physical Laboratory, 2011,
[117] P.J. Fensham, Self-Diffusion in Tin Crystals, Australian Journal of Scientific Research, Series A: Physical Sciences, 3 (1949).
[118] S.H. Ma, R.A. Swalin, Self-Diffusion in Liquid Tin, The Journal of Chemical Physics, 36(11) (1962) 3014-3018.

[119] G.E.K. Freitag, G. Rummel, H. Mehrer, Volume and grain boundary diffusion of implanted ^{113}Sn in Aluminium, Applied Physics A: Solids and Materials, 53(4) (1991) 297-302.
[120] A. Sawatzky, Diffusion of Indium in Tin Single Crystals, Journal of Applied Physics, 29(9) (1958) 1303-1305.
[121] C.H. Ma, R.A. Swalin, Self-Diffusion in Liquid Tin, The Journal of Chemical Physics, 36(11) (1962) 3014-3018.
[122] M. Beyeler, Y. Adda, Détermination des volumes d'activation pour la diffusion des atomes dans l'or, le cuivre et l'aluminium, J. Phys. France, 29(4) (1968) 345-352.
[123] D.B. Butrymowicz, J.R. Manning, M.E. Read, Diffusion in Copper and Copper Alloys: Part 1. Volume and Surface Self-Diffusion in Copper, Journal of Physical and Chemical Reference Data, 2(3) (1973) 643-655.
[124] M.S. Anand, R.P. Agarwala, Diffusion of Copper in Iron, Journal of Applied Physics, 37(11) (1966) 4248-4251.
[125] G. Salje, M. Feller-Kniepmeier, The diffusion and solubility of copper in iron, Journal of Applied Physics, 48(5) (1977) 1833-1839.
[126] D.B. Butrymowicz, J.R. Manning, M.E. Read, Diffusion in Copper and Copper Alloys Part IV. Diffsuion in Systems Involving Elements of Group VIII, Journal of Physical and Chemical Reference Data, 5(1) (1973) 103-200.
[127] F.S. Buffington, K. Hirano, M. Cohen, Self diffusion in iron, Acta Metallurgica, 9(5) (1961) 434-439.
[128] L. Xiaowei, R. Jean-Charles, Y. Suyuan, Effect of temperature on graphite oxidation behavior, Nuclear Engineering and Design, 227(3) (2004) 273-280.
[129] R.J. Lancashire, Some chemistry of Iron, 2008, http://wwwchem.uwimona.edu.jm/courses/iron.html.
[130] J. Roy, S. Chandra, S. Das, S. Maitra, Oxidation Behaviour of Silicon Carbide a Review, Reviews on Advanced Materials Science, 38 (2014) 29-39.
[131] I Squared R Element Co. Inc., Silicon Carbide Heating Element Use by Atmosphere, in: I Squared R Element Co. Inc. (Ed.),
[132] KANTHAL, Silicon Carbide - Electric heating elements, in: Sandvik (Ed.), http://heatingelements.hitempproducts.com/Asset/Silicon-Carbide-Electric-Heating-Elements.pdf.
[133] E.N. Coker, The oxidation of aluminium at high temperature studied by Thermogravimetric Analysis and Differential Scanning Calorimetry, SAND2013-8424, Sandia National Laboratories, 2013.
[134] Scott Metals, Black Steel Pipe, in: Scott Metals (Ed.), 2015, http://www.scottmetals.com.au/pipe.php.
[135] All Things Stainless, Stainless Steel Sheet, 2015, http://allthingsstainless.com.au/stainless-steel-sheet.html.
[136] Materials Handling, 205 Litre Stainless Steel Drums, 2015, http://www.materialshandling.com.au/products/205-litre-steel-drums/.
[137] Australian Trade & Shipping, Container Sizes, 2015, http://www.australiatrade.com.au/Shipping/ContainerSizeSales/.
[138] Dempsey's Forge, Thermal Ceramics Kaowool, 2015, http://www.anvilfire.com/sales/pages/kaowool_index.htm.

[139] R.H.S. Winterton, Where did the Dittus and Boelter equation come from?, International Journal of Heat and Mass Transfer, 41(4-5) (1997) 809-810.
[140] Graphite Energy, Technology Demonstration, 2016, http://www.graphiteenergy.com/technology-demonstration.php.
[141] Y.C.S. Too, R. Olivares, R. Benito, J.-S. Kim, G. Duffy, J. Edwards, High Temperature Thermal Energy Storage Systems for Open-Cycle Solar Air Brayton Plant, CSIRO, 2012.
[142] Y. Tian, C.Y. Zhao, A review of solar collectors and thermal energy storage in solar thermal applications, Applied Energy, 104 (2013) 538-553.
[143] S. McCracken, Quotes of Thermal Oils for Wallsend Solar Thermal Plant, in: A. Rawson (Ed.), 2014,
[144] R. Bayon, E. Rojas, L. Valenzula, E. Zarza, J. Leon, Analysis of the experimental behaviour of a 100 kW_{th} latent heat storage system for direct steam generation in solar thermal power plants, Applied Thermal Engineering, 30 (2010) 2643-2651.
[145] D.F. Williams, L.M. Toth, K.T. Clarno, Assessment of Candidate Molten Salt Coolants for the Advanced High-Temperature Reactor (AHTR), ORNL/TM-2006/12, Oak Ridge National Laboratory, Oak Ridge, Tennessee, USA, 2006.
[146] D. Laing, C. Bahl, T. Bauer, M. Fiss, N.B.M. Hempel, High-Temperature Solid Media Thermal Energy Storage for Solar Thermal Power Plants, Proceedings of the IEEE, 100(2) (2012) 516-524.
[147] P. Hidnert, H.S. Krider, Thermal Expansion of Some Copper Alloys, Journal of Research of the National Bureau of Standards, 39 (1947) 419-424.
[148] G.R. Gathers, Thermophysical properties of liquid copper and aluminum, Int J Thermophys, 4(3) (1983) 209-226.
[149] A.T.D. Butland, R.J. Maddison, The Specific Heat of Graphite: An evaluatation of measurements, Journal of Nuclear Materials, 49 (1973) 45-56.
[150] M.J. Richardson, Specific Heat Capacities, Kaye & Laby, Tables of Physical & Chemical Constants, 2015, http://www.kayelaby.npl.co.uk/general_physics/2_3/2_3_6.html.
[151] G.K. White, S.J. Collocott, Heat Capacity of Reference Materials: Cu and W, Journal of Physical and Chemical Reference Data, 13(4) (1984) 1251-1257.
[152] V.Y. Chekhovskoi, V.D. Tarasov, Y.V. Gusev, Calorific properties of liquid copper, High Temp, 38(3) (2000) 394-399.
[153] P.D. Desai, Thermodynamic Properties of Iron and Silicon, Journal of Physical and Chemical Reference Data, 15(3) (1986) 967-983.
[154] P.J. McGonigal, A.D. Kirshenbaum, A.V. Grosse, The Liquid Temperature Range, Density and Critical Constants of Magnesium, The Journal of Physical Chemistry, 66(4) (1962) 737-740.
[155] C.B. Albock, M.W. Chase, V. Itkin, Thermodynamic Properties of the Group IIA Elements, Journal of Physical and Chemical Reference Data, 22(1) (1992) 1-85.
[156] A.H. Rashed, Properties and Characteristics of Silicon Carbide, Poco Graphite, Inc., 2002.
[157] M.J. Assael, I.J. Armyra, J. Brillo, S.V. Stankus, J. Wu, W.A. Wakeham, Reference Data for the Density and Viscosity of Liquid Cadmium, Cobalt, Gallium, Indium, Mercury, Silicon, Thallium and Zinc, Journal of Physical and Chemical Reference Data, 41(3) (2012).

[158] M.E. Levinshtein, S.L. Rumyantsev, M.S. Shur, Properties of Advanced Semiconductor Materials: GaN, AIN, InN, BN, SiC, SiGe, Wiley, 2001.
[159] B.B. Alchagirov, A.M. Chochaeva, Temperature dependence of the density of liquid tin, High Temp, 38(1) (2000) 44-48.
[160] eFunda, Heat Capacity: Aluminum, 2016, http://www.efunda.com/materials/elements/HC_Table.cfm?Element_ID=Al.
[161] F. Grønvold, S. Stølen, Heat capacity of solid zinc from 298.15 to 692.68 K and of liquid zinc from 692.68 to 940 K: thermodynamic function values, Thermochimica Acta, 395(1–2) (2002) 127-131.
[162] Australian Aluminium Council Ltd., Aluminium Smelting, 2014, http://aluminium.org.au/flowchart/aluminium-smelting.html.
[163] InfoMine Inc., Historical Aluminum Prices and Price Chart, (2014), http://www.infomine.com/investment/metal-prices/aluminum/all/.
[164] J.S. Kharakwal, L.K. Gurjar, Zinc and Brass in Archaeological Perspective. , Ancient Asia, (2006) 139-159.
[165] Australian Government: Geoscience Australia, Copper - Mineral Fact Sheets, 2012, http://www.australianminesatlas.gov.au/aimr/commodity/copper.html.
[166] InfoMine Inc., Historical Copper Prices and Price Chart, (2014), http://www.infomine.com/investment/metal-prices/copper/all/.
[167] S. Moores, Flake Graphite: Supply, Demand, Prices - GMP Securities, 2014, http://americanresources.org/wp-content/uploads/2012/12/Industrial-Minerals-Data-Report.pdf.
[168] Canada Carbon, What is Graphite, 2014, http://www.canadacarbon.com/what-is-graphite.
[169] Australian Government: Geoscience Australia, Iron Ore - Mineral Fact Sheets, 2012, http://www.australianminesatlas.gov.au/aimr/commodity/iron_ore.html.
[170] Australian Government: Geoscience Australia, Magnesium - Mineral Fact Sheets, 2012, http://www.australianminesatlas.gov.au/education/fact_sheets/magnesium.html.
[171] Skylighter Inc., Magnesium, Atomized, +200-325 Mesh, in: Skylighter Inc. (Ed.), 2014, http://www.skylighter.com/mall/product-details.asp?id=2477.
[172] InfoMine Inc., Historical Magnesium Prices and Price Chart, (2014), http://www.infomine.com/investment/metal-prices/magnesium/all/.
[173] Silicon (Si), in: Encyclopaedia Britannica, 2014, http://www.britannica.com/EBchecked/topic/544301/silicon.
[174] silicon carbide, in: Encyclopædia Britannica, 2015, http://www.britannica.com/EBchecked/topic/544369/silicon-carbide.
[175] Australian Government: Geoscience Australia, Tin - Mineral Fact Sheets, 2012, http://www.australianminesatlas.gov.au/education/fact_sheets/tin.html.
[176] InfoMine Inc., Historical Tin Prices and Price Chart, (2014), http://www.infomine.com/investment/metal-prices/tin/all/.
[177] Australian Government: Geoscience Australia, Zinc, Lead, Silver - Mineral Fact Sheets, 2012, http://www.australianminesatlas.gov.au/aimr/commodity/zinc_lead_silver.html.
[178] Zinc (Zn), in: Encyclopedia Britannica, 2014, http://www.britannica.com/EBchecked/topic/657264/zinc-Zn.

[179] InfoMine Inc., Historical Zinc Prices and Price Chart, (2014), http://www.infomine.com/investment/metal-prices/zinc/all/.

APPENDIX A: LISTING OF NOMINAL THERMAL PROPERTIES AND COST OF THERMAL STORAGE MATERIALS

APPENDIX A: LISTING OF NOMINAL THERMAL PROPERTIES AND COST OF THERMAL STORAGE MATERIALS

Material	Type	Tm [°C]	k [W/mK]	C [J/kgK]	ρ [kg/m^3]	e [kJs$^{0.5}$/m^{4}K]	λ [kJ/kg]	ρe [kWh/L]	Cost [USD/T]	Cost [USD/L]	Cost [USD/kWh]	ρe,eff [J^{2}s$^{0.5}$/m^{5}K]	Mat Prop Ref	Mat Cost Ref
Si50-SiC	MGA	1411	76.4	837	2720	13.2	834	0.69	2000	5.44	7.85	3.29E+13	This Work	This Work
FeSi50-C	MGA	1205	61.7	788	2725	11.5	836	0.69	1740	4.74	6.84	2.87E+13	This Work	This Work
Cu50-Fe	MGA	1084	198.5	407	8295	25.9	107	0.34	5793	48.05	141.30	3.17E+13	This Work	This Work
Cu50-C	MGA	1084	182.7	467	5520	21.7	167	0.33	6200	34.22	104.66	2.55E+13	This Work	This Work
Al50-Si	MGA	660	165.1	862	2515	18.9	303	0.27	1799	4.53	16.66	1.85E+13	This Work	This Work
ZnFe50-Fe	MGA	780	82.6	407	7468	15.8	86	0.26	1273	9.51	36.21	1.50E+13	This Work	This Work
Brass(60/40)-C	MGA	895	79.0	456	5325	13.8	128	0.26	4582	24.40	95.08	1.28E+13	This Work	This Work
Zn50-C	MGA	420	68.2	467	4693	12.2	88	0.18	2168	10.17	57.91	7.73E+12	This Work	This Work
Zn50-Si	MGA	420	122.9	467	4733	16.5	86	0.17	2034	9.63	55.24	1.03E+13	This Work	This Work
Mg50-Fe	MGA	650	99.4	568	4769	16.4	67	0.16	1201	5.73	34.92	9.68E+12	This Work	This Work
Sn50-Zn	MGA	198	88.8	253	7208	12.7	45	0.14	17254	124.36	885.19	6.44E+12	This Work	This Work
Sn50-Al	MGA	230	118.4	399	4990	15.4	43	0.12	16554	82.60	718.21	6.36E+12	This Work	This Work
Silicon	Metal	1411	130.0	710	2330	14.7	1926	1.29	2000	4.66	3.61	6.82E+13	[102]	Append F
Iron	Metal	1127	55.0	460	7800	14.0	272	0.69	800	6.24	9.06	3.48E+13	[102]	Append F
Copper	Metal	1084	400.0	390	8790	37.0	205	0.60	7367	64.76	108.69	7.94E+13	[102]	Append F
Brass 95/5	Metal	1055	272.0	377	8850	30.1	200	0.59	7101	62.84	107.36	6.35E+13	[102]	Append F
Brass 70/30	Metal	910	146.4	460	8550	24.0	177	0.53	5770	49.34	92.99	4.58E+13	[102]	Append F
Brass 60/40	Metal	895	142.3	376	8400	21.2	168	0.48	5238	44.00	91.63	3.66E+13	[102]	Append F
Aluminium	Metal	660	205.0	910	2700	22.4	398	0.37	1736	4.69	12.78	2.96E+13	[102]	Append F
Zinc	Metal	420	116.0	390	7135	18.0	113	0.30	2045	14.59	48.43	1.95E+13	[102]	Append F
Magnesium	Metal	650	156.0	1050	1738	16.9	368	0.23	2500	4.35	19.03	1.39E+13	[102]	Append F

Tin	Metal	230	67.0	210	7280	10.1	59	0.16	22050	160.52	992.25	5.89E+12	[102]	Append F
Lead-Bismuth Eutectic	Metal	125	20.1	138	9676	5.2	39	0.14	15500	149.98	1064.89	2.63E+12	[141]	[102]
Synthetic Oil	Oil	300	0.1	2300	900	0.5	0	0.06	3000	2.70	46.96	9.88E+10	[142]	[142]
MOBILETHERM 605	Oil	200	0.1	2700	750	0.5	0	0.06	5285	3.96	70.47	9.98E+10	[142]	[143]
Mineral Oil	Oil	250	0.1	2600	770	0.5	0	0.06	300	0.23	4.15	9.81E+10	[142]	[142]
Silicone Oil	Oil	350	0.1	2100	900	0.4	0	0.05	5000	4.50	85.71	8.22E+10	[142]	[142]
DowTherm A	Oil	300	0.1	2230	800	0.4	0	0.05	6342	5.07	102.38	7.54E+10	[142]	[143]
LiF	PCM	848	0.6	1366	2526	1.4	1087	0.86	2000	5.05	5.88	4.30E+12	[141]	[1]
NaF	PCM	995	0.6	1366	2526	1.4	790	0.65	800	2.02	3.11	3.25E+12	[141]	[1]
LiF-NaF-MgF2	PCM	693	0.6	1366	2526	1.4	690	0.58	1600	4.04	6.97	2.90E+12	[141]	[1]
FeF2	PCM	1100	0.6	1366	2526	1.4	550	0.48	10000	25.26	52.43	2.41E+12	[141]	[1]
LiF-MgF2	PCM	728	0.6	1366	2526	1.4	520	0.46	1800	4.55	9.87	2.31E+12	[141]	[1]
LiF20-80LiOH	PCM	426	0.5	1000	1600	0.9	869	0.43	4540	7.26	16.87	1.39E+12	[23]	[23]
Li2CO335-65K2CO3	PCM	505	1.9	1760	2260	2.7	344	0.33	880	1.99	6.09	3.22E+12	[23]	[23]
KCl25-27CaCl2-48MgCl2	PCM	487	0.9	920	2530	1.4	342	0.31	180	0.46	1.49	1.57E+12	[23]	[23]
NaCl33-67CaCl2	PCM	500	1.0	1000	2160	1.5	281	0.23	70	0.15	0.66	1.22E+12	[23]	[23]
KCl5-29NaCl-66CaCl2	PCM	504	1.0	1000	2150	1.5	279	0.23	70	0.15	0.66	1.19E+12	[23]	[23]
LiNO3	Salt	254	1.4	2030	1780	2.2	360	0.28	8000	14.24	51.15	2.23E+12	[20]	[1]
Nitrate Salts	Salt	221	0.5	1500	2100	1.3	100	0.15	750	1.58	10.80	6.59E+11	[144]	[1]
KNO3-NaNO3	Salt	222	0.5	1530	1950	1.2	100	0.14	750	1.46	10.67	6.09E+11	[20]	[1]
KNO3	Salt	337	0.5	1430	1890	1.2	100	0.13	1000	1.89	14.81	5.34E+11	[20]	[1]
LiF-NaF-KF	Salt	454	0.9	1883	2020	1.9	0	0.11	1900	3.84	36.33	7.12E+11	[145]	[1]

Carbonate Salts	Salt	650	2.0	1800	2100	2.7	0	0.11	2400	5.04	48.00	1.04E+12	[142]	[142]
NaF-ZrF4	Salt	500	0.5	1171	3140	1.3	0	0.10	3000	9.42	92.23	4.94E+11	[145]	[1]
LiF-NaF-ZrF4	Salt	436	0.5	1231	2920	1.4	0	0.10	1900	5.55	55.56	4.96E+11	[145]	[1]
Nitrate Salts	Salt	415	0.5	1600	1870	1.2	0	0.08	500	0.94	11.25	3.73E+11	[142]	[142]
KF-ZrF4	Salt	390	0.5	1045	2800	1.1	0	0.08	3000	8.40	103.35	3.36E+11	[145]	[1]
Hitec solar salt	Salt	410	0.5	1500	1899	1.2	0	0.08	930	1.77	22.32	3.40E+11	[142]	[142]
HitecXL solar salt	Salt	310	0.5	1400	1992	1.2	0	0.08	1190	2.37	30.60	3.36E+11	[142]	[142]
Nitrite Salts	Salt	350	0.6	1500	1825	1.2	0	0.08	1000	1.83	24.00	3.42E+11	[142]	[142]
NaF-NaBF4	Salt	385	0.4	1505	1750	1.0	0	0.07	5000	8.75	119.62	2.70E+11	[145]	[1]
Alumina	Sensible Storage	1925	8.2	1256	3890	6.3	0	0.14	800	3.11	22.93	3.09E+12	[102] [141]	[102]
Silicon Carbide	Sensible Storage	1650	35.7	1239	3110	11.7	0	0.11	2000	6.22	58.11	4.52E+12	[102] [141]	[102]
Rocks	Sensible Storage	1050	1.9	1172	2600	2.4	0	0.08	60	0.16	1.84	7.33E+11	[141]	[1]
Concrete	Sensible Storage	0	1.5	1050	2250	1.9	0	0.07	250	0.56	8.57	4.37E+11	[146]	[1]
Silica Sand	Sensible Storage	1200	1.5	750	2200	1.6	0	0.05	100	0.22	4.80	2.60E+11	[141]	[1]
Graphite	Sensible Storage	0	32.0	710	2250	7.1	0	0.04	2500	5.63	126.76	1.14E+12	[102] [141]	[102]
Liquid Sodium	Sensible Storage	400	71.0	1300	850	8.9	0	0.03	2000	1.70	55.38	9.79E+11	[142]	[142]
Paraffin Wax	Wax	64	0.3	2900	916	1.0	266	0.14	1500	1.37	9.71	4.88E+11	[15]	[1]
Paraffin C22-C45	Wax	60	0.2	2900	920	0.7	189	0.12	1500	1.38	11.27	3.30E+11	[15]	[1]

[1]Price assumed.

APPENDIX B: DERIVATION OF HOMOGENISATION EQUATIONS FOR EQUILIBRIUM PROPERTIES

This brief appendix contains a derivation of the homogenisation equations for effective density and heat capacity.

The effective density of a composite of n constituents is the volume weighted average of the constituent densities. This can be shown through conservation of mass. The total mass is intuitively the sum of all the constituents' masses.

$$m_t = \sum_{i=1}^{n} m_i \qquad 107.$$

Substituting the product of volume and density for mass yields:

$$m_i = \rho_i V_i \qquad 108.$$

$$m_t = \sum_{i=1}^{n} \rho_i V_i \qquad 109.$$

The total mass is by definition the product of an effective density and the total volume.

$$\rho_{eff} V_t = \sum_{i=1}^{n} \rho_i V_i \qquad 110.$$

Dividing through by the total volume and considering the constituent volume fraction $\varphi_i = \frac{m_i}{m}$:

$$\rho_{eff} = \frac{\sum_{i=1}^{n} \rho_i V_i}{V} \qquad 111.$$

$$\rho_{eff} = \sum_{i=1}^{n} \rho_i \varphi_i \qquad 112.$$

APPENDIX B: DERIVATION OF HOMOGENISATION EQUATIONS FOR EQUILIBRIUM PROPERTIES

The effective heat capacity of a composite is the mass weighted average of its constituents. This may be shown by summing the sensible heat contributions of each constituent.

$$H=\sum_{i=1}^{n} H_i \qquad 113.$$

Where the only form of energy available is in sensible heat the ith constituent will contribute:

$$H_i=m_i C_i \Delta T \qquad 114.$$

Thus the sum of constituent energies can be written as:

$$H=\sum_{i=1}^{n} m_i C_i \Delta T \qquad 115.$$

By definition the effective heat capacity is:

$$H=m_t C_{eff} \Delta T \qquad 116.$$

Substituting and dividing through by the temperature increment gives:

$$m_t C_{eff} \Delta T=\sum_{i=1}^{n} m_i C_i \Delta T \qquad 117.$$

$$C_{eff}=\frac{\sum_{i=1}^{n} m_i C_i}{m} \qquad 118.$$

Introducing the mass fraction as $\psi_i=\frac{m_i}{m}$ simplifies the above equation to:

$$C_{p,eff}=\sum_{i=1}^{n} \psi_i C_{p,i} \qquad 119.$$

Thus the effective density and effective heat capacity are defined on the constituent volume or mass fractions and relevant properties.

APPENDIX C: SELECTED LISTING OF IDENTIFIED MISCIBILITY GAP ALLOYS

Table 21 Listing of selected identified Miscibility Gap Alloys, adapted from [3].

Fusible Phase	Matrix Phase	T_m [°C]	Composition	Fusible Phase	Matrix Phase	T_m [°C]	Composition
Ga	Sn	21	4 – 86.3%Ga	Zn	B	419	all
Ga	Zn	25	2 – 96.5%Ga	Zn	ZnSe	419	0 – 46%Zn
Ga	Bi	29	0 – 99.3%Ga	Zn	Si	419	all
Ga	B	29.6	all	Zn	TeZn	419	0 – 34%Zn
Ga	Tl	29.7	3 – 95%Ga	Te	TeZn	447	66 – 100%Te
Ga	GaSb	29.7	0 – 36%Ga	Sb	B	631	all
Ga	Re	29.8	all	Mg	Nb	650	all
Ga	Ge	29.8	all	Mg	Fe	650	0 – 99.9%Mg
In	Bi	109	0 - 33%In	Mg	V	650	all
In	Zn	144	0 - 97%Zn	Bi	Ni	654	0 - 74%Bi
In	Al	156	17.3 – 97%In	Al	Nb	661	0 – 54% Al
In	Fe	156	1 – 99%In	CdNi	Ni	690	66 – 100%Cd
In	B	157	all	Sr	Y	739	2 – 99.5%Sr
Sn	Pb	183	0 – 40%Pb	Sr	Sc	768	3 – 100%Sr
Sn	Zn	198	0 – 91%Sn	Sr	Ti	769	all
Se	ZnSe	221	54 – 100%Se	Sr	V	769	all
Sn	Al	228	0 – 99.4%Sn	Mo_3Sb_7	Mo	780	0 – 74%Sb
Sn	Cr	230	0 – 99%Sn	Zn	Fe	780	46%<Zn<92%
Sn	B	232	0 – 99%Pb	Ge	B	938	8 – 100%Ge
Sn	Si	232	all	Ge	C	938	all
Pb	Sb	252	3 – 89%Pb	Ag	W	962	all
Bi	Zn	255	0 – 97.3%Bi	Cu	Cr	1077	0 – 98%Cu
Bi	Co	258	7 – 97%Bi	Cu	Mo	1083	0 – 99%Cu
Cd	Zn	266	0 – 83%Cd	Cu	C	1085	all
Bi	Al	270	3.4 – 97.6%Bi	Cu	Nb	1085	0.8 – 100%Cu
Bi	B	271	all	Cu	V	1085	3 – 100%Cu
Bi	Fe	271	all	Cu	Fe	1085	8 – 96%Cu
Bi	Cu	271	0 – 99.8%Bi	Cu	Co	1112	21 – 90%Cu
Bi	Ge	271	all	Cu	Fe	1154	<95.7 %Fe
Bi	Cr	271	all	Fe-Si alloy	FeSi	1200	25 - 50%Si
Tl	Zn	292	3 – 96%Tl	Co	C	1320	0 – 97%Co
Tl	Cu	302	1 – 94%Tl	Ni	C	1327	0 – 99.4%Ni
Tl	Ni	304	4 – 100%Tl	Zr-Cr alloy	$ZrCr_2$	1332	50 – 86%Zr
Cd	Ge	318	0 – 99.85%Cd	Y	Ti	1355	4 – 42%Y
Pb	Zn	318	0 – 99.5%Pb	Si	SiC	1404	70 - 100%Si
Cd	Al	320	7 – 98.7%Cd	Sc	V	1410	2 – 86%Sc
Cd	Mo	321	0 – 99%Cd	Y	Mo	1430	0 – 90%Y
Cd	B	321	all	Y	V	1455	0 – 93%Y
Pb	Ni	324	3 – 99.9%Pb	Y	Ta	1478	0 – 99.5%Y
Pb	Cu	326	all	Ni	W	1495	0 – 65%Ni
Pb	Co	326	all	Sc	W	1510	0 – 90%Sc
Pb	Al	327	0 – 99.2%Pb	Sc	Ta	1519	0 – 88.3%Sc
Pb	Fe	327	all	Y	W	1520	0.25 – 100%Y
Pb	B	327	0 - 99%Pb	Pd	W	1815	>68%Pd
Pb	Cr	327	all	Ti	TiB_2	2080	32 – 100%B
Pb	Mn	327	all				

APPENDIX C: SELECTED LISTING OF IDENTIFIED MISCIBILITY GAP ALLOYS

APPENDIX D: DERIVATION OF GROWTH-DECAY MODEL

The growth-decay model described in §3.4.1 is given a more thorough treatment in this appendix. The core assumptions of the model are that:

1) The system may consist of two concentric spheres of A rich alpha and B rich beta phase whose equilibrium compositions are known for all temperatures of interest.
2) The outer sphere is in contact with an alpha phase reservoir that extends to infinity.
3) The flux of atoms is dominated by dissolution and deposition of the solid alpha phase into or from the high temperature beta or liquid phase.

The model has two separate sets of equations that model evolution with or without a central spherical nucleus. Repetition of the sets of equations allows cycling to be modelled.

If there is no central nucleus a sphere of beta phase with n_β moles at some composition x_β is being heated or cooled to an equilibrium composition of $x_\beta^{'}$. To approach equilibrium the pocket may dissolve (reject) material from (to) the matrix at a composition of x_α. If complete equilibrium is not obtained either a stable or unstable solution of β' will exist. If the $\beta^{'}$ phase is unstable it will decompose to equilibrium $\beta^{'}$ by crystallising a central sphere of $\alpha^{'}$ at the composition $x_\alpha^{'}$. If the radius of the new nucleus is less than that for an energetically favourable nucleation the unstable solution will persist. This general formulation may be used for cooling or heating.

The radius of the β phase may be used to determine the number of moles and the breakdown through the general formulae:

$$n=\rho\frac{4\pi}{3}r^3 \quad (120.)$$

$$n_a=n(1-x) \quad (121.)$$

$$n_b=nx \quad (122.)$$

If equilibrium is achieved through the heating or cooling event the following two conditions must be satisfied:

$$\left(1-x'_{\beta,eq}\right)n'_{\beta,eq}=\left(1-x_\beta\right)n_\beta+(1-x_\alpha)\Delta n_\alpha \quad (123.)$$

$$x'_{\beta,eq}n'_{\beta,eq}=x_\beta n_\beta+x_\alpha\Delta n_\alpha \quad (124.)$$

These two equations may be solved simultaneously for n'_β and Δn_α yielding the system and the solutions:

$$\begin{bmatrix}\left(1-x'_{\beta,eq}\right) & -(1-x_\alpha)\\ x'_{\beta,eq} & -x_\alpha\end{bmatrix}\begin{bmatrix}n'_{\beta,eq}\\ \Delta n_\alpha\end{bmatrix}=\begin{bmatrix}\left(1-x_\beta\right)n_\beta\\ x_\beta n_\beta\end{bmatrix} \quad (125.)$$

$$n'_{\beta,eq}=n_\beta\frac{x_\beta-x_\alpha}{x'_{\beta,eq}-x_\alpha} \quad (126.)$$

$$\Delta n_\alpha=n_\beta\frac{x_\beta-x'_{\beta,eq}}{x'_{\beta,eq}-x_\alpha} \quad (127.)$$

The equilibrium moles in the new beta phase may now be converted to the respective number of moles of a and b atoms using equations 120 and 121. The equilibrium approach is then applied by modifying the flux of each atom species:

$$n'_{\beta,a}=n_{\beta,a}+\eta\left(n'_{\beta,eq,a}-n_{\beta,a}\right) \quad (128.)$$

$$n'_{\beta,b}=n_{\beta,b}+\eta\left(n'_{\beta,eq,b}-n_{\beta,b}\right) \quad (129.)$$

An equilibrium approach of unity will yield the equilibrium value whilst an approach of zero indicates no change from the initial breakdown.

The composition of the new beta phase is:

$$x_{\beta}^{'}=\frac{n_{\beta,b}^{'}}{n_{\beta,a}^{'}+n_{\beta,b}^{'}} \quad 130.$$

If the composition found above is greater than the equilibrium composition then the phase is stable. If the composition is less than an unstable phase exists and might crystallise an alpha phase. If $x_{\beta}^{'}<x_{\beta,eq}^{'}$ then the following conditions will be met if crystallisation can proceed:

$$n_{\beta,a}^{'}=\left(1-x_{\beta,eq}^{'}\right)n_{\beta,Shell}^{'}+\left(1-x_{\alpha}^{'}\right)n_{\alpha,Nucleus}^{'} \quad 131.$$

$$n_{\beta,b}^{'}=x_{\beta,eq}^{'}n_{\beta,Shell}^{'}+x_{\alpha}^{'}n_{\alpha,Nucleus}^{'} \quad 132.$$

This may be solved for $n_{\beta,Shell}^{'}$ and $n_{\alpha,Nucleus}^{'}$ simultaneously:

$$\begin{bmatrix}\left(1-x_{\beta,eq}^{'}\right) & \left(1-x_{\alpha}^{'}\right)\\ x_{\beta,eq}^{'} & x_{\alpha}^{'}\end{bmatrix}\begin{bmatrix}n_{\beta,Shell}^{'}\\ n_{\alpha,Nucleus}^{'}\end{bmatrix}=\begin{bmatrix}n_{\beta,a}^{'}\\ n_{\beta,b}^{'}\end{bmatrix} \quad 133.$$

$$n_{\beta,Shell}^{'}=\frac{n_{\beta,a}^{'}x_{\alpha}^{'}-n_{\beta,b}\left(1-x_{\alpha}^{'}\right)}{x_{\alpha}^{'}-x_{\beta}^{'}} \quad 134.$$

$$n_{\alpha,Nucleus}^{'}=\frac{n_{\beta,a}^{'}x_{\beta}^{'}-n_{\beta,b}^{'}\left(1-x_{\beta}^{'}\right)}{x_{\beta}^{'}-x_{\alpha}^{'}} \quad 135.$$

If a nucleus is formed on this operation its radius can be found from the general equation:

$$r_{\alpha,Nucleus}^{'}=\sqrt[3]{\frac{3n_{\alpha,Nucleus}^{'}}{4\rho_{\alpha}^{'}\pi}} \quad 136.$$

The radius may be compared to the energetically favourable size discussed in section §3.4.1. If the radius of the nucleus is stable the unstable beta sphere may decompose to the nucleus described above with an outer shell of equilibrium beta phase with radius:

$$r_{\beta}^{'}=\sqrt[3]{\frac{3}{4\pi}\left(\frac{n_{\alpha,\mathrm{Nucleus}}^{'}}{\rho_{\alpha}^{'}}+\frac{n_{\beta,\mathrm{Shell}}^{'}}{\rho_{\beta}^{'}}\right)} \qquad 137.$$

Thus the flux of atoms may be described for a sphere of β phase undergoing heating or cooling.

The following applies if there is a central nucleus of n_{α} moles at composition x_{α} within a shell of beta phase with n_{β} moles at some composition x_{β} being heated or cooled to an equilibrium composition of $x_{\beta}^{'}$. To approach equilibrium the shell may dissolve (reject) material from (to) the nucleus and matrix at a composition of x_{α}. The nucleus and matrix will accept (reject) material in proportion to their surface area. If equilibrium is not obtained the $\beta^{'}$ shell may be a stable or unstable solution. If the $\beta^{'}$ phase is unstable it will decompose to equilibrium $\beta^{'}$ by adding material to the central sphere of $\alpha^{'}$ at the composition $x_{\alpha}^{'}$.

Equilibrium is satisfied when the following two equations are true:

$$\left(1-x_{\beta,\mathrm{eq}}^{'}\right)n_{\beta,\mathrm{eq}}^{'}+\left(1-x_{\alpha}^{'}\right)\left(1+\frac{r_{\beta}^{2}}{r_{\alpha}^{2}}\right)n_{\alpha,\mathrm{eq}}^{'}=\left(1-x_{\beta}\right)n_{\beta}+\left(1-x_{\alpha}\right)n_{\alpha}\left(1+\frac{r_{\beta}^{2}}{r_{\alpha}^{2}}\right) \qquad 138.$$

$$x_{\beta,\mathrm{eq}}^{'}n_{\beta,\mathrm{eq}}^{'}+x_{\alpha}^{'}\left(1+\frac{r_{\beta}^{2}}{r_{\alpha}^{2}}\right)n_{\alpha,\mathrm{eq}}^{'}=x_{\beta}n_{\beta}+x_{\alpha}n_{\alpha}\left(1+\frac{r_{\beta}^{2}}{r_{\alpha}^{2}}\right) \qquad 139.$$

These two equations may be solved simultaneously for $n_{\beta,eq}^{\prime}$ and $n_{\alpha,eq}^{\prime}$ yielding the system and the solutions:

$$\begin{bmatrix}\left(1-x_{\beta,\mathrm{eq}}^{'}\right) & \left(1-x_{\alpha}^{'}\right)\left(1+\frac{r_{\beta}^{2}}{r_{\alpha}^{2}}\right)\\ x_{\beta,\mathrm{eq}}^{'} & x_{\alpha}^{'}\left(1+\frac{r_{\beta}^{2}}{r_{\alpha}^{2}}\right)\end{bmatrix}\begin{bmatrix}n_{\beta,\mathrm{eq}}^{'}\\ n_{\alpha,\mathrm{eq}}^{'}\end{bmatrix}=\begin{bmatrix}\left(1-x_{\beta}\right)n_{\beta}+\left(1-x_{a}\right)n_{a}\left(1+\frac{r_{\beta}^{2}}{r_{\alpha}^{2}}\right)\\ x_{\beta}n_{\beta}+x_{a}n_{a}\left(1+\frac{r_{\beta}^{2}}{r_{\alpha}^{2}}\right)\end{bmatrix} \qquad 140.$$

$$n'_{\beta,eq}=\frac{n_\beta\left(x_\beta-x'_\alpha\right)+n_\alpha\left(x_\alpha-x'_\alpha\right)\left(1+\frac{r_\beta^2}{r_\alpha^2}\right)}{x'_\beta-x'_\alpha} \quad 141.$$

$$n'_{\alpha,eq}=\frac{n_\beta\left(x'_\beta-x_\beta\right)+n_\alpha\left(x'_\beta-x_\alpha\right)\left(1+\frac{r_\beta^2}{r_\alpha^2}\right)}{\left(x'_\beta-x'_\alpha\right)\left(1+\frac{r_\beta^2}{r_\alpha^2}\right)} \quad 142.$$

The equilibrium moles in the new beta shell may now be converted to the respective number of moles of a and b atoms using equations 120 and 121. The equilibrium approach is then applied by modifying the flux of each atom species:

$$n'_{\beta,a}=n_{\beta,a}+\eta\left(n'_{\beta,eq,a}-n_{\beta,a}\right) \quad 143.$$

$$n'_{\beta,b}=n_{\beta,b}+\eta\left(n'_{\beta,eq,b}-n_{\beta,b}\right) \quad 144.$$

The alpha nucleus will have received (released) a proportion of this according to the squared ratio of radii:

$$n'_{\alpha,a}=n_{\alpha,a}-\eta\left(n'_{\beta,eq,a}-n_{\beta,a}\right)\frac{r_\alpha^2}{r_\alpha^2+r_\beta^2} \quad 145.$$

$$n'_{\alpha,b}=n_{\alpha,b}-\eta\left(n'_{\beta,eq,b}-n_{\beta,b}\right)\frac{r_\alpha^2}{r_\alpha^2+r_\beta^2} \quad 146.$$

This is equivalent to:

$$n'_{\alpha,a}=n_{\alpha,a}+\eta\left(n'_{\alpha,eq,a}-n_{\alpha,a}\right) \quad 147.$$

$$n'_{\alpha,b}=n_{\alpha,b}+\eta\left(n'_{\alpha,eq,b}-n_{\alpha,b}\right) \quad 148.$$

Now the composition of the β shell and α nucleus have compositions according to:

$$x'_\beta=\frac{n'_{\beta,b}}{n'_{\beta,a}+n'_{\beta,b}} \quad 149.$$

$$x'_{\alpha}=\frac{n'_{\alpha,b}}{n'_{\alpha,a}+n'_{\alpha,b}} \quad 150.$$

These compositions may be unstable. If either are unstable then the alpha nucleus and beta shell will be modelled to decompose to the equilibrium phases:

$$n'_{\beta,a}+n'_{\alpha,a}=\left(1-x'_{\beta,eq}\right)n'_{\beta,Shell}+\left(1-x'_{\alpha,eq}\right)n'_{\alpha,Nucleus} \quad 151.$$

$$n'_{\beta,b}+n'_{\alpha,b}=x'_{\beta,eq}n'_{\beta,Shell}+x'_{\alpha,eq}n'_{\alpha,Nucleus} \quad 152.$$

This simple pair of equations may be solved simultaneously for n'_{β} and n'_{α}:

$$\begin{bmatrix}\left(1-x'_{\beta,eq}\right) & \left(1-x'_{\alpha,eq}\right)\\ x'_{\beta,eq} & x'_{\alpha,eq}\end{bmatrix}\begin{bmatrix}n'_{\beta,Shell}\\ n'_{\alpha,Nucleus}\end{bmatrix}=\begin{bmatrix}n'_{\beta,a}+n'_{\alpha,a}\\ n'_{\beta,b}+n'_{\alpha,b}\end{bmatrix} \quad 153.$$

$$n'_{\beta,Shell}=\frac{x'_{\alpha}\left(n'_{\alpha,a}+n'_{\alpha,b}+n'_{\beta,a}+n'_{\beta,b}\right)-n'_{\beta,b}-n'_{\alpha,b}}{x'_{\alpha,eq}-x'_{\beta,eq}} \quad 154.$$

$$n'_{\alpha,Nucleus}=\frac{x'_{\beta}\left(n'_{\alpha,a}+n'_{\alpha,b}+n'_{\beta,a}+n'_{\beta,b}\right)-n'_{\beta,b}-n'_{\alpha,b}}{x'_{\beta,eq}-x'_{\alpha,eq}} \quad 155.$$

It is possible that the nucleus will dissolve during heating. This is indicated by a zero or negative $n'_{\alpha,Nucleus}$. The additional material required to achieve equilibrium in the beta phase will be taken from the matrix. If this occurs during a ramp in a thermal cycle, the system may recrystallise on cooling in the next cycle.

The nucleus radius can be found from the general equation:

$$r'_{\alpha,Nucleus}=\sqrt[3]{\frac{3n'_{\alpha,Nucleus}}{4\rho'_{\alpha}\pi}} \quad 156.$$

The outer shell of equilibrium beta phase has radius:

$$r'_{\beta}=\sqrt[3]{\frac{3}{4\pi}\left(\frac{n'_{\alpha,Nucleus}}{\rho'_{\alpha}}+\frac{n'_{\beta,Shell}}{\rho'_{\beta}}\right)} \quad 157.$$

Thus the flux of atoms may be described for a shell of β phase and central nucleus of α phase undergoing heating or cooling.

APPENDIX D: DERIVATION OF GROWTH-DECAY MODEL

APPENDIX E: TABULAR DATA OF MGA PROPERTIES

The following section contains tabular data for the Copper–Graphite, Copper-Iron, Magnesium-Iron, Silicon-Silicon Carbide, Tin-Aluminium and Zinc-Graphite systems.

Copper-Graphite												Ref	Ref
Volume Fraction												C	Cu
	0	0.1	0.2	0.3	0.4	0.5	0.6	0.7	0.8	0.9	1		
Mass Fraction at Room Temperature													
	0.000	0.344	0.541	0.669	0.759	0.825	0.876	0.917	0.950	0.977	1.000		
Atomic Fraction at Room Temperature													
	0.000	0.090	0.182	0.276	0.373	0.471	0.572	0.675	0.781	0.889	1.000		
Effective Theoretical Density [kg/m3]													
Temperature [°C]													
0	1900	2606	3312	4018	4724	5430	6136	6842	7548	8254	8960	[105]	[147]
100	1900	2601	3303	4004	4706	5407	6109	6810	7512	8213	8915	[105]	[147]
300	1900	2592	3285	3977	4670	5362	6055	6747	7440	8132	8825	[105]	[147]
500	1900	2584	3267	3951	4635	5319	6002	6686	7370	8053	8737	[105]	[147]
1000	1900	2563	3225	3888	4550	5213	5875	6538	7200	7863	8525	[105]	[147]
1085	1900	2559	3218	3877	4536	5195	5854	6513	7172	7831	8490	[105]	[147]
1086	1900	2512	3124	3736	4349	4961	5573	6185	6797	7409	8021	[105]	[148]
1200	1900	2496	3092	3688	4284	4880	5476	6072	6668	7264	7860	[105]	[148]
Effective Theoretical Heat Capacity [J/kgK]													
Temperature [°C]													
0	637	548	497	464	441	424	411	400	392	385	379	[149]	[150]
100	919	740	637	571	524	489	462	441	423	409	397	[149]	[150]
300	1348	1032	849	730	646	584	536	498	466	441	419	[149]	[150]
500	1595	1201	972	822	717	638	578	529	490	457	430	[149]	[150]
1000	1876	1421	1152	975	849	756	683	626	578	539	506	[149]	[151]
1085	1903	1439	1166	985	857	761	687	628	580	540	506	[149]	[151]
1086	1903	1502	1258	1094	976	888	818	763	717	679	647	[149]	[152]
1200	1933	1525	1275	1105	983	890	818	760	712	672	638	[149]	[152]

Theoretical Upper Weiner Bound [W/mK]													
Temperature [°C]	Moulded												
0	108.0	137.5	167.0	196.5	226.0	255.5	285.0	314.5	344.0	373.5	403.0	[90]	[90]
100	102.5	131.7	161.0	190.2	219.5	248.7	278.0	307.2	336.5	365.7	395.0	[90]	[90]
300	81.7	111.7	141.6	171.5	201.4	231.4	261.3	291.2	321.1	351.1	381.0	[90]	[90]
500	66.1	96.3	126.5	156.7	186.9	217.1	247.3	277.4	307.6	337.8	368.0	[90]	[90]
1000	45.3	74.2	103.0	131.9	160.8	189.6	218.5	247.4	276.3	305.1	334.0	[90]	[90]
1085	43.4	71.8	100.3	128.8	157.2	185.7	214.2	242.6	271.1	299.5	328.0	[90]	[90]
1086	43.4	55.6	67.9	80.2	92.4	104.7	116.9	129.2	141.5	153.7	166.0	[90]	[90]
1200	41.1	54.0	66.9	79.8	92.7	105.6	118.4	131.3	144.2	157.1	170.0	[90]	[90]
Theoretical Latent Heat of Fusion [J/kg]													
	0	70483	110918	137143	155529	169134	179609	187922	194679	200281	205000		
Theoretical Latent Energy Density [kWh/L]													
	0.000	0.047	0.094	0.141	0.188	0.235	0.282	0.329	0.376	0.423	0.470		
Theoretical Energy Density [kWh/L]													
Temperature Change [Δ°C]													
10	0.010	0.057	0.105	0.152	0.199	0.247	0.294	0.341	0.389	0.436	0.483		
20	0.020	0.068	0.115	0.163	0.211	0.258	0.306	0.354	0.401	0.449	0.497		
50	0.050	0.099	0.147	0.196	0.245	0.293	0.342	0.390	0.439	0.488	0.536		
100	0.100	0.151	0.201	0.251	0.301	0.351	0.402	0.452	0.502	0.552	0.602		
Other Information													
Copper Molar Mass	63.5	[kg/kmol]											
Graphite Molar Mass	12.0	[kg/kmol]											
Copper Latent Heat of Fusion	205	[kJ/kg]											
Copper Melting Point	1085	[°C]											
Graphite Melting Point		[°C]											

Copper-Iron												Ref	Ref
Volume Fraction												Fe	Cu
	0	0.1	0.2	0.3	0.4	0.5	0.6	0.7	0.8	0.9	1		
Mass Fraction at Room Temperature													
	0.000	0.112	0.222	0.328	0.431	0.532	0.631	0.727	0.820	0.911	1.000		
Atomic Fraction at Room Temperature													
	0.000	0.100	0.200	0.300	0.400	0.500	0.600	0.700	0.800	0.900	1.000		
Effective Theoretical Density [kg/m3]													
Temperature [°C]													
0	7870	7979	8088	8197	8306	8415	8524	8633	8742	8851	8960	[153]	[147]
100	7842	7949	8056	8164	8271	8378	8485	8593	8700	8807	8915	[153]	[147]
300	7786	7890	7994	8098	8202	8305	8409	8513	8617	8721	8825	[153]	[147]
500	7731	7831	7932	8033	8133	8234	8335	8435	8536	8637	8737	[153]	[147]
1000	7597	7689	7782	7875	7968	8061	8154	8247	8339	8432	8525	[153]	[147]
1085	7574	7666	7757	7849	7941	8032	8124	8215	8307	8399	8490	[153]	[148]
1086	7574	7619	7663	7708	7753	7798	7842	7887	7932	7977	8021	[153]	[148]
1200	7544	7576	7607	7639	7670	7702	7733	7765	7797	7828	7860	[153]	[148]
Effective Theoretical Heat Capacity [J/kgK]													
Temperature [°C]													
0	442	435	428	421	415	408	402	396	390	385	379	[153]	[150]
100	480	471	462	453	444	436	428	420	412	404	397	[153]	[150]
300	562	546	530	515	500	486	472	458	445	432	419	[153]	[150]
500	662	636	611	586	562	539	516	494	472	451	430	[153]	[151]
1000	619	606	594	582	571	559	548	537	527	516	506	[153]	[151]
1085	633	619	605	592	579	566	553	541	529	518	506	[153]	[152]
1086	633	635	636	637	639	640	642	643	644	646	647	[153]	[152]
1200	636	636	636	636	637	637	637	637	638	638	638	[153]	[152]

Theoretical Upper Weiner Bound [W/mK] Temperature [°C]													
0	83.5	115.5	147.4	179.4	211.3	243.3	275.2	307.2	339.1	371.1	403.0	[90]	[90]
100	72.0	104.3	136.6	168.9	201.2	233.5	265.8	298.1	330.4	362.7	395.0	[90]	[90]
300	56.4	88.9	121.3	153.8	186.2	218.7	251.2	283.6	316.1	348.5	381.0	[90]	[90]
500	44.8	77.1	109.4	141.8	174.1	206.4	238.7	271.0	303.4	335.7	368.0	[90]	[90]
1000	29.6	60.0	90.5	120.9	151.4	181.8	212.2	242.7	273.1	303.6	334.0	[90]	[90]
1085	37.2	66.3	95.4	124.4	153.5	182.6	211.7	240.8	269.8	298.9	328.0	[90]	[90]
1086	37.2	50.1	63.0	75.8	88.7	101.6	114.5	127.4	140.2	153.1	166.0	[90]	[90]
1200	31.9	45.7	59.5	73.3	87.1	101.0	114.8	128.6	142.4	156.2	170.0	[90]	[90]
Theoretical Latent Heat of Fusion [J/kg]													
	0	23020	45420	67225	88457	109138	129291	148935	168090	186772	205000		
Theoretical Latent Energy Density [kWh/L]													
	0.000	0.047	0.094	0.141	0.188	0.235	0.282	0.329	0.376	0.423	0.470		
Theoretical Energy Density [kWh/L] Temperature Change [Δ°C]													
10	0.013	0.060	0.107	0.154	0.201	0.248	0.295	0.342	0.389	0.436	0.483		
20	0.027	0.074	0.121	0.168	0.215	0.262	0.309	0.356	0.403	0.450	0.497		
50	0.067	0.114	0.160	0.207	0.254	0.301	0.348	0.395	0.442	0.489	0.536		
100	0.133	0.180	0.227	0.274	0.321	0.368	0.415	0.462	0.508	0.555	0.602		
Other Information													
Copper Molar Mass	63.5	[kg/kmol]											
Iron Molar Mass	55.8	[kg/kmol]											
Copper Latent Heat of Fusion	205	[kJ/kg]											
Copper Melting Point	1086	[°C]											

Magnesium-Iron												Ref	Ref
Volume Fraction												Fe	Mg
	0	0.1	0.2	0.3	0.4	0.5	0.6	0.7	0.8	0.9	1		
Mass Fraction at Room Temperature													
	0.000	0.025	0.054	0.089	0.132	0.186	0.255	0.347	0.477	0.672	1.000		
Atomic Fraction at Room Temperature													
	0.000	0.055	0.116	0.183	0.259	0.344	0.440	0.550	0.677	0.825	1.000		
Effective Theoretical Density [kg/m3]													
Temperature [°C]													
0	7870	7262	6655	6047	5440	4832	4224	3617	3009	2402	1794	[153]	[102]
100	7842	7236	6630	6023	5417	4811	4205	3599	2993	2387	1780	[153]	[102]
200	7814	7209	6604	6000	5395	4790	4186	3581	2976	2372	1767	[153]	[102]
400	7758	7157	6555	5953	5351	4750	4148	3546	2945	2343	1741	[153]	[102]
600	7704	7105	6506	5907	5308	4710	4111	3512	2913	2315	1716	[153]	[102]
650	7690	7092	6494	5896	5298	4700	4102	3504	2906	2308	1710	[153]	[154]
651	7690	7080	6470	5860	5250	4640	4030	3420	2810	2200	1590	[153]	[154]
700	7677	7067	6457	5847	5236	4626	4016	3406	2796	2186	1576	[153]	[154]
Effective Theoretical Heat Capacity [J/kgK]													
Temperature [°C]													
0	442	456	472	492	516	546	585	636	709	819	1002	[153]	[155]
100	480	495	512	532	557	588	629	683	758	872	1064	[153]	[155]
200	521	535	552	573	598	629	670	724	800	915	1109	[153]	[155]
400	612	626	643	663	688	718	758	812	887	1000	1193	[153]	[155]
600	649	665	683	706	733	768	812	872	956	1084	1301	[153]	[155]
650	649	666	685	709	737	773	820	882	971	1105	1332	[153]	[155]
651	632	649	670	695	726	765	816	886	985	1139	1411	[153]	[155]
700	636	653	674	699	730	768	819	887	986	1139	1411	[153]	[155]

Theoretical Upper Weiner Bound [W/mK]													
Temperature [°C]													
0	83.5	90.9	98.2	105.6	112.9	120.3	127.6	135.0	142.3	149.7	157.0	[90]	[90]
100	72.0	80.2	88.4	96.6	104.8	113.0	121.2	129.4	137.6	145.8	154.0	[90]	[90]
200	63.4	72.3	81.1	90.0	98.8	107.7	116.6	125.4	134.3	143.1	152.0	[90]	[90]
400	50.4	60.2	69.9	79.7	89.4	99.2	109.0	118.7	128.5	138.2	148.0	[90]	[90]
600	39.4	50.0	60.5	71.1	81.6	92.2	102.8	113.3	123.9	134.4	145.0	[90]	[90]
650	38.0	48.7	59.4	70.1	80.8	91.5	102.2	112.9	123.6	134.3	145.0	[90]	[90]
651	38.0	42.1	46.2	50.3	54.4	58.5	62.6	66.7	70.8	74.9	79.0	[90]	[90]
700	34.0	38.9	43.7	48.6	53.4	58.3	63.2	68.0	72.9	77.7	82.6	[90]	[90]
Theoretical Latent Heat of Fusion [J/kg]													
	0	9091	19841	32752	48547	68315	93768	127774	175513	247407	368000		
Theoretical Latent Energy Density [kWh/L]													
	0.000	0.017	0.034	0.051	0.067	0.084	0.101	0.118	0.135	0.152	0.169		
Theoretical Energy Density [kWh/L]													
Temperature Change [Δ°C]													
10	0.014	0.030	0.046	0.062	0.078	0.094	0.110	0.127	0.143	0.159	0.175		
20	0.027	0.043	0.058	0.074	0.089	0.104	0.120	0.135	0.150	0.166	0.181		
50	0.068	0.082	0.095	0.108	0.121	0.134	0.147	0.161	0.174	0.187	0.200		
100	0.137	0.146	0.156	0.165	0.175	0.184	0.194	0.203	0.213	0.222	0.232		
Other Information													
Magnesium Molar Mass	24.3	[kg/kmol]											
Iron Molar Mass	55.8	[kg/kmol]											
Magnesium Latent Heat of Fusion	368	[kJ/kg]											
Magnesium Melting Point	650	[°C]											
Iron Melting Point	1538	[°C]											

Silicon-Silicon Carbide												Ref	Ref
Volume Fraction												SiC	Si
	0	0.1	0.2	0.3	0.4	0.5	0.6	0.7	0.8	0.9	1		
Mass Fraction at Room Temperature													
	0.000	0.075	0.154	0.238	0.327	0.421	0.522	0.629	0.744	0.868	1.000		
Atomic Fraction at Room Temperature													
	0.000	0.103	0.206	0.308	0.409	0.509	0.609	0.708	0.806	0.903	1.000		
Effective Theoretical Density [kg/m3]													
Temperature [°C]													
0	3200	3113	3026	2938	2851	2764	2677	2590	2502	2415	2328	[156]	[102]
100	3197	3110	3023	2936	2849	2762	2675	2588	2500	2413	2326	[102]	[102]
300	3192	3105	3018	2931	2844	2757	2670	2584	2497	2410	2323	[102]	[102]
500	3187	3100	3013	2927	2840	2753	2666	2579	2493	2406	2319	[102]	[102]
1000	3174	3088	3001	2915	2829	2742	2656	2569	2483	2397	2310	[102]	[102]
1414	3164	3078	2992	2906	2819	2733	2647	2561	2475	2389	2303	[102]	[102]
1415	3164	3102	3041	2980	2918	2857	2795	2734	2673	2611	2550	[102]	[157]
1500	3162	3098	3035	2971	2908	2844	2781	2718	2654	2591	2527	[102]	[157]
Effective Theoretical Heat Capacity [J/kgK]													
Temperature [°C]													
0	642	647	653	659	665	672	679	686	694	703	712	[156]	[153]
100	799	797	794	792	790	787	784	781	778	775	771	[156]	[153]
300	1030	1018	1004	990	975	959	942	924	905	884	862	[156]	[153]
500	1144	1126	1107	1088	1066	1044	1020	995	967	938	907	[156]	[153]
1000	1264	1243	1220	1197	1172	1145	1117	1087	1055	1020	983	[156]	[153]
1414	1311	1289	1266	1242	1216	1188	1159	1128	1094	1059	1020	[156]	[153]
1415	1311	1283	1254	1223	1191	1158	1124	1087	1050	1010	969	[156]	[153]
1500	1319	1290	1260	1229	1197	1163	1128	1091	1052	1011	969	[156]	[153]

Theoretical Upper Weiner Bound [W/mK]													
Temperature [°C]													
0	120.0	124.8	129.6	134.4	139.2	143.9	148.7	153.5	158.3	163.1	167.9	[158]	[90]
100	114.0	113.8	113.6	113.4	113.2	113.0	112.8	112.7	112.5	112.3	112.1	[158]	[90]
300	102.0	98.4	94.7	91.1	87.5	83.9	80.2	76.6	73.0	69.4	65.7	[158]	[90]
500	90.0	85.5	81.0	76.5	71.9	67.4	62.9	58.4	53.9	49.4	44.8	[158]	[90]
1000	60.0	56.5	53.0	49.5	46.0	42.4	38.9	35.4	31.9	28.4	24.9	[158]	[90]
1414	51.7	52.4	53.1	53.8	54.5	55.2	55.8	56.5	57.2	57.9	58.6	[158]	[90]
1415	51.7	52.4	53.1	53.8	54.5	55.2	55.8	56.5	57.2	57.9	58.6	[158]	[90]
1500	50.0	50.9	51.7	52.6	53.4	54.3	55.2	56.0	56.9	57.7	58.6	[158]	[90]
Theoretical Latent Heat of Fusion [J/kg]													
	0	144042	296386	457772	629030	811094	1005020	1212006	1433417	1670816	1926000		
Theoretical Latent Energy Density [kWh/L]													
	0.000	0.130	0.260	0.389	0.519	0.649	0.779	0.909	1.038	1.168	1.298		
Theoretical Energy Density [kWh/L]													
Temperature Change [Δ°C]													
10	0.012	0.141	0.270	0.400	0.529	0.658	0.787	0.917	1.046	1.175	1.305		
20	0.023	0.152	0.281	0.410	0.538	0.667	0.796	0.925	1.054	1.183	1.311		
50	0.058	0.185	0.312	0.440	0.567	0.695	0.822	0.949	1.077	1.204	1.332		
100	0.115	0.240	0.365	0.490	0.615	0.740	0.865	0.990	1.115	1.240	1.365		
Other Information													
Silicon Molar Mass	28.1	[kg/kmol]											
Silicon Carbide Molar Mass	40.1	[kg/kmol]											
Silicon Latent Heat of Fusion	1926	[kJ/kg]											
Silicon Melting Point	1414	[°C]											
Silicon Carbide Melting Point	2730	[°C]											

Tin-Aluminium												Ref	Ref
Volume Fraction												Al	Sn
	0	0.1	0.2	0.3	0.4	0.5	0.6	0.7	0.8	0.9	1		
Mass Fraction at Room Temperature													
	0.000	0.225	0.395	0.528	0.635	0.723	0.797	0.859	0.913	0.959	1.000		
Atomic Fraction at Room Temperature													
	0.000	0.062	0.129	0.203	0.283	0.372	0.471	0.581	0.704	0.842	1.000		
Effective Theoretical Density [kg/m3]													
Temperature [°C]													
0	2800	3251	3702	4153	4604	5055	5506	5957	6408	6859	7310	[102]	[102]
50	2797	3247	3698	4148	4599	5049	5500	5950	6401	6851	7302	[102]	[102]
100	2794	3244	3694	4144	4594	5044	5494	5944	6394	6844	7294	[102]	[102]
150	2791	3240	3690	4139	4589	5038	5488	5937	6387	6836	7286	[102]	[102]
200	2788	3237	3686	4135	4584	5033	5482	5931	6380	6829	7278	[102]	[102]
231	2786	3234	3683	4132	4581	5029	5478	5927	6376	6824	7273	[102]	[102]
232	2786	3205	3624	4043	4463	4882	5301	5720	6140	6559	6978	[102]	[159]
300	2781	3195	3609	4022	4436	4849	5263	5676	6090	6503	6917	[102]	[159]
Effective Theoretical Heat Capacity [J/kgK]													
Temperature [°C]													
0	860	716	608	523	454	398	351	311	277	247	221	[160]	[150]
50	908	755	640	550	478	418	369	326	290	259	231	[160]	[150]
100	955	794	673	577	501	438	385	341	302	269	240	[160]	[150]
150	975	810	685	587	509	444	390	344	305	271	241	[160]	[150]
200	994	825	697	597	516	450	395	348	308	273	242	[160]	[150]
231	1014	840	709	606	524	456	399	351	309	274	242	[160]	[150]
232	1014	846	717	614	531	462	404	355	312	275	242	[160]	[150]
300	1034	863	731	626	541	471	411	360	316	278	244	[160]	[150]

Theoretical Upper Weiner Bound [W/mK]													
Temperature [°C]													
0	236.0	219.2	202.4	185.7	168.9	152.1	135.3	118.5	101.8	85.0	68.2	[90]	[90]
50	239.0	221.8	204.5	187.3	170.0	152.8	135.5	118.3	101.0	83.8	66.5	[90]	[90]
100	240.0	222.3	204.6	187.0	169.3	151.6	133.9	116.2	98.6	80.9	63.2	[90]	[90]
150	239.0	221.3	203.6	186.0	168.3	150.6	132.9	115.2	97.6	79.9	62.2	[90]	[90]
200	237.0	219.3	201.6	184.0	166.3	148.6	130.9	113.2	95.6	77.9	60.2	[90]	[90]
231	236.0	218.4	200.7	183.1	165.4	147.8	130.1	112.5	94.8	77.2	59.5	[90]	[90]
232	236.0	216.5	196.9	177.4	157.8	138.3	118.7	99.2	79.6	60.1	40.5	[90]	[90]
300	233.0	213.9	194.8	175.7	156.6	137.5	118.4	99.3	80.2	61.1	42.0	[90]	[90]
Theoretical Latent Heat of Fusion [J/kg]													
	0	13266	23300	31155	37471	42660	46999	50680	53844	56591	59000		
Theoretical Latent Energy Density [kWh/L]													
	0.000	0.012	0.023	0.035	0.047	0.058	0.070	0.082	0.093	0.105	0.117		
Theoretical Energy Density [kWh/L]													
Temperature Change [Δ°C]													
10	0.008	0.019	0.031	0.042	0.053	0.065	0.076	0.087	0.099	0.110	0.122		
20	0.016	0.027	0.038	0.049	0.060	0.071	0.082	0.093	0.104	0.115	0.126		
50	0.039	0.049	0.060	0.070	0.080	0.090	0.100	0.110	0.120	0.131	0.141		
100	0.078	0.087	0.096	0.104	0.113	0.122	0.130	0.139	0.147	0.156	0.165		
Other Information													
Tin Molar Mass	118.7	[kg/kmol]											
Aluminium Molar Mass	27.0	[kg/kmol]											
Tin Latent Heat of Fusion	59	[kJ/kg]											
Tin Melting Point	232	[°C]											
Aluminium Melting Point	660	[°C]											

Zinc-Graphite												Ref	Ref
Volume Fraction												C	Zn
	0	0.1	0.2	0.3	0.4	0.5	0.6	0.7	0.8	0.9	1		
Mass Fraction at Room Temperature													
	0.000	0.295	0.484	0.617	0.715	0.790	0.849	0.898	0.938	0.971	1.000		
Atomic Fraction at Room Temperature													
	0.000	0.071	0.147	0.228	0.315	0.408	0.509	0.617	0.734	0.861	1.000		
Effective Theoretical Density [kg/m3]													
Temperature [°C]													
0	1900	2424	2948	3472	3996	4520	5044	5568	6092	6616	7140	[105]	[102]
50	1900	2421	2942	3462	3983	4504	5025	5546	6067	6587	7108	[105]	[102]
100	1900	2418	2935	3453	3971	4488	5006	5524	6042	6559	7077	[105]	[102]
200	1900	2411	2923	3434	3946	4457	4969	5480	5992	6503	7015	[105]	[102]
300	1900	2405	2911	3416	3922	4427	4932	5438	5943	6449	6954	[105]	[102]
419	1900	2398	2897	3395	3893	4392	4890	5388	5886	6385	6883	[105]	[102]
420	1900	2366	2832	3298	3763	4229	4695	5161	5627	6093	6559	[105]	[157]
500	1900	2359	2818	3276	3735	4194	4653	5111	5570	6029	6488	[105]	[157]
Effective Theoretical Heat Capacity [J/kgK]													
Temperature [°C]													
0	637	564	517	485	461	442	427	416	406	397	390	[149]	[161]
50	779	666	593	542	504	475	452	433	418	405	394	[149]	[161]
100	919	768	670	601	550	511	480	455	434	416	401	[149]	[161]
200	1162	946	805	706	632	576	531	494	464	439	417	[149]	[161]
300	1348	1084	912	791	701	631	576	531	494	462	435	[149]	[161]
419	1511	1212	1015	877	774	694	630	579	536	499	468	[149]	[161]
420	1512	1230	1041	906	803	724	660	608	564	527	496	[149]	[161]
500	1595	1294	1091	945	835	748	679	622	575	535	500	[149]	[161]

Theoretical Upper Weiner Bound [W/mK]													
Temperature [°C]	Moulded												
0	108.0	108.9	109.8	110.7	111.6	112.5	113.4	114.3	115.2	116.1	117.0	[90]	[90]
50	106.8	107.6	108.4	109.2	110.1	110.9	111.7	112.5	113.4	114.2	115.0	[90]	[90]
100	102.5	103.4	104.4	105.3	106.3	107.2	108.2	109.1	110.1	111.1	112.0	[90]	[90]
200	91.8	93.4	95.0	96.7	98.3	99.9	101.5	103.1	104.8	106.4	108.0	[90]	[90]
300	81.7	84.0	86.2	88.4	90.6	92.9	95.1	97.3	99.6	101.8	104.0	[90]	[90]
419	71.8	74.5	77.3	80.1	82.9	85.7	88.5	91.3	94.1	96.9	99.6	[90]	[90]
420	71.7	69.5	67.2	65.0	62.8	60.6	58.4	56.2	54.0	51.7	49.5	[90]	[90]
500	66.1	64.9	63.7	62.6	61.4	60.2	59.0	57.8	56.6	55.4	54.2	[90]	[90]
Theoretical Latent Heat of Fusion [J/kg]													
	0	33285	54737	69714	80763	89250	95974	101432	105951	109755	113000		
Theoretical Latent Energy Density [kWh/L]													
	0.000	0.021	0.042	0.063	0.084	0.105	0.127	0.148	0.169	0.190	0.211		
Theoretical Energy Density [kWh/L]													
Temperature Change [Δ°C]													
10	0.008	0.029	0.050	0.072	0.093	0.114	0.135	0.156	0.178	0.199	0.220		
20	0.016	0.037	0.059	0.080	0.101	0.122	0.144	0.165	0.186	0.208	0.229		
50	0.040	0.061	0.083	0.105	0.126	0.148	0.170	0.191	0.213	0.234	0.256		
100	0.080	0.102	0.124	0.146	0.168	0.190	0.212	0.235	0.257	0.279	0.301		
Other Information													
Zinc Molar Mass	65.4	[kg/kmol]											
Graphite Molar Mass	12.0	[kg/kmol]											
Zinc Latent Heat of Fusion	113	[kJ/kg]											
Zinc Melting Point	419.5	[°C]											
Graphite Melting Point		[°C]											

APPENDIX F: RELEVANT MATERIAL PRICING

The following chapter provides an historical and current cost estimate of constituents involved in manufacturing Miscibility Gap Alloys. Prices were sourced from the London Metal Exchange, other commodity trading websites and contemporary trading websites like Alibaba.com and ebay.com.

Aluminium Price

Aluminium is produced through electrolytic refining of Alumina, which is itself separated from the ore Bauxite. It is an energy intensive refining process and electricity prices have a strong influence on the cost of production [162]. Aluminium is also very recyclable with over 75% of that produced still in use today. As a commodity the price appears to be steady in the long term (within ± 1000) around 2000 USD/T (see Figure 93).

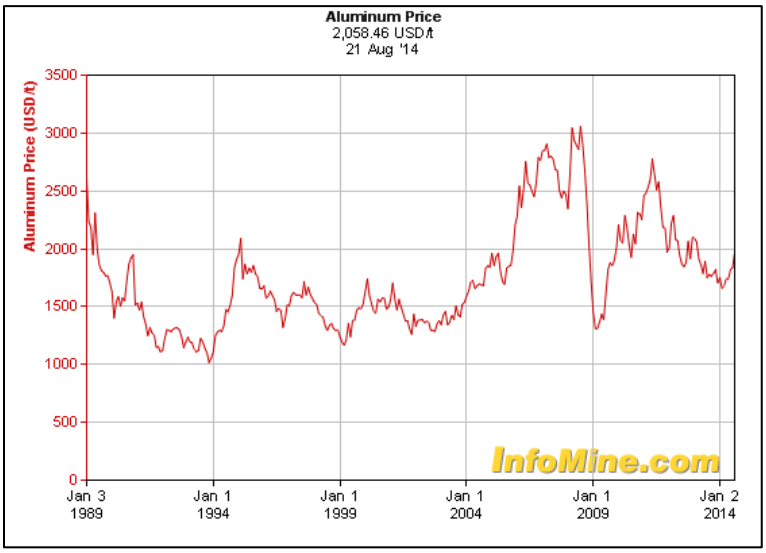

Figure 93 Aluminium Commodity price over the last 25 years [163].

Powdered aluminium appropriate for Miscibility Gap Alloys was found to have a commercially available price between 2400 and 5000 USD/Tonne.

Brass Price

Brass is a substitutional binary alloy of copper and zinc that has been utilised since as early as the last quarter of the third century BC in Ancient China [164]. A range of different brasses exist, the most common of which have concentrations up to 45% (atomic) Zn. Higher zinc concentrations are called beta-brasses and are uncommon due to limited engineering applications. They are however of great interest for Miscibility Gap Alloys.

The price of brass is dependent on both commodity prices and the cost of alloying the elements. Different alloys require different preparation methods and include different quantities of zinc and copper. Preparation of the alloy might be very roughly approximated by assuming a linear increase in manufacturing from unity for pure copper to double for pure zinc (varying over atomic fraction). This assumes that the more uncommon beta brasses are more expensive to manufacture than the common alpha (low zinc content) brasses.

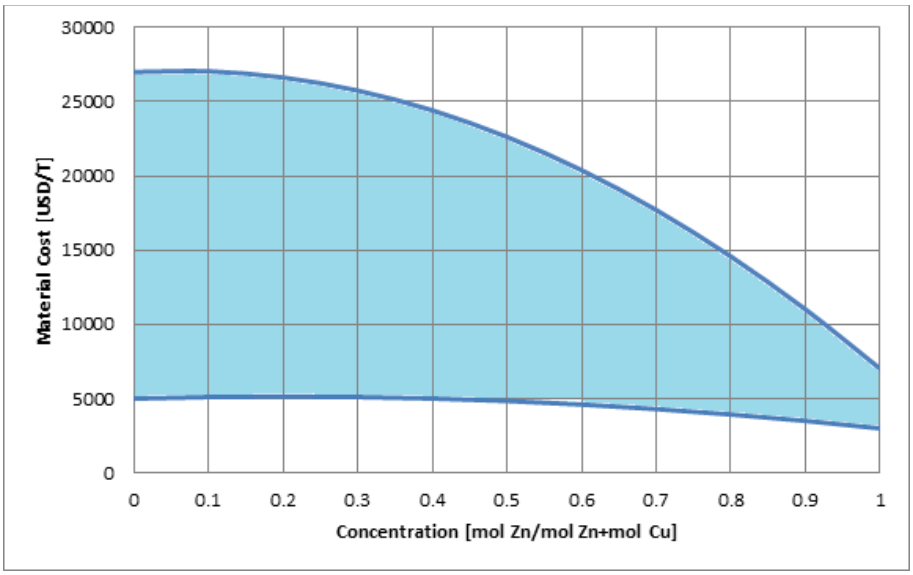

Figure 94 Estimate at how brass cost might vary with zinc concentration. The shaded region indicates estimated cost range.

Brass appropriate for Miscibility Gap Alloys was estimated to have a price between 3000 and 28000 USD/Tonne based on the assumed manufacturing modifier and commodity prices of copper and zinc.

Copper Price

Copper was the first metal widely used by mankind (perhaps as early as 7000 BC). Copper may be refined from copper sulphide ores or separated from leached copper oxide ores [165]. Copper is often traded as a commodity and currently has a price of around 7090 USD/Tonne. Ten years ago the copper price was less than half of what it is today.

Figure 95 Copper Commodity price over the last 25 years [166].

Powdered or chopped wire copper appropriate for Miscibility Gap Alloys was found to have a commercially available price between 5000 and 27000 USD/Tonne.

Graphite Price

Graphite appears to have three different commonly traded forms; lump, flake and amorphous. Lump graphite is the most valuable form and of the highest purity, Sri-Lanka contains the only mine producing this form [167]. Flake graphite is of relatively high purity 80-98% and is more common than lump graphite. Amorphous graphite is the cheapest form and the most commonly traded, it has around 70-75% carbon with the main impurity being ash [168]. Amorphous graphite is most appropriate for Miscibility Gap Alloys. Sodium silicate binder is added to bond the graphite on firing at around 1:12 mass fraction.

Amorphous graphite with sodium silicate binder appropriate for Miscibility Gap Alloys was found to have a commercially available price between 320 and 850 USD per Tonne.

Iron Price

Iron is an abundant metal in the Earth's crust chiefly occurring in the ores Hematite (Fe_2O_3) and Magnetite (Fe_3O_4) [169]. The metal may be produced from the ore through and oxidation-reduction reaction in a blast furnace. Iron, as steel, is ubiquitous in modern society and is undoubtedly the most utilised metal and alloy by humanity. Iron ore is traded as a commodity either as pellets (which may be fed directly into a blast furnace) or fines (which must be sintered prior to the furnace, attracting an additional processing cost). The current commodity price for iron ore pellets sits in a trough at around 121.35 USD/Tonne.

Figure 96 Iron Ore Pellet Commodity price over the last 5 years

Iron powder or pellets appropriate for Miscibility Gap Alloys was found to have a commercially available commodity price between 400 and 1000 USD/Tonne.

Magnesium Price

Magnesium is very common in the Earth's crust as many different compounds. The metal is extracted from a number of different minerals through heating and reduction of ores before electrolytic extraction or vapour deposition. The final processes are very energy intensive [170]. Magnesium in a powder form is often used in pyrotechnic products [171]. Magnesium has a commodity price of around 2550 USD/Tonne currently.

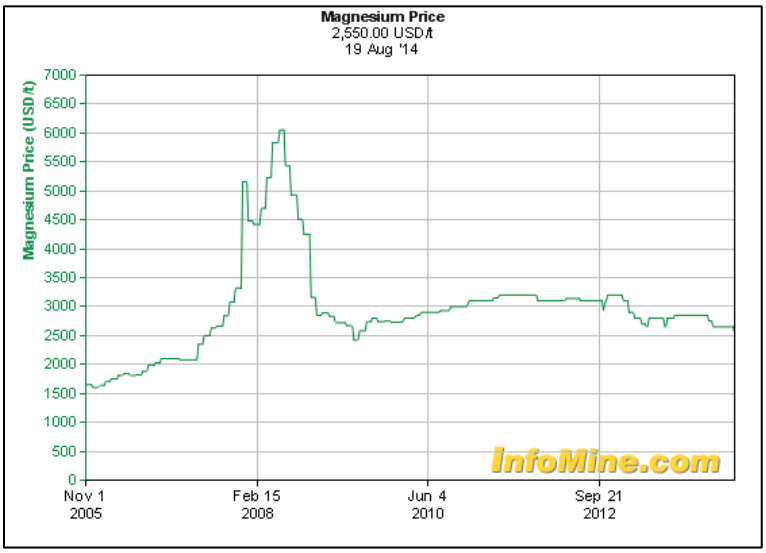

Figure 97 Magnesium Commodity price over the last 9 years [172].

Powdered magnesium appropriate for Miscibility Gap Alloys was found to have a commercially available price between 3000 and 6000 USD/Tonne.

Silicon Price

Silicon is the second most common element in the Earth's crust (after Oxygen) and is found in nearly all sand, rock and clay [173]. Very high purity silicon is used in the semiconductor industry whilst lower purity material is utilised in steels and aluminium alloys. Silicon is often refined by reducing Silica (SiO_2) with coke under heat. Electronics grade silicon is often considered a tradeable commodity. Silicon metal appropriate for Miscibility Gap Alloy applications does not require this purity.

Silicon metal powder appropriate for Miscibility Gap Alloys was found to have a commercially available price between 1700 and 2500 USD per Tonne.

Silicon Carbide Price

Silicon carbide is an extremely hard, chemically inert and thermally conductive compound used in abrasives and sintered parts. It was discovered in 1891 by Edward G. Acheson whilst attempting to create artificial diamonds [174]. Modern manufacturing methods involve heating alumina powder with crushed coke to very high temperatures (>2200 °C).

Owing to widespread use, particularly in abrasives, the cost of silicon carbide powder is low. However, for Miscibility Gap Alloy applications an appropriate binder is required to reaction bond the powder. A 1:12 mass ratio of Sodium Silicate binder is assumed for pricing.

Powdered silicon carbide with a binder appropriate for Miscibility Gap Alloys was found to have a commercially available price between 820 and 2050 USD/Tonne.

Sodium Silicate Binder Price

Sodium Silicate has been shown to be an effective binder for graphite and silicon carbide based matrices [114, 115]. Due to gelation reactions with water it finds other use in reducing unwanted water flow. The material has a commercially available price between 200 and 600 USD/Tonne

Tin Price

Tin has been used and traded by humanity for over 5000 years. Tin is refined from Cassiterite (SnO_2) primarily though is also extracted from sulphide minerals. The raw metal is extracted from the ore by heating with carbon before further heat refining steps are undertaken [175]. The commodity price has quadrupled over the last 10 years though appears to have stabilised at around 22 000 USD/Tonne (see Figure 98).

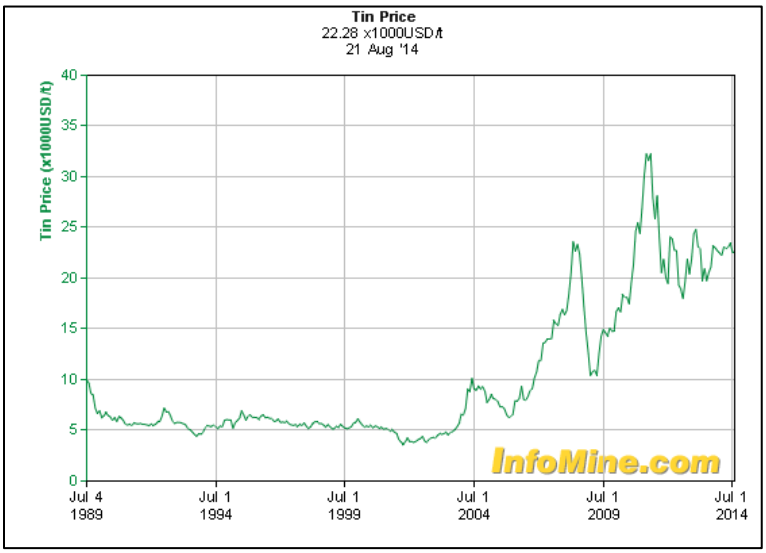

Figure 98 Tin Commodity price over the last 25 years [176].

Powdered tin appropriate for Miscibility Gap Alloys was found to have a commercially available price between 20000 and 45000 USD per Tonne.

Zinc Price

Zinc is commonly used as a galvanising coating on steel components and as a sacrificial anode on other structures. It is often found in veins that also contain Lead and Silver [177]. Zinc blende is the most common ore containing zinc. Zinc is refined from this ore though roasting and subsequent leaching or smelting operations [178]. Zinc is a traded commodity and has been reasonably stable in price (±500 USD/Tonne) over the last 5 years at around 2000 USD/Tonne [179].

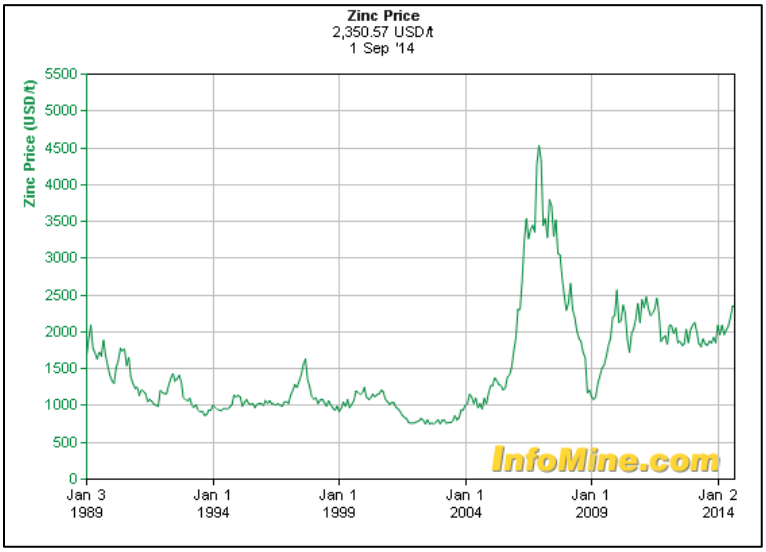

Figure 99 Zinc Commodity price over the last 25 years [176].

Powdered or shot zinc appropriate for Miscibility Gap Alloys was found to have a commercially available price between 1500 and 3500 USD per Tonne.

Summary

The following table summarises the bounds discussed in this appendix:

Table 22 Material cost bounds used in economic analysis.

Material	Cost Lower Bound [USD/T]	Cost Upper Bound [USD/T]
Al	2400	5000
Brass	3000	28000
Cu	5000	27000
C	320	850
Fe	400	1000
Mg	3000	6000
Si	1700	2500
SiC	820	2050
Sn	20000	45000
Zn	1500	3500

APPENDIX G: MANUFACTURING COST ESTIMATION

The cost of manufacturing Miscibility Gap Alloys must be considered when determining the total price of implementing a thermal storage system. All MGAs made thus far have been produced through powder metallurgy. Thus this manufacturing method was utilised in economic modelling. Typical bounds for material utilisation factors, capital costs, write off times, overhead costs and load factors were taken from the CES database [102]. Here item refers to a single $50mm^3$ piece of Miscibility Gap Alloy that would be subsequently joined to others to form a system.

Table 23 Bounds for manufacturing costs taken from the CES database [102].

Material	Units	Symbol	Bounds
Mass Utilisation Factor	[Mass in Product/Mass Used]	$u_{Mat\ Uti}$	[0.9, 0.99]
Tool Cost	[USD/Tool set]	c_{Tool}	[5050, 16100]
Tool Life	[Items/Tool set]	$N_{Tool\ life}$	[10000, 50000]
Production Rate	[Items/hour]	r_{Prod}	[120, 1200]
Overhead Cost	[USD/hour]	$c_{Overhead}$	[100, 200]
Capital Cost	[USD]	$c_{Capital}$	[70600, 2830000]
Capital Write off Time	[Years]	$\Delta t_{Write\ Off}$	[5, 10]
Load Factor	[Time Producing/Time]	$u_{Load\ Factor}$	[0.4,0.6]

The batch size was assumed to be different for the three different deployments analysed. The air heaters were assumed to be produced with a batch size of 2000 systems resulting in 1.152 million items, the barrels were assumed to be made in a batch of 1000 systems resulting in 1.6 million items and the central receiver was assumed to be a one off requiring 3.3629 million items. The batch size was selected to be large enough such that the manufacturing cost per item was independent of item number (that is, the systems would be produced with an economical batch size).

APPENDIX G: MANUFACTURING COST ESTIMATION

APPENDIX H: INFRASTRUCTURE COST ESTIMATION

When estimating a normalised capital cost of a Miscibility Gap Alloy Thermal Storage deployment several calculations were required. The requirements for three different deployments were considered:

1) Air heating.
2) Thermal storage.in a barrel implementation
3) Thermal storage where the device was the primary receiver.

The different deployments had different specific requirements on the thermal storage device, influencing the cost.

The air heater deployment was considered to be similar to the device presented in chapter §8.1. If further storage capacity were required it was assumed that several units would be employed. This discretisation introduces a large infrastructure cost in encapsulation.

The barrel implementation of thermal storage involves sealing the Miscibility Gap Alloy in a 200 L drum with one central pipe for heat exchange to a fluid. The drums were considered due to availability and ease of handling.

The directly irradiated storage concept is based off the receiver of the Salùcar PS10 10 MW Solar Thermal Power Plant at Sanlùcar de Mayor near Saville in Spain. The thermal storage volume was taken as a rectangular prism 8x14x12 m where a hemi-cylindrical section with radius 7 m had been cut from the front face. All surfaces were assumed to have an immediate encapsulation and a surrounding of atmosphere with 100

mm coverage. Pipes running vertically were assumed to be spaced at half metre intervals along the back surface yielding 28 pipes.

Table 24 Recommended infrastructure elements and price bounds for each Miscibility Gap Alloy of interest. Atmosphere costs have units of [USD/m^3], Piping costs [USD/m], Encapsulation costs [USD/m2] and Insulation costs [USD/m^2]. *Barrel implementation includes barrel encapsulation, foundation and shipping container costs.

MGA	Atmosphere		Piping		Encapsulation		Encapsulation*		Insulation	
Brass-C	Argon		SS Pipe		SS Sheet		SS Barrel		High Temp Min Wool	
	0.8	1.2	24	36	132	198	292	356	10	15
Cu-C	Argon		SS Pipe		SS Sheet		SS Barrel		High Temp Min Wool	
	0.8	1.2	24	36	132	198	292	356	10	15
Cu-Fe	Argon		SS Pipe		SS Sheet		SS Barrel		High Temp Min Wool	
	0.8	1.2	24	36	132	198	292	356	10	15
Mg-Fe	Air		MS Pipe		MS Sheet		Barrel		Min Wool	
	0	0	12	18	32	48	225	277	4	6
Si-SiC	Argon		Ceramic Pipe		Ceramic Coating		Ceramic Coated Barrel		High Temp Min Wool	
	0.8	1.2	48	72	264	396	850	1042	10	15
Sn-Al	Air		MS Pipe		MS Sheet		Barrel		Min Wool	
	0	0	12	18	32	48	225	277	4	6
Zn-C	Air		MS Pipe		MS Sheet		Barrel		Min Wool	
	0	0	12	18	32	48	225	277	4	6

Infrastructure prices were taken from a number of different resources. Atmosphere costs assumed. Piping was costed from [134] with assumptions made for stainless steel and ceramic equivalents. Encapsulation costs were taken from [135] ceramic coating was assumed. Barrel prices were found from, whilst shipping container costs were based on [137] with an assumption on retrofitting cost. The slab was assumed to be rectangular 7x3 m in dimension and a depth of 1 m. Concrete with reinforcement

was considered to cost 620 [USD/m^3]. Insulation prices were taken from [138]. An uncertainty of 20% was assumed for all costs.

APPENDIX H: INFRASTRUCTURE COST ESTIMATION

APPENDIX I: AIR HEATER ENGINEERING DRAWINGS

The following pages are engineering drawings for the air heater design discussed in section §8.1.

ITEM	PART NAME	QTY	MATERIAL	DRAWING NO
1	SHELL	1	SS	
2	SHELL FRONT	1	SS	
3	MGA BLOCK CADDY	1	SS	
4	FLOW DRIVEN SHUTTER	1	SS	
5	SHUTTER	4	SS	
6	LID	1	SS	
7	LID SHUTTER	1	SS	
8	FAN	1	SUPPLIED	
9	CERAMIC TILE	4	SUPPLIED	
10	MGA BLOCKS AND HEATER	1	SUPPLIED	

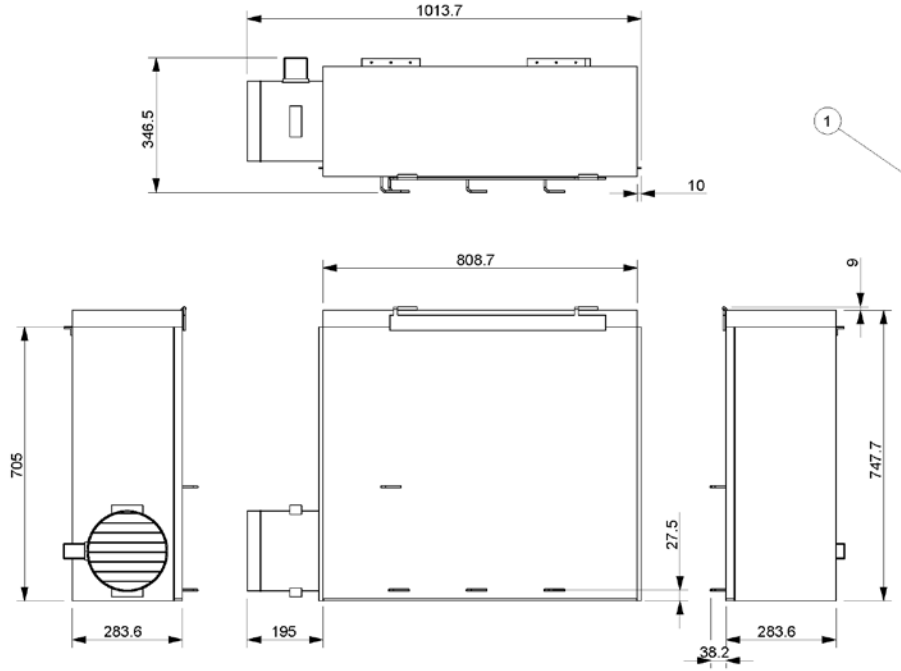

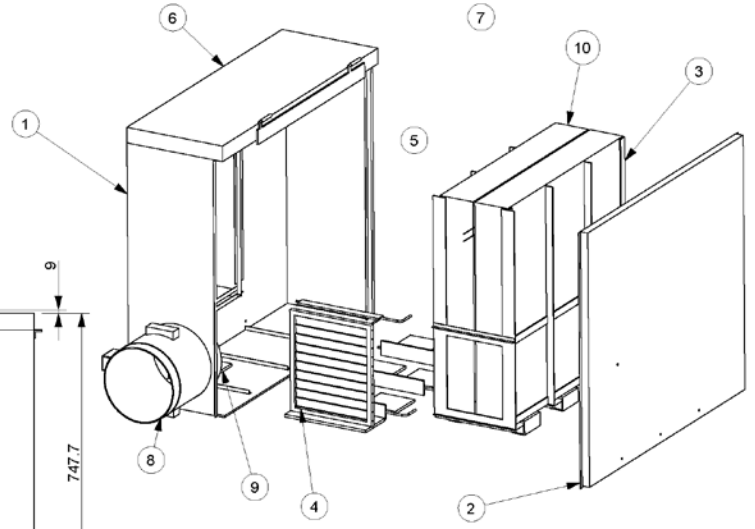

NO	BY	DATE	CHANGE	CH	DATE
2	AR	12/06/15	SHUTTER DESIGN AND TILES		
1	AR	18/09/14	TO BASELINE		

ANTHONY RAWSON	
AIR HEATER: GENERAL ASSEMBLY	
DEFAULT TOLERANCE UP TO 6MM:± 0.1 6MM TO 30MM:± 0.2 30MM TO 120MM:± 0.3 OVER 120MM:± 0.5	ASM-AHE-01
1:10	ALL DIMENSIONS IN MM (UNLESS STATED)

A3

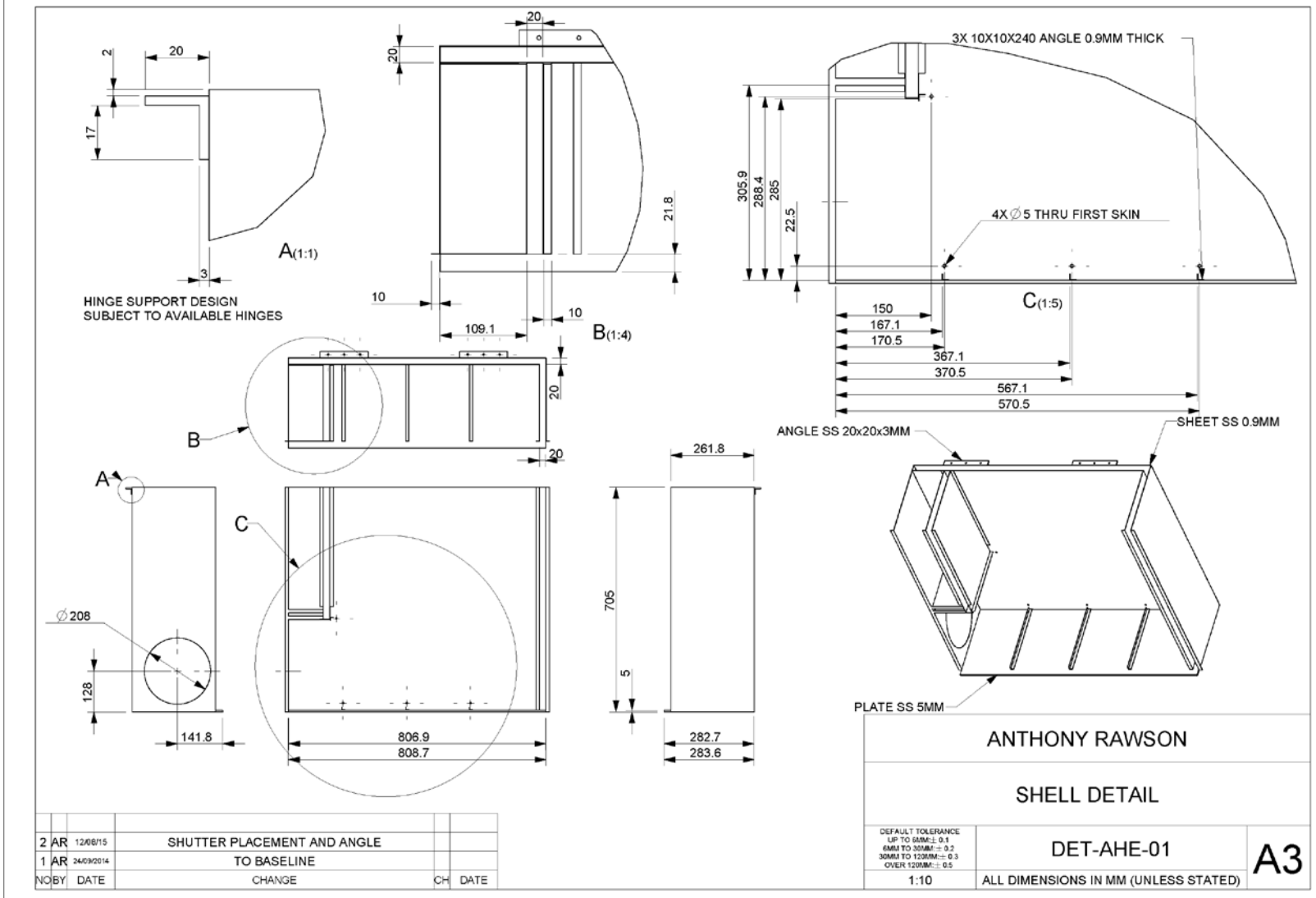
3X 10X10X240 ANGLE 0.9MM THICK
4X ∅5 THRU FIRST SKIN
HINGE SUPPORT DESIGN
SUBJECT TO AVAILABLE HINGES
A(1:1)
B(1:4)
C(1:5)
ANGLE SS 20x20x3MM
SHEET SS 0.9MM
PLATE SS 5MM
∅208
2 AR 12/06/15 SHUTTER PLACEMENT AND ANGLE
1 AR 24/09/2014 TO BASELINE
NO BY DATE CHANGE CH DATE
ANTHONY RAWSON
SHELL DETAIL
DET-AHE-01
A3
1:10
ALL DIMENSIONS IN MM (UNLESS STATED)

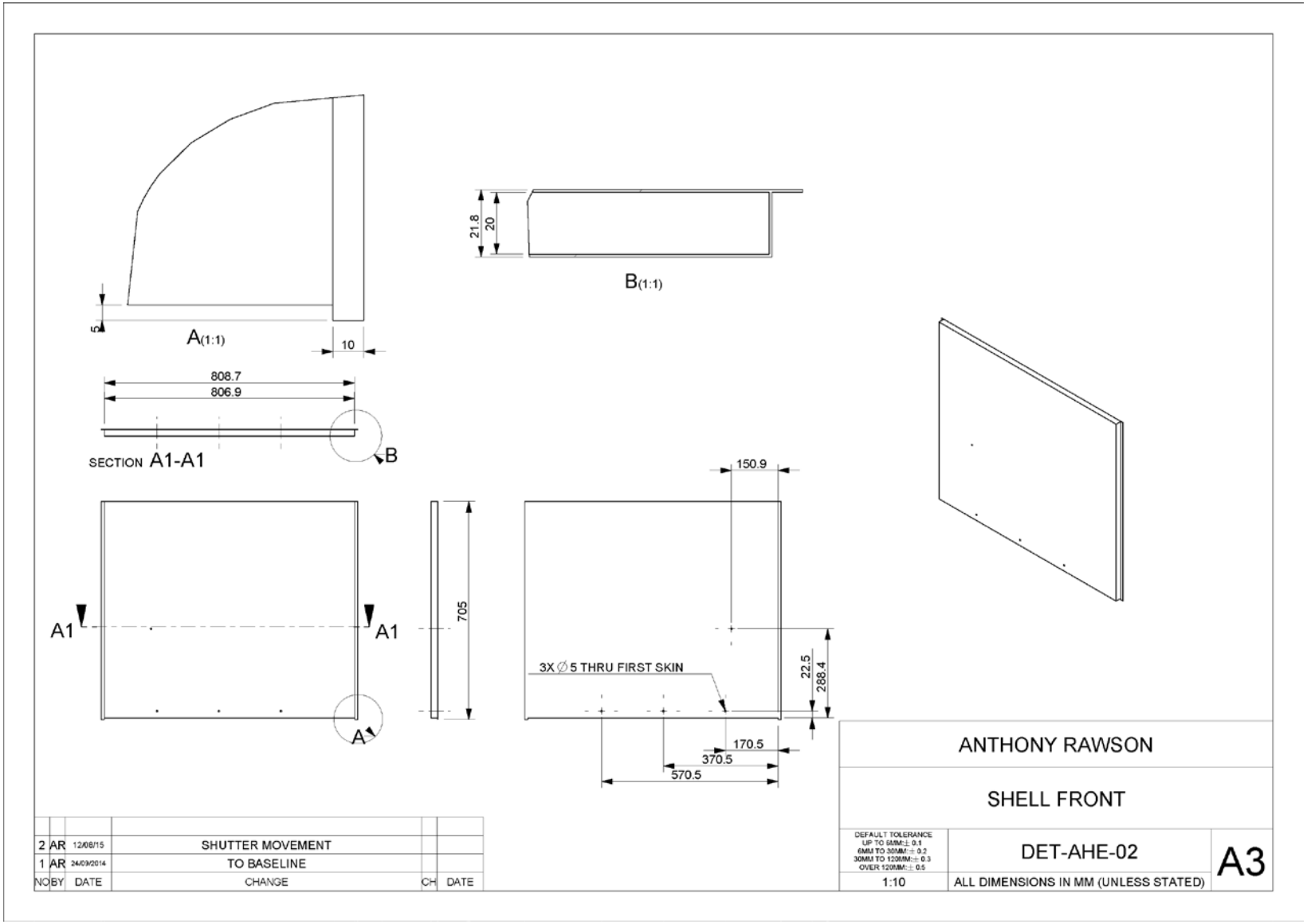
21.8
20
B(1:1)
5
A(1:1)
10
808.7
806.9
SECTION A1-A1
B
150.9
A1
A1
705
3X ∅ 5 THRU FIRST SKIN
22.5
288.4
170.5
370.5
570.5
A
2 AR 12/06/15 SHUTTER MOVEMENT
1 AR 24/09/2014 TO BASELINE
NO BY DATE CHANGE CH DATE
ANTHONY RAWSON
SHELL FRONT
DEFAULT TOLERANCE
UP TO 6MM: ± 0.1
6MM TO 30MM: ± 0.2
30MM TO 120MM: ± 0.3
OVER 120MM: ± 0.5
DET-AHE-02
A3
1:10
ALL DIMENSIONS IN MM (UNLESS STATED)

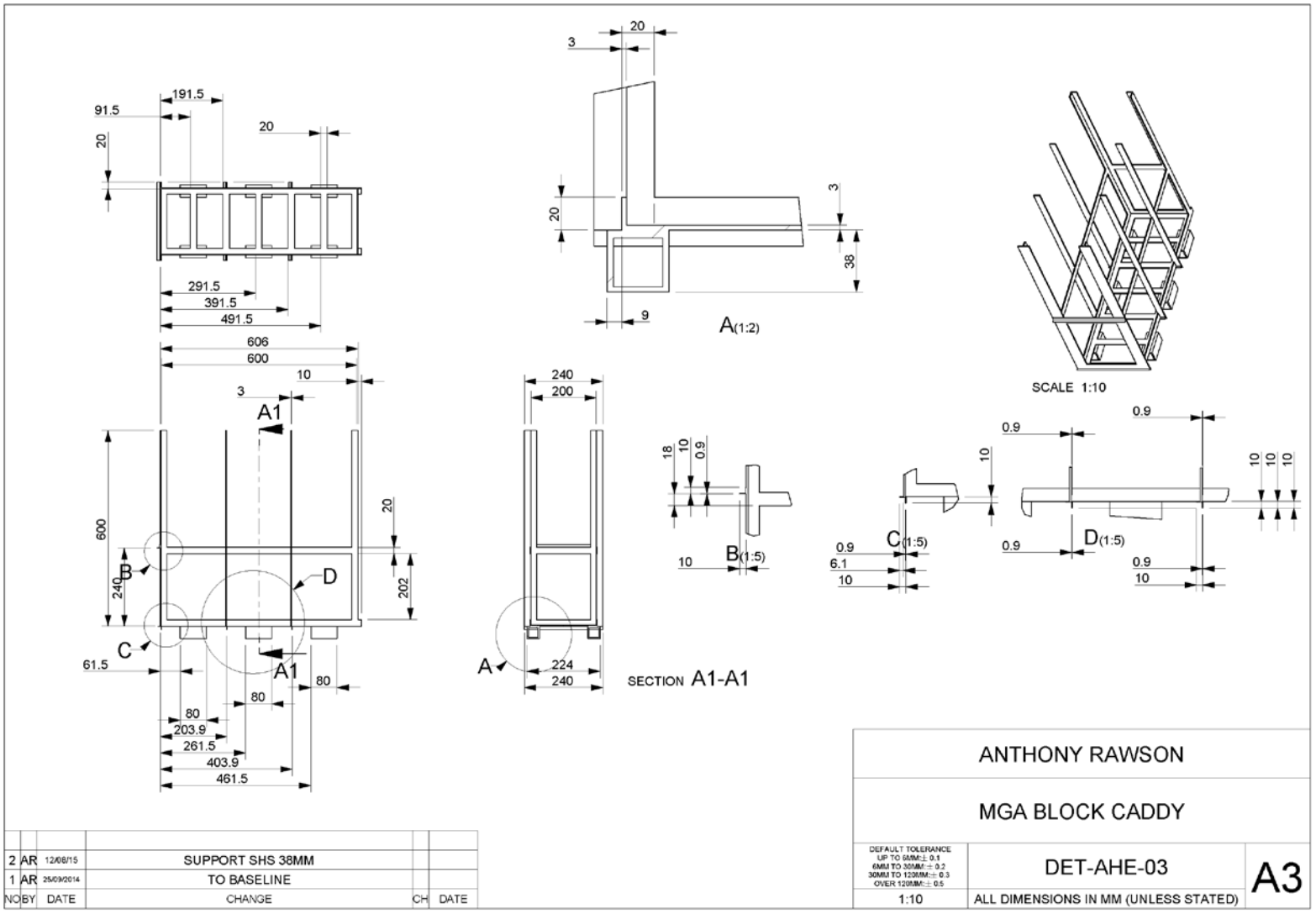
191.5
91.5
20
20
291.5
391.5
491.5
606
600
10
3
A1
600
240
B
D
C
A1
61.5
80
80
80
203.9
261.5
403.9
461.5
20
202
20
3
38
9
A(1:2)
240
200
A
224
240
SECTION A1-A1
18
10
0.9
B(1:5)
10
SCALE 1:10
0.9
0.9
10
C(1:5)
0.9
6.1
10
D(1:5)
0.9
0.9
10
10
10
10
2 AR 12/06/15 SUPPORT SHS 38MM
1 AR 25/09/2014 TO BASELINE
NO BY DATE CHANGE CH DATE
ANTHONY RAWSON
MGA BLOCK CADDY
DEFAULT TOLERANCE
UP TO 6MM:± 0.1
6MM TO 30MM:± 0.2
30MM TO 120MM:± 0.3
OVER 120MM:± 0.5
DET-AHE-03
A3
1:10
ALL DIMENSIONS IN MM (UNLESS STATED)

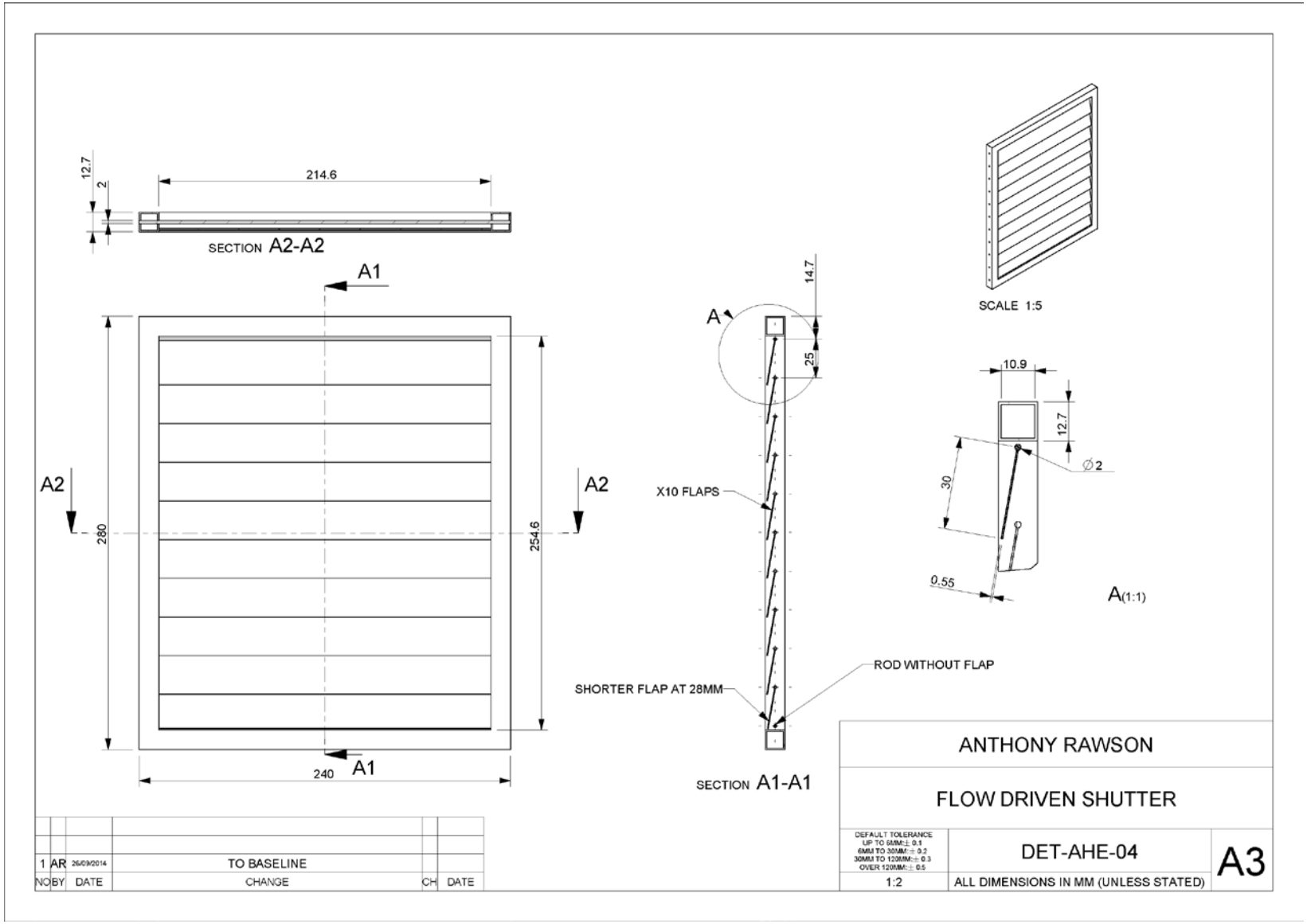
12.7
2
214.6
SECTION A2-A2
A1
A2
A2
280
254.6
240
A1
A
14.7
25
X10 FLAPS
SHORTER FLAP AT 28MM
ROD WITHOUT FLAP
SECTION A1-A1
SCALE 1:5
10.9
12.7
∅2
30
0.55
A(1:1)
1 AR 26/09/2014 TO BASELINE
NO BY DATE CHANGE CH DATE
ANTHONY RAWSON
FLOW DRIVEN SHUTTER
DEFAULT TOLERANCE
UP TO 6MM:± 0.1
6MM TO 30MM:± 0.2
30MM TO 120MM:± 0.3
OVER 120MM:± 0.5
DET-AHE-04
A3
1:2
ALL DIMENSIONS IN MM (UNLESS STATED)

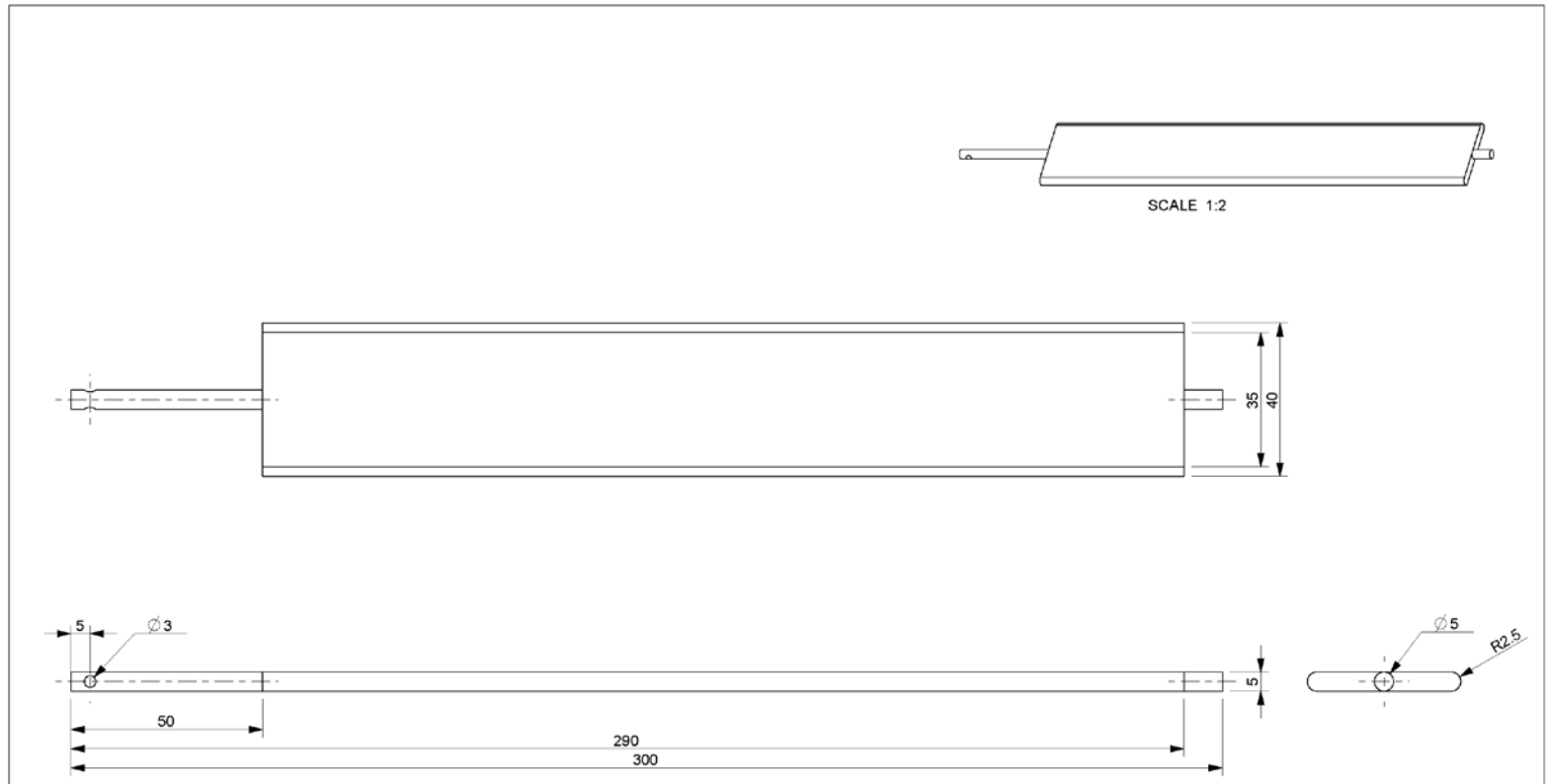

NO	BY	DATE	CHANGE	CH	DATE
1	AR	29/09/2014	TO BASELINE		

ANTHONY RAWSON

SHUTTER

DEFAULT TOLERANCE
UP TO 6MM:± 0.1
6MM TO 30MM:± 0.2
30MM TO 120MM:± 0.3
OVER 120MM:± 0.5

DET-AHE-05

A3

1:1

ALL DIMENSIONS IN MM (UNLESS STATED)

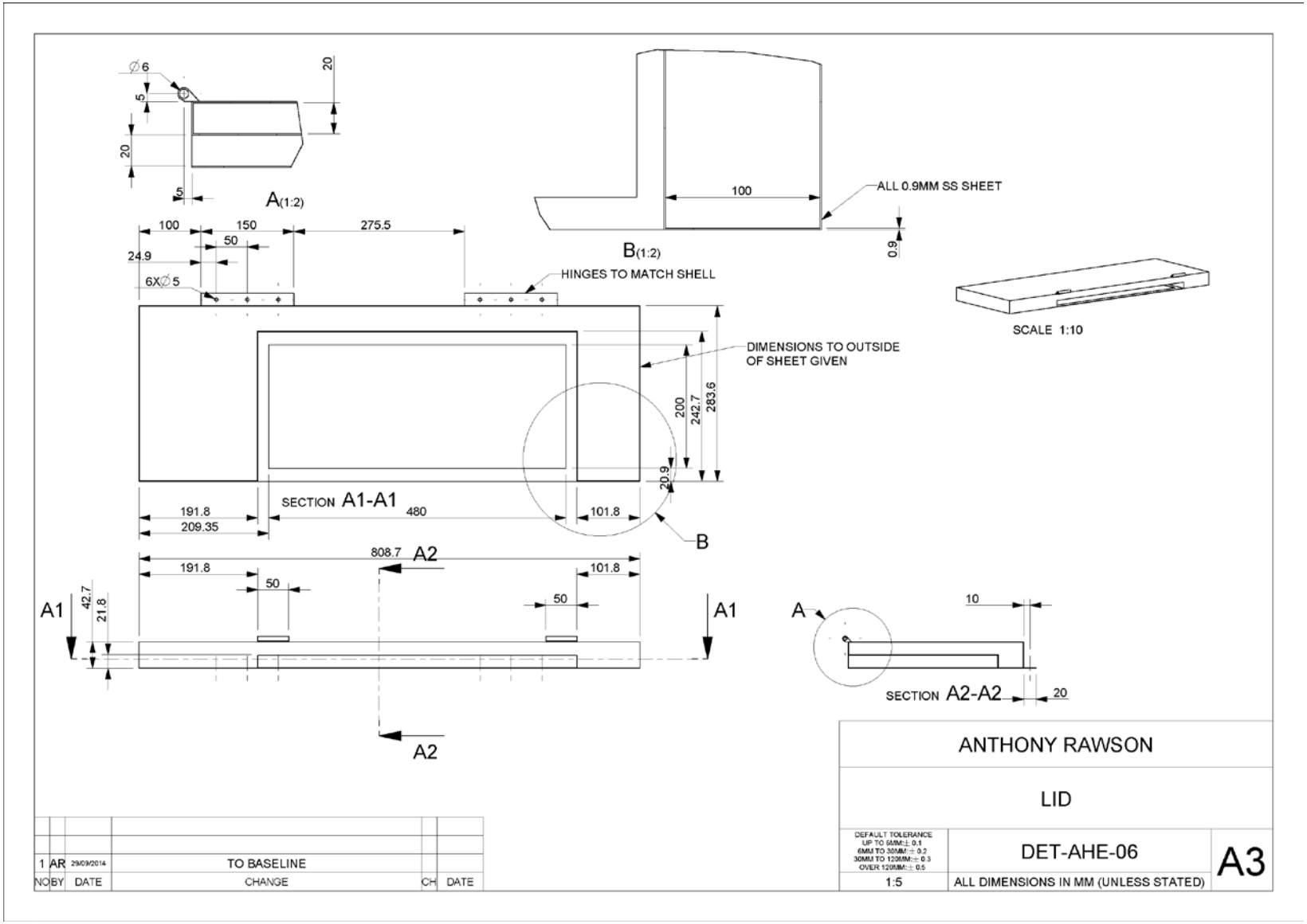
Ø6
5
20
20
5
A(1:2)
100
ALL 0.9MM SS SHEET
B(1:2)
0.9
100
150
275.5
50
24.9
6XØ5
HINGES TO MATCH SHELL
SCALE 1:10
DIMENSIONS TO OUTSIDE
OF SHEET GIVEN
200
242.7
283.6
20.9
SECTION A1-A1
191.8
209.35
480
101.8
B
808.7
A2
191.8
101.8
50
50
A1
42.7
21.8
A1
A
10
SECTION A2-A2
20
A2
ANTHONY RAWSON
LID
DEFAULT TOLERANCE
UP TO 6MM:± 0.1
6MM TO 30MM:± 0.2
30MM TO 120MM:± 0.3
OVER 120MM:± 0.5
DET-AHE-06
A3
1:5
ALL DIMENSIONS IN MM (UNLESS STATED)
1 AR 29/09/2014
TO BASELINE
NO BY DATE
CHANGE
CH DATE

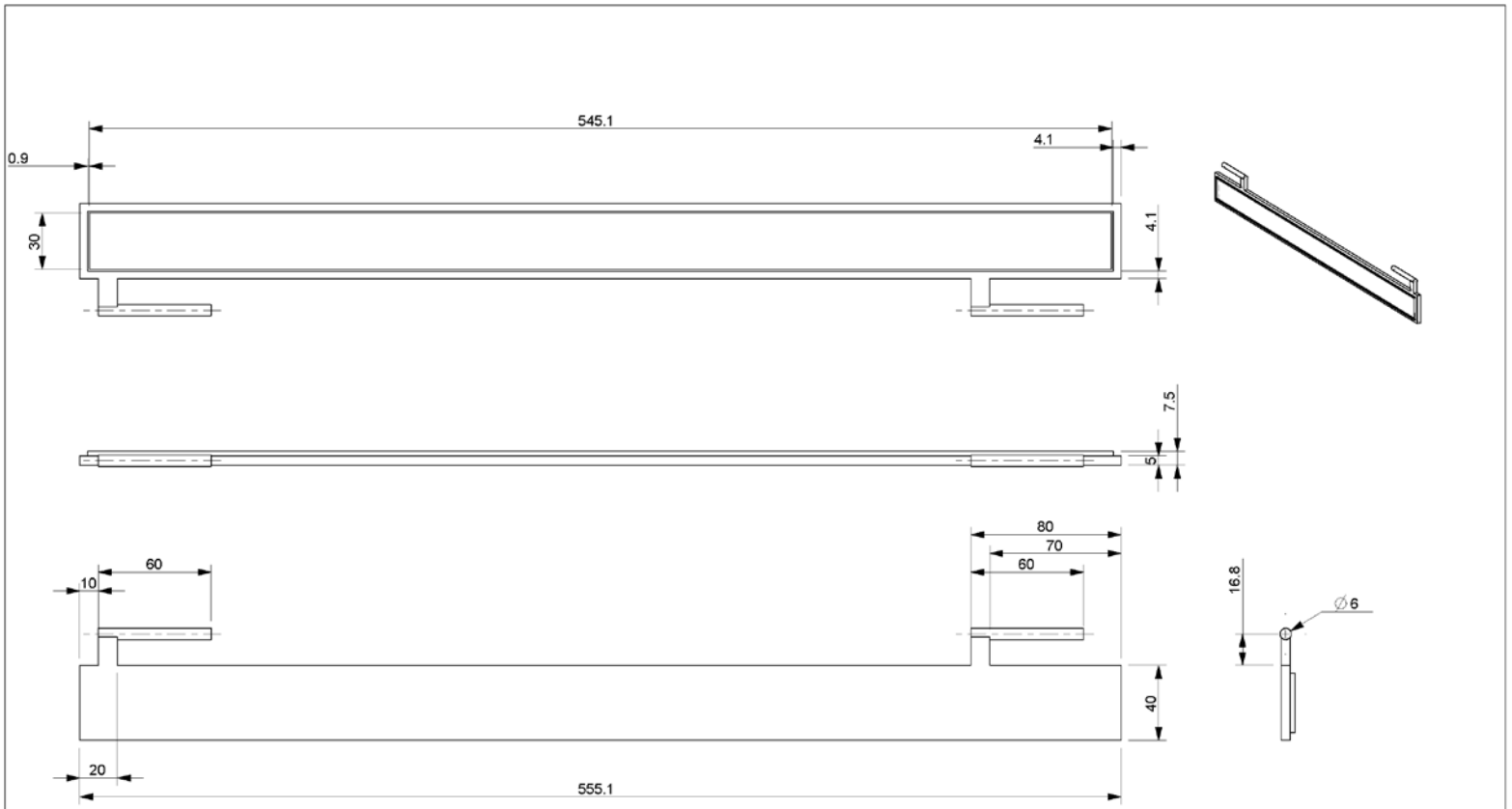

NO	BY	DATE	CHANGE	CH	DATE
1	AR		TO BASELINE		

ANTHONY RAWSON

LID SHUTTER

DEFAULT TOLERANCE
UP TO 6MM:± 0.1
6MM TO 30MM:± 0.2
30MM TO 120MM:± 0.3
OVER 120MM:± 0.5

DET-AHE-07

A3

1:2

ALL DIMENSIONS IN MM (UNLESS STATED)

APPENDIX I: AIR HEATER ENGINEERING DRAWINGS

APPENDIX J: AIR HEATER DISCHARGE CHARACTERISTIC CALCULATIONS

The Air Heater device introduced in §8.1 and shown in detail in the previous appendix was analysed using simple heat transfer theory to approximate discharge characteristics. The air heater was designed to have 5 different configurations which presented an airflow with 5 different cross sectional areas and heat transfer surfaces. The areas were as follows (Table 25):

Table 25 Flow cross sectional area and heat transfer surface for different configurations of the air heater.

Configuration	Description	Cross Sectional Area [m^2]	Heat Transfer Surface [m^2]
Bypass	Bypass Open, Shutters Closed	0.024	0.12
Level 1	Bypass Closed, 1 Shutter Open	0.007	0.12
Level 2	Bypass Closed, 1 & 2 Shutter Open	0.014	0.24
Level 3	Bypass Closed, 1, 2 & 3 Shutter Open	0.045	0.48
All Open	Bypass Open, 1, 2 & 3 Shutter Open	0.069	0.6

A time step was specified at which all properties would be calculated during the discharge operation. During each time step the Miscibility Gap Alloy would transfer some amount of energy to the flow, heating the air and cooling the material. The amount of energy transferred during each time step was evaluated by calculating the flow velocity and approximating the heat transfer through evaluation of the Reynolds, Prandtl and Nusselt numbers. Each simulation was ended when the block reached 370 °C after which the time to discharge and the average air temperature out could be evaluated.

The inlet volumetric flow rate ($\dot{v}_{Air,Inlet}$) and inlet temperature (T_{Air}) were specified for each case and constant through the discharge operation. The air was treated as an ideal gas, allowing the density of the flow at the inlet and outlet to be calculated.

$$\rho_{Air} = \frac{p_{Atm}}{R_{Air} T_{Air}} \quad 158.$$

Here ρ_{Air} is the air density at the inlet, p_{Atm} it atmospheric pressure and R_{Air} is the specific gas constant for air .

The density could then be used to calculate the mass flow rate ($\dot{m}_{Air}$):

$$\dot{m}_{Air} = \dot{v}_{Air,Inlet} \rho_{Air} \quad 159.$$

The mean velocity ($v_{Air,Mean}$) was then found using the mass flow rate, mean density and specified cross sectional area:

$$v_{Air,Mean} = \frac{\dot{m}_{Air}}{\rho_{Air,Mean} A_{CS}} \quad 160.$$

The Reynolds number and Prandtl numbers could then be evaluated:

$$Re = \frac{\rho_{Air,Mean} v_{Air,Mean} L}{\mu_{Air,Mean}} \quad 161.$$

$$Pr = \frac{c_{p,Air,Mean} \mu_{Air,Mean}}{k_{Air,Mean}} \quad 162.$$

Here $\mu_{Air,Mean}$ is the mean dynamic viscosity of the air through the flow path, $c_{p,Air,Mean}$ is the mean heat capacity of the air through the flow path and $k_{Air,Mean}$ is the mean thermal conductivity of air through the flow path.

The flow was approximated as that over a flat plate such that the Nusselt number could be estimated using [89]:

$$\mathrm{Nu}=\begin{cases} 0.664\mathrm{Re}^{1/2}\mathrm{Pr}^{1/3} & \mathrm{Re}<10000 \\ 0.0296\mathrm{Re}^{4/5}\mathrm{Pr}^{1/3} & \mathrm{Re}\geq 10000 \end{cases} \quad 163.$$

The Nusselt number then yields the heat transfer coefficient with knowledge of the length of the flow path and the thermal conductivity of the air:

$$\mathrm{Nu}\equiv\frac{\dot{q}L}{k_{\mathrm{Air,Mean}}} \quad 164.$$

Here $\dot{q}$ is the heat flux between the surface(s) and the air and L is the length of the flow path.

The heat transfer coefficient establishes the heat transfer ($\dot{Q}$) with knowledge of the specified heat transfer area (A):

$$\dot{Q}=\dot{q}A\left(T_{\mathrm{Block}}-T_{\mathrm{Air,Mean}}\right) \quad 165.$$

The air will exit the air heater at temperature according to:

$$T_{\mathrm{Air,exit}}=T_{\mathrm{Air,Inlet}}+\frac{\dot{Q}}{C_{\mathrm{p,Air,Mean}}\dot{m}_{\mathrm{Air}}} \quad 166.$$

The energy (Q) exchanged to the air during the time step is:

$$Q=\dot{Q}\Delta t \quad 167.$$

The total block enthalpy (H_{Block}) will hence be reduced by the amount E and suffer a reduction in temperature or progress towards freezing.

$$H_{\mathrm{Block,New}}=H_{\mathrm{Block,Previous}}\text{-}Q \quad 168.$$

$$h_{\mathrm{Block}}=\frac{H_{\mathrm{Block}}}{m_{\mathrm{Block}}} \quad 169.$$

$$h_{block}=\begin{cases}\int_0^{T} c_p(T)\,dT & T<T_m \\ \int_0^{T_m} c_p(T)\,dT+\lambda(1-\psi) & T=T_m \\ \int_0^{T_m} c_p(T)\,dT+\lambda+\int_{T_m}^{T} c_p(T)\,dT & T>T_m\end{cases} \quad 170.$$

Here ψ represent the mass fraction of molten material, λ the latent heat of fusion and c_p is the block heat capacity as a function of temperature. The temperature may be back calculated using interpolation methods. The new outlet temperature and block temperature are then carried to the next time step and the calculations performed iteratively.